ANL-77-65
Part I

ANL-77-65
Part I

MASTER

RADIOLOGICAL AND ENVIRONMENTAL RESEARCH DIVISION ANNUAL REPORT

Fundamental Molecular Physics and Chemistry

October 1976—September 1977

U of C-AUA-USERDA

ARGONNE NATIONAL LABORATORY, ARGONNE, ILLINOIS

Prepared for the U. S. ENERGY RESEARCH AND DEVELOPMENT ADMINISTRATION under Contract W-31-109-Eng-38

DISCLAIMER

The facilities of Argonne National Laboratory are owned by the United States Government. Under the terms of a contract (W-31-109-Eng-38) between the U. S. Department of Energy, Argonne Universities Association and The University of Chicago, the University employs the staff and operates the Laboratory in accordance with policies and programs formulated, approved and reviewed by the Association.

MEMBERS OF ARGONNE UNIVERSITIES ASSOCIATION

The University of Arizona
Carnegie-Mellon University
Case Western Reserve University
The University of Chicago
University of Cincinnati
Illinois Institute of Technology
University of Illinois
Indiana University
Iowa State University
The University of Iowa
Kansas State University
The University of Kansas
Loyola University
Marquette University
Michigan State University
The University of Michigan
University of Minnesota
University of Missouri
Northwestern University
University of Notre Dame
The Ohio State University
Ohio University
The Pennsylvania State University
Purdue University
Saint Louis University
Southern Illinois University
The University of Texas at Austin
Washington University
Wayne State University
The University of Wisconsin

Printed in the United States of America
Available from
National Technical Information Service
U. S. Department of Commerce
5285 Port Royal Road
Springfield, Virginia 22161
Price: Printed Copy $9.50; Microfiche $3.00

Distribution Category:
Biology and Medicine (UC-48)

ANL-77-65
Part I

ARGONNE NATIONAL LABORATORY
9700 South Cass Avenue
Argonne, Illinois 60439

RADIOLOGICAL AND ENVIRONMENTAL RESEARCH DIVISION ANNUAL REPORT

Fundamental Molecular Physics and Chemistry

October 1976 through September 1977

R. E. Rowland, Division Director
Mitio Inokuti, Section Head

Preceding Report: ANL-76-88, Part I, July 1975-September 1976

FOREWORD

The seventh Annual Report of this section should convey an idea of the continuing and vigorous progress of our scientific endeavors. The Section's activities belong to three general scientific areas — electron collisions with molecules, photoabsorption and its consequences, such as photoelectron emission, and pertinent theories.

The central programmatic goal of the activities, supported by DOE-DBER, is twofold. First, we generate cross-section data for electron and photon interactions required for detailed analyses of radiation actions on matter, including biological substances. The need for such analyses arises in the evaluation of health effects of nuclear fission and fusion technologies. Second, we study chemical physics of atmospheric-pollutant and related molecules, so as to provide some of the basic spectroscopic information needed for modeling atmospheric chemistry. The motivation here is to contribute to the evaluation of environmental effects of non-nuclear energy technologies.

The basic nature of our expertise implies the possibility of its application to a wide variety of problems in energy generation technologies as well. A case in point is theoretical study on spectral and collision properties of atomic ions, now supported by DOE-DMFE and DBES (see papers 33–41). Another program for studying electron collisions with molecules of MHD interest has been initiated.

The articles in the present volume are loosely grouped and arranged according to subjects treated. Papers 1–6 chiefly concern oscillator-strength distributions; papers 7–17, photoionization, photoelectrons, and photofragmentation; papers 18–32, electron-molecule collisions and secondary electrons; papers 13–52, theoretical atomic and radiation physics; and finally papers 53–54, reviews of physical problems in radiation research.

One of the notable accomplishments was the initiation of the photoelectron spectroscopy of molecular clusters (discussed in papers 8–11). This technique is highly promising for studying electronic structure of molecular clusters in much greater detail than ever before. Apart from basic scientific

novelty, this development has significant programmatic importance insomuch as many of the chemical reactions of atmospheric pollutants occur in cluster phases.

One of our strengths is close contact with numerous other research groups in the world, as indicated by the papers in the present volume jointly authored with our friends. We take this opportunity to thank, collectively, all of our collaborators, too many to be listed individually. Furthermore, we have participated in a number of international activities. They include organizational work for the International Conference on the Physics of Electonic and Atomic Collisions (Paris 1977 and Kyoto 1979), the report committee work for the International Commission on Radiation Units and Measurements (see paper 53), as well as the editorial and other functions of the Radiation Research Society. The Workshop on Computational Methods for Atomic and Molecular Wavefunctions, organized by Y.-K. Kim in August 1977, was highly successful.

TABLE OF CONTENTS

Fundamental Molecular Physics and Chemistry

ELECTRON ENERGY-LOSS SPECTROSCOPY OF ATMOSPHERIC CONSTITUENTS AND POLLUTANTS*

Russell H. Huebner†

Electron-scattering experiments have become a major tool in elucidating the energy-absorbing properties of atoms and molecules. It is possible to relate[1-3] energy-loss intensities measured for small-angle scattering to the oscillator strength of the corresponding optically-induced transition. Thus, electron energy-loss spectra, properly corrected for the finite amount of momentum transferred in an electron-scattering experiment,[4,5] can provide a data base for models of energy transfer between atmospheric constituents and pollutants.

Apparent oscillator-strength distributions for a number of atmospheric molecules (e.g., O_2, N_2O, H_2O, CH_4) have been obtained by the small-angle method.[6-8] Comparisons of the electron impact derived values show good agreement (±15%) with optical values generally considered reliable. These studies have been broadened to include pollutant vapors of common solvents and combustible liquids and aerosol propellants. The latter, namely the chlorofluoromethanes, are recognized as environmental pollutants capable of destroying stratospheric ozone by a photochemically-induced sequence of reactions. Our studies detected errors in earlier optical results by factors as large as two to four for the two molecules of greatest concern in this regard.[9]

Of a more fundamental nature, however, is the growing need for reliable oscillator-strength values for comparison with quantum chemical calculations. The higher theoretical accuracies now feasible for some of the simple diatomic, triatomic, and polyatomic molecules are beginning to make comparisons of both

---

*Abstract of an invited paper presented at the NATO Advanced Study Institute on Spectroscopy and Kinetics of Atmospheric Constituents, Arabba/Dolomiti, Italy, March 13–26, 1977.

†Since June 1977, Program Coordinator, Biomedical and Environmental Research Programs, Office of the Director, ANL.

transition energies and oscillator strengths with experimental values meaningful. For many molecules, reliable oscillator-strength densities are still not available, particularly in spectral regions approaching and extending beyond the first ionization potential. Electron energy-loss measurements provide an important way of studying this spectral region.

REFERENCES

1. M. Inokuti, Rev. Mod. Phys. 43, 297 (1971).
2. E. N. Lassettre and A. Skerbele, "Inelastic Electron Scattering" in Methods in Experimental Physics, Vol. 3, Part B, Academic Press, New York, pp. 868–951 (1974).
3. E. N. Lassettre, Chemical Spectroscopy and Photochemistry in the Vacuum Ultraviolet, C. Sandorfy, P. Ausloos, and M. B. Robin, Eds., D. Reidel Publ. Soc., Dordrecht-Holland, pp. 43–73 (1974).
4. C. E. Kuyatt, Methods in Experimental Physics, Vol. 7, Atomic and Electron Physics, Academic Press, New York, pp. 1–35 (1968).
5. R. J. Celotta and R. H. Huebner, Electron Impact Spectroscopy: An Overview of the Low Energy Aspects, Electron Spectroscopy, Vol. II, C. R. Brundle and A. D. Baker, Eds., Academic Press, to be published.
6. R. H. Huebner, R. J. Celotta, S. P. Mielczarek, and C. F. Kuyatt, J. Chem. Phys. 63, 241 (1975); 63, 4490 (1975).
7. R. H. Huebner, C. H. Fergurson, R. J. Celotta, and S. P. Mielczarek, Vacuum Ultraviolet Radiation Physics, E. F. Koch, R. Haensel, and C. Kunz, Eds., Pergamon-Vieweg, Hamburg, pp. 181–183 (1974).
8. R. H. Huebner, R. J. Celotta, S. R. Mielczarek, and C. E. Kuyatt, Electron and Atomic Collisions, Abstracts of Papers, VIII ICPEAC, Beograd, Vol. 1, B. C. Cobic and M. V. Kurega, Eds., Institute of Physics, Yugoslavia (1973).
9. R. H. Huebner, D. L. Bushnell, Jr., R. J. Celotta, S. P. Mielczarek, and C. E. Kuyatt, Nature 251, 376 (1975).

PERFORMANCE OF THE ELECTRON ENERGY-LOSS SPECTROMETER

H. Tanaka* and R. H. Huebner†

Performance characteristics of the electron energy-loss spectrometer incorporating a new high-resolution hemispherical monochromator are reported. The apparatus achieved an energy-resolution of 25 meV in the elastic scattering mode, and angular distributions of elastically scattered electrons were in excellent agreement with previous workers. Preliminary energy-loss spectra for several atmospheric gases demonstrate the excellent versatility and stable operation of the improved system.

The Electron Energy-Loss Spectrometer (EELS) has been modified with the design and construction of a high-resolution electron monochromator. Design details of the new hemispherical monochromator were reported previously.[1] This and other improvements[2] have significantly increased the performance and flexibility of the EELS system and have particularly enhanced its usefulness for studying atmospheric gases and pollutant vapors.

Tests of the operating characteristics of the modified EELS were begun early in 1977. Energy resolution was the first characteristic studied. For this the resonance scattering mode was selected because it could give a good measure of the effectiveness of the new monochromator. In this mode, both the monochromator and analyzer are tuned to the same energy, and then the energies of both are scanned together. With the monochromator and analyzer set for a scattering angle of 35 degrees only elastically scattered electrons are detected. Figure 1 shows the well-known helium resonance at 19.3 eV observed in this manner. A resolution of 25 meV can be estimated from the observed sharpness of the rise between intensity minimum and maximum across the resonance, which is almost entirely due to the resolution of the monochromator.

*Postdoctoral Appointee from Sophia University, Tokyo.

†Now Program Coordinator for Biomedical and Environmental Research in the Office of the Director, ANL.

Operation in the resonance scattering mode at lower impact energies was also tested. The low-energy resonance in N_2 is shown in Figure 2. Clear evidence of the vibrational structure is observed in this spectrum for a scattering angle of 35°. The positions of the maxima and the overall shape of this resonant feature are in excellent accord with previous measurements.[3] Data accumulation time over the 4 eV range of this spectral feature was less than two minutes.

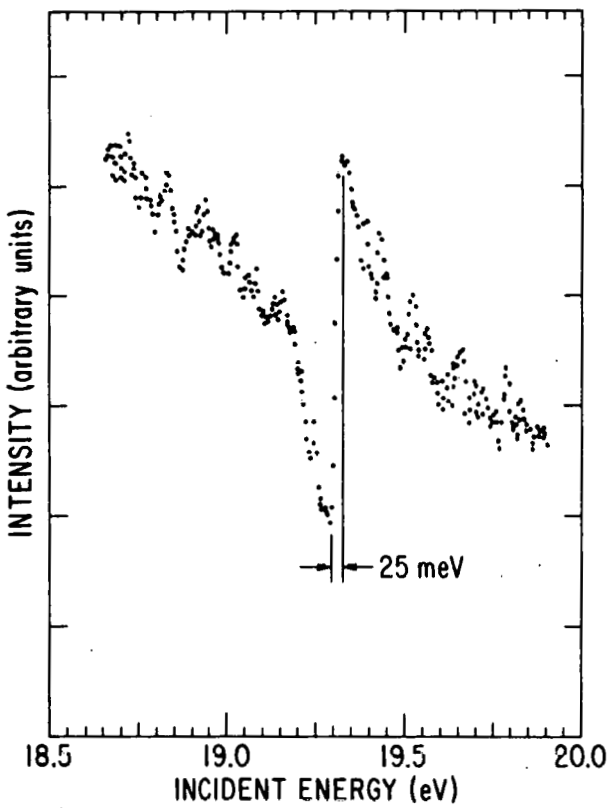

FIG. 1.--The $(1s2s^2)^2S$ resonance in helium at a 35° angle of observation. The energy width of 25 meV between minimum and maximum is a measure of the instrumental resolution due to the extreme sharpness of this resonance feature.
(ANL Neg. 149-78-92)

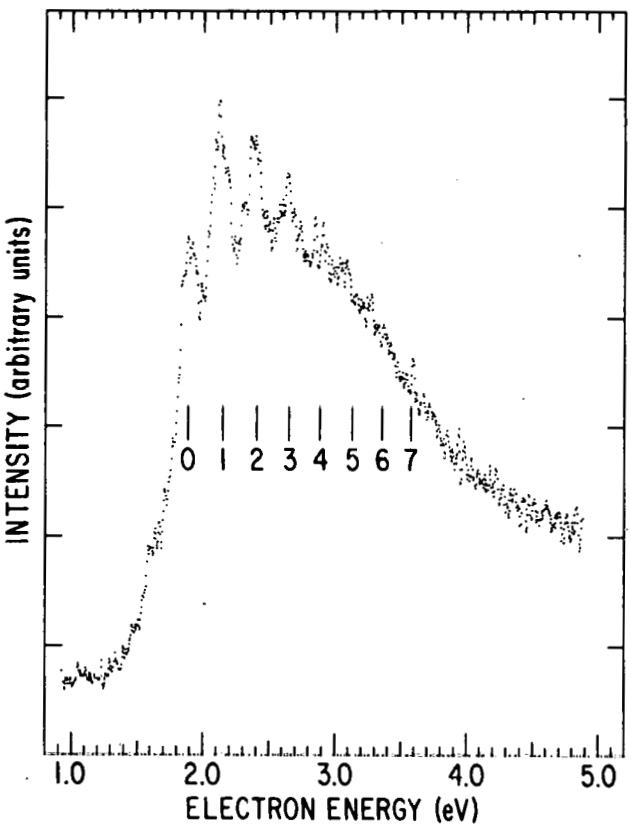

FIG. 2.--Energy dependence of the elastic scattering of electrons at 35° in the region of the $^2\Pi_g$ negative ion state of N_2. Indicated positions of the vibrational structure ($v=0 \rightarrow v'=0,1,2,\ldots$) were taken from observations reported in Ref. 3.
(ANL Neg. 149-78-91)

Tests were also made of the ability of the EELS to measure angular distributions of scattered electrons. As reported previously,[2] extensive modifications of the magnetic shielding and redesign of the collision region were made to improve the EELS measurements of angular distributions. Figures 3, 4, and 5 show angular distributions measured for electrons elastically scattered from argon at incident energies of 20, 50, and 100 eV and compare the data with the measurements of Williams and Willis.[4] The energy resolution of the incident beam was maintained at 56 meV FWHM throughout these measurements. Nominally, the incident beam current was 10^{-9} ampere with an estimated pressure of 10^{-3} torr in the molecular beam. The EELS data were arbitrarily adjusted to the cross-section value[4] at a point between 20 and 40 degrees. No other correction was applied. The close agreement in shapes of the three angular distributions demonstrated the excellent control of stray magnetic and electric fields provided by the present design. Examination of the sharp minimum observed at 66° in Figure 4 indicates that the EELS angular resolution is somewhat greater than 3° compared with 1.5° obtained by Williams and Willis.[4]

Preliminary electron energy-loss measurements have also been conducted for a variety of gases and operating conditions. Spectra for helium, argon, nitrogen, and sulfur hexafluoride were obtained and recorded in digital form, and these data are being processed. Typical system energy resolutions of 50 to 100 meV have been achieved for incident electron energies from to 20 to 300 eV and a variety of scattering angles.

For oscillator-strength determinations by the small-angle method, energy-loss spectra must be obtained for zero-angle scattering. Figure 6 shows a typical energy-loss spectrum for argon obtained at a scattering angle of 0°. In this spectrum, the scattering intensity (i.e., total counts per channel) is plotted vs. the channel number, which is proportional to the amount of energy lost. The incident energy for this spectrum was 200 eV, and the energy-loss range extends from 10 to 50 eV. A portion of the spectrum corresponding to the ionization continuum region between channel numbers 400 and 500 was examined in more detail. Figure 7 shows the energy-loss spectrum

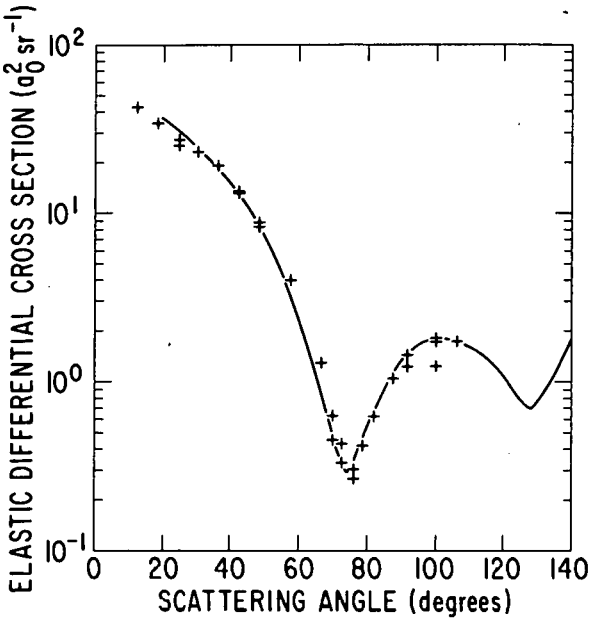

FIG. 3.--Comparison of the angular distribution of 20 eV incident electrons elastically scattered from argon. Our results (+) were adjusted to match the measurements (solid line) of Ref. 4.
(ANL Neg. 149-78-88)

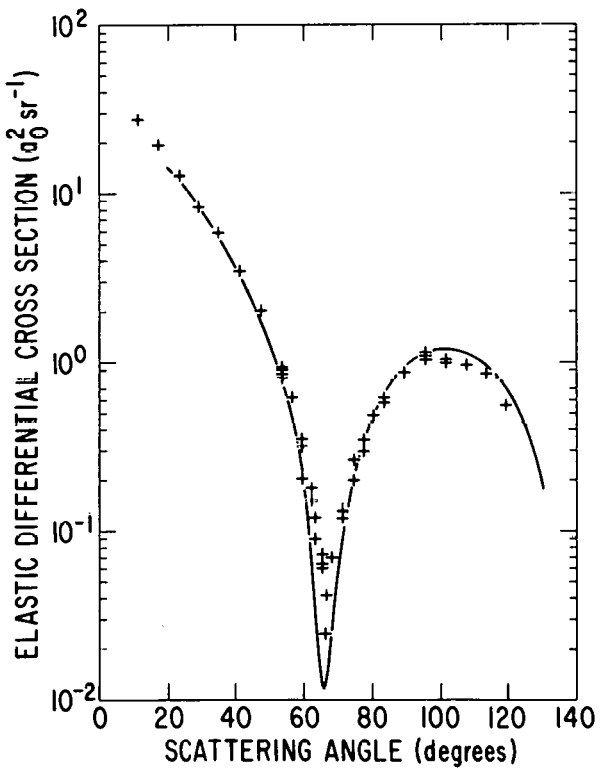

FIG. 4.--Comparison of the angular distribution of 50 eV incident electrons elastically scattered from argon.
(See Figure 3).
(ANL Neg. 149-78-87)

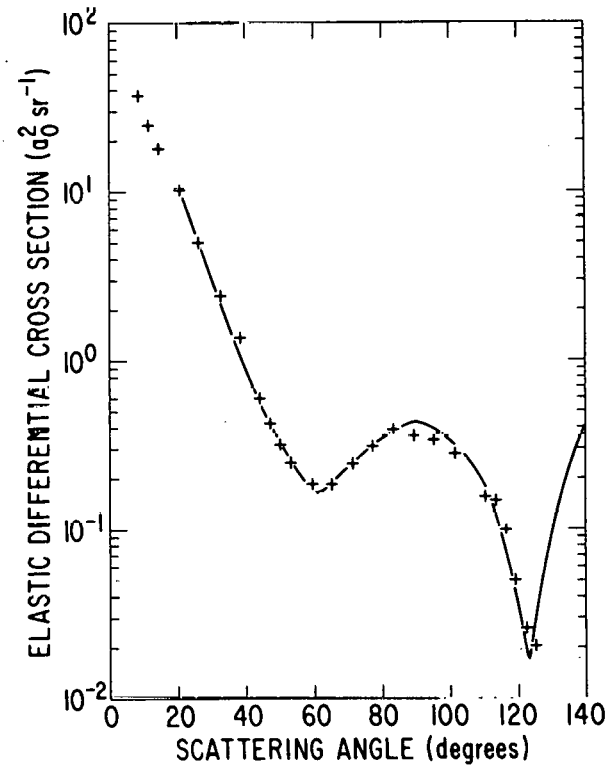

FIG. 5.--Comparison of the angular distribution of 100 eV incident electrons elastically scattered from argon.
(See Figure 3).
(ANL Neg. 149-78-94)

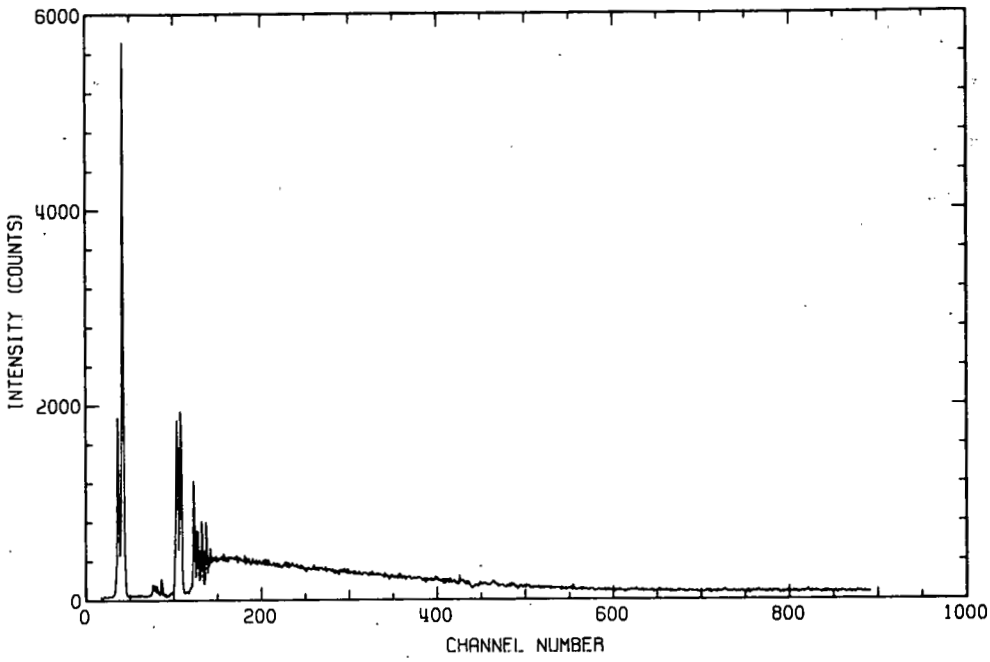

FIG. 6.--The electron energy loss spectrum of argon for 200 eV incident electrons observed at 0°. (ANL Neg. 149-78-89)

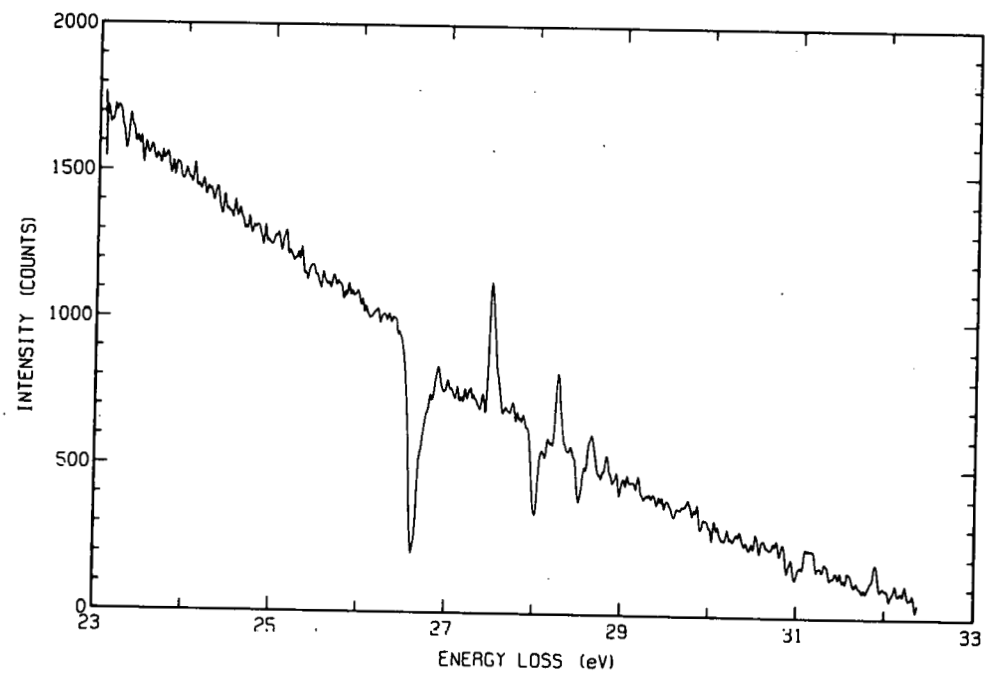

FIG. 7.--The autoionization resonances in argon. These measurements were obtained for 200 eV incident electrons and a 0° scattering angle. For better display the true zero-intensity level is suppressed, and the data have been smoothed three times by a three-point averaging routine. (ANL Neg. 149-78-90)

of argon in the region from 23 to 33 eV. Here the channel numbers have been converted to the appropriate energy loss scale. The number of electrons scattered at 0° from the 200 eV incident beam were accumulated during 1000 sweeps of the spectrum alternately for increasing and decreasing energy loss. The dwell time per channel per sweep was 50 ms with a total spectrum accumulation time of approximately 7.5 hr. The voltage increment per channel was 9.33 mV between voltage sweep end points of 23.60 and 32.59 V as measured with a digital voltmeter. No other adjustment of the energy loss scale was found necessary.

The sharp maxima and minima observed in Figure 7 correspond to the $3s3p^6 np(^1P)$ and $3s3p^6 nd(^1D)$ autoionization states in argon. The positions of the sharp minima of the ^1P autoionization series are in excellent agreement with the photoabsorption measurements of Madden et al.[5] A collection of previous observations[6-10] of the resonance structures are compared with the present results in Table 1. Only the $3s3p^6 np(^1P)$ resonances are observed in the photoabsorption measurements.[5] The optically forbidden excitation of the ^1D states, however, have been detected by electron impact techniques: electron transmission,[6] energy loss,[7-9] and ejected-electron spectra.[11] Calculations[10,11] based on empirical data are also given for comparison. Our results are in excellent agreement with both experimental and calculated values and provide a more extensive observation of the higher-lying resonance structures.

In summary, performance of the modified EELS system has been demonstrated in three modes of operation for a broad range of operating conditions. Preliminary new results have been obtained, and future research with the EELS system looks quite promising.

TABLE 1. Comparison of Observed Autoionization Resonance Positions in Argon

Autoionization state designation	Feature	Observed Resonance Position, eV							
		Ref. 5	Ref. 6	Ref. 7	Ref. 8	Ref. 9	Ref. 10	Ref. 11[a]	Present results
4p (^{1}P)	minimum	26.614	26.60	26.72	26.62	26.63	—	26.62	26.62
3d (^{1}D)	maximum	—	27.61	27.55	27.51	27.48	(27.57)	27.48	27.49
5p (^{1}P)	minimum	27.996	—	28.1	27.977	28.02	—	27.99	28.00
4d (^{1}D)	maximum	—	—	—	28.27	28.29	(28.30)	28.24	28.26
6p (^{1}P)	minimum	28.509	—	—	28.51	28.50	—	28.49	28.51
5d (^{1}D)	maximum	—	—	—	28.62	28.70	(28.64)	28.59	28.65
7p (^{1}P)	minimum	28.76	—	—	28.75	—	—	28.71	28.75
6d (^{1}D)	maximum	—	—	—	28.85	—	(28.83)	(28.79)	28.83
8p (^{1}P)	minimum	28.89	—	—	28.89	—	—	(28.86)	28.89
7d (^{1}D)	maximum	—	—	—	—	—	(28.94)	(28.91)	28.94
9p (^{1}P)	maximum	28.98	—	—	—	—	—	(28.96)	28.97
8d (^{1}D)	maximum	—	—	—	—	—	(29.01)	(28.99)	29.01

[a]Values shown in parentheses are calculated values.

References

1. H. Tanaka and R. H. Huebner, Radiological and Environmental Research Division Annual Report, July 1975–September 1976, ANL-76-88, Part I, p. 14.
2. H. Tanaka, R. H. Huebner, O. J. Steingraber, and D. Spence, Radiological and Environmental Research Division Annual Report, July 1975–September 1976, ANL-76-88, Part I, p. 10.
3. G. J. Schulz, Rev. Mod. Phys. 45, 424 (1973).
4. J. F. Williams and B. A. Willis, J. Phys. B 8, 1670 (1975).
5. R. P. Madden, D. L. Ederer, and K. Codling, Phys. Rev. 177, 136 (1969).
6. E. Bolduc, J. J. Quemener, and P. Marmet, Can. J. Phys. 49, 3095 (1971).
7. J. A. Simpson, G. E. Chamberlain, and S. R. Mielczarek, Phys. Rev. 139A, 1039 (1965).
8. T. Bergmark, R. Spohr, N. Magnussen, L. O. Werme, C. Nordling, and K. Siegbahn, Uppsala Univ. Inst. Phys. Report 589 (1969).
9. J. W. McConkey and J. A. Preston, J. Phys. B 6, L138 (1973).
10. C. E. Brion and L. A. R. Olsen, J. Phys. B 3, 1020 (1970); Chem. Phys. Lett. 22, 400 (1973).
11. J. Fryar and J. W. McConkey, J. Phys. B 9, 619 (1976).

APPARENT OSCILLATOR STRENGTHS FOR MERCURY VAPOR

R. H. Huebner,† R. J. Celotta,* and S. R. Mielczarek*

Apparent oscillator strengths for mercury vapor from electron energy-loss measurements by the small-angle method.

Energy-loss measurements for mercury show many interesting excitation phenomena commonly occurring in complex atomic systems. This system has been studied extensively by Lassettre and co-workers.[1-4] We have obtained energy-loss spectra for mercury vapor for zero-angle scattering of 100 eV incident electrons. These data were analyzed to yield the apparent oscillator strength distribution shown in Figure 1. The analysis was carried

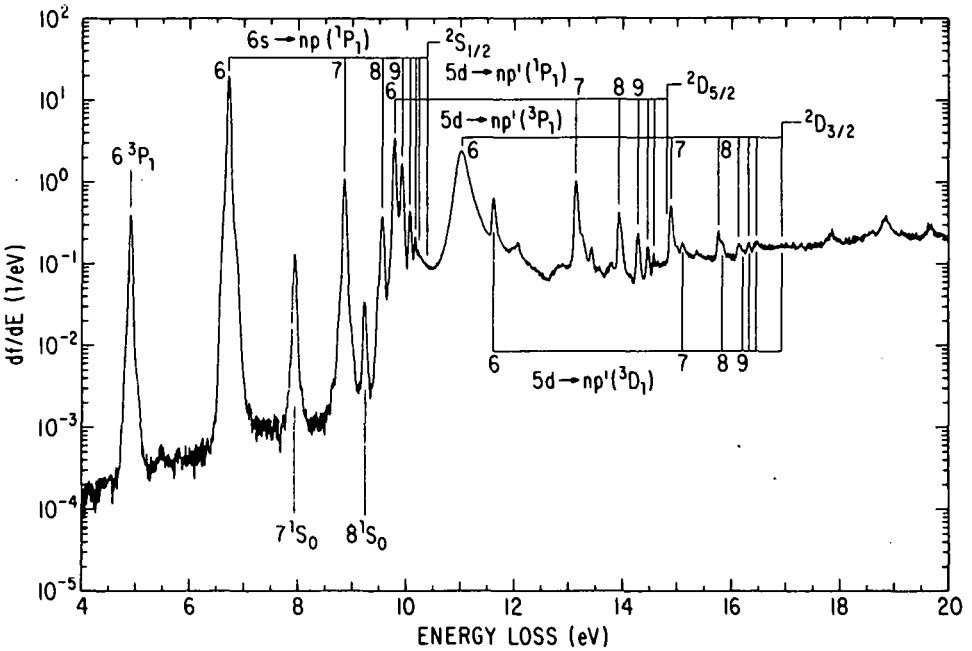

FIG. 1.--Apparent oscillator-strength distribution for mercury vapor derived from 100 eV incident electrons inelastically scattered within 20 milliradians of the incident direction. The spectrum was normalized to yield an integrated f value of 1.11 for the $6^1P_1 \leftarrow 6^1S_0$ transition (Ref. 2).
(ANL Neg. 149-78-93)

†Now Program Coordinator, Biomedical and Environmental Research Programs, Office of the Director, ANL.
*National Bureau of Standards, Washington, D.C.

out using the small-angle method described in detail elsewhere.[5] The spectra were normalized to yield an f value of 1.11 for the intense $6^1P_1 \leftarrow 6^1S_0$ transition observed at 6.71 eV.

The energy resolution of this spectrum is 29 meV FWHM as is apparent in the very narrow widths of the transitions to the 6^3P_1 (4.89 eV) and 6^1P_1 (6.71 eV) states. Singlet-triplet transitions are fairly intense in the mercury spectrum, even at higher impact energies,[1] owing to a breakdown of the $\Delta S = 0$ selection rule through strong spin-orbit mixing in this heavy atom. However, the rigorous $J = 0 \rightarrow J = 0$ selection rule is also violated under electron impact, as can be seen by the occurrence of the $7^1S_0 \leftarrow 6^1S_0$ transition in the spectrum at 7.926 eV. The variation of this transition with incident energy and scattering angle will be discussed later.

The lowest ionization potential of mercury is 10.42 eV. As can readily be seen in Figure 1, the energy loss peaks at 9.91 eV (9^1P_1), 10.06 eV (10^1P_1). 10.16 eV (11^1P_1), 10.22 eV (12^1P_1), and 10.27 eV (13^1P_1) belong to a Rydberg series converging smoothly to this ionization potential. Earlier members of the $n^1P_1 \leftarrow 6^1S_0$ series occur at 6.70, 8.84, and 9.48 eV, corresponding to $n = 6$, 7, and 8. This series exhibits an anomaly in intensity and energy spacing between the $n = 8$ and 9 members. For an unperturbed series, the energies of the Rydberg states, E_n, are given by the well-known Rydberg formula

$$E_n = I - \frac{R}{(n - \delta)^2} \quad ,$$

where R is the Rydberg energy (13.606 eV), I is the ionization limit, δ is the quantum defect, and n is an integer. The transition intensities are expected[6] to decrease approximately as n^{-3}. However, for the mercury spectrum, the intensity $8^1P_1 \leftarrow 6^1S_0$ transition is abnormally small, while the $9^1P_1 \leftarrow 6^1S_0$ intensity is nearly equal to that of the $7^1P_1 \leftarrow 6^1S_0$ transition. Also, the energy spacing between 8^1P_1 and 9^1P_1 differs markedly from that expected from the Rydberg formula.[1] Both of these deviations are evidence of the opening of a new channel of excitation in the region between 8 and 9 eV. Shenstone and Russell[6] first explained such perturbation as being due to configuration

TABLE 1. Apparent Oscillator Strengths for Mercury Vapor

Excited state designation	Observed peak energy, eV	Oscillator strength determined by electron impact		
		Present work	Ref. 1 (T = 300 eV)	Refs. 2 and 3 (extrapolation)
6^3P_1	4.89	0.022	0.035[a]	0.0285 ± 0.0043
6^1P_1	6.71	1.110[b]	1.11	1.11 ± 0.010
7^1S_0	7.93	0.0085	0.00377	
7^1P_1	8.85	0.0673	0.046	
8^1S_0	9.23	0.0026	—	
8^1P_1	9.55	0.0282	0.0198	
$6p'^1P_1$	9.78	0.202	0.226	
9^1P_1	9.92	0.104	0.108	
10^1P_1	10.06	0.0270	0.0273	
$6p'^3P_1$	11.01	0.684[a]	0.72[a]	0.704 ± 0.070
$6p'^3D_1$	11.61	0.028 − 0.038[a]	0.075	
$7p'^1P_1$	13.13	0.0711[a]	0.082[a]	0.067 ± 0.009

a. Corrected for contributions from underlying continuum and other transitions as discussed in Ref. 3
b. Present results normalized to this value.

interaction between series members and a foreign term of the same parity and J value. For mercury, the perturbing term in the $5d^{10}6s.np$ series is the $6p'\,^1P_1$ ($5d^9 6s^2 6p$) state at 9.77 eV.

Just above the ionization potential of mercury the energy-loss spectrum shows a broad smooth maximum at about 11 eV superimposed on the ionization continuum. This was first assigned to the $6p'\,^3P_1 \leftarrow 6\,^1S_0$ transition by an analysis of optical data by Beutler.[7] The extreme broadness of this state is indicative of a very short lifetime due to a strong interaction between this discrete level and the ionization continuum, i.e., the excited state decays spontaneously into the available ionization channel. Coupling between the discrete state and the continuum states of the same energy is a form of configuration interaction and in general is governed by the same selective rules that apply to the mixing of discrete states.

A comparison of the integrated oscillator strengths for transitions observed below 200 V with values determined by Lassettre and co-workers[1-4] is given in Table 1. Consistent results are obtained for all allowed transitions. However, our f values for optically forbidden transitions to the $7\,^1S_0$ and $8\,^1S_0$ states are nonzero. This can be understood by taking into account the finite values of momentum transfer (Ka_0) actually included by the apparatus. Previous measurements of the generalized oscillator strength (GOS) for these transitions exhibit a maximum at small momentum transfer [$(Ka_0)^2 \simeq 10^{-1}$] followed by a sharp decline to the optical limit of zero. Under the conditions of our measurement the values of momentum transfer included correspond to about $(Ka_0)^2 = 10^{-2}$ in the region of sharp decline. Thus the small-angle method yields apparent f values for these optically forbidden transitions. The values we have determined actually correspond to a "mean" GOS value appropriate to the range of momentum transfer included by the apparatus.

References

1. A. Skerbele, K. J. Ross, and E. N. Lassettre, J. Chem. Phys. 50, 4486 (1969).
2. A. Skerbele and E. N. Lassettre, J. Chem. Phys. 52, 2708 (1970).
3. A. Skerbele and E. N. Lassettre, J. Chem. Phys. 56, 845 (1972).

4. A. Skerbele and E. N. Lassettre, J. Chem. Phys. 58, 2887 (1973).
5. R. J. Celotta and R. H. Huebner, Electron Impact Spectroscopy: An Overview of the Low Energy Aspects, to be published in Electron Spectroscopy, Vol. II, C. R. Brundle and A. D. Baker, Eds., Academic Press, New York.
6. A. G. Shenstone and H. N. Russell, Phys. Rev. 39, 415 (1932).
7. H. Beutler, Z. Phys. 86, 710 (1933).

THE OSCILLATOR-STRENGTH DISTRIBUTION OF WATER. A COMPARISON OF NEW PHOTOABSORPTION AND ELECTRON ENERGY-LOSS MEASUREMENTS*

J. C. Person, R. H. Huebner, R. J. Celotta,† and S. R. Mielczarek

---

New measurements of the electron energy-loss (EEL) spectrum of water have been made using electrons with an incident energy of T = 100 eV, and the data have been converted into values of the differential oscillator strength df/dE. These relative df/dE values are compared with photoabsorption data, including new measurements for excitation energies E from 13 to 21 eV.

The EEL spectra were measured using the NBS model AN-1 electron-impact spectrometer[1,2] with an energy resolution of 25 meV (FWHM) for incident electrons scattered within 0.02 radians of the incident direction. The data were corrected for dead time in the counting circuitry, and repeated scans were averaged to remove effects due to pressure and electron-beam fluctuations.

Conversion of the EEL spectrum into df/dE values requires a correction for θ, the acceptance angle of the apparatus, and if F', the derivation of df/dE with respect to the square of the momentum transfer, is known, one can improve the data conversion procedure previously used[3–5] by including a second term[4,5] to give

$$df/dE \propto I\,[TE\theta^2/\ln(1+X)]\,(1+A)^{-1}\,, \qquad (1)$$

where $X = 4T^2\theta^2(1-E/T)/E^2$, $A = (E^2/4RT)\,[X/\ln(1+X)]\,[F'/(df/dE)]\,(1-E/T)^{-\frac{1}{2}}$, I is the intensity in the EEL spectrum, and R = 13.6 eV. In order to make a realistic estimate of the magnitude of the $(1+A)^{-1}$ correction term, we have used F'/(df/dE) values reported by Backx et al.[6] on methane, which is isoelectronic with water. The $(1+A)^{-1}$ factor is shown in the upper portion of Figure 1. This factor is a correction to the earlier procedure, but the variation of this factor over a range of only 10% suggests that neglecting this term does

---

*Summary of a paper presented at the Xth Int. Conf. on the Physics of Electronic and Atomic Collisions, Paris, July 1977.

†National Bureau of Standards, Washington, D.C. 20234.

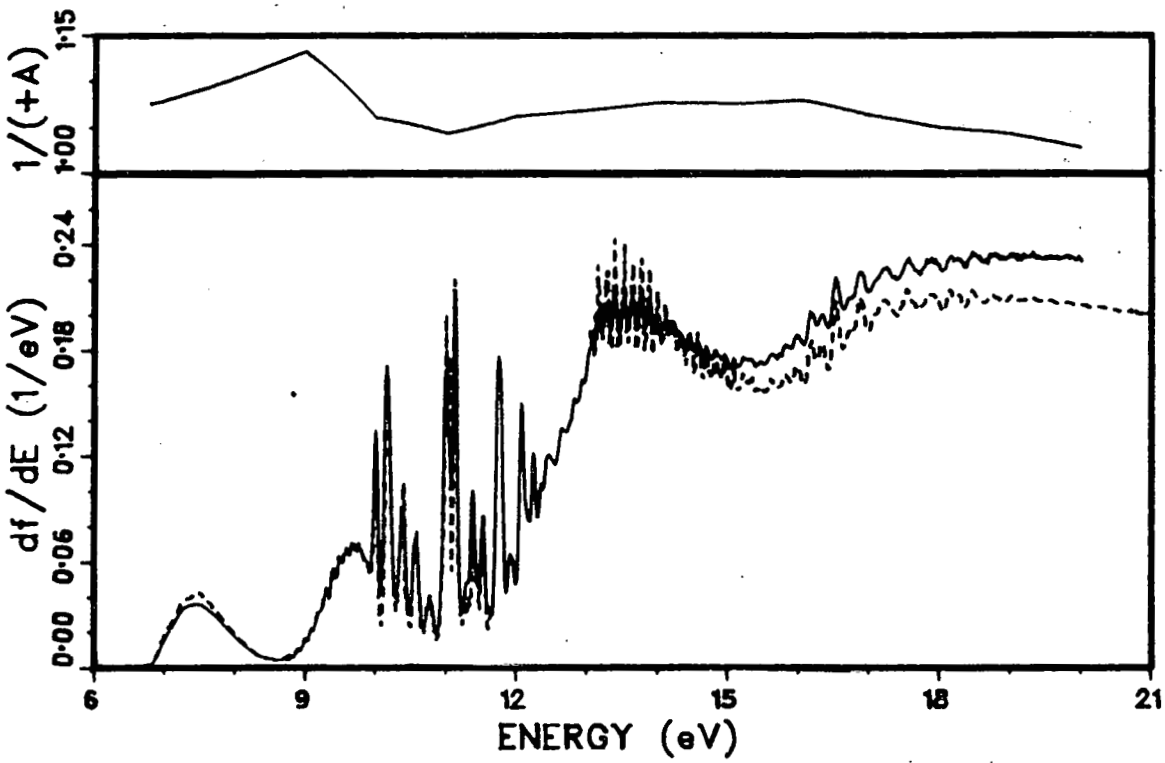

FIG. 1.--(Upper) The correction factor in Eq. 1. (Lower) The oscillator strength distribution.

not seriously alter the results.

The photon data were measured[7] using the ANL double-ion chamber and a calibrated Baratron pressure meter; a small correction was made for the effects of scattered light. The new results are in good agreement with those reported by Katayama, et al.,[8] and they are shown on Figure 1 as a dashed line for E = 13 to 20 eV. Photon data from Watanabe and Zelikoff[9] are shown as a dashed line for E = 6.7 to 11.6 eV. The solid line represents the EEL data converted using Eq. 1 after normalization to the new photon results at 14.2 eV. The EEL data agree with the photon data within ± 12% over the wide energy range shown with excellent agreement from 8 to 11 eV; additional experiments to test the effects of increasing T are in progress.

References

1. J. A. Simpson, Record of the 10th Symp. on Electron, Ion, and Laser Beam Technology, L. Marton, Ed., San Francisco Press, San Francisco, p. 345 (1969).

2. R. J. Celotta, S. R. Mielczarek, and C. E. Kuyatt, Electron Spectroscopy for Gas Analysis, National Bureau of Standards Report No. 10915 (1972).
3. R. H. Huebner, R. J. Celotta, S. R. Mielczarek, and C. E. Kuyatt, J. Chem. Phys. 59, 5434 (1973); 63, 241 and 4490 (1975).
4. R. H. Huebner and R. J. Celotta, Argonne National Laboratory Radiological and Environmental Research Division Annual Report, July 1971–June 1972, ANL-7960, Part I, p. 49.
5. R. J. Celotta and R. H. Huebner, Electron Impact Spectroscopy: An Overview of the Low Energy Aspects, Electron Spectroscopy: Techniques, Theory, and Applications, C. R. Brundle and A. D. Baker, Eds., Academic Press, New York, to be published.
6. C. Backx, G. R. Wight, R. R. Tol, and M. J. Van der Wiel, J. Phys. B 8, 3007 (1975).
7. J. C. Person, D. E. Fowler, and P. P. Nicole, Argonne National Laboratory Radiological and Environmental Research Division Annual Report, July 1974–June 1975, ANL-75-60, Part I, p. 26.
8. D. H. Katayama, R. E. Huffman, and C. L. O'Bryan, J. Chem. Phys. 59, 4309 (1973).
9. K. Watanabe and M. Zelikoff, J. Opt. Soc. Am. 43, 753 (1953).

ABSORPTION CROSS SECTIONS AT HIGH ENERGIES. NEOPENTANE FROM 10 TO 21 eV AND ETHANE FROM 22 TO 54 eV*

James C. Person and Paul P. Nicole

As part of a program to determine accurate oscillator-strength distributions, we are measuring absorption cross sections σ over a wide range of photon energy E. Here we report σ values for ethane from 22.2 to 53.7 eV, together with σ values for 2,2-dimethyl propane (neopentane) from 10.4 to 21.1 eV, and we also discuss our method of correcting for scattered light.

The absorption cross sections for neopentane are shown in Figure 1. The relative values reported by Koch et al.[1] do not agree very well. Figure 2 is an enlargement of the 15 to 18 eV region, showing the Rydberg series for the ionization of the $2a_1$ electron. We find the limit to be 17.64 ± 0.01 eV, compared with earlier values of 17.60 eV[2] and 17.68 eV.[1] Each Rydberg level shows three to six members of a vibrational progression with a spacing of 0.17 eV, which is assigned[1,2] to the totally symmetric C-H bending mode; the members of this series for the n = 3 to 9 Rydberg levels are shown as ticks on Figure 2. We have fit the Beutler-Fano line profiles using the parameterization of Shore,[3] and the dashed lines that show the fit of four levels from 15.2 to 15.7 eV and the fit of six levels from 16.35 to 17.02 eV fit the data so well that they are almost indistinguishable in Figure 2. These fits indicate autoionization rates around 10^{14} sec^{-1} for n = 3 and 3 to 5 × 10^{13} sec^{-1} for n = 4 and 5.

The σ values for ethane, shown in Figure 3, show a lack of significant structure from 22 to 50 eV. The values reported by Lee et al.[4] agree within ± 10% from 23 to 44 eV, but their values are 12% lower around 22 eV and 17% higher near 54 eV, as shown by the dashed line in Figure 3. However, the values reported by Koch and Skibowski for E < 35 eV are 8 to 35% lower, as

---

*Summary of a paper presented at the Vth International Conference on Vacuum-Ultraviolet Radiation Physics, Montpellier, France, September 5–9, 1977.

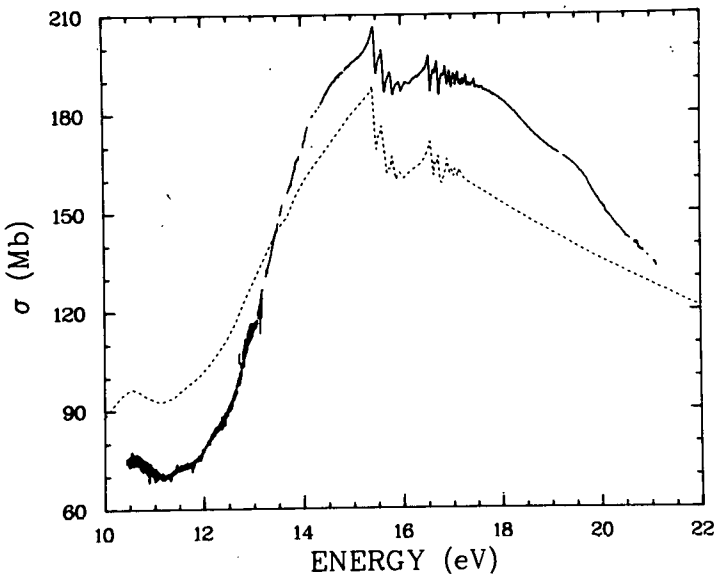

FIG. 1.--Absorption cross sections for neopentane [$C(CH_3)_4$]. (1 Mb = 10^{-18} cm^2). ---- Koch et al.[1] (normalized); —— present results.

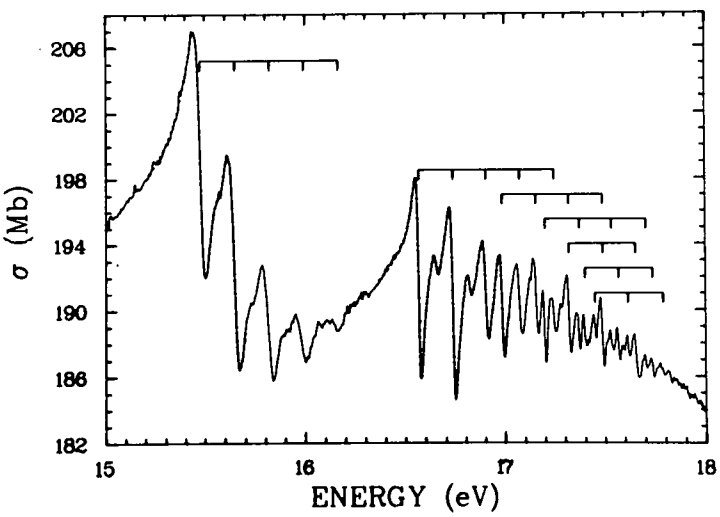

FIG. 2.--Rydberg series in neopentane. The bars show the n = 3 to 9 Rydberg levels, and the ticks show the vibrational progression in the symmetrical C-H bend.

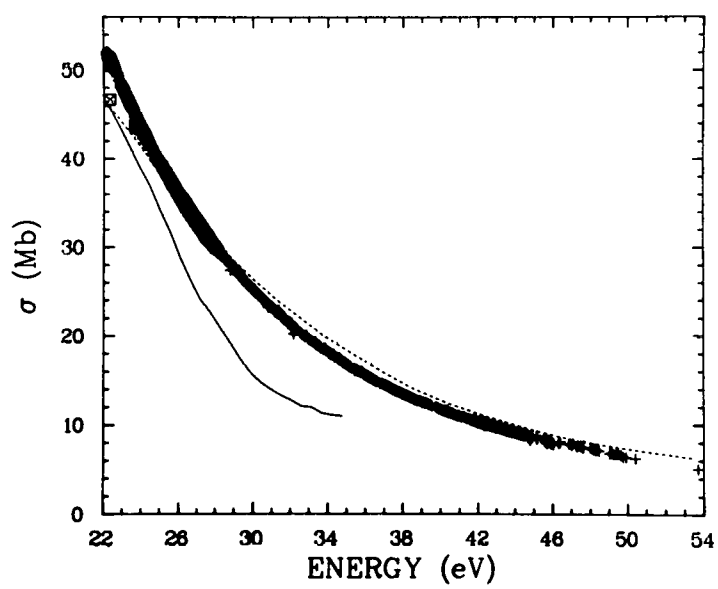

FIG. 3.--Absorption cross sections for ethane [C_2H_6]. ⊠ Schoen[6]; --- Lee et al.[4]; —— Koch and Skibowski[5]; +++ present results.

shown by the solid curve. The two values reported by Schoen[6] are 3 and 9% lower than ours.

We used a double ion chamber to determine σ from the ratio of the ion currents, i_F and i_R, in the front and rear ion chambers. The ethane data were taken using a low-pressure spark in argon as a light source, and Figure 4a shows the photon flux. We made a preliminary correction for scattered light by measuring the ion currents, a and b, produced with the monochromator set at an energy above the emission limit of the lamp. We allowed for the variation in the scattered light as E is changed by introducing a parameter c so that σ is determined from the corrected ion current ratio $(i_F - a - c)/(i_R - b)$. The c parameter is adjusted at emission peaks by a least-squares fitting procedure that minimizes the variation in σ as the light intensity changes. Figure 4b shows the a, b, and c correction for three different experiments with ethane. As Figure 4 shows, the values of a, b, and c are small in comparison with the total photon flux for most of the emission peaks at energies below 44 eV.

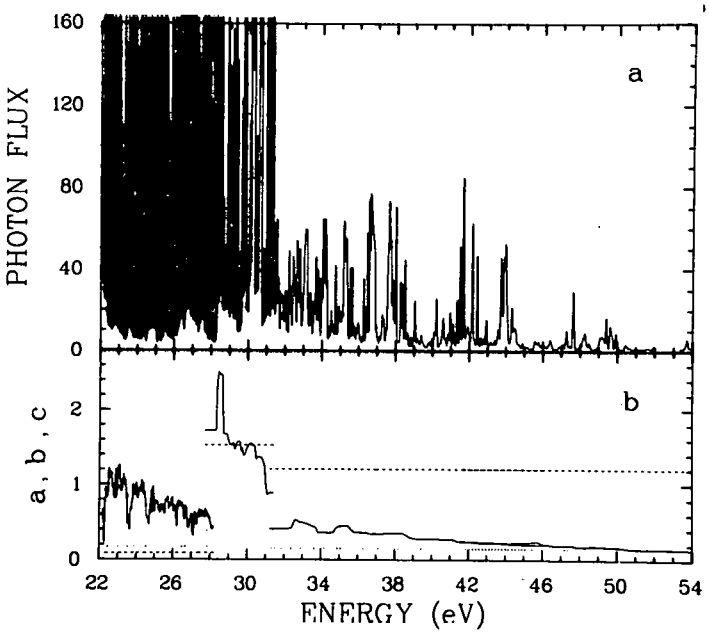

FIG. 4.--a, Photon flux for ethane experiments; b, correction factors for scattered light for three experiments in ethane. ---- a; .... b; —— c.

References

1. E. E. Koch, V. Saile, and N. Schwentner, Chem. Phys. Lett. 33, 322 (1975).
2. A. E. Jonas, G. K. Schweitzer, F. A. Grimm, and T. A. Carlson, J. Electron Spectrosc. 1, 29 (1972/73).
3. B. W. Shore, Phys. Rev. 171, 43 (1968).

4. L. C. Lee, R. W. Carlson, D. L. Judge, and M. Ogawa, J. Quant. Spectrosc. Radiat. Transfer 13, 1023 (1973).
5. E. E. Koch and M. Skibowski, Chem. Phys. Lett. 9, 429 (1971).
6. R. I. Schoen, J. Chem. Phys. 37, 2032 (1962).

THE OSCILLATOR-STRENGTH DISTRIBUTION OF NEOPENTANE FROM 10.4 TO 21.1 eV

James C. Person, David Fowler,* and Paul P. Nicole

Experimental data on the oscillator-strength distribution of 2,2-dimethyl propane (neopentane) are tabulated for energies from 10.44 to 21.13 eV.

In this report we tabulate our experimental results on the oscillator-strength distribution of 2,2-dimethyl propane (neopentane). We have measured the absorption cross section, σ, using monochromatic light to define the excitation energy E. Figures illustrating σ vs. E are given elsewhere, along with details of the measurement.[1,2] We have converted the σ values into values of the differential oscillator strength, df/dE, using $df/dE = 0.0091116\ \sigma$, for σ in Mb (1 Mb = 10^{-18} cm^2) and df/dE in units of $(eV)^{-1}$.

The cross sections were measured using a double ion chamber and electrometers. The gas pressure was measured using an MKS Baratron Type 77H-1 capacitive manometer that we calibrated[1] with an oil manometer. The Baratron calibration by MKS Instruments gave pressure readings 0.7% greater than our calibration. We used our calibration and assume the uncertainty in the gas density measurement to be about 1%. The uncertainty in the ion-chamber length is also about 1%, and the uncertainty in df/dE as a result of the electrometer calibration is estimated to be 1 to 2%. We did not recognize any effects as being produced by impurity absorption, and we believe impurities contributed less than 1% of the absorption. Small corrections were made for scattered light, and we estimate the uncertainty in this correction to contribute 1 to 3% uncertainty in df/dE. The precision of the data is about 0.2 to 0.4%, so that the overall accuracy of the data should be better than 5 to 8%.

The monochromator bandpass for E < 13.2 eV was 0.045 nm (ca. 0.005 eV), and it was 0.09 nm (ca. 0.02 eV) for higher energies. The data given in Table 1 represent averages of three energies centered about the energy reported,

* Undergraduate Research Participant from Macalester College, St. Paul, Minnesota 55101.

TABLE 1. The Oscillator-Strength Distribution of Neopentane

E,eV	df/dE,1/eV	E,eV	df/dE,1/eV	E,eV	df/dE,1/eV	E,eV	df/dE,1/eV
10.437	0.680	11.020	0.649	11.378	0.650	11.766	0.661
10.496	0.668	11.026	0.647	11.385	0.648	11.777	0.668
10.504	0.691	11.032	0.648	11.391	0.654	11.783	0.676
10.537	0.691	11.038	0.638	11.397	0.651	11.790	0.665
10.543	0.703	11.046	0.646	11.404	0.653	11.797	0.677
10.549	0.682	11.053	0.639	11.410	0.654	11.804	0.678
10.554	0.692	11.059	0.647	11.416	0.649	11.810	0.682
10.560	0.693	11.065	0.640	11.423	0.656	11.817	0.680
10.580	0.687	11.071	0.644	11.429	0.657	11.824	0.679
10.605	0.687	11.077	0.643	11.435	0.658	11.831	0.681
10.610	0.691	11.083	0.643	11.442	0.667	11.837	0.681
10.632	0.693	11.089	0.640	11.448	0.656	11.844	0.684
10.638	0.698	11.095	0.642	11.454	0.657	11.851	0.685
10.643	0.693	11.101	0.641	11.461	0.655	11.858	0.683
10.649	0.684	11.107	0.643	11.467	0.657	11.865	0.686
10.654	0.690	11.113	0.639	11.473	0.658	11.871	0.686
10.660	0.677	11.119	0.642	11.480	0.655	11.878	0.686
10.665	0.689	11.125	0.642	11.486	0.660	11.885	0.682
10.671	0.694	11.131	0.642	11.493	0.655	11.892	0.692
10.676	0.693	11.137	0.636	11.499	0.661	11.911	0.682
10.682	0.689	11.143	0.633	11.505	0.661	11.917	0.693
10.687	0.688	11.149	0.634	11.512	0.662	11.924	0.694
10.693	0.693	11.155	0.641	11.518	0.666	11.931	0.693
10.714	0.677	11.161	0.632	11.525	0.662	11.938	0.685
10.719	0.688	11.167	0.639	11.533	0.663	11.947	0.695
10.724	0.665	11.173	0.639	11.540	0.666	11.954	0.693
10.733	0.677	11.180	0.636	11.546	0.662	11.961	0.700
10.742	0.682	11.187	0.637	11.553	0.657	11.968	0.699
10.749	0.681	11.193	0.631	11.559	0.663	11.975	0.705
10.773	0.672	11.199	0.638	11.565	0.664	11.982	0.711
10.778	0.674	11.206	0.636	11.572	0.663	11.989	0.708
10.805	0.665	11.212	0.638	11.578	0.661	11.996	0.709
10.810	0.674	11.218	0.638	11.585	0.666	12.003	0.706
10.816	0.667	11.224	0.639	11.591	0.668	12.010	0.711
10.822	0.675	11.230	0.640	11.600	0.662	12.017	0.713
10.827	0.674	11.236	0.637	11.607	0.663	12.024	0.715
10.833	0.673	11.242	0.636	11.613	0.668	12.031	0.718
10.840	0.665	11.248	0.642	11.620	0.665	12.038	0.720
10.848	0.658	11.254	0.639	11.626	0.669	12.045	0.722
10.859	0.670	11.261	0.639	11.633	0.666	12.052	0.722
10.886	0.627	11.267	0.639	11.639	0.667	12.059	0.722
10.909	0.666	11.273	0.639	11.646	0.670	12.066	0.726
10.915	0.655	11.279	0.641	11.653	0.663	12.073	0.728
10.921	0.658	11.285	0.639	11.659	0.670	12.080	0.730
10.930	0.652	11.291	0.642	11.668	0.665	12.087	0.733
10.938	0.660	11.298	0.641	11.674	0.669	12.094	0.735
10.944	0.651	11.304	0.643	11.681	0.671	12.101	0.737
10.950	0.650	11.310	0.631	11.689	0.667	12.108	0.733
10.956	0.657	11.316	0.641	11.699	0.668	12.115	0.735
10.962	0.647	11.322	0.640	11.705	0.668	12.122	0.727
10.971	0.643	11.329	0.647	11.712	0.671	12.151	0.748
10.979	0.648	11.335	0.646	11.719	0.669	12.160	0.750
10.985	0.652	11.341	0.648	11.725	0.668	12.168	0.743
10.991	0.646	11.347	0.644	11.732	0.671	12.175	0.751
10.997	0.650	11.353	0.649	11.739	0.674	12.182	0.753
11.002	0.638	11.360	0.650	11.745	0.673	12.189	0.752
11.008	0.634	11.366	0.649	11.752	0.673	12.196	0.757
11.014	0.654	11.372	0.651	11.759	0.672	12.204	0.759

TABLE 1. (contd.)

E,eV	df/dE,1/eV	E,eV	df/dE,1/eV	E,eV	df/dE,1/eV	E,eV	df/dE,1/eV
12.211	0.758	12.668	0.893	13.288	1.204	14.481	1.694
12.220	0.760	12.676	0.892	13.301	1.212	14.497	1.697
12.228	0.767	12.683	0.901	13.314	1.220	14.512	1.699
12.235	0.766	12.691	0.904	13.327	1.226	14.527	1.703
12.242	0.768	12.699	0.908	13.340	1.233	14.543	1.707
12.249	0.765	12.707	0.896	13.353	1.241	14.558	1.711
12.257	0.774	12.715	0.911	13.366	1.248	14.573	1.716
12.264	0.768	12.723	0.922	13.379	1.260	14.589	1.717
12.271	0.765	12.731	0.908	13.392	1.267	14.604	1.721
12.279	0.772	12.741	0.914	13.405	1.276	14.620	1.724
12.286	0.770	12.749	0.932	13.418	1.285	14.635	1.728
12.293	0.775	12.757	0.943	13.431	1.295	14.651	1.729
12.301	0.773	12.766	0.940	13.444	1.303	14.667	1.731
12.308	0.774	12.775	0.948	13.457	1.308	14.682	1.732
12.315	0.780	12.783	0.947	13.470	1.317	14.698	1.738
12.323	0.785	12.791	0.948	13.484	1.322	14.714	1.742
12.330	0.785	12.799	0.946	13.497	1.328	14.729	1.743
12.337	0.780	12.807	0.964	13.510	1.337	14.745	1.741
12.345	0.783	12.815	0.974	13.554	1.359	14.761	1.745
12.355	0.790	12.824	0.971	13.559	1.362	14.777	1.749
12.362	0.774	12.839	0.986	13.572	1.371	14.793	1.751
12.369	0.799	12.851	0.987	13.586	1.381	14.809	1.753
12.377	0.797	12.863	0.997	13.599	1.386	14.825	1.753
12.384	0.797	12.871	1.002	13.712	1.421	14.841	1.755
12.392	0.799	12.879	1.013	13.717	1.423	14.894	1.764
12.399	0.796	12.889	1.012	13.730	1.429	14.910	1.769
12.408	0.785	12.900	1.009	13.744	1.433	14.926	1.769
12.416	0.787	12.911	1.034	13.758	1.439	14.943	1.771
12.424	0.795	12.919	1.016	13.771	1.443	14.959	1.771
12.431	0.810	12.927	1.023	13.785	1.445	14.975	1.774
12.439	0.807	12.935	1.049	13.799	1.457	14.992	1.777
12.448	0.809	12.943	1.033	13.813	1.463	15.008	1.780
12.456	0.810	12.951	1.028	13.827	1.472	15.024	1.782
12.465	0.807	12.960	1.036	13.841	1.479	15.041	1.783
12.474	0.816	12.970	1.035	13.855	1.485	15.057	1.785
12.482	0.822	12.979	1.049	13.869	1.492	15.074	1.787
12.490	0.818	12.987	1.044	13.883	1.505	15.090	1.789
12.504	0.829	12.995	1.042	13.897	1.511	15.107	1.791
12.512	0.824	13.003	1.054	13.911	1.513	15.123	1.793
12.520	0.830	13.014	1.052	13.925	1.515	15.140	1.796
12.530	0.836	13.022	1.060	13.939	1.519	15.157	1.796
12.537	0.831	13.033	1.054	14.034	1.553	15.173	1.798
12.545	0.840	13.043	1.059	14.048	1.562	15.190	1.800
12.552	0.831	13.058	1.059	14.062	1.566	15.207	1.803
12.560	0.845	13.067	1.066	14.077	1.576	15.224	1.807
12.568	0.846	13.080	1.065	14.091	1.588	15.241	1.808
12.575	0.850	13.103	1.095	14.105	1.594	15.257	1.812
12.583	0.848	13.115	1.100	14.120	1.602	15.274	1.817
12.591	0.858	13.128	1.110	14.203	1.632	15.291	1.819
12.598	0.856	13.140	1.113	14.217	1.633	15.308	1.825
12.606	0.855	13.153	1.126	14.232	1.636	15.325	1.829
12.614	0.867	13.165	1.138	14.305	1.651	15.343	1.834
12.621	0.869	13.178	1.154	14.356	1.659	15.360	1.837
12.629	0.873	13.191	1.153	14.406	1.673	15.377	1.848
12.637	0.878	13.203	1.156	14.421	1.675	15.394	1.851
12.645	0.869	13.254	1.192	14.436	1.680	15.411	1.864
12.652	0.888	13.263	1.191	14.451	1.684	15.429	1.876
12.660	0.890	13.275	1.206	14.466	1.689	15.446	1.879

TABLE 1. (contd.)

E,eV	df/dE,1/eV	E,eV	df/dE,1/eV	E,eV	df/dE,1/eV	E,eV	df/dE,1/eV
15.463	1.859	16.568	1.733	17.811	1.698	19.347	1.513
15.481	1.800	16.588	1.708	17.834	1.694	19.374	1.510
15.498	1.755	16.608	1.735	17.858	1.693	19.402	1.507
15.515	1.757	16.628	1.754	17.881	1.691	19.429	1.505
15.533	1.774	16.648	1.757	17.904	1.690	19.456	1.501
15.551	1.785	16.668	1.753	17.927	1.688	19.484	1.498
15.568	1.793	16.688	1.767	17.951	1.685	19.512	1.494
15.586	1.799	16.708	1.782	17.974	1.684	19.539	1.491
15.627	1.802	16.729	1.750	17.998	1.680	19.567	1.485
15.645	1.756	16.749	1.695	18.021	1.677	19.595	1.480
15.663	1.708	16.770	1.713	18.045	1.676	19.623	1.477
15.680	1.704	16.790	1.738	18.069	1.673	19.651	1.473
15.698	1.719	16.811	1.747	18.092	1.671	19.679	1.468
15.716	1.732	16.831	1.744	18.116	1.667	19.707	1.462
15.734	1.737	16.852	1.749	18.140	1.664	19.735	1.458
15.752	1.743	16.872	1.765	18.164	1.661	19.764	1.449
15.770	1.752	16.893	1.756	18.188	1.658	19.792	1.440
15.788	1.752	16.914	1.723	18.212	1.655	19.821	1.433
15.807	1.732	16.935	1.730	18.236	1.651	19.849	1.426
15.825	1.703	16.955	1.750	18.260	1.646	19.878	1.420
15.843	1.693	16.976	1.749	18.285	1.646	19.907	1.413
15.861	1.703	16.997	1.716	18.309	1.641	19.936	1.406
15.879	1.713	17.018	1.727	18.333	1.636	19.964	1.403
15.898	1.719	17.039	1.743	18.358	1.634	19.993	1.395
15.916	1.722	17.061	1.746	18.382	1.629	20.023	1.388
15.935	1.725	17.082	1.725	18.407	1.625	20.052	1.385
15.953	1.727	17.103	1.729	18.432	1.622	20.081	1.379
15.972	1.720	17.124	1.748	18.456	1.617	20.110	1.372
15.990	1.707	17.146	1.750	18.481	1.614	20.140	1.363
16.009	1.704	17.167	1.725	18.506	1.609	20.169	1.359
16.027	1.711	17.188	1.729	18.531	1.606	20.199	1.355
16.046	1.717	17.210	1.721	18.556	1.601	20.229	1.350
16.065	1.721	17.231	1.732	18.581	1.598	20.258	1.343
16.084	1.726	17.253	1.722	18.606	1.595	20.288	1.339
16.102	1.725	17.275	1.729	18.631	1.590	20.318	1.333
16.121	1.725	17.296	1.742	18.656	1.587	20.348	1.326
16.140	1.723	17.318	1.733	18.682	1.584	20.378	1.324
16.159	1.722	17.340	1.719	18.707	1.579	20.409	1.319
16.178	1.723	17.362	1.719	18.733	1.577	20.439	1.315
16.197	1.727	17.384	1.721	18.758	1.574	20.469	1.309
16.216	1.731	17.406	1.718	18.784	1.571	20.500	1.305
16.235	1.736	17.428	1.722	18.809	1.567	20.530	1.296
16.255	1.737	17.450	1.725	18.835	1.564	20.561	1.295
16.274	1.738	17.472	1.732	18.861	1.560	20.592	1.290
16.293	1.740	17.494	1.716	18.887	1.558	20.726	1.277
16.312	1.743	17.517	1.715	18.913	1.555	20.757	1.274
16.332	1.741	17.539	1.714	18.939	1.553	20.789	1.262
16.351	1.745	17.561	1.713	18.965	1.550	20.820	1.257
16.371	1.746	17.584	1.709	18.991	1.546	20.852	1.251
16.390	1.751	17.606	1.712	19.017	1.544	20.941	1.243
16.410	1.753	17.629	1.713	19.044	1.542	20.968	1.242
16.429	1.756	17.651	1.712	19.070	1.538	21.067	1.225
16.449	1.760	17.674	1.704	19.096	1.536	21.097	1.223
16.469	1.762	17.697	1.705	19.123	1.535	21.127	1.214
16.488	1.768	17.720	1.704	19.150	1.532		
16.508	1.776	17.742	1.701	19.176	1.529		
16.528	1.787	17.765	1.700	19.293	1.518		
16.548	1.794	17.788	1.700	19.320	1.516		

so that there is some distortion of the structure of the autoionizing peaks in the energy range from 15 to 18 eV.

References

1. J. C. Person, D. E. Fowler, and P. P. Nicole, Radiological and Environmental Research Division Annual Report, July 1974–June 1975, ANL-75-60, Part I, p. 26.
2. J. C. Person and P. P. Nicole, Absorption cross sections at high energies. Neopentane from 10 to 21 eV and ethane from 22 to 54 eV, this report.

PHOTOIONIZATION OF N_2 AT HIGH RESOLUTION*

P. M. Dehmer and W. A. Chupka†

The relative photoionization cross section for N_2 at 78°K has been measured at high resolution (0.016–0.035 Å) from the ionization threshold to 650 Å. The data are shown in Figure 1, and the prominent autoionizing Rydberg states converging to the $X^2\Sigma_g^+$, v = 1, the $A^2\Pi_u$, and the $B^2\Sigma_u^+$ electronic states of N_2^+ are indicated in the figure. Figure 2 shows the region between the ionization threshold and the $N_2^+ X^2\Sigma_g^+$, v = 1 convergence limits in greater detail, and at higher resolution (0.016 Å). In this region both vibrational and electronic autoionization is observed, with electronic autoionization greatly predominating. Rotational structure is partially resolved for a number of unidentified autoionizing states in this energy range. The observed halfwidths of these rotational lines of $< 1\ cm^{-1}$ yield autoionization rates k ($= 2\pi c\Delta\nu$) $< 1.9 \times 10^{11}\ sec^{-1}$, somewhat smaller than the rates calculated by Duzy and Berry[1] for states in this energy region. In general, the calculated rates of Duzy and Berry are consistent with observations above the $N_2^+ X^2\Sigma_g^+$, v = 1 convergence limit. Further work is currently in progress on the analysis of this spectrum, with emphasis on the identification of the bands near the ionization threshold, and the competition between autoionization and other decay paths such as predissociation.

Reference

1. C. Duzy and R. S. Berry, J. Chem. Phys. 64, 2421 (1976); 64, 2431 (1976).

---

*Summary of a paper presented at the VIIIth Annual Meeting of the Division of Electron and Atomic Physics, The American Physical Society, Lincoln, Nebraska, 6–8 December 1976.

†Department of Chemistry, Yale University, New Haven, Connecticut 06520.

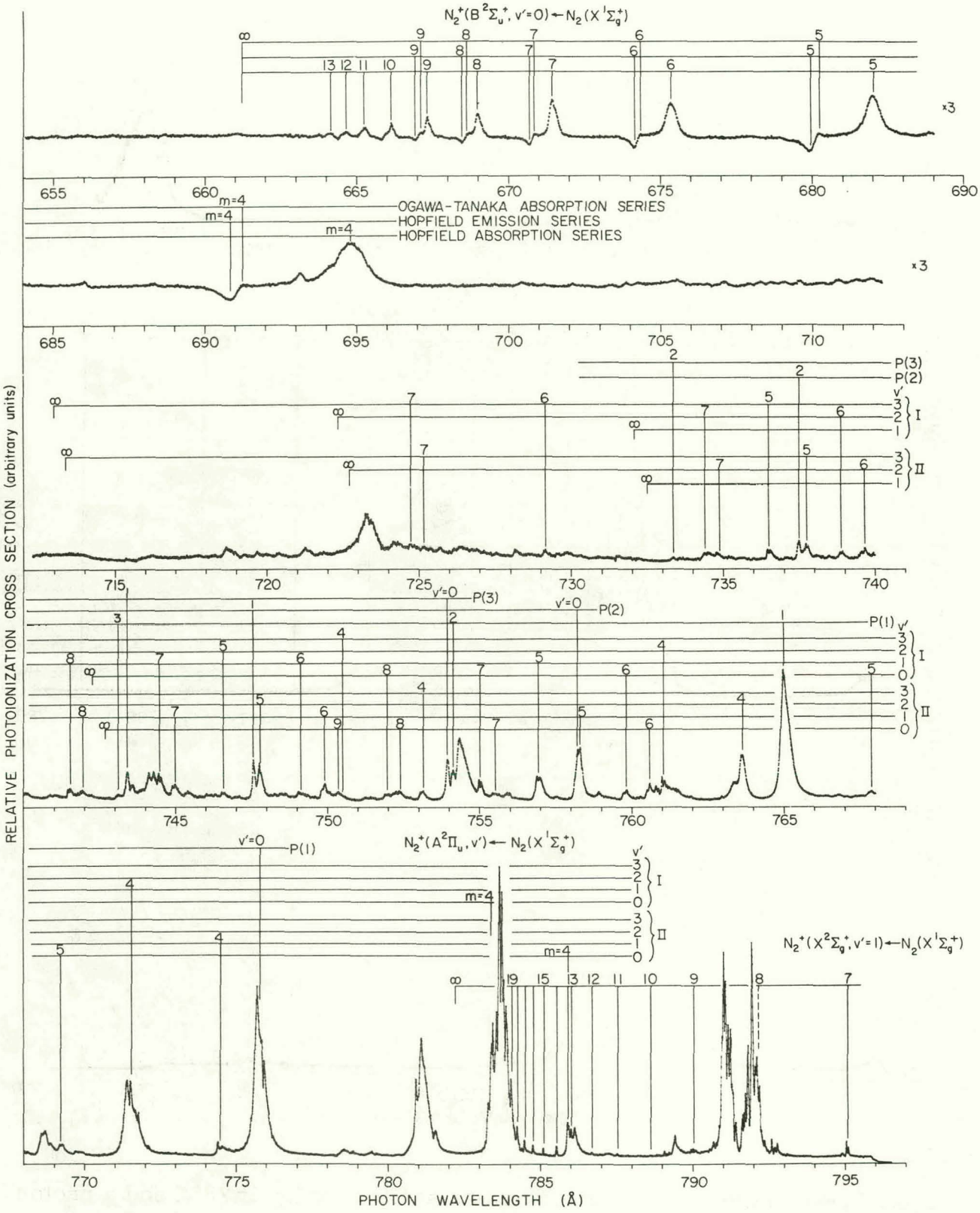

FIG. 1.--Relative photoionization cross section for N_2 at 78°K.
(ANL Neg. 209-76-679)

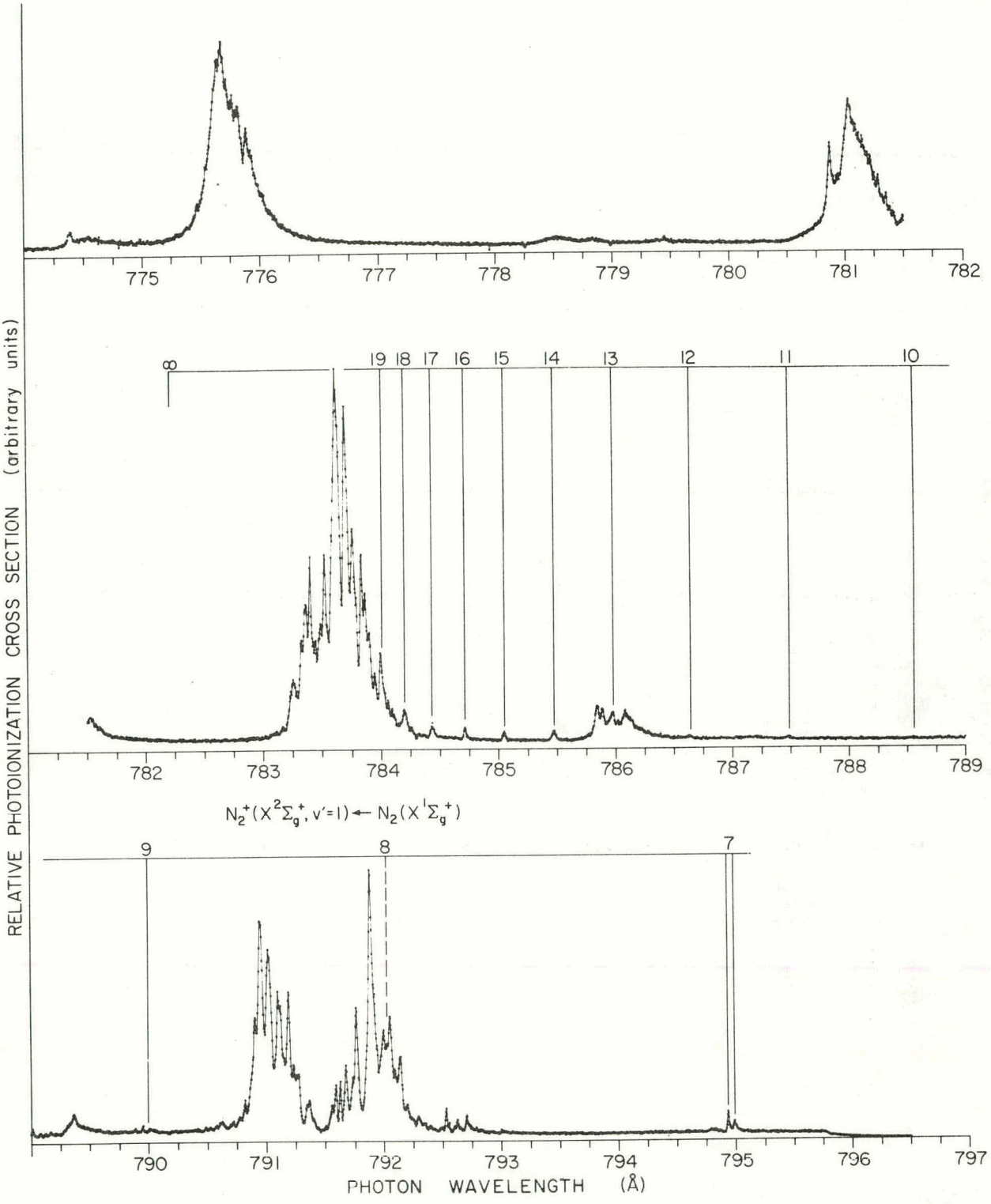

FIG. 2.--Relative photoionization cross section for N_2 at 78°K and a photon resolution of 0.016 Å in the energy region near the ionization threshold. (ANL Neg. 209-76-680)

PHOTOELECTRON SPECTROSCOPY OF THE RARE GAS DIMERS Ar_2, Kr_2, AND Xe_2 *

P. M. Dehmer and J. L. Dehmer

Mulliken[1] has discussed the potential energy curves and angular momentum coupling schemes for the rare gas (Rg) dimers and their ions. He showed that the dimer ions formed from $Rg(^1S_0) + Rg^+(^2P_{\frac{3}{2}}$ or $^2P_{\frac{1}{2}})$ have a bound $^2\Sigma^+_{\frac{1}{2}u}$ ground state and five excited states, all of which are predicted to be repulsive with only a small polarization minimum at large R (internuclear distance). At small R, a molecular orbital description of the excited states is appropriate and the states are, in order of increasing energy, $^2\Pi_{\frac{3}{2}g}$, $^2\Pi_{\frac{1}{2}g}$, $^2\Pi_{\frac{3}{2}u}$, $^2\Pi_{\frac{1}{2}u}$, and $^2\Sigma^+_{\frac{1}{2}g}$. At large R, the states are labeled according to case c (rather than case a or b) coupling rules, and their ordering may be different, but must be consistent with the appropriate noncrossing rules.[1] The ground state and first three excited states given above dissociate to $Rg(^1S_0) + Rg^+(^2P_{\frac{3}{2}})$, and the remaining two excited states dissociate to $Rg(^1S_0) + Rg^+(^2P_{\frac{1}{2}})$. In the present experiments, we have examined these dimer ion states using the technique of photoelectron spectroscopy. New information is obtained for the potential energy curves of the ionic states at large R, corresponding approximately to R_e of the neutral ground state.

The apparatus consists of a supersonic molecular beam source which produces the weakly bound rare gas dimers in combination with a high resolution hemispherical photoelectron spectrometer. The nozzle source, which is similar in concept to that described by Smalley et al.,[2] produced beams of approximately 1 percent dimer containing minimal concentrations of heavier clusters. Under typical operating conditions, the tip of the nozzle was located approximately 2 to 3 mm below the centerline of the photon beam, which was used to photoionize the target gas. The ejected photoelectrons were energy analyzed using a rotatable hemispherical photoelectron spectrometer, which incorporated 5.1 cm mean-radius copper hemispheres. The details of the

*Summary of two papers to be published in J. Chem. Phys.

analyzer and the hollow cathode lamp used to produce the He I 584 Å ionizing radiation have been given previously.[3,4] In this experiment, photoelectrons were sampled at 90° relative to the incident light beam in order to maximize the counting rate. With ~0.05 cm diameter entrance and exit apertures on the analyzer, and a photoelectron analysis energy of 2 eV, the observed photoelectron resolution was 17 meV. The resolution degraded to approximately 20 meV during day-long runs owing to contact-potential drifts.

Van Deursen and Reuss[5] have shown in a mass spectrometric investigation of cluster formation in supersonic expansions that there is a limiting nozzle stagnation pressure, P_L, below which only dimers are formed with negligible contamination from heavier clusters. In studies of supersonic expansion of Ne, Ar, H_2, N_2, and O_2, using a 26 μm diameter nozzle, they found that the value of P_L is given approximately by

$$P_L \approx 5.25 \times 10^{-4} \frac{\epsilon}{R_e^3} \left[\frac{kT_o}{\epsilon}\right]^{\frac{2-3\gamma}{2-2\gamma}} \left[\frac{R_e}{d}\right]^{0.55}, \qquad (1)$$

where γ and R_e are, respectively, the well depth in ergs and the equilibrium internuclear distance in cm of the neutral dimer ground state, γ is the specific heat capacity ratio of the bulk gas, d is the nozzle diameter in cm, T_o is the nozzle stagnation temperature in K, k is the Boltzmann constant, and P_L is the maximum nozzle stagnation pressure for pure dimer production in torr. For rare gases ($\gamma = 5/3$) at 298 K, Eq. 1 reduces to

$$P_L \approx 1.07 \times 10^{8} \frac{1}{R_e^{2.45}} \frac{1}{\epsilon^{1.25}} \frac{1}{d^{0.55}}, \qquad (1')$$

where ϵ and R are now in the more convenient units of cm^{-1} and Å, respectively, and d is in micrometers. One further correction factor should be added for calculations involving stagnation temperatures near room temperature, where van Deursen and Reuss found that Eq. 1 overestimates P_L. For example, for Ar at 294°K, Eq. 1 yields a value for P_L of 2400 torr, while the observed range of P_L was 1600 to 2300 torr. Thus, for rare gases at room temperature, an

additional multiplicative factor of 0.8 should be incorporated in Eq. 1. Table 1 gives the values of R_e and D_e for the rare gas dimers, and the values of P_L and d used in the present experiments. The combinations of nozzle size and optimum stagnation pressure were chosen so as to keep the pressure in the main vacuum chamber less than 1×10^{-4} torr in each experiment.

Figures 1–3 show the photoelectron spectra of Ar_2, Kr_2, and Xe_2, respectively, taken with the supersonic nozzle conditions listed in Table 1. For comparison, each figure also shows the spectrum of the appropriate atomic rare gas taken with an effusive source. The effusive spectra show that the peak shape obtained with this apparatus is excellent, with practically no distortion or tailing, even at the 1 percent level. The dimer ion photoelectron peaks are labeled 1 through 6. For a given spectrum, the peak labeled 1 refers to transitions from the ground state of the neutral dimer to the ground state of the dimer ion, while the peaks labeled 2 to 6 refer to transitions to the five excited states of the dimer ion, respectively. In several cases, dimer ion transitions are not observed because they are obscured by the much more intense atomic transitions.

It is interesting to note that, in each case, there is no discernable increase in photoelectron signal at the ionization threshold (indicated by the

TABLE 1. Estimate of Maximum Stagnation Pressure (P_L) for Pure Dimer Production

System	R_e (Å)	D_e (cm^{-1})	d (μ)	P_L from Eq. 1', torr	P_L used in present experiments,[a] torr
Ar_2	3.76[b]	98.7[b]	10	3782	3070
Kr_2	4.007[c]	140.33[c]	25	1259	980
Xe_2	4.362[c]	196.24[c]	35	559	460

a. The actual value of P_L used in the present experiments is ≈ 0.8 times the value calculated from Eq. 1'. See the text for details.
b. Ref. 6.
c. Ref. 7.

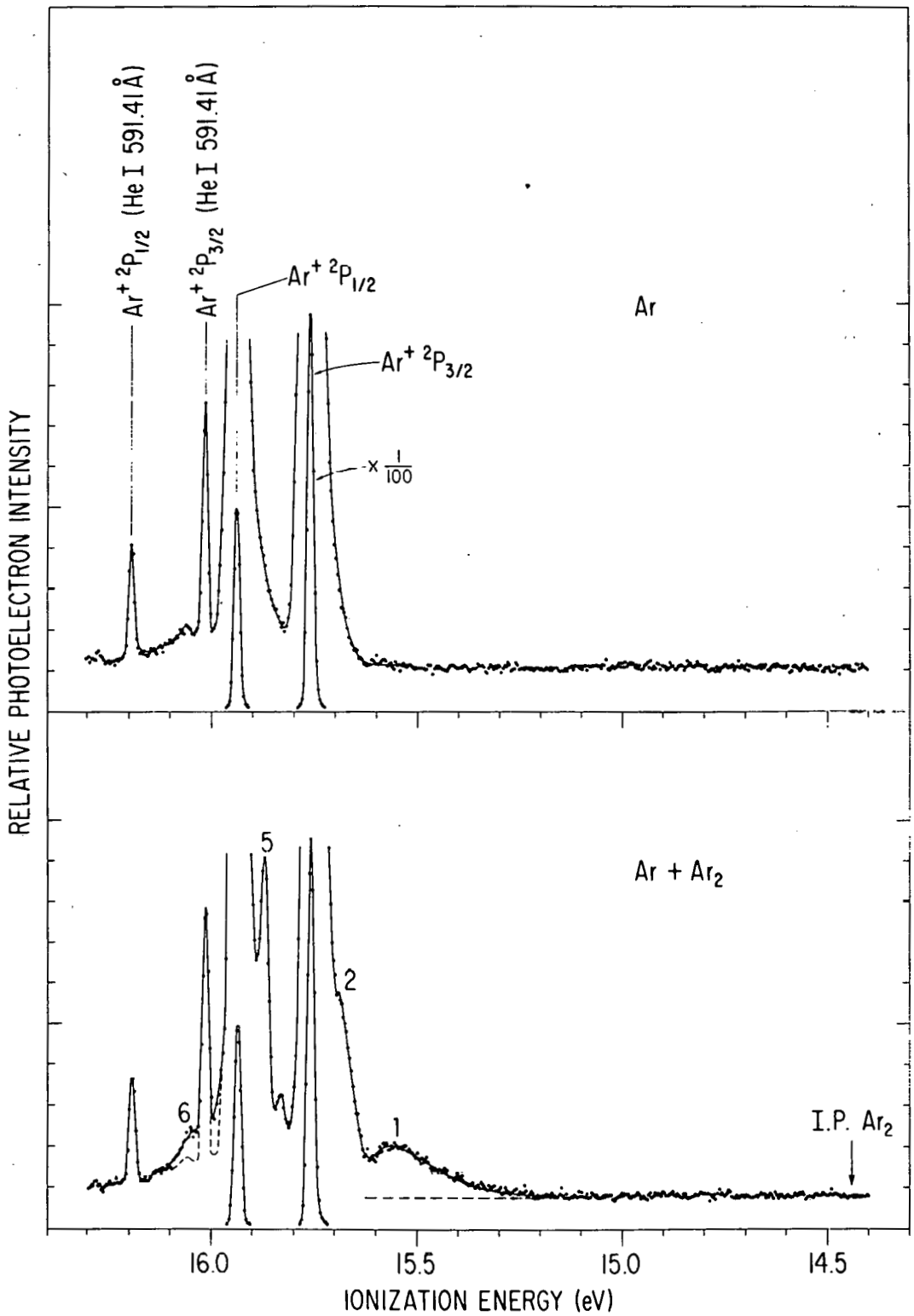

FIG. 1.--Photoelectron spectra of argon from an effusive source (top frame) and from a supersonic source (lower frame), both taken with He I 584 Å radiation and a photoelectron resolution of ~20 meV. (ANL Neg. 149-77-395 Rev. 1)

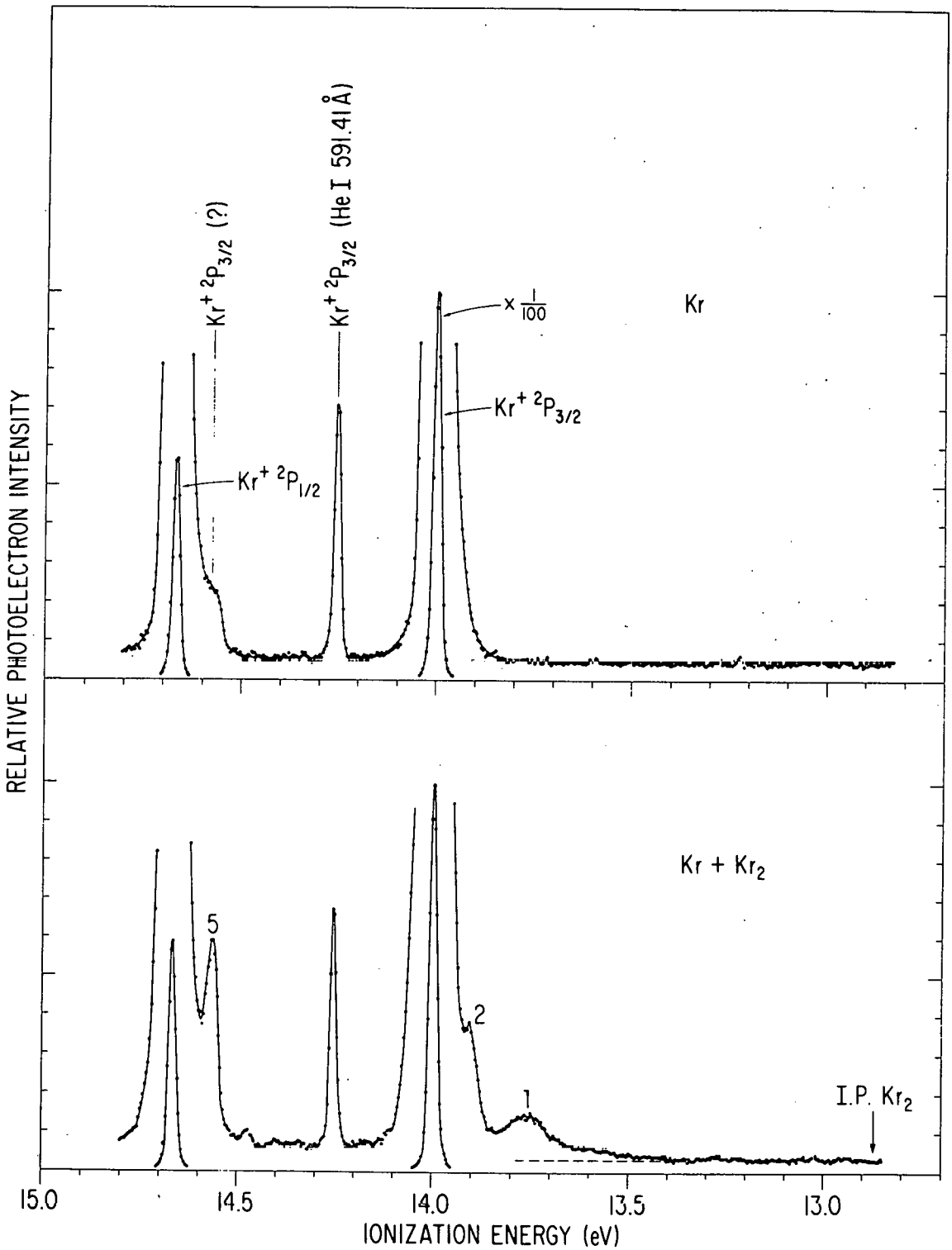

FIG. 2.--Photoelectron spectra of krypton from an effusive source (top frame) and from a supersonic source (lower frame), both taken with He I 584 Å radiation and a photoelectron resolution of ~20 meV. (ANL Neg. 149-77-396 Rev. 1)

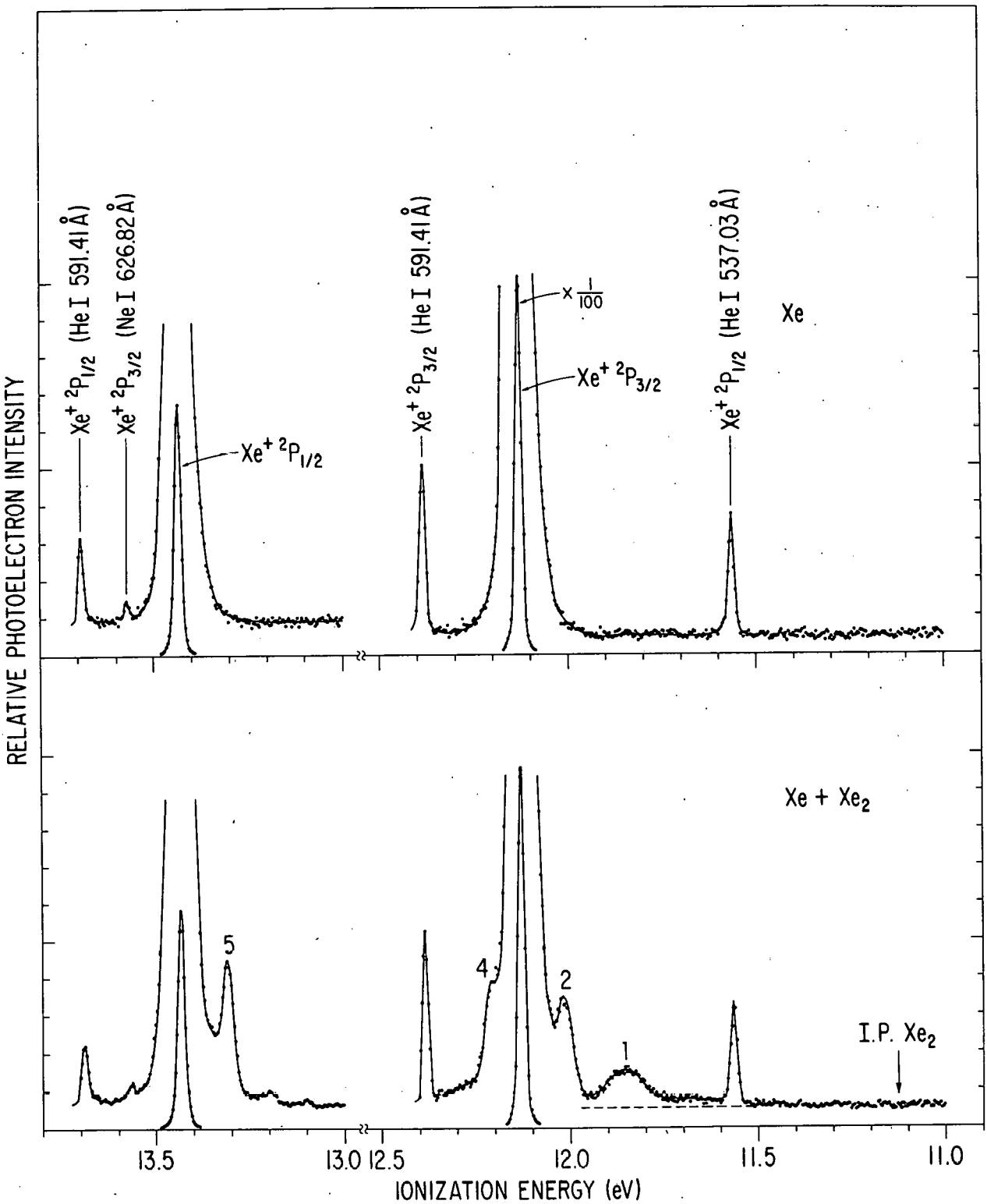

FIG. 3.--Photoelectron spectra of xenon from an effusive source (top frame) and from a supersonic source (lower frame), both taken with He I 584 Å radiation and a photoelectron resolution of ~20 meV.
(ANL Neg. 149-77-397 Rev. 1)

TABLE 2. Ionization Potentials and Dissociation Energies for Rare Gas Dimer Ions[a]

Peak[b]	State[c]	Ar_2^+ Adiabatic IP	Ar_2^+ Vertical IP	Ar_2^+ D_0	Kr_2^+ Adiabatic IP	Kr_2^+ Vertical IP	Kr_2^+ D_0	Xe_2^+ Adiabatic IP	Xe_2^+ Vertical IP	Xe_2^+ D_0
1	$A^2\Sigma^+_{\frac{1}{2}u}$	14.440[d]	15.545	1.330	12.866[e]	13.765	1.150	11.127[f]	11.851	1.026
2	$B^2\Pi_{\frac{3}{2}u}$	15.629	15.676	0.141	13.855	13.902	0.161	11.968	12.015	0.185
3	$C^2\Pi_{\frac{3}{2}u}$	—	—	—	—	—	—	—	—	—
4	$B^2\Pi_{\frac{1}{2}g}$	—	—	—	—	—	—	—	12.210	—[g]
5	$C^2\Pi_{\frac{1}{2}u}$	15.844	15.871	0.103	14.539	14.570	0.143	13.269	13.314	0.190
6	$D^2\Sigma^+_{\frac{1}{2}g}$	—	—	—[g]	—	—	—	—	—	—

a. All values are given in eV; errors are estimated at ±0.015 eV.
b. Peak numbers refer to Figures 1 to 3.
c. The assignments are based on the calculations of W. R. Wadt,[9] which show a curve crossing between the $B^2\Pi_{\frac{1}{2}g}$ and $C^3\Pi_{\frac{3}{2}u}$ states at small R, thus altering the ordering given by Mulliken.
d. Ref. 10.
e. Ref. 11.
f. Ref. 12.
g. Purely repulsive state in the Franck-Condon region.

arrow in Figures 1–3). These rare gas dimers provide excellent examples of Franck-Condon distributions greatly shifted from the adiabatic ionization potentials as a result of the displacements in R_e values between the upper and lower electronic states. The average value of the displacement in potential energy curves between the $Rg_2 X^1\Sigma_g^+$ and $Rg_2^+ A^2\Sigma_{\frac{1}{2}u}^+$ states for all the rare gases studied in this work is 1.23 Å.[8] This results in Franck-Condon distributions which are shifted from the adiabatic ionization potentials by as much as 1.0 eV.

Dissociation energies of the excited states of the dimer ions can be calculated from the relation

$$D_0(Rg_2^+) = IP(Rg) + D_0(Rg_2) - IP(Rg_2) , \qquad (2)$$

where $IP(Rg_2)$ and $IP(R_g)$ refer, respectively, to the adiabatic ionization potential of the excited state of the Rg_2^+ in question and the ionization potential of atomic Rg. The $Rg^+ {}^2P_{\frac{3}{2}}$ or $^2P_{\frac{1}{2}}$ ionization potential is used, depending on whether the Rg_2^+ state dissociates to $Rg(^1S_0) + Rg^+(^2P_{\frac{3}{2}})$ or $Rg(^1S_0) + Rg^+(^2P_{\frac{1}{2}})$. Table 2 gives the vertical and adiabatic ionization potentials for the states observed in the present experiments. The dissociation energy of these states is also included. There is very good agreement between the present experimental results and recent theoretical calculations of Wadt.[9]

References

1. R. S. Mulliken, J. Chem. Phys. 52, 5170 (1970); Radiat. Res. 59, 357 (1974).
2. R. E. Smalley, D. H. Levy, and L. Wharton, J. Chem. Phys. 64, 3266 (1976).
3. J. L. Dehmer, Argonne National Laboratory Radiological and Environmental Research Division Annual Report, July 1974–June 1975, ANL-75-60, Part I, pp. 61–63.
4. J. L. Dehmer and D. Dill, Photoion angular distributions for dissociative ionization of H_2 at 304 Å, Phys. Rev., in press.
5. A. van Deursen and J. Reuss, Int. J. Mass Spectrom. Ion Phys. 23, 109 (1977).
6. R. J. Leroy, J. Chem. Phys. 57, 573 (1972).
7. J. A. Barker, R. O. Watts, J. K. Lee, T. P. Schafer, and Y. T. Lee, J. Chem. Phys. 61, 3081 (1974).
8. P. M. Dehmer and J. L. Dehmer, Photoelectron spectra of Ar_2 and Kr_2 and potential energy curves for rare gas dimer ions, to be published.

9. W. R. Wadt, J. Chem. Phys. 68, 402 (1978).
10. J. T. Moseley, R. P. Saxon, B. A. Huber, P. C. Cosby, R. Abouaf, and M. Tadjeddine, J. Chem. Phys. 67, 1659 (1977).
11. C. Y. Ng, D. J. Trevor, B. H. Mahan, and Y. T. Lee, J. Chem. Phys. 66, 466 (1977).
12. C. Y. Ng, D. J. Trevor, B. H. Mahan, and Y. T. Lee, J. Chem. Phys. 65, 4327 (1976).

PHOTOELECTRON SPECTROSCOPY OF CLUSTER SPECIES—A GAS-PHASE TECHNIQUE FOR STUDYING MACROMOLECULAR SPECIES*

P. M. Dehmer and J. L. Dehmer

An investigation was made of the photoelectron spectra of xenon clusters, using an apparatus which combines a supersonic molecular beam source with a hemispherical photoelectron spectrometer. The exact mass distribution of the clusters is unknown, since the apparatus does not include provision for mass analysis; nevertheless, the present experiments show qualitatively how the photoelectron spectrum changes as the average cluster size is increased.

Data were taken with a 10 μm supersonic molecular beam source using three nozzle stagnation pressures between 1.70 atm and 6.76 atm. The spectra were measured with a hemispherical photoelectron spectrometer described previously.[1,2] With a 3 eV photoelectron analysis energy, the resolution of the apparatus was 27 meV. The results are given in Figure 1, along with an effusive spectrum shown for comparison. Photoelectron peaks resulting from weak impurity lines in the light source are identified on the effusive spectrum. The small asymmetric peak labeled with a question mark is due to photoelectrons from the $Xe^+ {}^2P_{\frac{3}{2}}$ ionic state photoionized by several weak impurity lines. An analogous peak due to photoelectrons from the $Xe^+ {}^2P_{\frac{1}{2}}$ ionic state is also observed, but does not fall within the energy range of Figure 1.

The spectrum taken at 1.70 atm is roughly comparable to the dimer spectrum, with only small amounts of contamination from heavier clusters.[3] Three dimer peaks are clearly visible in this spectrum and have maxima at 11.85 eV, 12.02 eV, and 13.31 eV. A fourth dimer peak is observed at higher resolution and has a maximum at 12.21 eV. These dimer peaks persist as the stagnation pressure is increased to 3.34 atm; however, new, very broad features are also observed at lower ionization potentials and are associated

---

*Excerpt from a paper to appear in J. Chem. Phys.

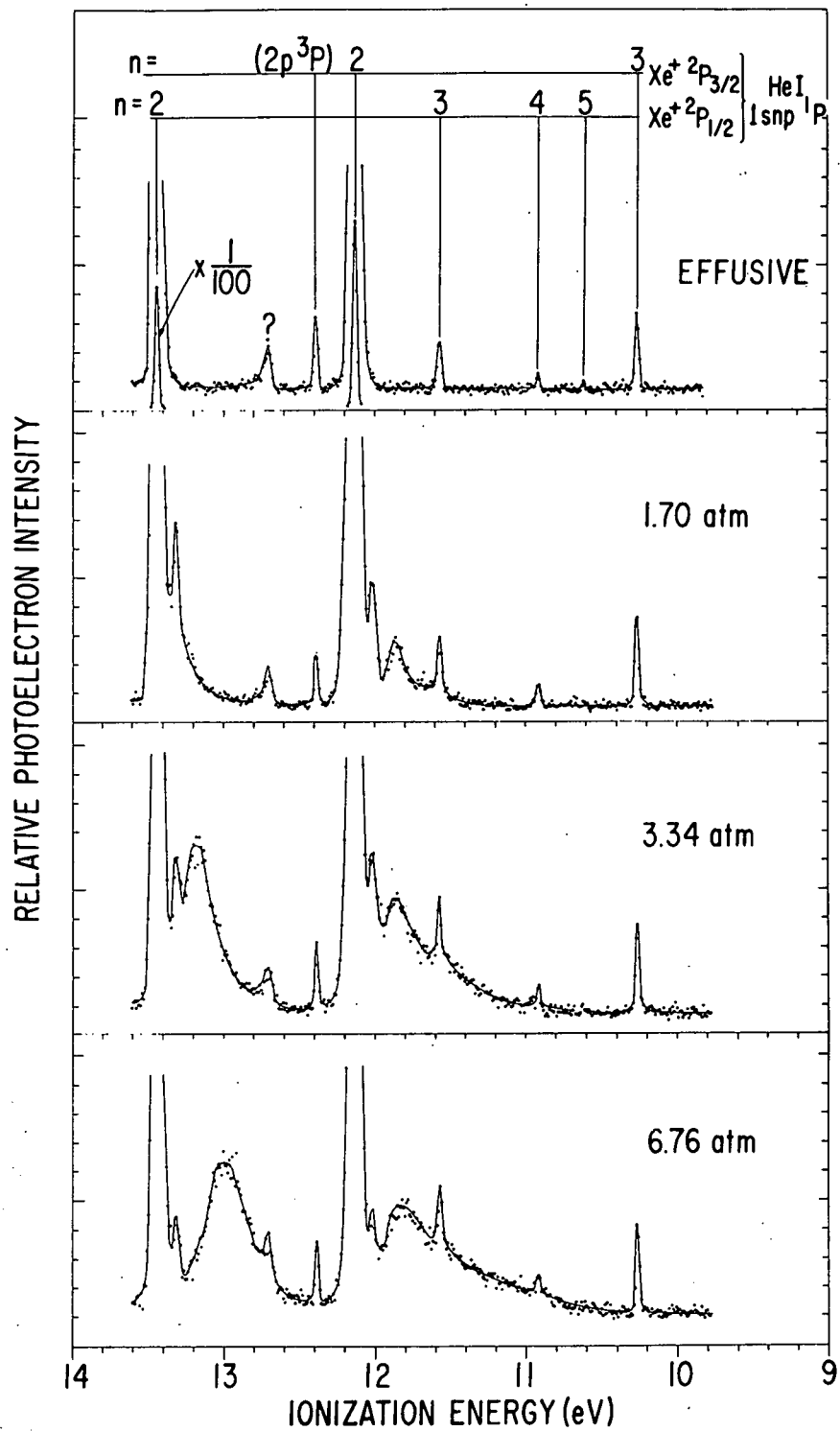

FIG. 1.--Photoelectron spectra of xenon from an effusive source (top frame) and from a supersonic source with a 10 μm diameter nozzle (lower frames), all taken with He I 584 Å radiation and a photoelectron resolution of ~ 27 meV. The nozzle stagnation pressures are indicated in the figure.
(ANL Neg. 149-77-349)

with both the upper and lower dissociation limits. These features, which are due to a distribution of heavier clusters, monotonically tend toward even lower ionization potentials as the stagnation pressure is increased further. This is clearly seen by comparing the spectra taken at 3.34 atm and 6.76 atm, which also show that the dimer peaks decrease in intensity relative to the cluster peaks as the stagnation pressure is increased. The "ionization potential" of solid Xe (more properly termed the threshold energy for photoemission), is 9.7 to 9.8 eV,[4,5] as compared to the ionization potential for Xe_2 of 11.127 eV.[6] The highest pressure spectrum in Figure 1 has a threshold energy of < 10.5 eV, which already is considerably below the ionization potential of the dimer.

While these experiments are preliminary, more refined experiments, which benefit from mass analysis, promise to provide a wealth of information on the energy-level structure of cluster species which are in the transition region between the gas and solid phases.

References

1. J. L. Dehmer, Argonne National Laboratory Radiological and Environmental Research Division Annual Report, July 1974–June 1975, ANL-75-60, Part I, pp. 61–63.
2. J. L. Dehmer and D. Dill, Photoion angular distributions in dissociative photoionization of H_2 at 304 Å, Phys. Rev. A, in press.
3. P. M. Dehmer and J. L. Dehmer, Photoelectron spectrum of Xe_2 and potential energy curves for Xe_2^+, J. Chem. Phys., in press.
4. N. Schwentner, M. Skibowski, and W. Steinmann, Phys. Rev. A 8, 2965 (1973).
5. N. Schwentner, F.-J. Himpsel, V. Saile, M. Skibowski, W. Steinmann, and E. E. Koch, DESY Report SR-74/17 (December 1974).
6. C. Y. Ng, D. J. Trevor, B. H. Mahan, and Y. T. Lee, J. Chem. Phys. 65, 4327 (1976).

FRANCK-CONDON FACTOR CALCULATIONS FOR THE $X\,^1\Sigma_g^+ \rightarrow A\,^2\Sigma_{\frac{1}{2}u}^+$ IONIZING TRANSITION IN THE RARE GAS DIMERS AND POTENTIAL ENERGY CURVES FOR $Rg_2^+\,A\,^2\Sigma_{\frac{1}{2}u}^+$ *

P. M. Dehmer

The rare gas (Rg) dimers Ar_2, Kr_2, and Xe_2 have values of R_e (equilibrium internuclear distance of the neutral dimer ground state) which are typically 1.2 Å larger than those of the corresponding dimer ion ground states. This means that the Franck-Condon distributions for the respective $X\,^1\Sigma_g^+$, $v'' = 0 \rightarrow A\,^2\Sigma_{\frac{1}{2}u}^+$, v' ionizing transitions will peak at very large values of v', and that the distributions will have no discernible intensity for small values of v'. As part of the analysis of our rare gas dimer photoelectron spectra,[1] Franck-Condon factor calculations were performed for this transition for each system to determine as accurately as possible the position and the shape of the Franck-Condon distributions. These calculations were an aid in assigning the ground state photoelectron peak, since the Franck-Condon distributions peak nearly 1 eV from the adiabatic ionization potential for each rare gas dimer. Small changes in the assumed potential energy curves for the upper and lower electronic states can change the positions of the maxima by more than 0.1 eV.

In the first set of calculations, Morse potentials were used to describe the upper and lower electronic states, and the vibrational wavefunctions were determined by numerical integration of the Schrödinger equation. Using this simplified description of the potential energy curves, the only parameters required for the calculations are R_e, D_e, and ω_e for the upper and lower electronic states, and the vibrational temperature of the neutral dimer formed in the supersonic expansion. The values of R_e, D_e, and ω_e for the rare gas dimer ions are summarized in Table 1.

In order to determine the vibrational distribution of the rare gas dimer

---

*Excerpt from a paper to be published in J. Chem. Phys.

TABLE 1. Morse Potential Parameters

State	R_e (Å)	D_0 (eV)	D_e (eV)	ω_e (cm^{-1})	$\omega_e x_e$ (cm^{-1})[a]
Ar_2	3.76[b]	84.0[b]	98.7[b]	30.68[c]	2.3841
Ar_2^+	2.48[d]	10724.67[c]	10870.67[f]	293.0 [d]	1.9743
Kr_2	4.007[g]	128.69[f]	140.33[g]	23.78[h]	1.0074
Kr_2^+	2.78 [d]	9275.30[e]	9365.30[f]	180.0[d]	0.8649
Xe_2	4.362[g]	185.2[i]	196.24[g]	20.93[i]	0.5581
Xe_2^+	3.22 [d]	8274.86[e]	8336.36[f]	123.0 [d]	0.4537

a. $\omega_e x_e = (\omega_e^2)/(4 \cdot D_e)$.

b. Ref. 2.

c. Ref. 3.

d. Ref. 4

e. $D_0(Rg_2^+) = IP(Rg) + D_0(Rg_2) - IP(Rg_2)$ where
$IP(Ar_2) = 14.4404$ eV (Ref. 5),
$IP(Kr_2) = 12.8655$ eV (Ref. 6),
$IP(Xe_2) = 11.127$ eV (Ref. 7),
IP(Ar) = 15.7597 eV
IP(Kr) = 13.9998 eV
IP(Xe) = 12.1300 eV
} Ref. 8,

f. $D_e = D_0 + \text{Zero Point Energy}$
$\cong D_0 + (\frac{1}{2}\omega_e - \frac{1}{4}\omega_e x_e)$

g. Ref. 9.

h. Ref. 10.

i. Ref. 11.

molecules formed in the supersonic expansion, it is necessary to estimate the vibrational temperature of the beam. In a study of supersonic expansions of alkali atom beams, Gordon et al.[12] found that 50 percent or more of the condensation energy (i.e., D_0) appears as vibrational excitation of the alkali dimer; however, alkali dimers have very large heats of condensation and large vibrational energy spacings compared to the van der Waals molecules studied here. A better comparison would be with the work of Smalley et al.[13] on the

fluorescence excitation spectrum of the NaAr van der Waals molecule, which was formed in a supersonic expansion. They found that the transition from $v'' = 0$ of the ground state to $v' = 8$ of the first excited state was a factor of 3.7 more intense than the corresponding transition from $v'' = 1$ of the ground state (see Table 1 of Ref. 13, Bands 7 and 8). Using their value of 11.26 cm^{-1} for the vibrational energy spacing and Franck-Condon factors of 0.111 and 0.094 for transitions from the $v'' = 1$ and 0 levels to the upper state, respectively,[14] this intensity ratio yields a vibrational temperature of 11°K, which is a factor of 5.5 greater than the stated rotational temperature of 2 ± 1°K, and is approximately 24 percent of the dissociation energy, $D_0 = 32.4$ cm^{-1}. The actual value of the dissociation energy may be somewhat larger than this,[15] so that perhaps 20 percent or less of the condensation energy appears as vibrational excitation of the dimer in experiments involving van der Waals molecules. For the present calculations using Morse potentials, the vibrational temperature was taken to be 25°K for Ar_2, 35°K for Kr_2, and 50°K for Xe_2. These values are approximately 7 to 10 times the respective rotational temperatures, and are probably upper limits to the vibrational temperatures.

The calculated Franck-Condon distributions are shown in Figure 1 as the curves labeled b, and are superimposed on the actual rare gas dimer photoelectron spectra. These spectra are shown in the region of the atomic $^2P_{\frac{3}{2}}$ photoelectron peak only. The broad photoelectron peaks with maxima at 15.45 eV in the Ar_2 spectrum, 13.77 eV in the Kr_2 spectrum, and 11.85 eV in the Xe_2 spectrum are now known to be due to transitions from the ground state of the dimer to the excited vibrational levels of the dimer ion ground state.[1] As is seen from Figure 1, the Franck-Condon distributions for this transition calculated using Morse potentials are too low in energy by at least 0.1 eV. They are also too broad; however, this can be corrected by lowering the estimated vibrational temperature. In order to shift the distributions to higher ionization energy, the values of R_e for the dimer must be decreased by approximately 0.2 Å, (this assumes that the R_e of the neutral dimers are well known). While a shift in R_e of 0.2 Å is possible for Xe_2^+, the R_e values of Ar_2^+ and Kr_2^+ should be much more accurately known from calculations.

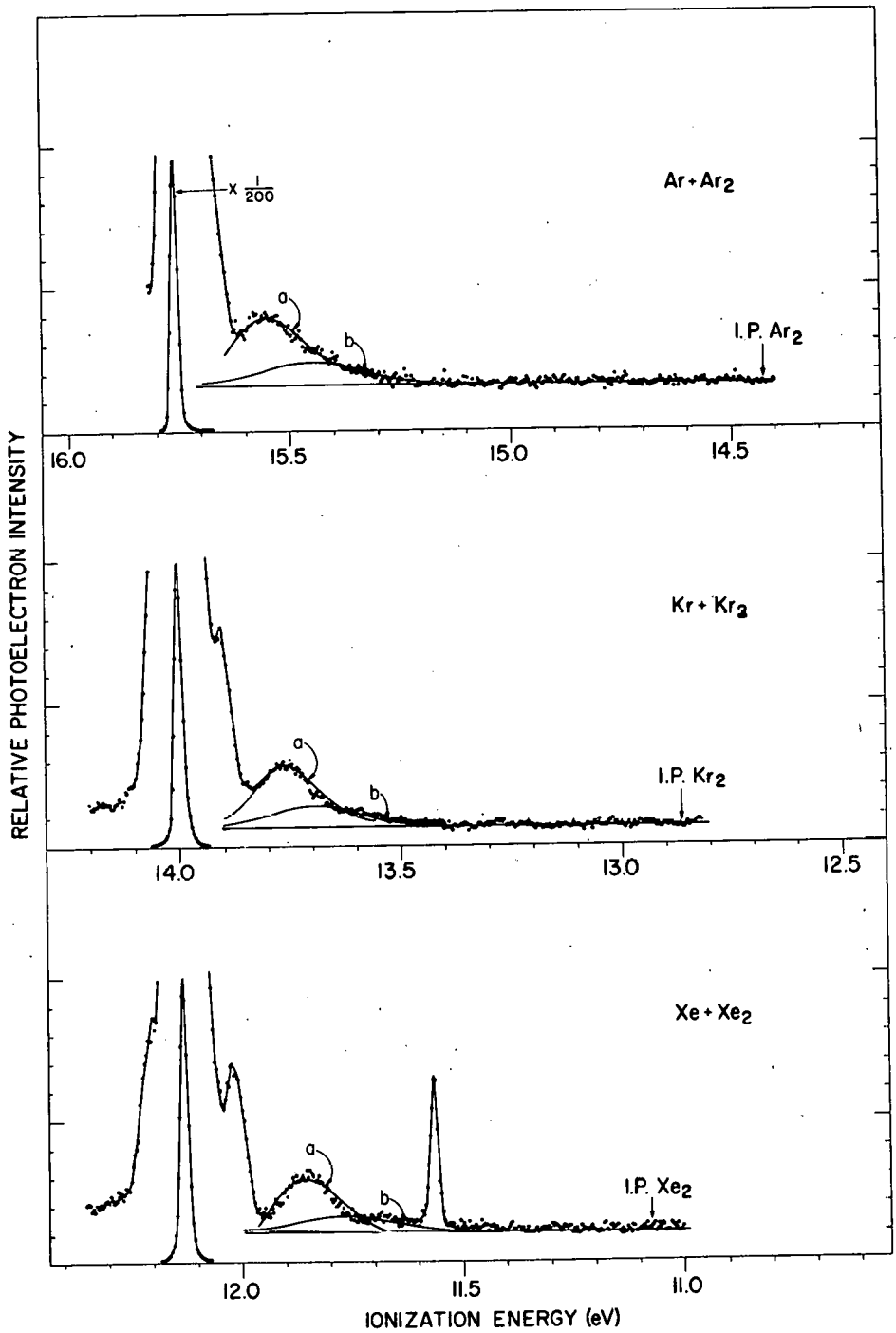

FIG. 1.--Calculated Franck-Condon distributions for the $Rg_2\ X^1\Sigma_g^+ \rightarrow Rg_e^+\ A\ ^2\Sigma_{\frac{1}{2}u}^+$ ionizing transitions in Ar_2, Kr_2, and Xe_2. Curve a was calculated using the modified theoretical potential of Wadt[4] for the $Rg_2 + A\ ^2\Sigma_{\frac{1}{2}u}^+$ state; curve b was calculated using a Morse potential for this state.

(ANL Neg. 149-78-73)

The error in these calculations results from the failure of the Morse function to adequately represent the dimer ion ground state potentials at large R. Hence, an attempt was made to construct more accurate potentials for these states, based on the calculated potentials of Wadt.[16] Wadt's potentials cannot be used directly since they are known to have incorrect dissociation energies; however, they should have better shapes than the Morse potential. The difference in shapes is shown in Figure 2, which gives the reduced potential energy curves for Xe_2^+. The curves for Xe_2^+ are representative of those for all the rare gas dimers. Wadt's potentials are more repulsive at large R than the Morse potential, and this is exactly what is required to shift the Franck-Condon distribution to higher energy and hence to bring it into alignment with the observed peak in the photoelectron spectrum. Numerical potentials were generated based on Wadt's potentials (calculated with spin-orbit interaction) by scaling the reduced potentials using the values of D_e in Table 1. The values of R_e were assumed to be the same as those calculated by Wadt. The vibrational temperature of the supersonic beam was varied until a good fit was obtained to the data. In all cases the final value of the vibrational temperature was approximately 15°K,[1,17] which is considerably lower than the estimated values. This may be due to residual errors in the potential energy curves, or to a failure of the Boltzmann distribution to represent the actual distribution of vibrational levels in the beam. The final Franck-Condon distributions are shown in Figure 1 as the curves labeled a. There is excellent agreement for Ar_2 and Kr_2 using the potential parameters given above. For the Xe_2 transition, the value of R_e for Xe_2^+ has to be decreased to 3.17 Å in order to obtain the good fit to the data shown in Figure 1. The small decrease in R_e from the calculated value is in agreement with Wadt's expectation.[18]

We conclude from these calculations that great care must be taken when using trial potentials in cases in which the results are sensitive to the long-range part of the potential. While the Morse function is an excellent approximation to the true potential near R_e, it can deviate from the true potential by as much as 10 percent of D_e at large R.

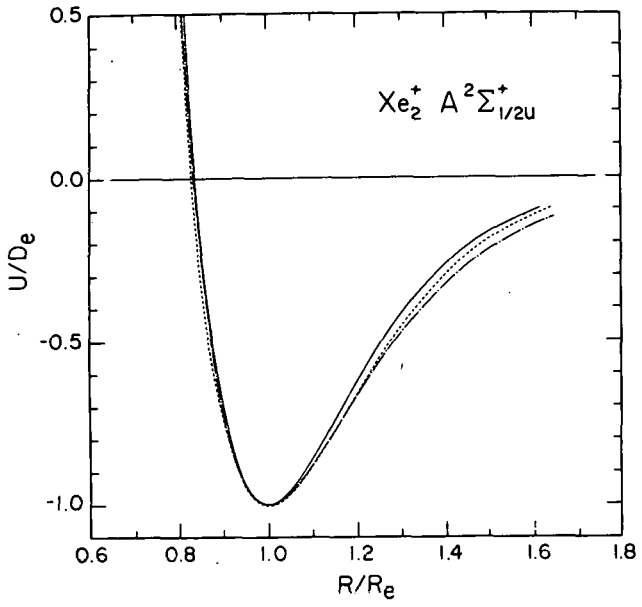

FIG. 2.--Reduced potential energy curves for the ground state of Xe_2^+. The solid and dashed curves are Wadt's theoretical potentials calculated with and without spin-orbit interaction, respectively, and the dash-dot curve is the Morse potential with the parameters given in Table 1.
(ANL Neg. 149-77-534)

References

1. P. M. Dehmer and J. L. Dehmer, Photoelectron spectra of Xe_2 and potential energy curves for Xe_2^+, J. Chem. Phys., in press.
2. R. J. Leroy, J. Chem. Phys. 57, 573 (1972).
3. Y. Tanaka and K. Yoshino, J. Chem. Phys. 53, 2012 (1970).
4. W. R. Wadt, J. Chem. Phys. 68, 402 (1978).
5. J. T. Moseley R. P. Saxon, B. A. Huber, P. C. Cosby, R. Abouaf, and M. Tadjeddine, J. Chem. Phys. 67, 1659 (1977).
6. C. Y. Ng, D. J. Trevor, B. H. Mahan, and Y. T. Lee, J. Chem. Phys. 66, 446 (1977).
7. C. Y. Ng, D. J. Trevor, B. H. Mahan, and Y. T. Lee, J. Chem. Phys. 65, 4327 (1976).
8. Atomic Energy Levels, U.S. National Bureau of Standards, Washington, D.C., Circular 467 (1948).
9. J. A. Barker, R. O. Watts, J. K. Lee T. P. Schafer, and Y. T. Lee, J. Chem. Phys. 61, 3081 (1974).
10. Y. Tanaka, K. Yoshino, and D. E. Freeman, J. Chem. Phys. 59, 5160 (1973).
11. D. E. Freeman, K. Yoshino, and Y. Tanaka, J. Chem. Phys. 61, 4880 (1974).
12. R. J. Gordon, Y. T. Lee, and D. R. Herschbach, J. Chem. Phys. 54, 2393 (1971).
13. R. E. Smalley, D. A. Auerbach, P.S.H. Fitch, D. H. Levy, and L. Wharton, J. Chem. Phys. 66, 3778 (1977).
14. J. B. Tellinghuisen, Vanderbilt University, private communication (1978).
15. R. P. Saxon, R. E. Olson, and B. Liu, J. Chem. Phys. 67, 2692 (1977) and references therein.
16. W. R. Wadt, J. Chem. Phys., in press.
17. P. M. Dehmer and J. L. Dehmer, Photoelectron spectra of Ar_2 and Kr_2 and dissociation energies of the rare gas simer ions, to be published.
18. W. R. Wadt, Los Alamos Scientific Lab., private communication (1977).

ON THE USE OF A SUPERSONIC MOLECULAR BEAM SOURCE FOR THE STUDY OF HIGH-RESOLUTION PHOTOELECTRON SPECTRA

P. M. Dehmer and J. L. Dehmer

The factors limiting resolution in a photoelectron spectroscopy experiment are discussed. We show that a supersonic molecular beam source can aid in high resolution by reducing the rotational and vibrational temperature and the Doppler broadening of the target gas.

Attempts to measure the high resolution photoelectron spectra of molecules are nearly always limited by the rotational, vibrational, and Doppler broadening of the target gas. Samson[1] has shown that the Doppler broadening of a photoelectron peak is given by

$$\delta = 0.723\ (ET/M)^{\frac{1}{2}} \qquad \text{(meV)}\ , \tag{1}$$

where M is the mass of the target gas in amu, T is the temperature of the gas in °K, and E is the energy of the ejected photoelectron in eV. In general, very light target gases will experience the largest Doppler broadening. For example, the photoelectrons ejected from H_2 at 300°K by 584 Å radiation will have a half-width of 21 meV. This is considerably larger than the state-of-the-art resolution of a photoelectron spectrometer, which is 5 to 10 meV. Heavier target gases will experience very little Doppler broadening; however, molecular targets will have a manifold of closely-spaced rotational levels, and consequently their photoelectron spectra will be rotationally broadened. In certain cases, vibrational broadening can also be significant.

Rotational, vibrational, and Doppler broadening can all be substantially reduced by lowering the temperature of the target gas; however, most gases will condense and form a liquid phase long before significant cooling can occur. We have chosen to circumvent this problem of condensation by using supersonic expansion to provide the cooling. In supersonic expansion, which is an approximately isentropic expansion, a gas at high pressure is expanded through a small orifice into a vacuum. During this expansion, random thermal motion is converted into directed mass flow with the result that the translational

temperature T decreases, while the velocity associated with the directed flow increases. Thus, random thermal energy is converted into a uniform kinetic energy of mass motion plus a shrinking thermal component. This is accomplished through collisions which, in the aggregate, scatter molecules into an ever narrowing range of velocity. When the collision frequency decreases and eventually falls to zero due to rarification in the beam, the cooling process ceases and a terminal Mach number (defined as the ratio of the velocity of the directed flow, u, to the speed of sound in the beam, $\alpha = (\gamma kT/M)^{\frac{1}{2}}$) is reached. The final translational temperature in the beam is related to the terminal Mach number M_T by[2]

$$T/T_0 = [1 - \tfrac{1}{2}(\gamma - 1)\, M_T^2]^{-1} \quad , \tag{2}$$

where γ is the specific heat capacity ratio, and T_0 is the nozzle stagnation temperature. Following Anderson and Fenn,[3] one can derive the generalized form for M_T

$$M_T \approx [(8/\pi\gamma)^{\frac{1}{2}} c]^{\theta} (2/A)^{1/\gamma\theta^{-1}} (D/\lambda)^{\theta} \quad , \tag{3}$$

where $\theta = (\gamma - 1)/\gamma$, c is the "collision effectiveness" equal to 0.25 for Ar[3] and assumed to be the same for other gases, A is a constant equal to 3.26 for atoms, 3.65 for diatomic molecules, and 3.96 for nonlinear polyatomic molecules,[4] D is the nozzle diameter, and λ is the mean free path in the nozzle. Thus,

for atoms ($\gamma = 5/3$),	$M_T \approx 469.8\, [DP_0 d^2/T_0)]^{0.4}$
for diatomic molecules ($\gamma = 7/5$),	$M_T \approx 121.2\, [DP_0 d^2/T_0)]^{0.2857}$
for nonlinear polyatomic molecules ($\gamma = 9/7$),	$M_T \approx 58.8\, [DP_0 d^2/T_0)]^{0.2222}$

(3')

where P_0 is the nozzle stagnation pressure in atm, T_0 is the nozzle stagnation temperature in °K, D is the nozzle diameter in cm, and d is the collision diameter in Å, which can be approximately determined from viscosity measurements.[5]

The properties of supersonic expansions described above are well known, and in recent years workers have used this technique to obtain the visible spectra of rotationally cooled species.[1] However, we are the first to combine a supersonic molecular beam source with a photoelectron spectrometer successfully. Technically, this is a much more difficult problem, since it requires that we analyze the energy of the ejected photoelectrons. The difficulty arises because the apparatus accepts ejected photoelectrons from only a very small solid angle corresponding to about 0.01 percent of the ejected electrons, and the experiment requires that the energy of the photoelectrons be analyzed with very high resolution (< 10 meV), thus requiring very careful attention to a number of details, such as surface preparation throughout the apparatus. In our apparatus we use a nozzle source similar in concept to that described by Smalley et al.[6] Stainless steel nozzle apertures ranging in size from 10 to 35 μm, and stagnation pressures up to 10 atm have been used to obtain high Mach numbers. Under typical operating conditions, the tip of the nozzle is located approximately 2 to 3 mm below the centerline of the photon beam which is used to photoionize the target gas. The ejected photoelectrons are analyzed using a rotatable hemispherical photoelectron spectrometer, which incorporates copper hemispheres with a mean radius of 5.1 cm. The details of the analyzer and the hollow cathode lamp used to produce the He I 584 Å ionizing radiation have been given previously.[7,8] In the present experiment, photoelectrons were sampled at 90° relative to the incident light beam in order to maximize the counting rate.

Figure 1 shows the photoelectron spectrum of the $O_2X^3\Sigma_g^- \rightarrow O_2^+X^2\Pi_g$, v= 0 transition in molecular oxygen. The ionizing radiation was the Ne I 736 Å resonance line, and the overall spectrometer resolution was 11 meV. This spectrum was taken with a 10 μm diameter nozzle aperture and a stagnation pressure of 7.5 atm, giving a terminal Mach number of 12.7 and a final translational temperature of 9°K. Since rotational degrees of freedom are very effectively relaxed in a supersonic expansion, the rotational temperature is assumed to be equal to the translational temperature. At this rotational temperature, approximately 80 percent of the beam is in the lowest rotational

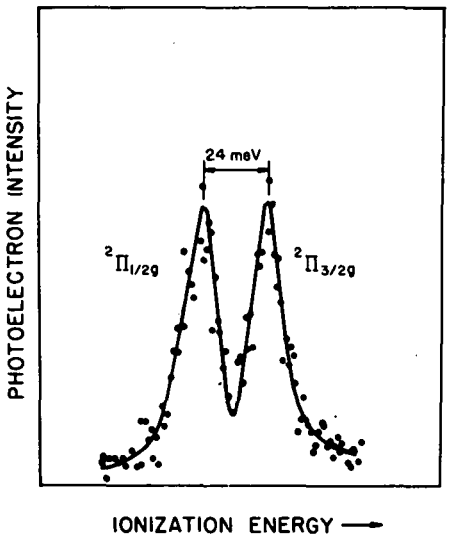

FIG. 1.--The Ne I (736 Å) photoelectron spectrum of the $O_2X^3\Sigma_g^- \rightarrow O_2^+X^2\Pi_g$, v=0 transition in molecular oxygen, taken with a spectrometer resolution of 11 meV using a supersonic molecular beam source. The rotational temperature is estimated to be 9°K. (ANL Neg. 149-78-74)

level (J=1), with nearly all of the remaining 20 percent in the first excited rotational level (J=3). Note that because O_2 is a homonuclear diatomic molecule with nuclear spin equal to zero, only the symmetric rotational levels are populated. In the case of O_2, the odd rotational levels are symmetric. Since the ground state of O_2^+ is a $^2\Pi$ state, each vibrational band will contain a $^2\Pi_{\frac{1}{2}}$ and a $^2\Pi_{\frac{3}{2}}$ component. The spin-orbit splitting of these levels in the v=0 vibrational band is 24 meV.[9] With a spectrometer resolution of 11 meV and no rotational excitation, these spin-orbit components should be split about 80 percent of the way to the baseline. This is almost exactly the degree of splitting actually observed in Figure 1, indicating that there is no rotational broadening in the spectrum.

Samson[10] has also investigated this band using a conventional (effusive) molecular beam source in an attempt to determine an accurate value of the O_2 ionization potential. In his experiment, the spectrometer resolution was 7 meV, and the Ar II 290 Å resonance line was used as the ionizing radiation. This low energy resonance line was used rather than the more intense (and "cleaner") He I or Ne I lines in order to reduce the Doppler broadening. Even with the lower energy resonance line and the significantly better spectrometer resolution, the resulting spectrum was only split about 30 percent of the way to the baseline.

The advantage of supersonic cooling is therefore obvious. One can use strong resonance lines for the ionizing radiation without worrying about Doppler broadening, work at moderate spectrometer resolution, and still obtain spectra which are better resolved than those obtained with a conventional source using a very high resolution spectrometer. Since intensity must be sacrificed when working at very high resolution, it is probably only feasible to measure high resolution spectra of very weak bands using a supersonic source in combination with a moderate resolution (10 to 20 meV) spectrometer.

At present we are using this apparatus to investigate the photoelectron spectra of a number of small polyatomic molecules at high resolution.

References

1. J.A.R. Samson, Rev. Sci. Instr. 40, 1174 (1969).
2. R. E. Smalley, L. Wharton, and D. H. Levy, J. Chem. Phys. 63, 4977 (1975).
3. J. B. Anderson and J. B. Fenn, Phys. Fluids 8, 780 (1965).
4. H. Ashkenhas and F. S. Sherman, Rarefied Gas Dynamics, Fourth Symposium, Vol. II, J. H. de Leeuw, Ed., Academic Press, New York, pp. 84–105 (1966).
5. J. O. Hirschfelder, C. F. Curtiss, and R. B. Bird, Molecular Theory of Gases and Liquids, John Wiley and Sons, Inc., New York, Table 1-A, pp. 1110–1113 (1954).
6. R. E. Smalley, D. H. Levy, and L. Wharton, J. Chem. Phys. 64, 3266 (1976).
7. J. L. Dehmer, Argonne National Laboratory Radiological and Environmental Research Division Annual Report, July 1974–June 1975, ANL-75-60, Part I, pp. 61–63.
8. J. L. Dehmer and D. Dill, Photoion angular distributions in dissociation photoionization of H_2 at 304 Å, Phys. Rev. A, in press.
9. P. H. Krupenie, J. Phys. Chem. Ref. Data 1, 423 (1972).
10. J.A.R. Samson, Can. J. Phys. 53, 1948 (1975).

ANGULAR DISTRIBUTIONS OF PHOTOELECTRONS AND NONTHERMAL PHOTOIONS FROM ATOMS AND MOLECULES*

J. L. Dehmer

During the last ten years, photoelectron angular distributions have been used extensively to study the dynamics of the photoionization process in atoms and molecules. Here we review some major advances in this body of work, with special emphasis on results emerging since the last Conference on Vacuum Ultraviolet Radiation Physics three years ago. By far the greatest progress has occurred for atoms, where interest is focussed on improving our zero-order (Hartree-Slater, Cooper-Zare) understanding of the asymmetry parameter $\beta(\epsilon)$, by considering electron correlations, relativistic effects, and anisotropic final-state interactions. The study of the rare gases has benefitted from extensive coordination between experiment and theory, whereas work on non-spherical atoms has been mainly theoretical, with the only measurements being performed very recently on atomic oxygen. Angular distribution studies of molecules are in a much earlier stage of development. Progress has been impeded by the lack of practical, realistic theoretical methods and of wave-length dependent measurements, both of which are becoming available only now. This recent work, together with selected topics from earlier resonance-line work on molecules is reviewed. In addition, a new class of angle-dependent studies of molecules will be discussed—the angular distribution of nonthermal ions formed by dissociative photoionization—which provides information complementary to the related measurements on photoelectrons.

---

*Abstract of an invited paper presented at the Fifth International Conference on Vacuum Ultraviolet Radiation Physics, Montpellier, France, 5–9 September 1977. The full article will be published in the Journal de Physique.

PHOTOION ANGULAR DISTRIBUTIONS IN DISSOCIATIVE PHOTOIONIZATION OF H_2 AT 304 Å *

J. L. Dehmer and Dan Dill †

Photoionization of H_2 by 304 Å radiation can produce the $2p\sigma_u$, $2p\pi_u$, and $2s\sigma_g$ repulsive states of H_2^+. The angular distributions of energetic (> 2 eV) protons from these states have been measured relative to the incident unpolarized light beam using a rotatable hemispherical electrostatic analyzer. Axial-recoil conditions apply in this situation, so that the photofragment angular distribution would be $\sin^2\theta$ for pure $\Sigma \rightarrow \Sigma$ electronic transitions and $(1 + \cos^2\theta)$ for pure $\Sigma \rightarrow \Pi$ electron transitions. However, unlike photodissociation processes forming neutral products, the present process also involves the ejection of photoelectrons with alternative symmetries, each associated with one of the above characteristic photoion angular distributions. Consequently, measurement of the net photoion angular distribution in dissociative photoionization yields the branching ratio between the alternative (degenerate) channels available to the photoelectron. This type of information cannot be deduced by observing the photoelectron itself. The present results indicate that the formation of the $2p\sigma_u$ state of H_2^+ at 304 Å is accompanied by ejection of photoelectrons with significant d-wave character.

The measurement of angular distributions and kinetic energies of photodissociation products yields, respectively, information on the symmetry and internal energy of the dissociating parent state(s). This can be a uniquely powerful spectroscopic tool, particularly in regions of the photoabsorption spectrum dominated by diffuse bands which are characteristic of repulsive final states. Moreover, such measurements can provide dynamical information on the photoexcitation process, such as branching ratios and dissociation lifetimes. There is significant literature on the theoretical (see, e.g., Refs. 1–4) and experimental (see, e.g., Refs. 1,4–6) aspects of this facet of molecular photodissociation; however, it is generally confined to the spectral range below the ionization potential.

---

* Summary of a paper to appear in Phys. Rev. A.

† Consultant, RER Division. Permanent address: Department of Chemistry, Boston University, Boston, Massachusetts 02215.

In dissociative photoionization, a new wrinkle emerges: When a molecular ion is produced in a repulsive state by photoionization, the process also involves the ejection of photoelectrons, which generally have available to them degenerate ionization channels of more than one symmetry type. Since the photoion angular distribution yields symmetry information about the total final state (molecular ion plus photoelectron), this complicates the determination of the symmetry of the repulsive ionic state alone. On the other hand, when the repulsive state is known, this affords us the rare opportunity to measure directly the branching ratio for the alternative, degenerate ionization channels. This branching ratio cannot be obtained from the electron energy spectrum owing to degeneracy; and the photoelectron angular distribution yields an implicit function of both the branching ratio and the relative phases of the alternative ionization channels from which the branching ratio cannot be isolated without further information. Once the branching ratio information is obtained from the photoion angular distribution, however, it can be combined with the photoelectron angular distribution data to help unravel the information contained in the photoelectron asymmetry parameter. Under favorable conditions (described in the paper to be published), the combination of photoion and photoelectron angular distributions can lead to a full determination of the dipole amplitudes and relative phases of the ionization channels, thus completely specifying all of the dynamical parameters of the photoionization process.

The theoretical background developed in the paper to be published can be summarized as follows. The differential cross section for photoions from dissociative photoionization of a cylindrically symmetric, randomly oriented target by unpolarized radiation in the dipole approximation has the form

$$d\sigma/d\Omega_m = (\sigma/4\pi)\,[1 - (\beta_m/2)\,P_2(\cos\theta_m)]\,, \tag{1}$$

$$\sigma = (4/3)\pi^2\alpha h\nu\,[D_\Sigma^2 + 2D_\Pi^2]\,, \tag{2}$$

$$\beta_m = 2\,[D_\Sigma^2 - D_\Pi^2]/[D_\Sigma^2 + 2D_\Pi^2]\,, \tag{3}$$

where the subscript m denotes molecular fragment (to distinguish from e for electron) and we have introduced the symbols

$$D_{\Sigma}^2 \equiv \sum_{\ell} |D_{\ell 00}^{(-)\Sigma}|^2 \quad , \tag{4}$$

$$D_{\Pi}^2 \equiv \sum_{\ell} |D_{\ell \pm 1 \pm 1}^{(-)\Sigma}|^2 \tag{5}$$

for the total $\Sigma \rightarrow \Sigma$ and $\Sigma \rightarrow \Pi$ ionization strengths. Under unpolarized excitation conditions, therefore, pure $\Sigma \rightarrow \Sigma$ ionization yields a $\sin^2\theta_m$ distribution and $\Sigma \rightarrow \Pi$ ionization a $(1+\cos^2\theta_m)$ distribution. In many cases, including those treated below, a mixture of $\Sigma \rightarrow \Sigma$ and $\Sigma \rightarrow \Pi$ transitions is allowed so that the net photoion angular distribution, as reflected in the value of β_m, gives the relative strength of the two types of transition

$$\frac{\sigma(\Sigma \rightarrow \Sigma)}{\sigma(\Sigma \rightarrow \Pi)} = \frac{D_{\Sigma}^2}{2D_{\Pi}^2} = \frac{1+\beta_m}{4-2\beta_m} \quad . \tag{6}$$

In the present experiment, 304 Å radiation was used to produce the $2p\sigma_u$, $2p\pi_u$, and $2s\sigma_g$ repulsive states of H_2^+. The reader is referred to the full paper for details of the experiment. The potential curves[7] of the states of H_2 and H_2^+ relevant to this experiment are shown in Figure 1 to show that H^+ ions from the $2p2\sigma_u$ will have kinetic energy in the range 7 to 10 eV, while the two higher H_2^+ states dissociate to produce slower protons. Typical data are shown in Figure 2. Following Gardner and Samson,[8] we assign the feature centered at ~8 eV to ions from $2p\sigma_u$ and the larger peak at ~5.5 eV to ions from both the $2p\pi_u$ and $2s\sigma_g$ states, with the strong likelihood that the $2p\pi_u$ state is the dominant one.

The two spectra in Figure 2 permit the qualitative observation that the 5.5 eV band is peaked forward, along the direction of the light, while the 8 eV band is slightly larger perpendicular to the light direction. Hence, one can expect that the asymmetry parameter, β_{H^+}, will be negative for the 5.5 eV peak and positive for the 8 eV peak. This qualitative observation is put on a quantitative basis in the lower part of Figure 3 where the β_{H^+} value was determined at evenly-spaced energy intervals between 3 and 9 eV. The spread

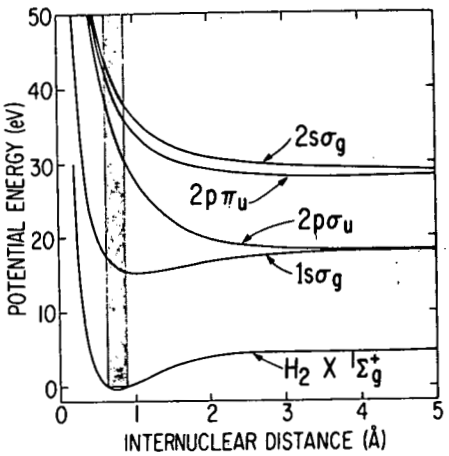

FIG. 1.--Selected potential energy curves (taken from Ref. 7) for states of H_2 and H_2^+ which participate in dissociative photoionization at $\lambda = 304$ Å. The shaded region represents the Franck-Condon region associated with the $H_2\, X\, ^1\Sigma_g^+ (v=0)$ ground state. (ANL Neg. 149-76-214)

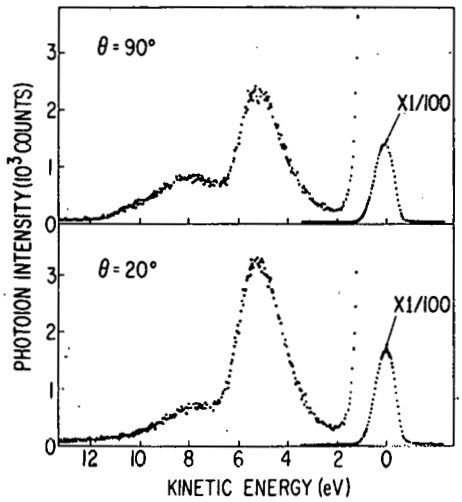

FIG. 2.--Photoion kinetic energy spectra for photoionization of H_2 ($\lambda = 304$ Å) at two observation angles ($\theta = 20°$ and $90°$) relative to the incident unpolarized light beam. The large peak near zero kinetic energy is comprised mostly of $H_2^+ 1s\sigma_g$ ground state ions which have a thermal energy distribution. (ANL Neg. 149-76-197 Rev. 1)

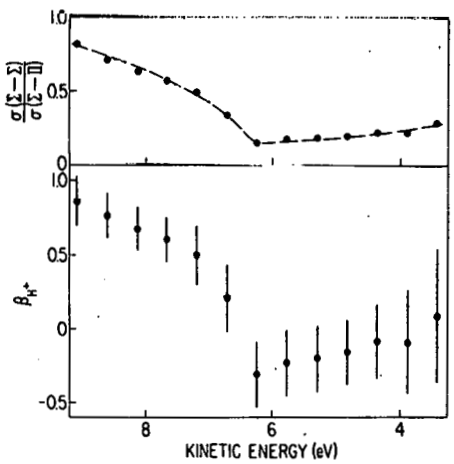

FIG. 3.--Asymmetry parameter and resulting relative cross sections for $\Sigma \rightarrow \Sigma$ and $\Sigma \rightarrow \Pi$ type transitions for 3 to 9 eV protons produced by dissociative photoionization of H_2 at $\lambda = 304$ Å.
(ANL Neg. 149-77-149)

in the data, due to weak signal and long counting times, necessitated the large error bars which were drawn, conservatively, to cover the range of variation of all runs. Despite the large uncertainty, a dramatic variation in the angular distribution of energetic protons from this process is observed. At 9 eV kinetic energy, where the protons are produced from the $2p\sigma_u$ state, $\beta_{H^+} \cong 0.86$. As the influence of the 5.5 eV peak increases at ~8 eV kinetic energy, the β_{H^+} value begins to plummet toward its low value of $\beta \cong -0.3$ near 6 eV. The data exhibit a very gradual net rise between 6 and 3 eV which we are not sure is significant.

The net ratio of cross sections for $\Sigma \rightarrow \Sigma$ and $\Sigma \rightarrow \Pi$ transitions are given in the upper part of Figure 3. This curve has been deduced from the β_{H^+} curve using Eq. 6, and the error bars have been omitted. The limit of $\sigma(\Sigma \rightarrow \Sigma)/\sigma(\Sigma \rightarrow \Pi) \cong 0.82$ at 9 eV can be taken as representative of dissociative photoionization via the H_2^+ $2p\sigma_u$ state. This indicates

$$\frac{\sigma(\Sigma \rightarrow \Sigma)}{\sigma(\Sigma \rightarrow \Pi)} = \frac{\sigma_{\sigma_g}}{\sigma_{\pi_g}} = 0.82$$

where the subscripts denote the photoelectron's symmetry so that production of π_g photoelectron is ~20% more probable than production of σ_g photoelectrons in connection with protons formed with ~9 eV kinetic energy. Since π_g and σ_g wavefunctions have $\ell = 2$ and $\ell = 0$ lead terms respectively (in a spherical harmonic representation) this observation implies that d waves contribute strongly to photoionization of H_2 at $\lambda = 304$ Å. The importance of high-ℓ partial waves to molecular photoionization has been recently emphasized[9] in photoionization of heavier first-row diatomic molecules. We re-emphasize that this partitioning of excitation probability between degenerate ionization channels would not be possible by measurements on the photoelectrons themselves. This new information provides a very detailed check of future theoretical calculations of dissociative photoionization of hydrogen, and, moreover, could be combined with photoelectron angular distributions to help unravel the relative phases of the alternative photoionization channels.

References

1. R. N. Zare, Mol. Photochem. 4, 1 (1972).
2. Sze-cheng Yang and R. Bersohn, J. Chem. Phys. 61, 4400 (1974).
3. R. C. Ormerod, W. R. Anderson, and T. L. Rose, J. Chem. Phys. 62, 127 (1975).
4. J. H. Ling and K. R. Wilson, J. Chem. Phys. 65, 881 (1976).
5. R. C. Ormerod, T. R. Powers, and T. L. Rose, J. Chem. Phys. 60, 5109 (1974).
6. E. J. Stone, G. M. Lawrence, and C. E. Fairchild, J. Chem. Phys. 65, 5083 (1976).
7. T. E. Sharp, At. Data 2, 119 (1971).
8. J. L. Gardner and J. A. R. Samson, Phys. Rev. A 12, 1404 (1975).
9. J. L. Dehmer and Dan Dill, J. Chem. Phys. 65, 5327 (1976).

PHOTOELECTRON ANGULAR DISTRIBUTION AND BRANCHING RATIOS FOR ATOMIC OXYGEN AT 304 Å *

J. L. Dehmer and P. M. Dehmer

The importance of atomic oxygen in the upper atmosphere and as a prototype open-shell atomic system has stimulated several theoretical investigations of both its integrated[1-9] and differential[7-9] photoionization cross sections. Recently, Starace et al.[7] and Manson et al.[8] have computed photoelectron angular distributions and branching ratios for the processes $O(2p^4\,^3P) \rightarrow O^+(2p^3\,^4S^o, {}^2D^o, {}^2P^o) + e^-$ using both Hartree-Slater and Hartree-Fock models. Smith[9] subsequently expanded on this by incorporating interchannel coupling in the final state by means of a close-coupling scheme, achieving good overall agreement with the earlier work. Measurements of the branching ratios for production of the $^4S^o$, $^2P^o$, and $^2D^o$ states of O^+ at 584 Å, by Samson and Petrosky,[10] and of the photoelectron angular distributions of the $^4S^o$ and $^2D^o$ states of O^+ at 736 Å and 584 Å by Samson and Hancock[11] exhibit good agreement with theory. Here we present photoelectron angular distributions and branching ratios for atomic oxygen at 304 Å in order to provide a high kinetic-energy test of the theoretical calculations.

A microwave discharge was used to produce atomic oxygen in a mixture with $O_2 X^3\Sigma_g^-$ and $O_2\, a^1\Delta_g$. A 584 Å photoelectron spectrum in the range 11 eV < I.P. < 14 eV is shown in Figure 1 to indicate the presence of these species.

In Figure 2 we show our $^2D^o/^4S^o$ and $^2P^o/^4S^o$ branching ratio measurements at 304 Å, the 584 Å measurements of Samson and Petrosky,[10] the Hartree-Slater results of Starace et al.,[7] and the close-coupling results of Henry.[3] The Hartree-Fock and Hartree-Slater results of Starace et al.[7] agree very well and only the latter are plotted in Figure 2. Here we see that the experimental points agree best with Henry's velocity results, although this conclusion is only tentative owing to the large error bars.

---

* Summary of a paper published in J. Chem. Phys. 67, 1782 (1977).

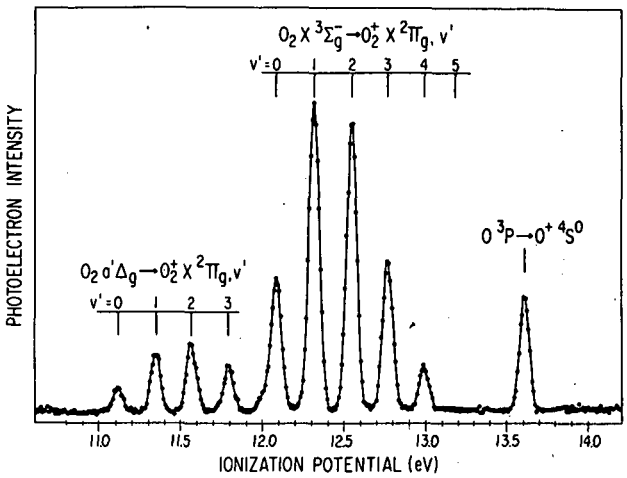

FIG. 1.--He I (584 Å) spectrum of the products of a microwave discharge in O_2 in the range 11 eV < I.P. < 14 eV. (ANL Neg. 149-77-6)

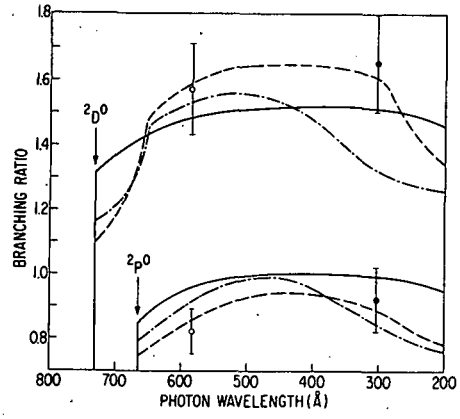

FIG. 2.--Comparison of the experimental $^2D^o/^4S^o$ and $^2P^o/^4S^o$ branching ratios presented here (●) and by Samson and Petrosky[10] (o) with the Hartree-Slater results of Starace et al.[7] (—) and the close-coupling length (-.-.) and velocity (---) results of Henry.[3] (ANL Neg. 149-77-35)

In Figure 3 we show our 304 Å measurement of the photoelectron angular distribution accompanying the production of the $O^+\,^4S^o$ state. It shows good agreement with the theoretical results by Starace et al.[7] and Smith,[9] as does the 584 Å measurement by Samson and Hancock.

Therefore, although the data are still extremely sparse, in every case they are in good agreement with existing theoretical treatments at the Hartree-Slater, Hartree-Fock, and close-coupling levels, confirming the conclusion of

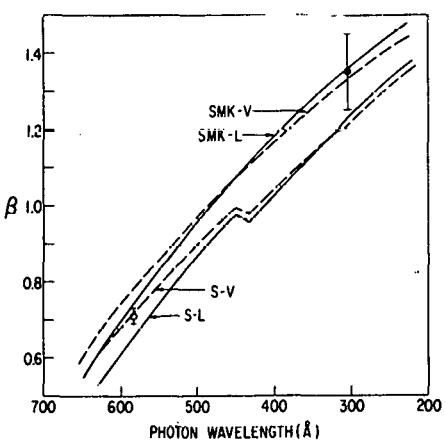

FIG. 3.--Comparison of theoretical and experimental results for the photoelectron angular distribution accompanying photoionization of atomic oxygen to form $O^+\,^4S^o$. Theoretical results include the Hartree-Fock results of Starace et al.[7] (SMK-L,V) and the close-coupling results of Smith[9] (S-L,V). The 304 Å data point is from the present work and the 584 Å point is that of Samson and Hancock.[11]

Starace et al.[7] and Manson et al.[8] that electron correlation effects play a minor role in the first-row atoms, even in open-shell cases.

References

1. A. Dalgarno and D. Parkinson, J. Atmos. Terr. Phys. 18, 335 (1960).
2. A. Dalgarno, R.J.W. Henry, and A. L. Stewart, Planet. Space Sci. 12, 235 (1964).
3. R.J.W. Henry, Planet. Space Sci. 15, 1747 (1967).
4. G. M. Thomas and T. M. Helliwell, J. Quant. Spectrosc. Radiat. Transfer 10, 423 (1970).
5. H. Kahler, J. Quant. Spectrosc. Radiat. Transfer 11, 1521 (1971).
6. P. S. Ganas, Phys. Rev. A 7, 928 (1973).
7. A. F. Starace, S. T. Manson, and D. J. Kennedy, Phys. Rev. A 9, 2453 (1974).
8. S. T. Manson, D. J. Kennedy, A. F. Starace, and D. Dill, Planet Space Sci. 22, 1535 (1974).
9. E. R. Smith, Phys. Rev. A 13, 1058 (1976).
10. J.A.R. Samson and V. E. Petrosky, Phys. Rev. A 9, 2449 (1974).
11. J.A.R. Samson and W. H. Hancock, Phys. Letters A 61, 380 (1977).

SHAPE RESONANCE EFFECTS IN X-RAY ABSORPTION SPECTRA OF MOLECULES*

Dan Dill† and J. L. Dehmer

X-ray absorption within molecular K shells acts as a highly localized source of electric-dipole excitation, with $\ell = 1$ (p symmetry) about the atomic excitation center. Over characteristic, narrow energy ranges, the molecular potential supports penetration by high-ℓ components of the excited state into the molecular core, where they are strongly coupled by the anisotropic molecular field to the $\ell = 1$ excitation. As a result, molecular inner-shell spectra exhibit strong concentrations of oscillator strength in narrow bands both above and below the ionization threshold, in contrast to the monotonic decrease characteristic of the corresponding free-atom spectra. This mechanism of shape resonance effects in molecular inner-shell absorption spectra has been elucidated by application of the multiple scattering method[1,2] to the calculation of these spectra (see, e.g., Ref. 3). This work is reviewed and extended, emphasizing (1) distribution of oscillator strength over the entire spectrum, (2) symmetry properties of resonant features in the ionization continuum as probed by photoelectron angular distribution measurements, and (3) a new, electron-optical interpretation of molecular resonance effects. Examples will include N_2, CO, NO, O_2, the hydrogen halides, and the diatomic halogens.

References

1. D. Dill and J. L. Dehmer, J. Chem. Phys. 61, 692 (1974).
2. J. Siegel, D. Dill, and J. L. Dehmer, J. Chem. Phys. 64, 3204 (1976).
3. J. L. Dehmer and D. Dill, J. Chem. Phys. 65, 5327 (1976).

---

*Abstract of invited paper presented at the 173rd National Meeting of the American Chemical Society, 20-25 March 1977, New Orleans. The same material was presented in an invited lecture at the Discussion Meeting on Inner-Shell Excitations, 15-17 September 1977, Chateau du CNRS, Gif-sur-Yvette, France. It was also a major part of a contributed paper to the 10th International Conf. on the Physics of Electronic and Atomic Collisions, 21-27 July 1977, Paris. (Book of Abstracts, Commisariat a l'Energie Atomique, Paris, p. 1182.)

†Consultant, RER Division. Permanent address, Department of Chemistry, Boston University, Boston, Mass. 02215.

MOLECULAR EFFECTS ON INNER-SHELL PHOTOIONIZATION. ELECTRON-OPTICAL ORIGIN OF THE SHAPE RESONANCES IN THE K-SHELL SPECTRA OF CO*

J. L. Dehmer and Dan Dill†

Integrated and differential photoionization cross sections are obtained for the K shells of CO using the multiple-scattering model.[1] A shape resonance in the $\sigma(\lambda=0)$ ionization channel is populated by excitation of the K shell of either oxygen or carbon. As seen in Figure 1, the greater strength of the carbon K spectrum indicates that this quasidiscrete resonance state is concentrated more heavily on the carbon end of the molecule. This σ resonance in CO is closely related to the σ_u resonance[2] in N_2, both being dominated by f-wave character at large r. Experimental evidence[3,4] for the occurrence and nature of these resonances will be discussed in the paper to be published.

In this work, we emphasize that cross sections for inner-shell photoionization of molecules are governed by electron-optical properties, e.g., photoelectron transmission functions and phase shifts, of the molecular field. As an example, the integrated cross sections for the K-shell spectra of CO are analyzed in terms of the amplitudes of the photoelectron's wavefunction at the atomic nuclei, using the relation[5]

$$\sigma = (\tfrac{4}{9})\pi^2 \alpha h\nu \, \bar{R}_{p\leftarrow s} \sum_{\ell,\lambda} |A^{(-)}_{\ell\lambda}|^2 \quad .$$

Here $\bar{R}_{p\leftarrow s}$ is the dipole matrix element for excitation of a K-shell electron to a p wave with energy-independent normalization at $r \to 0$, and $A^{(-)}_{\ell\lambda}$ normalizes this p wave to incoming-wave normalization corresponding to a particular (ℓ,λ) component of the total final-state wavefunction at $r \to \infty$. Mechanistically, $\bar{R}_{p\leftarrow s}$ corresponds to the photoabsorption step and $A^{(-)}_{\ell\lambda}$ correspond to

*Summary of a paper to be submitted for publication.

†Consultant, RER Division. Permanent address: Department of Chemistry, Boston University, Boston, Mass. 02215.

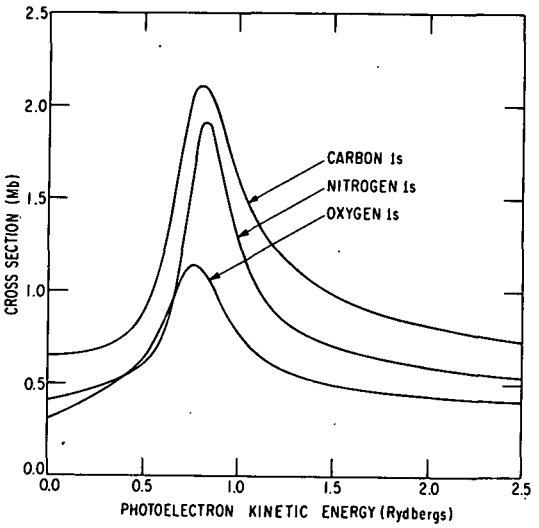

FIG. 1.--Integrated photoionization cross sections for the K shells of CO and N_2.

(ANL Neg. 149-76-90)

the escape of the initial p wave to infinity in the (ℓ, λ) component of the final-state wavefunction. This separation is useful when the photon is absorbed in a localized region of space near an atomic nucleus, thus rendering $\overline{R}_{p \leftarrow s}$ insensitive to variations of photon energy smaller than the initial state binding energy. This circumstance, then, isolates any rapid variation in the energy dependence of the process in the factor $A^{(-)}_{\ell\lambda}$, whose square can be identified as the relative transmission function of the molecular field for a component of the photoelectron's wavefunction. This electron-optical point of view has been discussed extensively in the context of atomic fields.[6] The main difference in the case of molecules is that the anisotropic molecular field can scatter a given ℓ in an atomic core into a range of ℓ's at $r \to \infty$, and each combination must be characterized by a "transmission coefficient."

Figure 2 shows the square of this function for the $\lambda = 0, 1$ ionization channels available for photoionization of the carbon and oxygen K shells of CO. The most striking feature here is the strong spike in the squared amplitude function for $\lambda = 0$ at the kinetic energy of the shape resonance in Figure 1. Comparison of the ordinate scales shows both that this peak is stronger on the carbon end than on the oxygen, and that, at the resonance position, the $\lambda = 0$ amplitude is much larger than the $\lambda = 1$ amplitude. Furthermore, it can be seen in Figure 2 that the $\ell = 3$ component is mainly responsible for the $\lambda = 0$ shape resonance, although $\ell = 0, 2$ components are non-negligible.

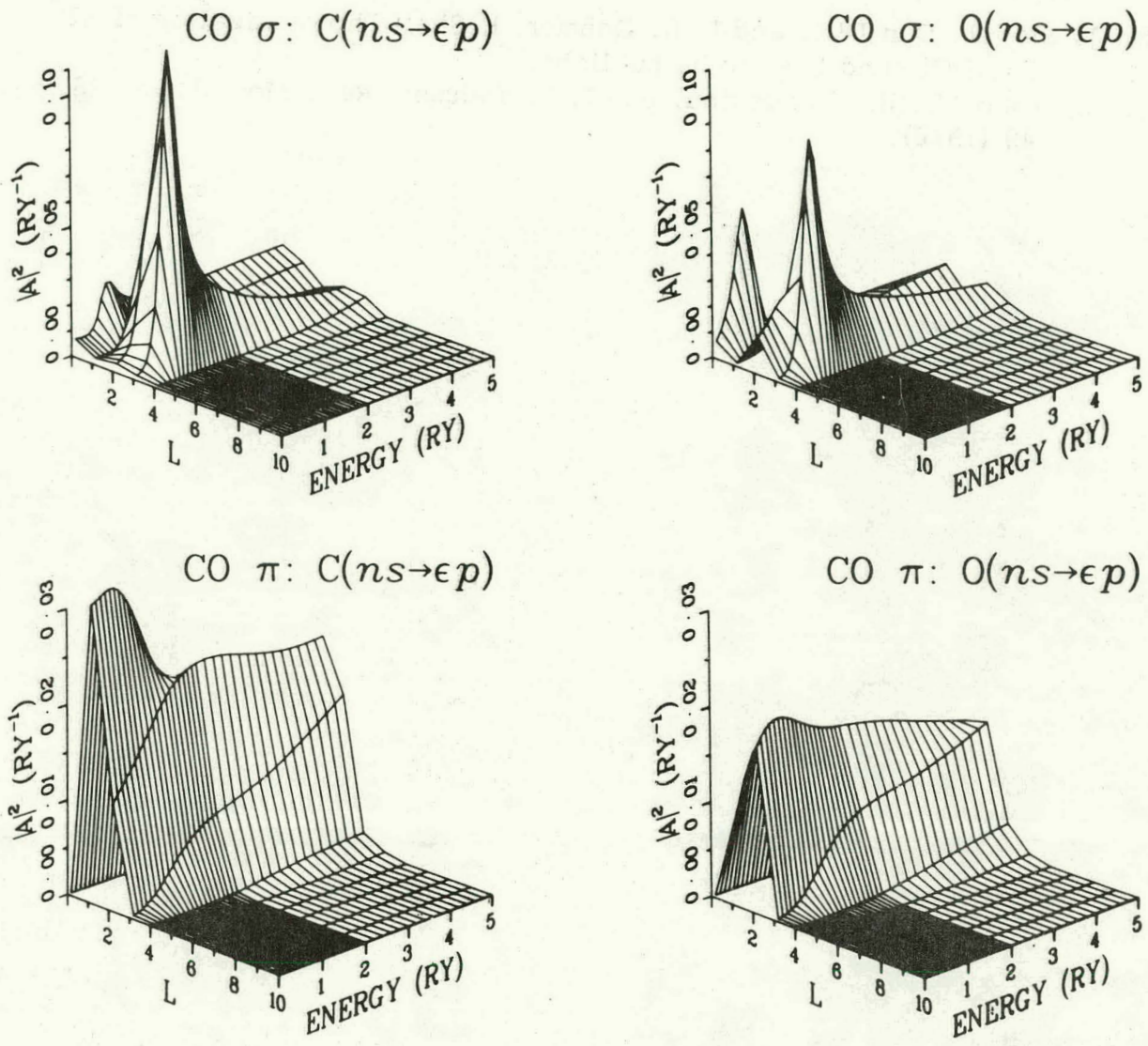

FIG. 2.--Squared amplitude functions $|A_{\ell\lambda}^{(-)}|^2$ for K-shell photoionization of CO.

References

1. Dan Dill and J. L. Dehmer, J. Chem. Phys. 61, 692 (1974).
2. J. L. Dehmer and Dan Dill, J. Chem. Phys. 65, 5327 (1977).
3. R. B. Kay, Ph.E. Van der Leeuw, and M. J. van der Wiel, J. Phys. B 10, 2513 (1977), and references therein.
4. C. L. Allyn, T. Gustafsson, and E. W. Plummer, Chem. Phys. Lett. 47, 127 (1977); and also a paper to be published.

5. J. Siegel, Dan Dill, and J. L. Dehmer, K-Shell Photoionization of HF, F_2, HCl, and Cl_2, to be published.
6. U. Fano, C. E. Theodosiou, and J. L. Dehmer, Rev. Mod. Phys. 48, 49 (1976).

DETECTOR-INTEGRATED ANGULAR DISTRIBUTIONS: CHEMISORPTION-SITE GEOMETRY, AXIAL-RECOIL FRAGMENTATION, AND MOLECULAR-BEAM ORIENTATION*

Scott Wallace† and Dan Dill‡

The seemingly diverse problems of chemisorption-site geometry, orientation of species in molecular beams, and the axial recoil of molecular photofragments can be analyzed by means of the dependence of photoexcitation on target orientation. Expressions are derived for this orientation dependence in terms of the electric-dipole excitation amplitudes of the target. For cylindrically symmetric targets a particularly simple single-parameter distribution $1+\beta_T P_2(\cos\theta_T)$ is obtained, analogous to the Yang-theorem result $1+\beta_D P_2(\cos\theta_D)$ familiar from random molecule-photoelectron angular distributions (T denotes target, D denotes detector). For targets of arbitrary symmetry the distribution has a maximum harmonic dependence of second order and is completely characterized by, at most, eight parameters in addition to the overall cross section. The special utility of elliptically polarized light is also discussed.

---

*Abstract of paper to be published in Phys. Rev. B 17, xxx (1978).

†Appointee, Center for Educational Affairs Thesis Parts Program, June 1–August 31, 1977. Present address: Department of Chemistry, Boston University, Boston, Mass. 02215.

‡Consultant, RER Division, Permanent address: Department of Chemistry, Boston University, Boston, Mass. 02215.

EVALUATION OF ELECTRON-MOLECULE COLLISION CROSS SECTIONS GOVERNING THE ELECTRICAL CONDUCTIVITY OF MHD PLASMAS*

J. L. Dehmer and Dan Dill†

The current effort to develop efficient coal-fired MHD power generators has created the need to evaluate realistic electron-scattering cross sections for many of the compounds of S, N, C, O, K, Si, etc. present in the MHD plasma. These basic cross sections govern the electrical conductivity of the MHD system and are, therefore, required to effectively model its efficiency and to identify molecular species which are especially detrimental to the performance of the system. Unfortunately the range of electron energies (0–10 eV) and the variety of molecular targets relevant to this problem are not straightforwardly handled by present experimental or theoretical methods. This has stimulated recent work to deal with various aspects of the problem, as evidenced by the papers presented in this session. The emphasis of the present work is on flexibility, so that a large sampling of important molecular targets can be treated in a realistic, quantum-mechanical way, regardless of the size of the target system. Here we report on the initial testing of the multiple-scattering method (MSM) as a means of achieving the required flexibility in the calculation of cross sections for electron-molecule scattering.

The formulation of a MSM approach to electron-molecule scattering and molecular photoionization is well documented elsewhere,[1,2] so we will give only a very brief summary of the method here. Briefly, the model is based on partitioning the molecular field into closely packed spherical regions centered on each atomic site and one surrounding the molecule. The one-electron wavefunctions are obtained by enforcing appropriate boundary condi-

---

*Extended abstract of paper presented at the Conference on High-Temperature Sciences Related to Open-Cycle, Coal-Fired MHD Systems, Argonne National Laboratory, April 4–6, 1977, ANL-77-21, pp. 91–93.

†Consultant, RER Division. Permanent address: Department of Chemistry, Boston University, Boston, Mass. 02215.

tions at the nuclei and at infinity, and by requiring that the wavefunction and its derivative be continuous on the spherical boundaries in the molecular field. Hence, the wavefunctions have full molecular symmetry, are mutually orthogonal, and have the appropriate long-range behavior, e.g., a phase-shifted outgoing-wave-normalized plane wave for electron-molecule scattering. Moreover, the MSM accurately describes the nuclear singularities which are distributed throughout the molecular field. This is essential to the realistic treatment of electron-molecule dynamics. The main drawback is the approximate form imposed on the potential in order to achieve separability of the multicenter molecular field. The usefulness of MSM in the study of molecular photoionization has already been demonstrated in our first application:[3-6] K-shell photoionization in N_2 and CO. We were able to realistically reproduce the entire discrete and continuum experimental spectrum and interpret the novel features as shape resonances stemming from $\ell = 2$ and 3 components of the final-state molecular wavefunction.

We have just completed the first application of MSM to electron-molecule scattering: integrated elastic e-N_2 scattering over the range 0 to 1000 eV. This system represents a stringent test of the MSM since the distinctive π_g shape resonance at 2.4 eV has been well characterized (see, e.g., Ref. 7), and accurate absolute cross sections over the entire range are available. Our results, reported fully elsewhere,[8] can be summarized as follows: (1) Semiquantitative agreement is achieved over four decades of the incident energy spectrum; (2) good agreement is obtained for the position and magnitude of the π_g shape resonance at 2.4 eV incident energy; and (3) subresonant features in the σ_u and δ_g channels are observed between 5 and 25 eV incident energy. This prototype study is very encouraging, although we are pursuing means to improve aspects of the computed cross sections which do not agree quantitatively with experiment, e.g., the excess σ_g cross section near zero incident energy.

Since our main thrust is to treat more complex systems, we have recently generalized our code to treat molecules of arbitrary symmetry in a symmetry-adapted basis. We now have some preliminary results on elastic

electron scattering from SF_6. The routine manner in which this 70-electron system was handled bodes well for extensive application of the MSM to the large variety of molecular species present in the coal-fired MHD system. The main features emerging from the e-SF_6 calculation are shape resonances in the t_{1u}, t_{2g}, and e_g elastic scattering channels. There is experimental evidence[9] for the t_{1u} resonance, although it was not identified as such. The other resonances have not been observed owing to the sparsity of data in the range 0 to 50 eV. It is instructive to note that the dominant features in inner-shell photoionization[10] of SF_6 are closely related to these e-SF_6 resonances. The close interconnection between strong spectral features in photoionization and electron-molecule scattering is a very important tool for interpreting and gaining insight into continuum properties of molecules.

The work to date has concentrated on systems whose cross sections are dominated by short-range, electron-core interactions. The results have indicated the wide-spread presence of shape resonances in the kinetic energy range from 0 to 10 eV and underline the need for a quantum mechanical treatment of this part of the problem. We are now adapting our treatment of the external field surrounding the molecule to enable incorporation of dipole, quadrupole, etc. moments in our calculation. At this stage it will be appropriate to incorporate the frame-transformation techniques described by Chang and Fano[11] in order to achieve a unified, efficient means of treating cases in which both long-range and short-range interactions contribute in a non-negligible way.

References

1. Dan Dill and J. L. Dehmer, J. Chem. Phys. 61, 692 (1974).
2. J. Siegel, Dan Dill, and J. L. Dehmer, J. Chem. Phys. 64, 3204 (1976).
3. J. L. Dehmer and Dan Dill, Phys. Rev. Lett. 35, 213 (1975).
4. J. L. Dehmer and Dan Dill, J. Chem. Phys. 65, 5327 (1976).
5. J. L. Dehmer and Dan Dill, Proc. 2nd Int. Conf. on Inner-Shell Ionization Phenomena—Invited Papers, March 29—April 2, 1976, Freiburg, West Germany, W. Mehlhorn and R. Brenn, Eds., Fakultät für Physik, Universität Freiburg, Freiburg, p. 221 (1976).
6. Dan Dill, J. Siegel, and J. L. Dehmer, J. Chem. Phys. 65, 3158 (1976).
7. G. J. Schulz, Rev. Mod. Phys. 45, 378 (1973).
8. Dan Dill and J. L. Dehmer, Phys. Rev. A 16, 1423 (1977).

9. A. Chutjian, S. K. Srivastava, and S. Trajmar, Electronic and Atomic Collisions, Abstracts of Papers of the IXth Int. Conf. on the Physics of Electronic and Atomic Collisions, Seattle, Washington, 24–30 July 1975, J. S. Risley and R. Geballe, Eds., University of Washington Press, Seattle, p. 137 (1975).
10. J. L. Dehmer, J. Chem. Phys. 56, 4496 (1972).
11. E. S. Chang and U. Fano, Phys. Rev. A 6, 173 (1972).

DIFFERENTIAL ELASTIC ELECTRON SCATTERING CROSS SECTIONS FOR N_2 FROM 0 TO 30 eV*

Jon Siegel,[†] Dan Dill,[†‡] and J. L. Dehmer

As part of our program to compute cross sections for electron scattering from complex molecular targets, we recently tested[1] the continuum multiple-scattering method[2,3] by computing the total elastic cross section for N_2 between 1 and 1000 eV. The highly simplified potential (potential A in Ref. 1) adopted for low incident energies (approximately 0 to 30 eV) succeeded in reproducing the well-known π_g shape resonance (see for example, Ref. 4) at 2.4 eV, but generally tended to overestimate the magnitude of the cross section. At energies below the resonance, this was traced to an overestimate of the cross section in the σ_g channel, but at higher energies it was felt that the source of the problem could be traced only with the aid of the differential cross section (DCS), which we report here for kinetic energies from 0 to 30 eV. In fact, the overall agreement between our DCS and both experiment and more laborious calculations is much better than that observed for the integrated cross section. The overestimate in the integrated cross section above the resonance position was traced to scattering angles near 90° (weighted heavily in the integrated cross section) which becomes apparent only when the DCS is expanded in a semilog plot. This prototype calculation shows that the multiple-scattering potential generally predicts the DCS rather well, and pinpoints the angular range where improvements are most needed, underscoring the fact that the DCS is a much more definitive test of a theoretical procedure than the integrated cross section.

Details of the calculation are given in the paper to be published. Here we will only summarize the results. Figure 1 shows the DCS calculated at 81 energies from 0.001 to 2.0 Ry using potential A from Ref. 1. The DCS

---

*Summary of a paper to be published in Phys. Rev. A.

[†]Department of Chemistry, Boston University, Boston, Mass. 02215.

[‡]Consultant, RER Division.

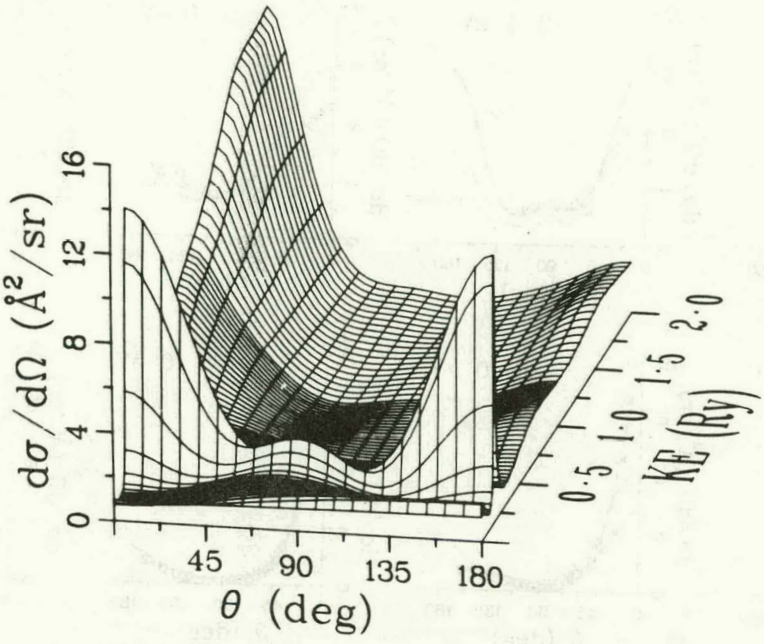

FIG. 1.--Electron-nitrogen differential scattering cross section from 0.001 to 2.0 Ry.

is isotropic near zero kinetic energy where centrifugal forces exclude all except the $(\ell, \lambda) = (0, 0)$ partial wave. As the energy increases, backscattering dominates briefly, until the π_g shape resonance is reached at 0.18 Ry (2.4 eV). The d-wave ($\ell = 2$) character of the 2.4 eV resonance stands out dramatically in this differential scattering surface. Above 0.5 Ry the spectral variation becomes more gradual and the angular distribution becomes progressively more peaked in the forward direction, as the electron transfers less and less momentum to the target. Note the strong resemblance to the experimental differential scattering surface plot in Fig. 30 of Ref. 5.

Figure 2 shows slices of the DCS surface at eight energies between 1.4 and 30 eV, for which comparison with other experimental[6–9] and theoretical[10–15] work is possible. The construction of Figure 2 requires some explanation. For those cases in which the experimental data were reported on a relative scale, we normalized the entire set of data to our calculations at a single energy and angle: Ehrhardt and Willmann[6] at 2.4 eV, 90°; Shyn et al.[7] at 5 eV, 30°; and Finn and Doering[9] at 15 eV, 30° (their 24 eV data are included in our 25 eV plot). The data of Srivastava et al.[8] were put on an

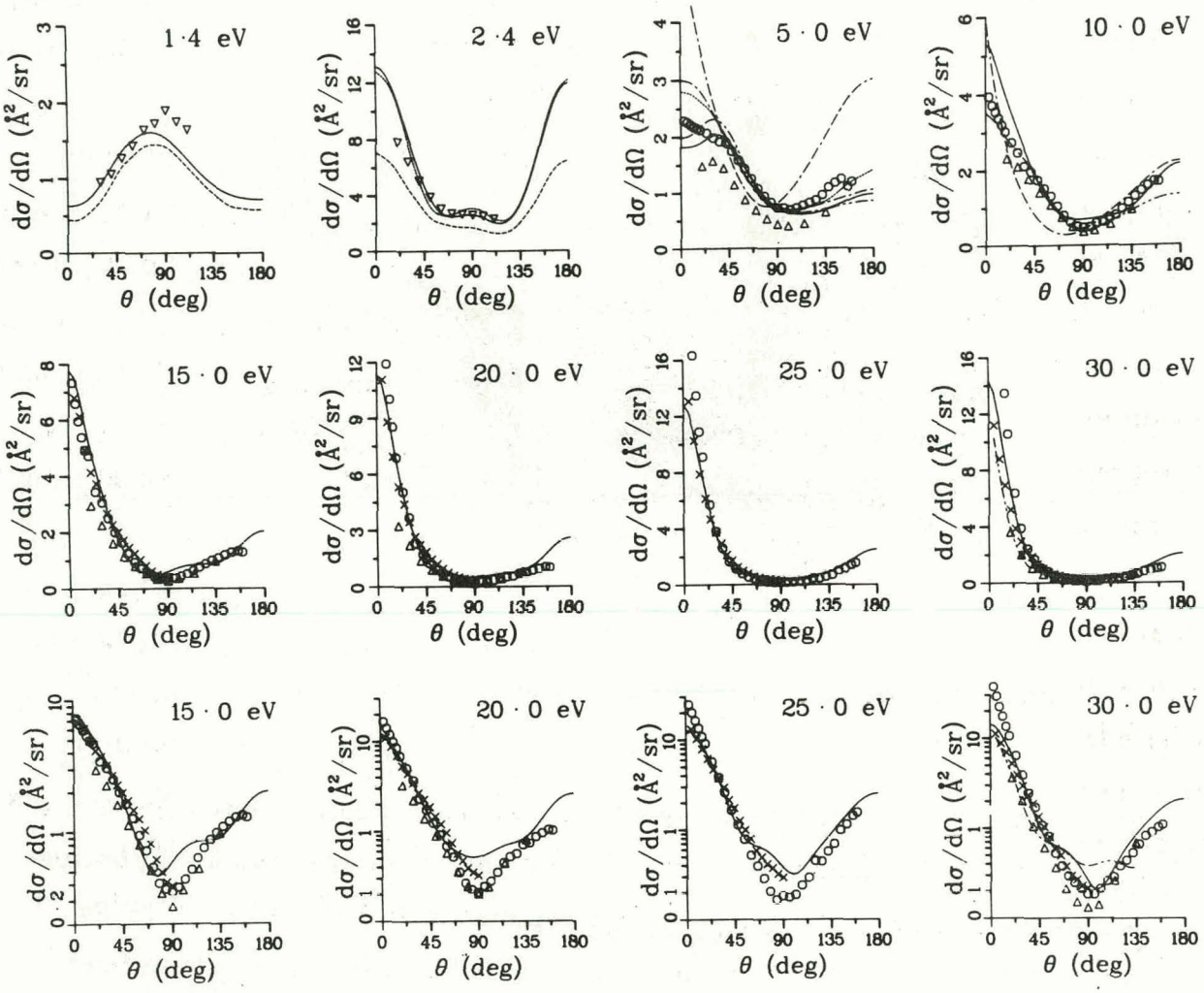

FIG. 2.--Comparison of experimental and theoretical results for the e-N_2 differential cross section between 1.4 and 30.0 eV. Theoretical results include: —, this work; — — —, Chandra and Temkin;[10] ...., Buckley and Burke;[11] -.-.-., Davenport et al.;[12] -..-..-. Chandra and Temkin;[13] --.--.--. Truhlar et al.;[14] and --.,--..--, Brandt et al.[15] Experimental results include: ▽, Ehrhardt and Willmann;[6] o, Shyn et al.;[7] △, Srivastava et al.;[8] and x, Finn and Doering.[9]

absolute scale by the authors. Theoretical results were, of course, already on an absolute scale. In making a comparison with the "hybrid" theory results of Chandra and Temkin,[10] which exhibit the vibrational structure of the π_g shape resonance, we chose their 2.3 eV data as most comparable with our on-resonance results. Similarly, we followed Davenport et al.[12] in comparing their 6 eV results with the 5 eV experimental data.

Several aspects of the comparison in Figure 2 are worth noting. First, below resonance at 1.4 eV, our results agree very well with both experiment and the more sophisticated calculation of Chandra and Temkin. Second, at the 2.4 eV resonance the two fixed-nuclei theories agree exactly with one another and are considerably in excess of the Chandra-Temkin result, which is reduced and broadened by vibrational effects. Third, at 5.0 eV, our results and those of Chandra and Temkin show a turnover near $\theta = 0$ in agreement with experiment. Results from Refs. 11 and 12, which include only $\lambda \leq 2$, continue to increase monotonically as $\theta \rightarrow 0$. The results by Truhlar et al.[14] show poor agreement with experiment and the other theories. Fourth, in the second row of Figure 2, one is struck with the exceptionally good agreement between experiment and the multiple-scattering calculation. Only when the near-zero cross sections at $\theta \sim 90°$ is blown up on a semilog plot, are the imperfections in the theory made apparent. Thus, in the third row of Figure 2, a systematic disagreement between theory and experiment for right-angle scattering clearly emerges. We believe this accounts for the observation that the theoretical integrated cross section from Ref. 1 uniformly exceeds the experimental results in this energy region.

The present results and those of Ref. 1 indicate that the multiple-scattering method can produce a realistic description of the electron-molecule scattering process. In view of the major approximations adopted in this preliminary study, the results must attest to the importance of an accurate representation of the electron-molecule interaction in the atomic core regions, which is accomplished in the multiple-scattering potential. Thus, we feel confident in attempting similar calculations on more complex targets, for which more sophisticated treatments are not yet practical. At the same time, it is necessary to develop a more ab initio means of producing the potential which represents the electron-molecule interaction. Several possibilities were touched upon in Ref. 1, e.g., incorporating the scattered electron in a self-consistent field procedure in determining the effective potential. The present DCS work contributes significantly to this by clearly displaying the source of the disagreement present in the integrated cross section so that the effect of future improvements can be unambiguously monitored.

References

1. D. Dill and J. L. Dehmer, Phys. Rev. A 16, 1423 (1977).
2. D. Dill and J. L. Dehmer, J. Chem. Phys. 61, 692 (1974).
3. J. Siegel, D. Dill, and J. L. Dehmer, J. Chem. Phys. 64, 3204 (1976).
4. G. J. Schulz, Rev. Mod. Phys. 45, 378 (1973).
5. D. C. Cartwright, A. Chutjian, S. Trajmar, and W. Williams, Phys. Rev. A 16, 1013 (1977).
6. H. Ehrhardt and K. Willmann, Z. Physik 204, 462 (1967).
7. T. W. Shyn, R. S. Stolarski, and G. R. Carignan, Phys. Rev. A 6, 1002 (1972).
8. S. K. Srivastava, A. Chutjian, and S. Trajmar, J. Chem. Phys. 64, 1340 (1976).
9. T. G. Finn and J. P. Doering, J. Chem. Phys. 63, 4399 (1975).
10. N. Chandra and A. Temkin, Phys. Rev. A 13, 188 (1976).
11. B. D. Buckley and P. G. Burke, J. Phys. B 10, 725 (1977).
12. J. W. Davenport, W. Ho, and J. R. Schrieffer, Phys. Rev. B, to be published.
13. N. Chandra and A. Temkin, J. Chem. Phys. 65, 4537 (1976).
14. D. G. Truhlar, M. A. Brandt, A. Chutjian, S. K. Srivastava, and S. Trajmar, J. Chem. Phys. 65, 2962 (1976).
15. M. A. Brandt, D. G. Truhlar, and F. A. Van-Catledge, J. Chem. Phys. 64, 4957 (1976).

A NEW AID TO THE CLASSIFICATION OF FESHBACH RESONANCES: Ne, Kr, Ar, AND Xe *

David Spence

Using published values of resonance energies $E_{n\ell\ell'}$ in the rare gases Ne, Kr, Ar, and Xe, together with the known ionization potential I(m), we show that an empirical relation between $E_{n\ell\ell'}$ and I(m) may be expressed as

$$E_{n\ell\ell'}(m) = A_{n\ell\ell'} I(m) + B_{n\ell\ell'} \quad , \tag{1}$$

where $E_{n\ell\ell'}$ is the nth resonance with excited angular momenta ℓ and ℓ' in atom (m), and $A_{n\ell\ell'}$ and $B_{n\ell\ell'}$ are constants which are independent of atomic species m.

A graphical presentation of this relation is shown in Figure 1 where we have plotted the resonance energies determined by Sanche and Schulz[1] and by Brunt et al.[2] as functions of ionization potential I(m). Figure 1 shows how resonances of a given electron configuration (indicated above) lie with a high degree of precision on the plotted straight lines.

One should note that these data represent only those resonances associated with $^2P_{\frac{3}{2}}$ ion cores. Of the 50 to 55 known resonances with this ion core, 46 are incorporated in Figure 1, showing the great power of this simple classification scheme. The precision to which these data fit the least-squares straight lines is illustrated more clearly in Table 1, which indicates the deviation of each point from the lines. In most cases, the deviation is < 20 meV, well within the experimental accuracy, stated to be 50 meV.

Thus, we see that most resonance energies $E_{n\ell\ell'}$ in the rare gases Ne, Ar, Kr, and Xe can be fitted to a set of straight lines by the formula

$$E_{n\ell\ell'}(m) = A_{n\ell\ell'} I(m) + B_{n\ell\ell'} \quad , \tag{2}$$

where I(m) is the ionization potential of species m and $A_{n\ell\ell'}$ and $B_{n\ell\ell'}$ are constants independent of m. The binding energy (BE) of a pair of excited

---

*Summary of a paper published in Phys. Rev. A 15, 883 (1977).

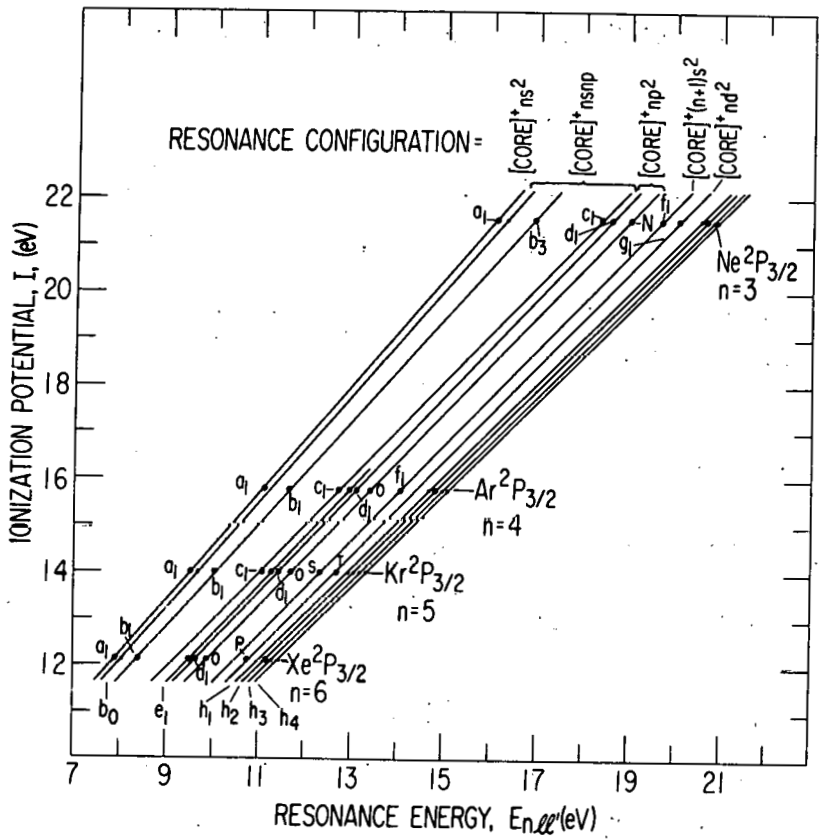

FIG. 1.--Plots of resonance energies $E_{n\ell\ell'}$ vs. the appropriate ionization potential I. Data a_1 tabulated by Sanche and Schulz[1] (light points), b_0, h_1 - h_4 measured from spectra of Sanche and Schulz, all other data from Brunt et al.[2] (heavy points). Only resonances associated with $np^5(^2P_{\frac{3}{2}})$ ion cores are plotted for the sake of simplicity, although $^2P_{\frac{1}{2}}$ ion core resonances tabulated in Refs. 1 and 2 will also fit these same plots. Almost all known resonances in Ne, Ar, Kr, and Xe are incorporated in this figure, of which about 75% fit the plots of $E_{n\ell\ell'} = A_{n\ell\ell'} I + B_{n\ell\ell}$ to better than 0.02 eV. Only three points are more than 0.04 eV of these plots. (ANL Neg. 149-76-260)

electrons to the positive ion core is then given by

$$BE = I(m) - E_{n\ell\ell'm}$$

$$= (1 - A_{n\ell\ell'}) I(m) + B_{n\ell\ell'} \quad . \tag{3}$$

Table 1 shows that as the orbital angular momenta of the excited electrons increase, $A_{n\ell\ell'} \rightarrow 1$, and the binding energy of the pair of electrons is simply $B_{n\ell\ell'}$, i.e., it is independent of atomic species. This is easily understood because as ℓ increases, the excited electrons are held out from the ion core

TABLE 1. Difference, ΔE, between measured[a] and calculated resonance energies obtained using Eq. 2. $A_{\ell\ell'}$ and $B_{\ell\ell'}$ are obtained by a least-squares fit to the data.

ΔE (eV)				$A_{\ell\ell'}$	$B_{\ell\ell'}$	Probable configuration
Ne	Ar	Kr	Xe			
a_1 0.04	a_1 0.07	a_1 -0.01	a_1 0.01	0.868	-2.644	$np^5(^2P_{\frac{3}{2}})(n+1)s^2$
b_0 +0.01		b_0 -0.02	b_0 +0.02	0.878	-2.599	
b_3 0.013	b_1 -0.021	b_1 -0.-37	b_1 0.043	0.903	-2.574	$np^5(^2P_{\frac{3}{2}})(n+1)s\,(n+1)p$
c_1 0.01	c_1 -0.03	c_1 0.03		0.966	-2.488	
	e_1 -0.003	e_1 0.014	e_1 0.001	0.947	-1.990	
d_1 0.006	d_1 -0.003	d_1 0.001	d_1 -0.007	0.950	-1.909	$np^5(^2P_{\frac{3}{2}})(n+1)p^2$
N -0.018	O 0.085	O -0.035	O -0.004	0.963	-1.799	
f_1 -0.011	f_1 0.003	S -0.012		0.974	-1.296	$np^5(^2P_{\frac{3}{2}})(n+2)s^2$
g_1 0.00		T 0.04	P -0.03	0.982	-1.122	$np^5(^2P_{\frac{3}{2}})(n+1)d^2$
h_1 -0.02	h_1 0.00	h_1 +0.03		1.014	-1.292	
Q +0.01	Q -0.004	h_2 +0.04	Q -0.01	1.001	-0.948	???
h_3 +0.01	h_3 -0.02	h_3 +0.02	h_3 -0.02	1.009	-0.947	
h_4 +0.01	h_4 -0.01	h_4 +0.03	h_4 0.00	1.004	-0.758	

[a]Resonances a_1, b_0, $h_1h_2h_3h_4$ from Ref. 1. All others from Ref. 2.

by a centrifugal barrier and their penetration into the core is small. Thus for high ℓ, the excited electrons simply see unit charge at the core and their binding energy is independent of m.

For low ℓ, however, the excited electrons can penetrate significantly into the core, although this penetration will decrease with increasing numbers of closed shells, due to Pauli exclusion. Thus, qualitatively, one expects a decrease in binding energy for a pair of electrons of given (low) quantum number (ℓ, ℓ') along the sequence Ne, Ar, Kr, Xe. At present it is not clear why in such cases a strict linearity of binding energy with I is maintained. However, this strict linearity, and the fact that $A_{11\ell\ell'}$ is very close to unity, does demonstrate that for Feshbach resonances excited electron dynamics are dominated by electron-electron interactions in the external field of the ionic core, so that the minor role played by electron interactions within the ion core can be represented by a single energy-independent parameter similar to the quantum defect used in Rydberg state analyses. The same conclusion has been reached by Read[3] from other considerations.

Finally, we would like to point out that Eq. 2 can be used to predict resonance energies in helium, although in this case there is a systematic error of about 0.5 eV between the predicted and measured energies. No doubt the reason for this discrepancy is the fact that He does not naturally fall into the family Ne, Ar, Kr, Xe, as pointed out by Read et al.[3]

REFERENCES

1. L. Sanche and G. J. Schulz, Phys. Rev. A 5, 1672 (1972).
2. J. N. H. Brunt, G. C. King, and E. H. Read, J. Phys. B 9, 2195 (1976).
3. F. H. Read, J. N. H. Brunt, and G. C. King, J. Phys. B 9, 2209 (1976).

EXCITATION OF RYDBERG STATES IN O_2 BY LOW ENERGY ELECTRON IMPACT*

David Spence and R. H. Huebner

Discrete features superimposed upon the slowly varying Schumann-Runge background continuum of O_2 were first observed in electron-impact energy-loss spectra by Schulz and Dowell.[1] They used the trapped-electron technique, and other than correlation of several peaks with a few features observed in the optical absorption spectrum of Watanabe et al.,[2] no detailed interpretation was possible because of poor energy resolution.

Recently this same energy regime of O_2 has been studied in more detail by Trajmar et al.[3] using a hemispherical monochromator-analyzer operating at high resolution and capable of making angular measurements. Trajmar et al.[3] found the discrete spectrum of O_2 to be extremely rich, and tentatively assigned several peaks to two vibrational series associated with the $^3\Pi_g$ and $^1\Pi_g$ Rydberg states of O_2. The apparatus of Trajmar et al.[3] was operated in the "constant-residual-energy" mode, and measurements were made for final (scattered) energies between 0.2 and 8.0 eV in steps of about 0.5 to 1.0 eV. Their spectra were complicated by the fact that some peaks appeared to shift in energy as a function of scattered energy, and they suggested this might be due to structures in the background continuum caused by decay of negative-ion states which are known to exist in this energy region.[4] Such a decay process would cause shifting structures if an apparatus were operated in the constant-residual-energy mode (see Eqs. 1 and 2, Ref. 5).

Using a modification of the trapped-electron technique,[6] we have studied discrete excitation in the energy region of the Schumann-Runge continuum of O_2. Our technique also detects electrons of constant residual energy as a function of incident electron energy, and structures in the spectra are proportional to the total (i.e., integrated w.r.t. angle) cross sections for

*Summary of a paper presented at the 30th Gaseous Electronics Conference, Palo Alto, October 1977.

electron impact. This technique is analogous to that used by Trajmar et al.,[3] who measured a signal proportional to the differential cross section. However, using a much closer mesh of different residual energies (0.05 eV as opposed to 0.5 to 1.0 eV), our measurements indicate the very rapid variation in cross sections within 1.0 eV of thresholds shown in Figure 1, where we have plotted the inelastically scattered current as a function of incident electron energy for several values of fixed scattered (final) energy E_R. Note not only the rapid variation in cross sections, but also the apparent peak shifts, for example peak B.

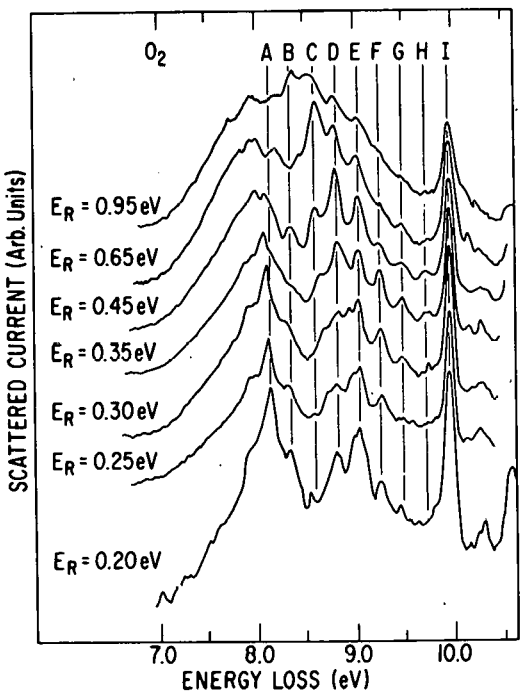

FIG. 1.--Spectra of inelastically scattered electrons in O_2 as a function of energy loss for different values of final (scattered) electron energy.
(ANL Neg. 149-77-437)

Interpretation of Figure 1 is facilitated by the matrix shown in Figure 2. Here we have plotted the peaks and shoulders appearing in Figure 1 as a function of energy for different values of final electron energy (E_R). The negative ion (Feshbach resonances) energy locations plotted on the bottom of Figure 2 are obtained from Sanche and Schulz.[4] In this matrix, for constant residual energy operation, discrete inelastic features will appear as a series of vertical dots (crosses), whereas resonances decaying into background continuum will appear as dots (crosses) lying along the sloping solid lines (i.e., the structure will appear to shift down in energy by an amount equal to

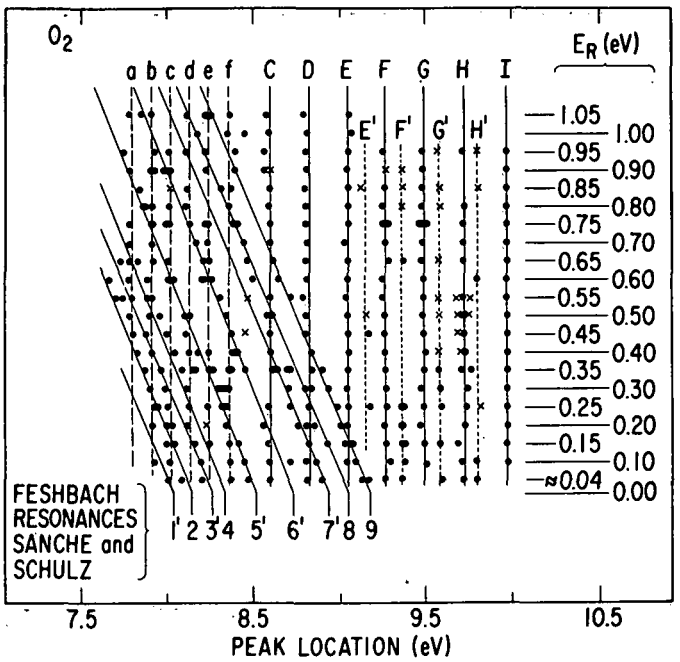

FIG. 2.--Matrix of peaks (solid circles) and shoulders (crosses) of Figure 1. Feshbach resonance locations are plotted on the bottom. Vertical lines represent discrete inelastic processes, and the sloping lines identify structures in the background continuum caused by the decay of Feshbach resonances.
(ANL Neg. 149-77-436)

the final energy (E_R).

One should note that for values of E_R at which a sloping line passes through a vertical line, that particular resonance will decay into a discrete state and should cause resonant enhancement of that state. For example, note resonance 9, as E_R increases, will first enhance structures E, then D, C, f (B of Figure 1), as is indeed observed in Figure 1.

Though the spectrum is very complicated for low E_R below incident energy ≈ 9.0 eV, this plot demonstrates vividly that the suggestion of Trajmar et al. concerning shifting peaks is indeed true.

Whereas Trajmar et al. assigned the lowest Rydberg state of O_2, the $^3\Pi_g$ state, to a vibrational sequence d, f, C, D, E, F of Figure 2 starting at 8.15 eV, this would make the electron affinity of this state only 0.10 eV (d − 1' eV). This value is extraordinarily low for a low-lying molecular Rydberg state. Using Eq. 4 of Ref. 7 and a reasonable value of 0.26 for the electron screening constant would place the lowest Rydberg state of O_2 at 8.60 eV rather than 8.15 eV, i.e., the location of C, Figure 2. Though this approximation is, to some extent, crude, it has proved useful in predicting Rydberg state energies in many more complicated molecules[8] to an accuracy of about

0.12 eV. Our estimate of the location of the $^3\Pi_g$ state is supported by a priori calculations of Saxon et al.[9] However, such an assignment leaves us an open question—the identity of the discrete structures below 8.60 eV. Additional measurements and calculations will be necessary to resolve this question.

REFERENCES

1. G. J. Schulz and J. T. Dowell, Phys. Rev. 128, 174 (1962).
2. K. Watanabe, E. C. Y. Inn, and M. Zelikoff, J. Chem. Phys. 21, 1026 (1953).
3. S. Trajmar, D. C. Cartwright, and R. I. Hall, J. Chem. Phys. 65, 5275 (1976).
4. L. Sanche and G. J. Schulz, Phys. Rev. A 6, 69 (1972).
5. D. Spence, A new technique to differentiate between negative ion and natural autoionization states in the rare gases, this report.
6. D. Spence, Phys. Rev. A 12, 2353 (1975).
7. D. Spence, Prediction of low energy molecular Rydberg states from Feshbach resonance spectra, this report.
8. D. Spence, J. Chem. Phys. 66, 669 (1977).
9. R. P. Saxon, SRI International, Menlo Park, California, private communication.

A POSSIBLE NEW MECHANISM FOR THE PRODUCTION OF FAST (0 to 1.5 eV) N ATOMS IN THE UPPER ATMOSPHERE*

David Spence and P. D. Burrow†

Many previous measurements of threshold electron spectra in N_2 at low incident energy (< 15 eV) have indicated a sharp rise in signal at approximately the dissociation limit,[1,2] followed by a slow decrease in signal over the next 1.5 eV. All previous measurements of this prominent feature have been limited to essentially zero scattered electron energy (e.g., the SF_6 scavenger[2] and the trapped-electron method[1]). Using a modified AC trapped-electron technique[3] we were able to measure slow scattered electrons at other than zero energy as a function of incident energy. Our measurements shown in Figure 1 indicate that the triangular-shaped structure at 9.7 eV has an essentially vertical onset at the dissociation limit (within 0.05 eV), and that this structure disappears for scattered energies ($= E_R$) other than zero, at least within our resolution of about 0.12 eV. The question is "What type of mechanism will cause the production of only zero energy electrons?" Stated slightly differently, what mechanism will cause an incident electron to lose all of its energy and lose none if the incident energy is above the threshold for excitation of this process? Obviously some type of resonance mechanism is involved. One answer to the above questions would be that in the range 9.7 to $\approx$ 11.0 eV there is a whole series of inelastic cross sections which peak at threshold and are zero thereafter. However, this seems highly unrealistic.

We would like to propose a new type of mechanism to answer the above questions.

Referring to the schematic potential energy diagram of N_2 shown in Figure 2, we have sketched in the well-known $X^2\Pi(N_2^-)$ state,[4] whose minimum is located at about 2.3 eV and whose dissociation limit is $N(^4S) + N^-(^3P)$

---

*Summary of a paper to be submitted for publication.

†Consultant RER Division, University of Nebraska Lincoln.

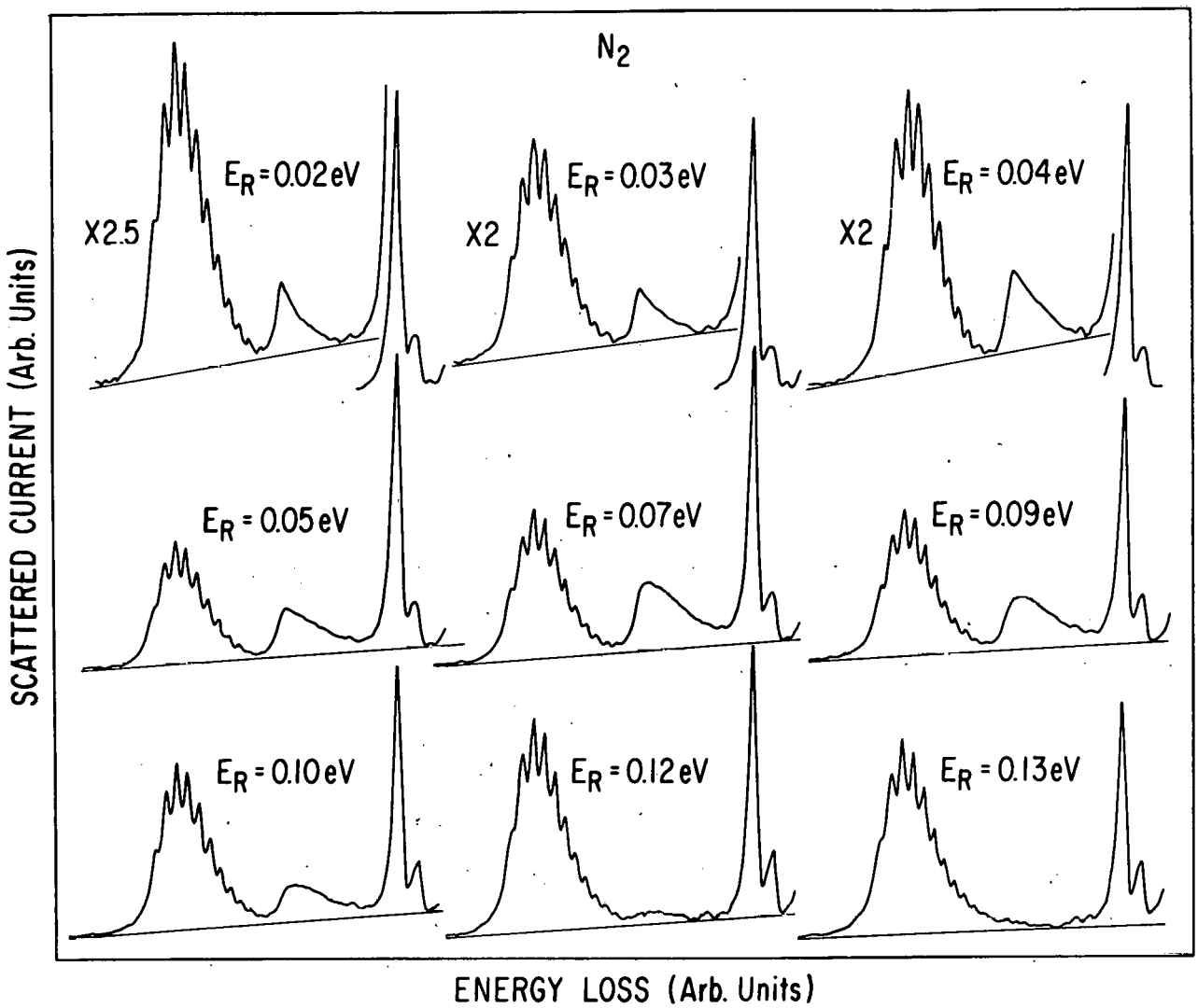

FIG. 1.--Spectra of inelastically scattered electrons from N_2 for different values of final electron energy (E_R). Note the disappearance of the triangular-shaped feature which peaks at 9.7 eV for final energies greater than the energy resolution of about 0.12 eV. (ANL Neg. 149-72-433)

(which is unstable against autoionization). So far there are no other known negative-ion states which dissociate into those same products, although doubtless others do exist, for example, a $^2\Sigma N_2^-$ state.

In order to explain our observations, we need to make only two very reasonable assumptions: 1) Such a N_2^- state exists, and it crosses the dissociation limit within the Franck-Condon region of N_2. This is necessary to explain the vertical onset. 2) This N_2^- state has a lifetime at least equal to one vibrational period, $\approx 10^{-14}$ sec. This is certainly true for the $X^2\Pi N_2^-$ state.[4] We propose that the incident electron can become attached to this

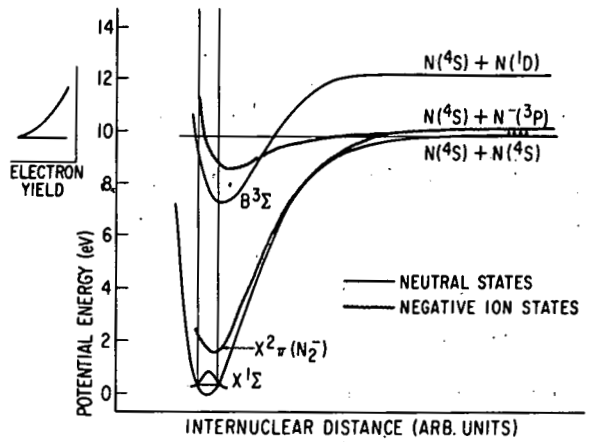

FIG. 2.--Schematic potential energy diagram of N_2 and N_2^- with a sketch of the expected yield of slow electrons produced by decay of the upper N_2^- state. (ANL Neg. 149-78-15)

upper N_2^- state when the incident energy lies between 9.7 and $\approx$ 11.0 eV. This N_2^- state then dissociates into the products $N(^4S) + N^-(^3P)$, the latter of which is unstable and autoionizes into $e(E) + N(^4S)$, where E is the energy of the ejected electron and will be equal to minus the electron affinity of N, which is believed to be of the order of < 0.05 eV.[5]

Thus, in the energy region 9.7 $\rightarrow$ 11.0 eV we have a source of slow ($\approx$ 0.05 eV) electrons, with a concomitant production of fast ($\approx$ 0 $\rightarrow$ 1.5 eV) N atoms. Although we have not put our estimates of the cross section for this process on an absolute basis, it is quite large and may be an important source of N atoms in the upper atmosphere.

References

1. B. I. Hall, J. Mazeau, J. Reinhardt, and C. Schumann, J. Phys. B 3, 991 (1970).
2. R. N. Compton, R. H. Huebner, P. W. Reinhardt and L. G. Christophorou, J. Chem. Phys. 48, 901 (1968).
3. D. Spence, Phys. Rev. A 12, 2353 (1975).
4. G. J. Schulz, Rev. Mod. Phys. 45, 378 (1975).
5. P. G. Burke, K. A. Berrington, M. Le Dourneuf, and Vo Ky Lan, J. Phys. B 7, L531 (1974).

STUDIES OF POST-COLLISION INTERACTIONS IN Ne FROM SCATTERED ELECTRON SPECTRA*

David Spence

Recent studies of the effect of post-collision interactions (PCI) between the scattered and ejected electrons, following the decay of short-lived autoionizing state excited by electron impact, have indicated that the exchange of energy δE between the two electrons is given by $\delta E = AE_1^{-1.2}$, where A is a constant and E_1 is the energy the scattered electron would have had in the absence of PCI. It has been suggested[1] that the exponent 1.2 may be a universal constant applicable to all transitions in which PCI plays a role. However, a recent quantum-mechanical calculation by Bottcher and Schneider,[2] which includes in a qualitative manner, the effects of dynamical screening of the ion core by a pair of receding electrons, shows that whereas for sufficiently large values of E_1 the energy exchange is expected to fall off at least as fast as $E^{-1.0}$. For lower values of E_1, the energy exchange δE should be of the order $E^{-0.5}$ in agreement with the classical predictions of Barker and Berry.[3]

In order to clarify this situation, we have made precision measurements of the energy exchange between the scattered and ejected electrons following autoionization of the $2s2p^6\,3s(^1S)$ state of Ne, using a technique we have described previously.[4] Our results are shown in the log-log plot of Figure 1, which also includes the previous data of Wilden et al.[1] from ejected electron spectra obtained over a more limited range of E_1. The two sets of data show good agreement over the common range of E_1. However, the present data to lower E_1 show a definite reduction of slope, as predicted by Bottcher and Schneider,[2] and indeed demonstrate the importance of dynamical screening of the ion core in the energy exchange process.

---

*Expanded abstract of a paper presented at the 30th Gaseous Electronics Conference, Palo Alto, October 1977. Expanded abstract from J. Phys. B 11, 6243 (1978).

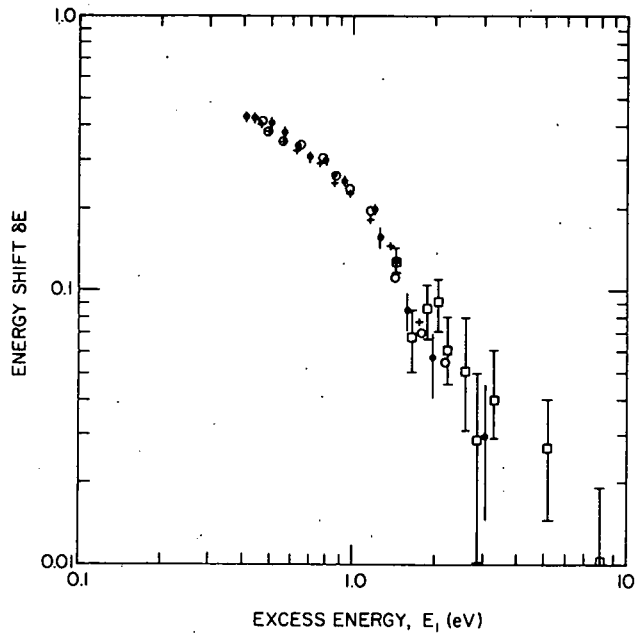

FIG. 1.--Log-log plot of the energy exchange δE between scattered and ejected electrons following autoionization of the $2s2p^6 3s(^1S)$ state of Ne from measurements of scattered electron energies (+, ●, o, present data), and ejected electron energies (□ Wilden et al.[1]).
(ANL Neg. 149-77-439 Rev. 1)

REFERENCES

1. D. G. Wilden, P. J. Hicks, and J. Comer, J. Phys. B 10, 1477 (1977).
2. C. Bottcher and K. R. Schneider, J. Phys. B 9, 911 (1976).
3. R. B. Barker and H. W. Berry, Phys. Rev. 151, 14 (1966).
4. D. Spence, Phys. Rev. A 12, 2353 (1975).

MEASUREMENT OF AUTOIONIZING STATES OF Ne FROM SCATTERED ELECTRON SPECTRA*

David Spence

The spectroscopy of autoionizing states in Ne have been studied by excitation with fast[1,2] and slow[3] ions, electrons,[4] and photons,[5] with detection of scattered electrons,[4,2] ejected electrons,[1,3,6,7] photoabsorption,[5] electroionization,[8,9] and broad-band photons.[10] An attempt to correlate these measurements[11] showed apparent large discrepancies, even taking into account different selection rules. It has been suggested[6] that some discrepancies may be caused by so-called "post-collision interaction (PCI) effect" (see Ref. 6 and references therein) where energy is exchanged between the ejected and scattered electrons for sufficiently low electron-impact energies and short autoionization lifetimes. Such conditions may apply in near-threshold measurements of scattered and ejected electrons, electroionization, and broad-band photons.

To resolve these discrepancies we have studied the quantitative effect of PCI on the apparent thresholds of autoionizing states in Ne between 40 and 50 eV by measuring the yield of scattered electrons of chosen fixed final energies between ~0 eV and 3 eV in steps of 0.10 eV. We have made these measurements with a modification of the trapped-electron method we have described in detail previously.[12]

Although scattered-electron, positive-ion, and broad-band photon spectra in the autoionization region of Ne are often complicated by the presence of negative-ion structures, we can demonstrate that our scattered-electron spectra in Ne are not complicated by this effect. To do this we utilize the technique for enhancing negative-ion structures described elsewhere in this report[13] and shown in the spectra of Figure 1, where the top trace shows the

---

*Expanded abstract of a paper presented at the 30th Gaseous Electronics Conference, Palo Alto, October 1977. Part of the paper is in preparation.

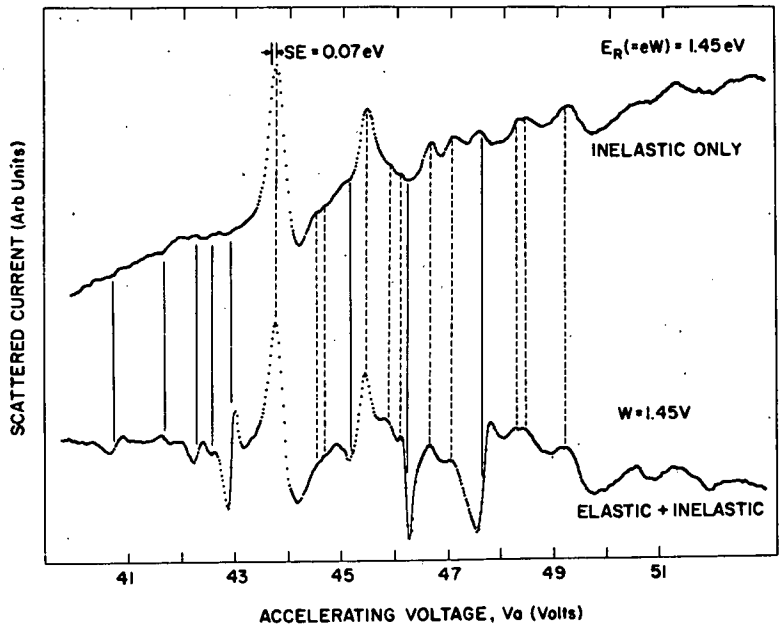

FIG. 1.--Spectra of inelastic (upper) and inelastic plus elastic (lower) showing enhancement of negative ion structures in the lower core. These spectra demonstrate the lack of negative ion structures in our spectra in Ne when only inelastically scattered electrons are measured. ---, neutral autoionizing energy = eVa(δE); —, negative ion states energy = e(Va + W).

(ANL Neg. 149-77-441)

usual trapped-electron current resulting from inelastically scattered electrons only. The lower trace shows enhancement of negative-ion features (indicated by the solid vertical lines) obtained by modulating V_a instead of W_{out}.[13] These spectra, which were obtained at the same well depth (W= 1.45 V) show no evidence of resonance features in the upper trace.

Having demonstrated that our inelastic spectra are due only to neutral autoionizing states, we take a series of spectra similar to the upper trace of Figure 2 at many values of fixed final energy E_R, and a small sample of these are shown in Figure 2 for values of E_R = 0.1 eV, 0.3 eV, 1.1 eV, and 1.9 eV. The peaks in these spectra tend asymptotically towards the locations of the long vertical arrows as E_R increases, the displacement of each peak of the lower spectra being indicated by the short vertical lines.

The data of Figure 2 are plotted in a more concise way in Figure 3, where our data are plotted in rows 2 and 3 from the top. Row 2 shows the location of our peak positions of Figure 2 for essentially zero scattered energy, i.e., near threshold. The zero-scattered-energy spectra of row 2 agree excellently with

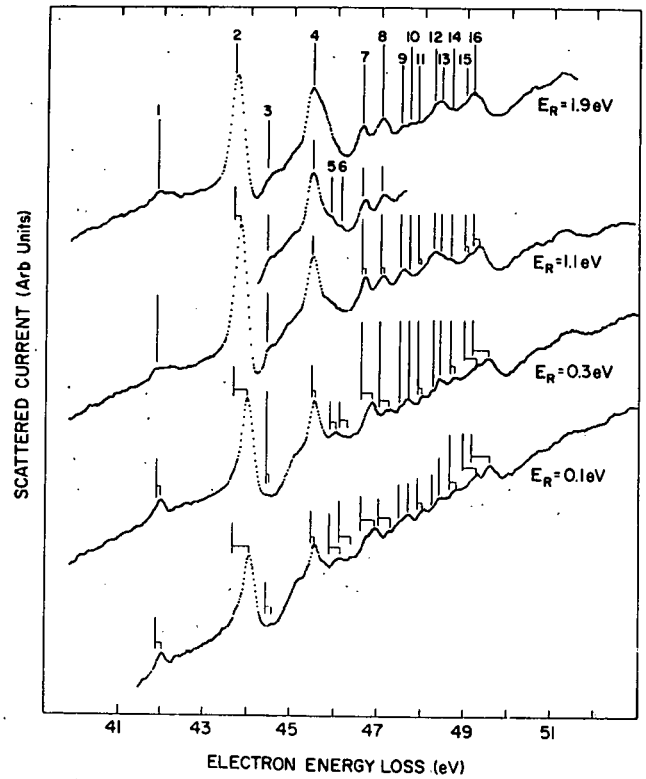

FIG. 2.--Spectra showing the apparent shift in energy locations of autoionizing states of Ne as the excess energy (= E_R + shift) of the incident electron is reduced. (ANL Neg. 149-77-438)

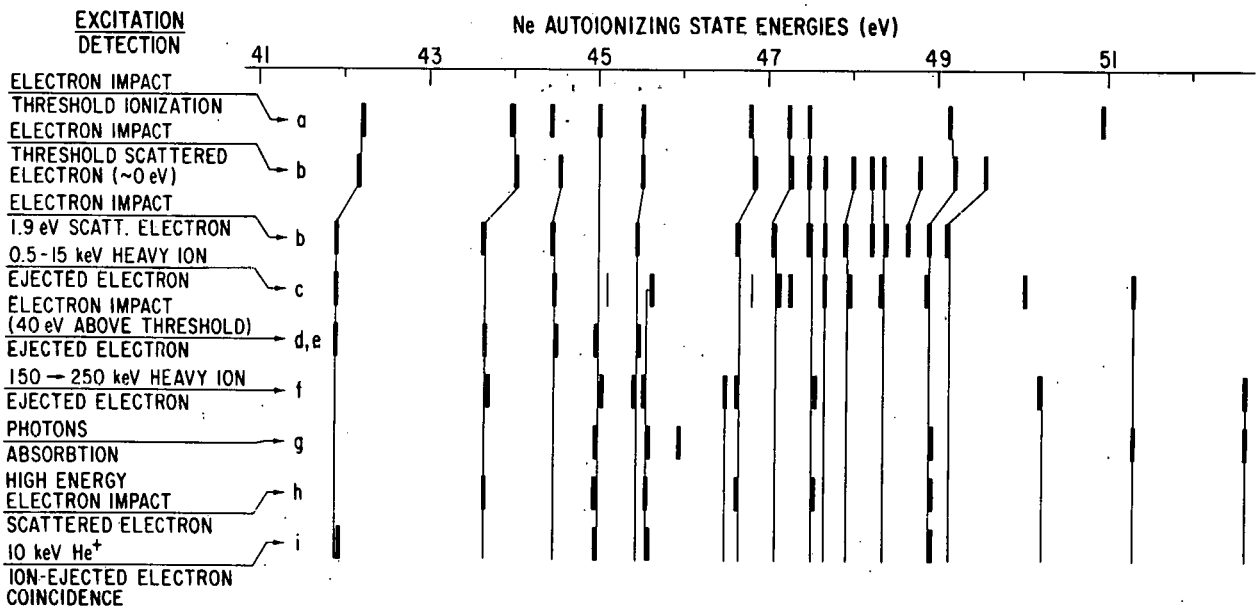

FIG. 3.--Comparison of energy levels of autoionizing states of Ne obtained using the indicated experimental techniques, illustrating the effects of post-collision interactions on the results of the two top rows. a, Refs. 8,9; b, present data; c, Ref. 3; d,e, Refs. 6,7; f, Ref. 1; g, Ref. 5; h, Ref. 4; i, Ref. 2.
(ANL Neg. 149-77-481)

the electro-ionization data of Bolduc, Quemener, and Marmet.[8] We know, however, that the apparent energy levels derived from our zero-energy spectra of row 2 are shifted from their true positions owing to PCI.[12] Energy levels determined from scattered energies other than zero show the systematic shift of the apparent thresholds toward lower energy (shown in Figure 2), indicated by the sloping lines between row 2 and row 3 of Figure 3, asymptotically approaching the measured energy locations shown in row 3. The energy levels of row 3 agree well with energy levels determined by a variety of other techniques[1-4,5-7] where, according to Marchand, Veillette, and Marmet,[14] PCI is not expected to play any role. In that our observations can be completely understood in terms of PCI, it appears the results of electro-ionization measurements[8,9] of row 1 are similarly affected by PCI, as suggested by Sharp, Comer, and Hicks.[7]

Incidentally, one should note that, where observed, optically allowed transitions occur only very weakly in our spectra, whereas optically forbidden transitions are relatively intense, as expected.

REFERENCES

1. A. K. Edwards and M. E. Rudd, Phys. Rev. 170, 140 (1968).
2. G. Gerber and A. Niehaus, Phys. Rev. Lett. 31, 1231 (1973).
3. J. Ostgaard Olsen and N. Andersen, J. Phys. B 10, 101 (1977).
4. T. Bergmark, N. Spohr, N. Magnusson, L. O. Werme, C. Nordling, and K. Siegbahn, Int. Rep. 589, Institute of Physics, Uppsala University, Uppsala, Sweden (1969).
5. K. Codling, R. P. Madden, and D. L. Ederer, Phys. Rev. 155, 26 (1967).
6. D. G. Wilden, P. J. Hicks, and J. Comer, J. Phys. B10, 1477 (1977).
7. J. M. Sharp, J. Comer, and P. J. Hicks, J. Phys. B8, 2512 (1975).
8. E. Bolduc, J. J. Quemener, and P. Marmet, J. Chem. Phys. 57, 1957 (1972).
9. E. Bolduc and P. Marmet, Can. J. Phys. 51, 2108 (1973).
10. P. Veillette and P. Marchand, Can. J. Phys. 54, 1208 (1976).
11. D. Spence, Review article "Two electron excitations in atoms, ions, and molecules," in preparation.
12. D. Spence, Phys. Rev. A 12, 2353 (1975).
13. D. Spence, Evidence supporting tentative identification of Feshbach resonances observed in the atomic halogens, this report.
14. P. Marchand, P. Veilette, and P. Marmet, J. Chem. Phys. 67, 2908 (1977).

PREDICTION OF LOW ENERGY MOLECULAR RYDBERG STATES FROM FESHBACH RESONANCE SPECTRA*

David Spence

An electron transmission spectrometer is used to study Feshbach resonances in the derivative of the transmitted electron current through gaseous targets of CH_3X(X= Cl, Br, I). A typical spectrum, that for CH_3I, is shown in Figure 1. Combination of data obtained in HX[1] and CH_3X yields an empirical relationship between resonance energies $E_{n\ell\ell'}(m)$ and the corresponding ionization potential I(m) given by

$$E_{n\ell\ell'}(m) = A_{n\ell\ell'}I(m) + B_{n\ell\ell'} , \qquad (1)$$

where $A_{n\ell\ell'}$ and $B_{n\ell\ell'}$ are constants independent of molecular species m, and ℓ and ℓ' are angular-momentum quantum numbers of the two excited electrons.

This empirical relation is shown graphically in Figure 2 for resonance configuration (ion core)$^+$ s^2, p^2, d^2 in the above-mentioned molecules.

The energy location of Feshbach resonances in other halogenated hydrocarbons and related molecules may be predicted from Eq. 1 with no other knowledge than the ionization potential I(m) and its $A_{n\ell\ell}$ and $B_{n\ell\ell}$ obtained from the data of Figure 2.

As Feshbach resonances are usually associated with Rydberg states rather than valence states, the above relation may be used, together with an effective core screening factor σ, to predict the energies of low-lying Rydberg states in molecules similar to those discussed above. An outline of this method is as follows. We must first give a brief description of Read's[2] modification of the Rydberg-Ritz formula. The familiar Rydberg-Ritz formula describes the energies $E_{n\ell}$ of atomic Rydberg states of configuration (core) $n\ell$ as

$$E_{n\ell} = I - \frac{RZ^2}{(n - \delta_{n\ell})^2} , \qquad (2)$$

---

*Summary of a paper published in J. Chem. Phys. 66, 669 (1977).

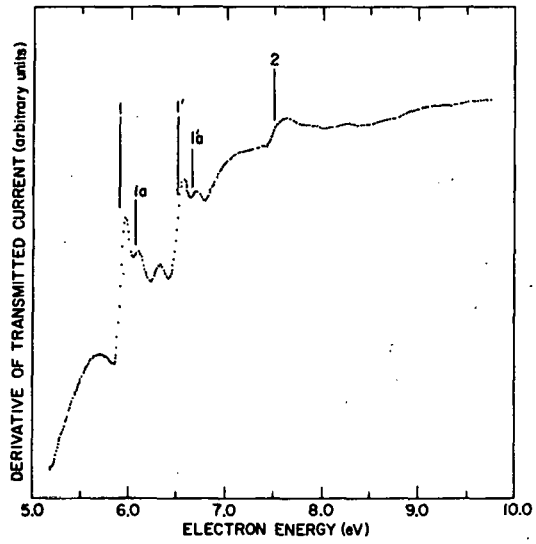

FIG. 1.--Derivative of the transmitted electron current vs. electron energy in methyl iodide. Structures 1 – 1' derive from the binding of a pair of 6s electrons to the $X^2E_{\frac{3}{2},\frac{1}{2}}$ positive ion cores, and 1a - 1a' are vibrationally excited resonances associated with 1 - 1'. (ANL Neg. 149-75-243)

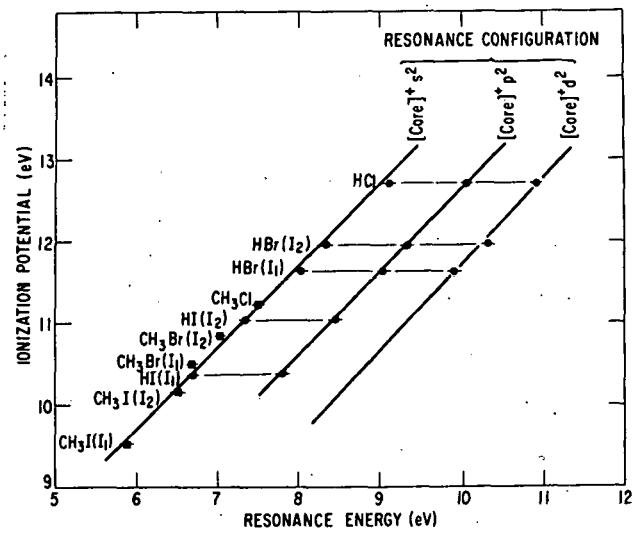

FIG. 2.--Plot of the ionization potential vs. Feshbach resonance energy for resonance configurations (core) s^2, p^2, d^2 in the acid and aklyl halides. The slope is unity, implying strong electron-electron correlation for the pairs of excited electrons moving in the non-spherical Coulomb field of the ion core. (ANL Neg. 149-76-221)

where I is the ionization potential, R is the Rydberg energy, Z is the charge on the core, n and ℓ are the principal and angular momentum quantum numbers, and $\delta_{n\ell}$ is the quantum defect of the state $E_{n\ell}$.

As Feshbach resonances consist of a pair of electrons in Rydberg-like orbitals, Read[2] has modified Eq. 2 by the simple expedient of accounting for 2 electrons and replacing the core charge Z by a reduced charge $(Z - \sigma)$, where σ is a screening constant representing the mutual screening of the ion core by the two electrons. For a pair of equivalent excited electrons, Feshbach resonance energies $E_{(n\ell)^2}$ are then given by

$$E_{(n\ell)^2} = I - \frac{2R(Z-\sigma)^2}{(n-\delta_{n\ell})^2} \quad . \tag{3}$$

The screening constant σ is obtained by combination of Eqs. 2 and 3

$$\sigma = Z - \left[\frac{I - E_{(n\ell)^2}}{2(I - E_{n\ell})} \right]^{\frac{1}{2}} \quad . \tag{4}$$

Using known resonance and Rydberg-state energies, Read[2] has shown that for the binding of a pair of s electrons to an atomic ion core, σ is often very close to 0.25. We note here that for such systems, σ is in fact confined to $0.25 < \sigma < 0.29$. Minimized mutual screening of the core, i.e., maximum electron-electron correlation, implies $\sigma = 0.25$, and for a resonance to be bound at all $E_{(n\ell)^2} \leq E_{n\ell}$, i.e., $\sigma \leq 0.29$.

Rearrangement of Eq. 4 allows the prediction of Rydberg state energies $E_{(n\ell)^2}$ from known Feshbach resonance energies, $E_{(n\ell)^2}$

$$E_{n\ell} = I - (I - E_{(n\ell)^2})/2(Z - \sigma)^2 \quad . \tag{5}$$

Substituting Eq. 1 into Eq. 5 yields

$$E_{n\ell} = I - [I(1 - A_{n\ell\ell'}) - B_{n\ell\ell'}]/2(Z - \sigma)^2 \quad . \tag{6}$$

Thus, armed with a knowledge of $A_{n\ell\ell'}$ and $B_{n\ell\ell'}$ from Figure 2 and σ, the prediction of low energy Rydberg states in structurally related molecules is a straightforward matter.

Using the values of $A_{n\ell\ell'}$, $B_{n\ell\ell'}$, and σ obtained from the data of Figure 2, and with no knowledge other than the ionization potential, we are able to calculate the energies of the lowest energy Rydberg states in chemically related molecules. This we have done in Table 1, where we have chosen the same set of molecules (listed in column 1) as used by Hochmann et al.[3] in their prediction of Rydberg states from known Rydberg energies in other molecules.

Table 1 vividly demonstrates that the technique described here is as accurate as that described by Maria,[4] and applied by Hochmann et al.[3] to estimate the energies of unknown Rydberg states.

TABLE 1. Comparison of predictions of the lowest energy Rydberg states using Rydberg-state spectra (Eq. 1) and Feshbach resonance spectra (Eq. 1). ΔE represents the error in the predictive ability. I_1 and I_2 represent the two spin-orbit components of the positive ion core.

Molecule	Ionization potential I,[a] eV	Rydberg state energy E_{ns} (measured),[a] eV	$\Delta E = E_{ns}$ (measured) $- E_{ns}$ (calculated), eV		
			Calculated from Rydberg spectra		Calculated from resonance spectra[b]
			$A_{n\alpha} = 0.95$ $B_{n\alpha} = -2.971$[b]	$A_{n\alpha} = 0.98$ $B_{n\alpha} = -3.20$[c]	$A_{ns} = 1.015$ $B_{ns} = -3.872$ $\sigma = 0.269$
HCl (I_2)	12.85	9.360	+0.123	-0.033	-0.047
HCl (I_1)	12.75	9.279	+0.138	+0.016	-0.028
ClCN (I_2)	12.631	9.233	+0.204	+0.054	+0.047
ClCN (I_1)	12.490	9.092	+0.198	+0.052	+0.049
BrCN (I_2)	12.197	8.465	-0.151	-0.288	-0.280
HBr (I_2)	11.98	8.544	+0.134	+0.004	+0.018
BrCN (I_1)	11.950	8.219	-0.162	-0.292	-0.276
HBr (I_1)	11.65	8.226	+0.130	+0.009	+0.034
ICN (I_2)	11.549	7.869	-0.132	-0.249	-0.219
CH_3Cl (I_2)	11.303	7.877	+0.108	-0.002	+0.035
CH_3Cl (I_1)	11.221	7.759	+0.070	-0.038	+0.003
HI (I_2)	11.05	7.545	+0.019	-0.084	-0.038
C_2H_cCl (I_2)	11.469	7.873	-0.052	-0.166	-0.134
C_2H_5Cl (I_1)	11.283	7.724	-0.024	-0.133	-0.095
ICN (I_1)	10.980	7.301	-0.159	-0.259	-0.211
CH_3Br (I_2)	10.856	7.341	-0.001	-0.099	-0.047
C_2H_5Br (I_2)	10.56	7.377	+0.316	+0.228	+0.292
CH_3Br (I_1)	10.54	6.951	-0.091	-0.178	-0.115
HI (I_1)	10.38	6.922	+0.032	-0.050	+0.018
C_2H_5Br (I_1)	10.24	6.993	+0.236	+0.158	+0.231
CH_3I (I_2)	10.166	6.775	+0.088	+0.012	+0.088
C_2H_5I (I_2)	9.88	6.752	+0.337	+0.270	+0.355
CH_3I (I_1)	9.538	6.162	+0.072	+0.015	+0.112
C_2H_5I (I_1)	9.30	6.163	+0.229	+0.249	+0.354
		Average ΔE =	0.14 eV	0.12 eV	0.13 eV

a, Ref. 5; b, Constants A and B calculated from methyl halide and acid halide data only; c, Constants A and B calculated using all listed molecules.

References

1. D. Spence and T. Noguchi, J. Chem. Phys. 63, 505 (1975).
2. F. H. Read, J. Phys. B. 10, 449 (1977).
3. P. Hochmann, P. H. Templet, H. T. Wang, and S. P. McGlynn, J. Chem. Phys. 62, 2588 (1975).
4. H. J. Maria, J. L. Meeks, P. Hochmann, and S. P. McGlynn, Chem. Phys. Lett. 19, 309 (1973).
5. Hydrogen halide data taken from S. G. Tilford, M. L. Ginter, and A. M. Bass, J. Mol. Spectrosc. 34, 327 (1970); M. L. Ginter and S. G. Tilford, ibid. 34, 206 (1970); S. G. Tilford, M. L. Ginter, and J. T. Vanderdice, ibid. 33, 505 (1970); H. J. Lempka, T. R. Passmore, and W. C. Price, Proc. R. Soc. (London) Ser. A 304, 53 (1968). Methyl halide data from Ref. 3 above. Ethyl halide data from R. A. Boschi and D. R. Salahub, Mol. Phys. 24, 289 (1972); W. C. Price, J. Chem. Phys. 4, 547 (1936). Cyanogen halide data from G. W. King and A. W. Richardson, J. Mol. Spectrosc. 21, 339 (1966).

A NEW TECHNIQUE TO DIFFERENTIATE BETWEEN NEGATIVE ION AND NATURAL AUTOIONIZATION STATES IN THE RARE GASES*

David Spence

Introduction

Autoionizing states in the rare gases have been studied by observation of scattered electrons,[1] ejected electrons (see Ref. 2 and references therein), photons,[3] and positive ions,[4] following excitation by electron impact. However, structures in the spectra obtained by the above techniques may often be attributed to energetically interspersed negative-ion states[2] (resonances). This effect is shown schematically in Figure 1, where we have sketched an energy-level diagram which includes only one neutral autoionizing state and one associated negative-ion state existing in the ionization continuum. Interferences between neutral and negative-ion states occur in the measured spectra in the following ways (neglecting only further complications from "post-collision interactions"[1,2] for the present).

Scattered-Electron Spectra

Neutral autoionizing states are usually located from scattered-electron spectra by measuring the final energy of the scattered electrons $E_R = E_i - E_o$. However, a negative ion located at $E_{o'}$, and associated with the neutral state at E_o can decay by emission of two electrons of energies E_1 and E_2, where $E_1 + E_2 = E_{o'} - E_I$. Both E_1 and E_2 can take any energy between zero and $E_{o'} - E_I$, and thus some will have energy $E_i - E_o = E_R$, and structures in the measured spectrum due to a negative ion may be interpreted as a neutral state.

Positive-Ion Spectra

In a similar manner, neutral autoionizing states are usually identified in positive-ion spectra by structures caused by interference between the

---

*Summary of a paper presented at the 30th Gaseous Electronic Conference, Palo Alto, October 1977. Full paper to be submitted for publication.

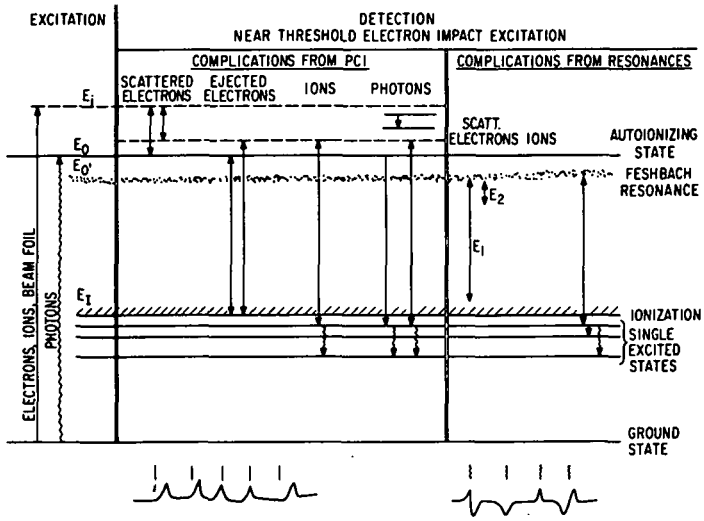

FIG. 1.--Schematic energy level diagram showing complications in scattered electron, positive ion, and broad-band photon autoionization spectra arising from nearby negative-ion states. Actual spectra contain a superposition of neutral and negative ion spectra. (ANL Neg. 149-78-16)

autoionizing state and the energetically coincident continuum. Such a situation also occurs, of course, when $E_i = E_{o'}$.

Photon Measurements

Neutral autoionizing states are often located by observing structures in the broad-band photon emissions which occur when the incident electron energy is swept through the energy location of a neutral autoionizing state. This may occur by cascading to lower-lying autoionizing states or by decay to a highly excited bound state followed by cascading. Negative ions can also, of course, decay by emission of a single electron to these same bound excited states, again causing structures in the photon yield whenever $E_i = E_{o'}$.

Techniques which have no adjustable experimental parameter other than the incident energy thus often cannot distinguish between structures due to negative and neutral autoionizing states. In actual practice, many neutral and negative-ion states will occur as a pair of "ladders." We have developed a technique dependent upon scattered electron spectra whereby the two "ladders" of resonances and doubly-excited states appear to move as a whole relative to one another, as a function of scattered energy.

Experimental Technique

The experimental technique we use is a modification of the trapped-electron technique, which we have described in some detail previously,[1] and

only the salient features will be outlined here.

Monochromatic electrons are accelerated to the desired energy E_i [$= e(V_a + W)$] inside a gas-filled collision chamber which contains a potential well W. Electrons which lose energy between eV_a and $e(V_a + W)$ in an inelastic collision remain trapped in the potential well, but use of a modulation technique results in the detection of only those whose final energy $E_R = eW$. Choice of W thus results in the choice of final energies detected as one sweeps the incident energy E_i by sweeping V_a for fixed W. However, as mentioned in the introduction, this technique will also detect negative-ion structures in the ionization continuun by the process of two-electron decay. Negative ions and neutral features can be separated by noting that negative-ion features occur only when $E_i = E_{o'}$, i.e., when

$$eV_a = E_{o'} - eW . \tag{1}$$

Neutral autoionizing features occur when

$$eV_a = E_o . \tag{2}$$

Thus, features due to negative ions and neutral autoionizing states can be separated by taking spectra at different fixed values of W. Whereas negative-ion features are very prominent in the scattered-electron spectra of He (and, in fact, dominate positive-ion spectra), they are rather weak in Ne. We employ one additional trick to enhance negative-ion features in this case. Note that if we modulate ΔW as shown in Figure 2, then our spectra contain only inelastic structures (neutral and negative ion), but if we modulate V_a instead, our spectra will contain the very same inelastic features, and in addition, the negative-ion structures will be greatly enhanced due to geometric trapping of some of the elastic negative-ion features, which are usually much larger than the inelastic features.

Results

Two spectra we obtain in the above manner are shown in Figure 3 for two values of W($W_1 = 0.125$ V and $W_2 = 0.65$ V). As predicted, some features

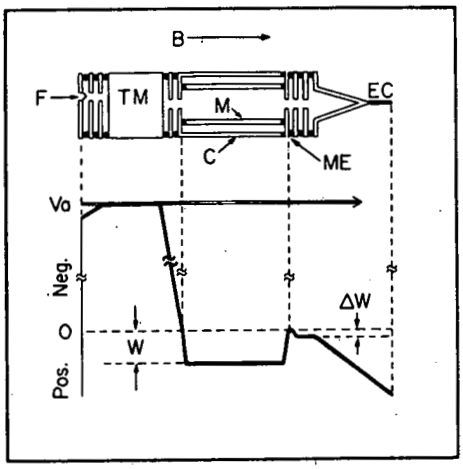

FIG. 2.--Schematic diagram of apparatus and potential along the axis. (ANL Neg. 149-6484)

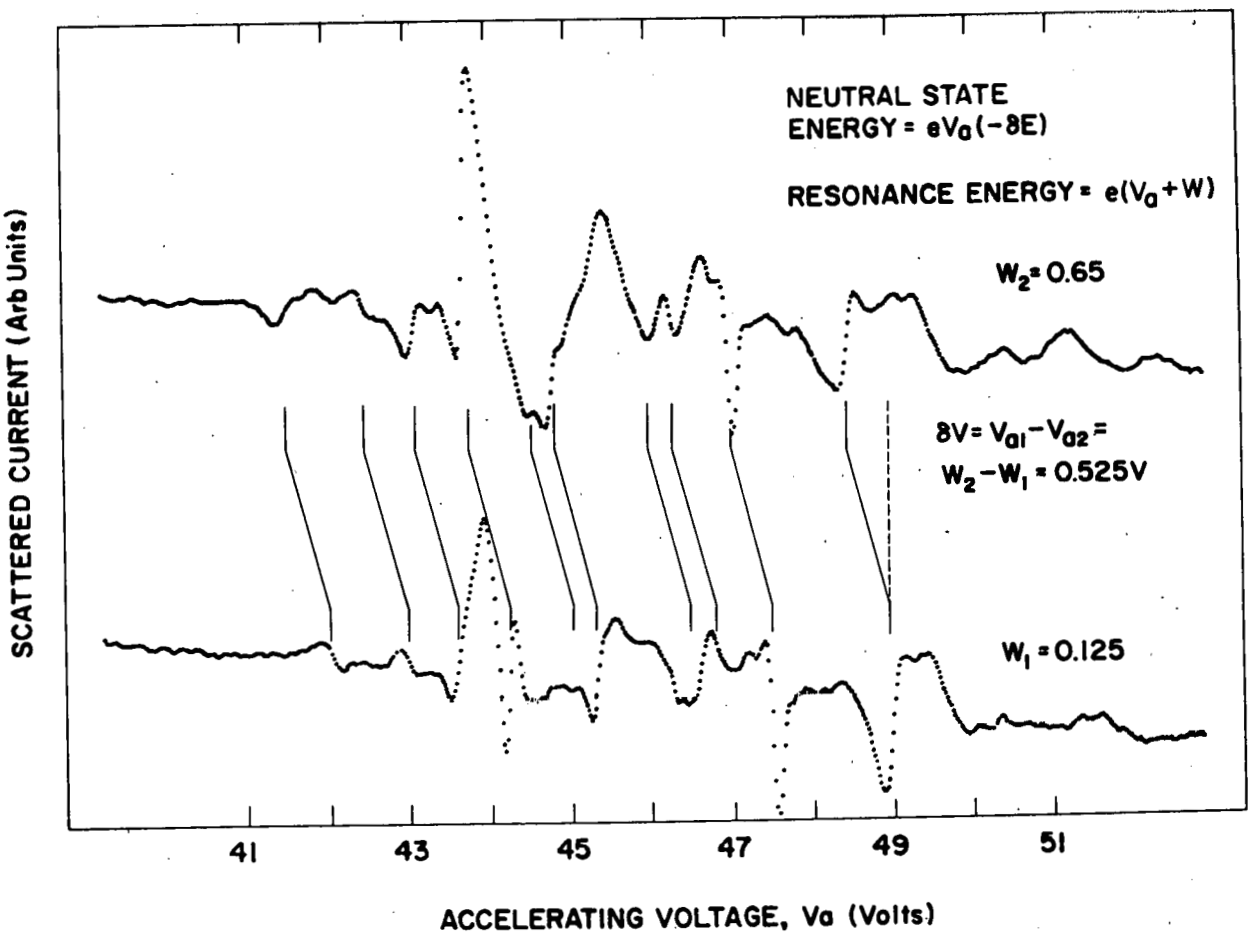

FIG. 3.--Negative ion and neutral states of Ne, with negative-ion peaks enhanced by modulating V_a as described in text. Negative-ion features move to lower values of V_a for larger values of W, as described by Eq. 1. Features at approximately the same value of V_a in both spectra are due to neutral autoionizing states. (ANL Neg. 149-72-440)

attributed to resonances are shifted to lower values of V_a by 0.525 V and are indicated by the sloping lines. Features which remain at approximately the same V_a are due to neutral autoionizing states (approximate in the sense that we are not taking post-collision interactions into account in this report).

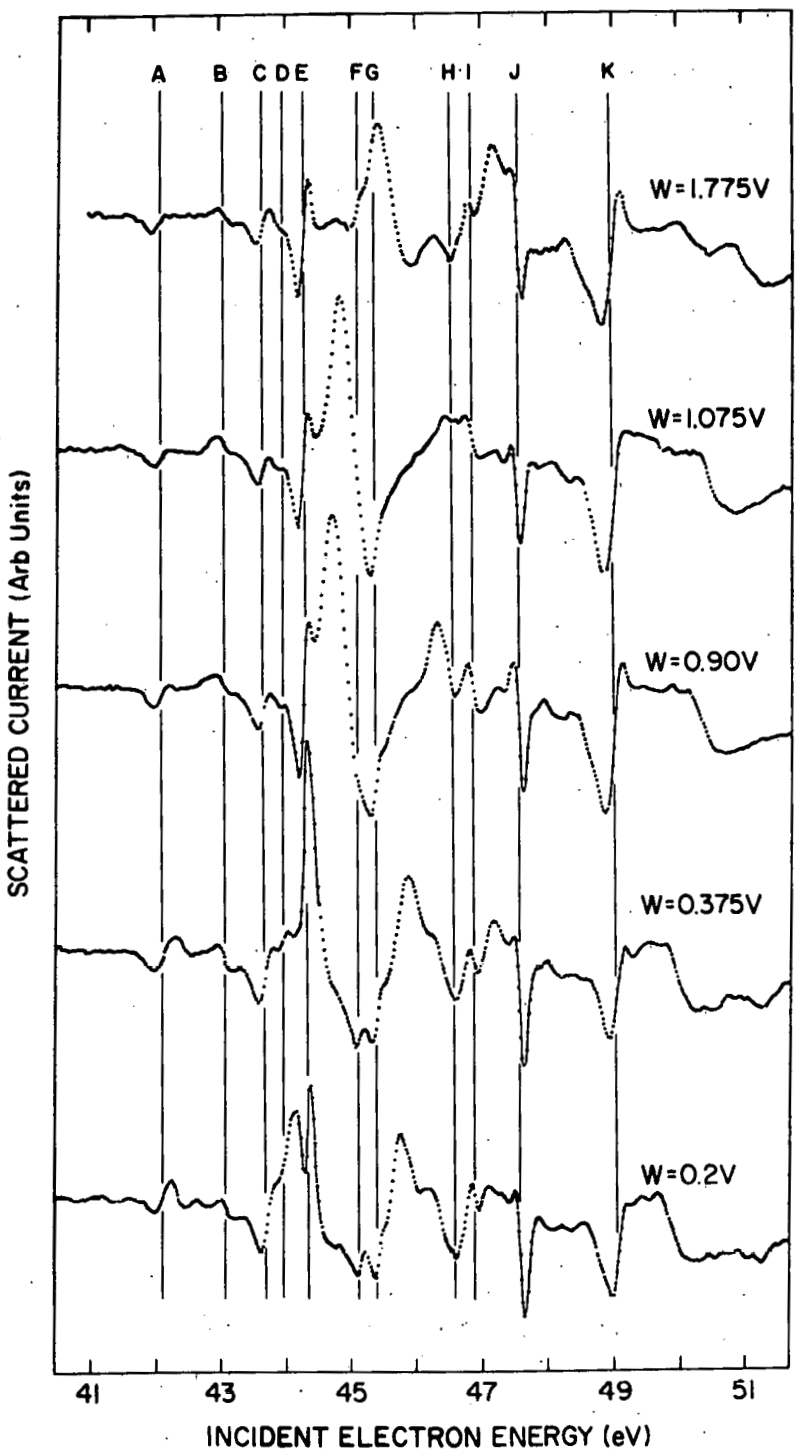

FIG. 4.--Spectra of scattered electron current as function of E_i [= $e(V_a + W]$ for different W's in Ne. Structures A → K connected by vertical lines are negative-ion states. All other features are neutral autoionizing states which, in this figure, occur at an energy $E_i = eW$. (ANL Neg. 149-77-435)

Taking many spectra similar to those in Figure 3 and shifting each spectrum to the right by the appropriate value of W results in the spectra shown in Figure 4. In this figure features which occur at the same incident electron energy $E_i = e(V_a + W)$ represent negative-ion states and are readily identifiable by the vertical lines marked A→K. The energies of these states are tabulated in Table 1 where they are seen to show very good agreement with the results of other workers using a variety of techniques. The neutral features which occur in Figures 3 and 4 are subject to complications from post-collision interaction effects and will be discussed in detail in a separate report.

TABLE 1. Comparison of N_e^- Energies in eV, Obtained in Present Experiments with previous data

Sanche and Schulz[a]	Wilden et al.[b]	Roy and Carrette[c]	Bolduc et al.[d]	Present experiment
41.98	42.10	42.11		42.13
43.05		43.07	43.11	43.09
43.67	43.68	43.67	43.72	43.71
	44.04	44.06		44.00
44.35	44.40	44.36		44.37
45.18	45.18	45.18		45.15
45.43	45.47	45.39	45.41	45.42
		45.63		
46.58	46.50	46.39		46.59
46.86				46.89
47.68	47.60			47.61
	48.00			
49.03		49.05		49.06

[a] Electron transmission, Ref. 5.
[b] Ejected electron spectra, Ref. 2.
[c] Structures in Ne $3p^5 3s1p$ excitation function, Ref. 6.
[d] Positive ions, Ref. 4.

References

1. D. Spence, Phys. Rev. A 12, 2353 (1975).
2. D. G. Wilden, P. J. Hicks, and J. Comer, J. Phys. B 10, 1477 (1977).
3. P. Veillette and P. Marchand, Can. J. Phys. 54, 1208 (1976).
4. E. Bolduc, J.J. Quemener, and P. Marmet, J. Chem. Phys. 57, 1957 (1972).
5. L. Sanche and G. J. Schulz, Phys. Rev. A 5, 1672 (1972).
6. D. Roy and J.D. Carette, J. Phys. B 7, L536 (1974).

EVIDENCE SUPPORTING TENTATIVE IDENTIFICATION OF FESHBACH RESONANCES OBSERVED IN THE ATOMIC HALOGENS

David Spence

From studies of the systematic energy locations of Feshbach resonances in atoms, we provide additional evidence supporting some tentative resonance-configuration assignments in Cl, Br, and I.

In a series of papers, Cunningham and Edwards[1-4] reported the observation of temporary negative-ion states (Feshbach resonances) in the atomic halogens F, Cl, Br, and I. Their experiments measured the energies of ejected electrons following collisional excitation of resonance states by the impact of fast ground state (stable) negative ions on gaseous targets, such as helium and hydrogen. Such an excitation/decay scheme is shown in Figure 1, which shows that, because of the doublet nature ($^2P_{\frac{3}{2},\frac{1}{2}}$) of the ground states of atomic halogens, each resonance gives rise to two possible electron energies, with the consequent doubling of many resonance features in the spectra of Cunningham and Edwards. However, because the magnitude of this splitting is known, Cunningham and Edwards were readily able to identify such doublet features. The assignment of electron configurations to the observed resonances was, however, less certain, and Cunningham and Edwards were able to give only tentative identification. The identifications were based on the recognition that the strongest resonance features were likely to consist of pairs of s electrons attached to positive-ion cores, and by analogies with previous resonance calculation in O by Matese, Rountree, and Henry.[5,6] Further calculations by Matese et al.[6] subsequently verified the assignments made by Cunningham and Edwards in Cl.

Using a graphical technique we developed to systematize resonances in the rare gases,[7] we are also able to verify the assignments of Edwards and Cunningham[1,3,4] in Br and I, and further, to identify unambiguously a few resonances whose configurations were uncertain. The basis of our original classification scheme was the observation that resonances of similar electron

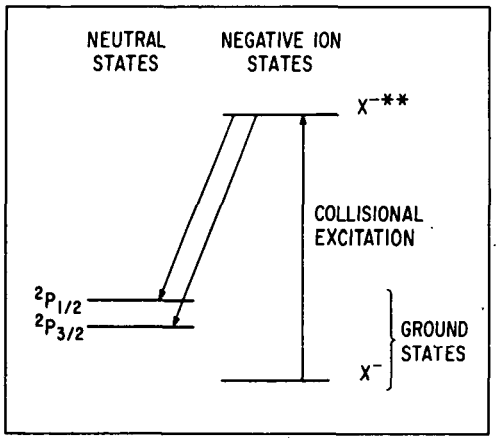

FIG. 1.--Schematic level diagram showing excitation from a ground negative ion state, and decay into neutral ground states in the atomic halogens. (ANL Neg. 149-78-14)

configurations in different atoms lay along straight lines when the resonance energies were plotted as a function of the ionization potential of the respective atom. In order to utilize this technique for classifying halogen resonances, we must first demonstrate that we can extend our graphical scheme to include excited positive ion-core states. We do this by using resonances in atomic oxygen as an example, where the resonance energies (see Ref. 8 and references therein) and configurations[5] are very well known. In Figure 2 we have made such a plot of resonance energy versus the energies of the known ion core[5,8] term values ^4S, ^2D, and ^2P. Figure 2 vividly demonstrates (with the exception of $[^2D]3s3p$ resonance) the excellent fits that can be obtained from such a plot for resonance configurations [core] s^2, sp, and p^2.

We are now able to use such a plot to classify the halogens (Figure 3), where we use only those energies corresponding to decay to the $^2P_{\frac{3}{2}}$ ground state (the "unprimed" energies listed by Cunningham and Edwards).

On the left we have plotted the various ground and excited positive ion state energies of Cl, Br, and I, suggested by Cunningham and Edwards, as forming the positive ion cores of the observed resonances. This plot, indeed, verifies the configurations suggested by Cunningham. Cunningham and Edwards were, however, unable to decide whether the ion core of the second resonance in I and Br had term values $^3P_0$ or $^3P_1$. Figure 3 shows that the correct choice is $^3P_0$ in both cases, as, indeed, we had previously determined in case of the rare gases.[9]

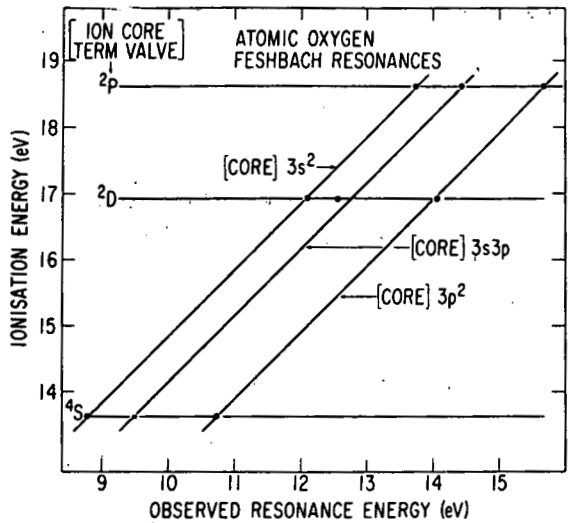

FIG. 2.--Plots of resonance energies vs. parent atom ionization potentials in atomic oxygen.
(ANL Neg. 149-78-18)

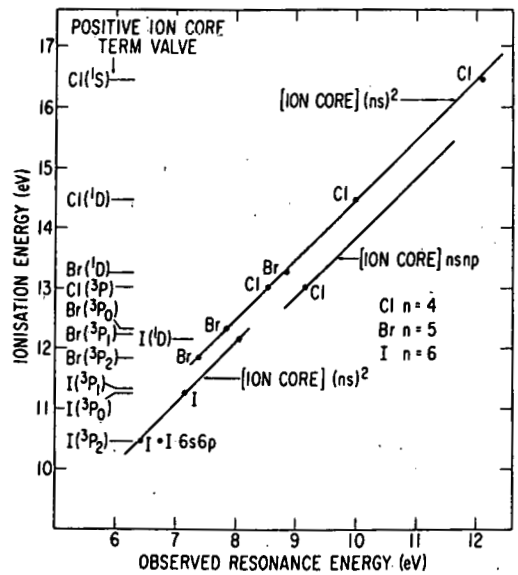

FIG. 3.--Plots of resonance energies vs. parent atom ionization potentials in Cl, Br, and I.
(ANL Neg. 149-78-17)

References

1. D. L. Cunningham and A. K. Edwards, Phys. Rev. A 8, 2960 (1973).
2. A. K. Edwards and D. L. Cunningham, Phys. Rev. A 9, 1011 (1974).
3. D. L. Cunningham and A. K. Edwards, Phys. Rev. Lett. 32, 915 (1974).
4. A. K. Edwards and D. L. Cunningham, Phys. Rev. A 10, 448 (1974).
5. J. J. Matese, S. P. Rountree, and R. J. W. Henry, Phys. Rev. A 7, 846 (1973).
6. J. J. Matese, S. P. Rountree, and R. J. W. Henry, Phys. Rev. A 8, 2965 (1973).
7. D. Spence, Phys. Rev. A 10, 1045 (1974).
8. D. Spence, Phys. Rev. A 12, 721 (1975).
9. D. Spence and T. Noguchi, J. Chem. Phys. 63, 505 (1975).

A NOTE ON THE ASSIGNMENT OF LOW-LYING RYDBERG STATES IN F_2

David Spence

We propose tentative configuration assignments to low-lying Rydberg states in F_2, based upon a systematic study of daughter Feshbach-resonance states.

Despite the very extensive studies of molecular fluorine by photoabsorption, photoemission, photoion, and photoelectron spectroscopy extending over a period of 50 years, relatively little is known about the spectrum or molecular structure of fluorine, especially assignment of low-lying Rydberg states. A recent detailed study of F_2 in absorption and emission by Colbourn et al.[1] analyzed rotational and vibrational structures of a few Rydberg states but failed to identify any Rydberg series.

At the energy location of the expected lowest Rydberg series corresponding to the promotion of a π_g electron to a $3s\sigma$ orbital, Colbourn et al.[1] found one vibrational sequence with B and ω values similar to those of the ground positive-ion state, which they very tentatively assigned as $(x^2\Pi)3s\sigma\,^1\Pi_g$, plus one additional isolated level also of similar B value, which they tentatively identified as a possible vibrational level of the $(x^2\Pi)3s\sigma\,^3\Pi_g$ component of the $^3\Pi$ manifold states. Colbourn et al., however, stress that they lack any possible proof of these assignments. In addition, there is some question as to whether the vibrational quantum number of the lowest levels in the vibrational sequence they observed is 0 or 1. This work apparently failed to take account of any help in state assignments that may have been available from published Feshbach resonance spectra,[2] which, as has been repeatedly pointed out (see Ref. 2 and references therein), are associated with such Rydberg states. In addition, very detailed systematic studies have been made[2,3-6] of Feshbach resonances and their parent Rydberg states which often made identification of these states possible.

In order to apply a knowledge of these systematics we have plotted in Figure 1 the energy of Feshbach resonance levels we have previously obtained in F_2,[6] together with the energy levels obtained by Colbourn et al.[1] in

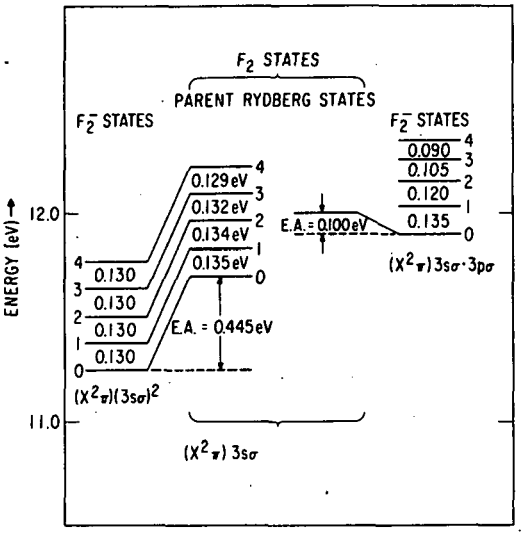

FIG. 1.--Energy level diagram of Feshbach resonances (Ref. 6) and Rydberg states (Ref. 1) observed in F_2. (ANL Neg. 149-78-19)

F_2 emission. In that the vibrational spacings of a resonance series is expected to be similar to that of the parent Rydberg and grandparent positive-ion states,[3] it is clear that the resonance sequence we observed with average spacing 130 meV is associated with the vibrational sequence observed in emission. Further, the electron affinity of the Rydberg states, 0.445 eV is entirely consistent with the value obtained from studies of many dozens of atoms and molecules,[2-6] which always lies in the range 0.4→0.5 eV for the binding of an additional s electron to the lowest Rydberg state, which itself is formed by adding an s electron to a positive-ion core. Because of the strength of the lowest resonance we observed, we believe that its vibrational quantum number is 0, and hence the lowest level observed in emission is 0 and not 1. If an additional lower vibrational level did exist in emission, its electron affinity would be only 0.31 eV, which would be unusually low. Further, also from systematic studies,[2] we expect the parent Rydberg state of the observed lowest sequences of resonances to have term value $^3\Pi_2$, rather than $^1\Pi$, as tentatively assigned by Colbourn et al.[1]

A second weaker series of resonances we observed at higher energy is plotted on the right of Figure 1, and the lowest member of this series is clearly associated with the isolated (weak) level observed in emission. In this case, the electron affinity of the parent Rydberg state is only 0.10 eV, which is consistent with the binding of an additional p electron to an excited system

with an s electron.[2,4,7] The reduced electron affinity occurs, of course, because of the increased mutual screening of the positive ion core by pairs of electrons in dissimilar orbitals. Again from systematic studies in many atoms and molecules, we expect the parent state of these latter resonances to be $^1\Pi$ and not a member of the $^3\Pi$ manifold suggested by Colbourn et al.[1]

References

1. E. A. Colbourn, M. Degenais, A. E. Douglas, and J. W. Raymonda, Can. J. Phys. 54, 1343 (1976).
2. D. Spence and T. Noguchi, J. Chem. Phys. 63, 505 (1975).
3. G. J. Schulz, Rev. Mod. Phys. 45, 378 (1975).
4. D. Spence, Phys. Rev. A 15, 883 (1977).
5. D. Spence, J. Chem. Phys. 66, 669 (1977).
6. D. Spence, Phys. Rev. A 10, 1045 (1974).
7. D. Spence, Phys. Rev. A 12, 721 (1975).

LOW ENERGY ELECTRON SCATTERING FROM METHANE

P. D. Burrow* and J. A. Michejda**

Transmission of electrons with kinetic energies below 1.5 eV through methane has been studied. The derivative of the transmitted current shows many features attributable to various vibrational modes and their combinations.

The total scattering cross sections of unsaturated hydrocarbon molecules display pronounced resonant variations due to the formation of temporary negative ions at energies below 5 eV. For the most part, these features are shape resonances created by the binding of the incoming electron into a low-lying, normally unfilled antibonding π orbital (see, for example, Ref. 1 and references therein). In saturated hydrocarbons, such as methane (CH_4), the lowest unfilled orbitals lie at relatively high energy and one does not expect, therefore, to find sharp resonant structure in the electron scattering cross section due to shape resonances.

We have examined the total cross sections of a number of saturated hydrocarbons, such as methane, ethane, propane, butane, and cyclohexane, at low energy using the electron transmission technique of Sanche and Schulz.[2] In each compound, relatively sharp structure is found in the energy range from 0 to 1.5 eV. Figure 1 illustrates this structure in methane. In this figure, the derivative with respect to energy of the current transmitted through a gas cell containing CH_4 is plotted as a function of the electron impact energy.

The energies of certain of the vibrational modes of methane are also shown in Figure 1 as vertical lines labeled by the relevant vibrational quantum numbers. The modes shown are infrared active fundamentals, overtones, or

*Consultant, Radiological and Environmental Research Division. Permanent address: Department of Physics and Astronomy, University of Nebraska, Lincoln, Nebraska 68588.

**Department of Engineering and Applied Sciences, Yale University, New Haven, Conn. Work supported by NSF. Present address: Bell Laboratories, Allentown, Pennsylvania 18103.

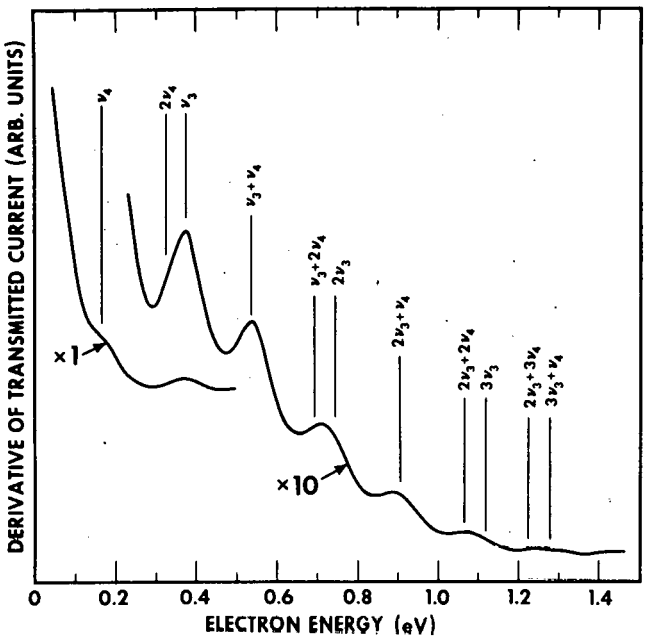

FIG. 1.--Derivative of the transmitted current as a function of electron energy in methane.

combination modes, and there appears to be good agreement between these energy levels and the structure seen in the transmission spectrum. It appears reasonable to assign these features to Wigner cusps associated with the opening of these channels of vibrational excitation.

Similar structure has been observed in the other compounds studied here as well as certain unsaturated hydrocarbons. It is likely that such effects are general in scope. The interpretation of structure attributed to temporary negative-ion states at these energies must also be carried out with these effects in mind.

References

1. P. D. Burrow, J. A. Michejda, and K. D. Jordan, J. Am. Chem. Soc. 98, 6392 (1976).
2. L. Sanche and G. J. Schulz, Phys. Rev. A 5, 1672 (1972).

RESONANCES IN ELECTRON SCATTERING FROM CADMIUM

P. D. Burrow* and J. A. Michejda**

Transmission of electrons with kinetic energies up to 13 eV through a heated collision chamber filled with Zn, Cd, or Hg vapors has been studied. Features in the derivative of the transmitted current as a function of electron energy are attributed to shape resonances, Feshbach resonances, or Wigner cusps.

Studies of temporary negative-ion formation in the elements have been confined largely to the rare gases.[1] With only a few exceptions, measurements over a wide energy range and efforts to classify resonances have been restricted to these closed-shell atoms. To improve our understanding of temporary electron attachment, it is desirable to extend experiments to elements in other columns of the periodic table. Furthermore, it is useful to choose columns in which as many of the elements as possible may be studied.

With this in mind, we have carried out electron transmission studies of the group IIb elements zinc, cadmium, and mercury, as well as magnesium from group IIa. Each of these atoms is characterized by an ns^2 outer electron configuration. Our measurements were made using the electron transmission method devised by Sanche and Schulz,[2] which has been amply described in the literature. Our only modification to this technique was to employ a heated collision chamber fed by a heated side arm containing the solid metal.

Representative data for cadmium are shown in Figure 1 which displays a plot of the derivative with respect to energy of the electron beam current transmitted through a cell containing the metal vapor. The energy range begins just below the excited states of Cd, shown as vertical lines, extends past the

*Consultant Radiological & Environmental Research Division. Permanent address: Department of Physics and Astronomy, University of Nebraska, Lincoln, Nebraska 68588.

**Department of Engineering and Applied Science, Yale University. Work supported by NSF. Present address: Bell Laboratories, Allentown, Pennsylvania 18103.

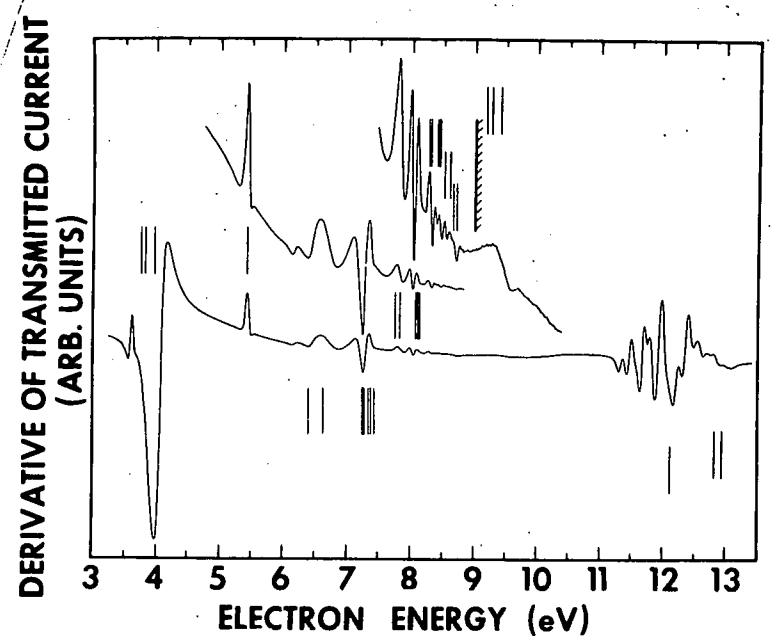

FIG. 1.--Derivative of the transmitted current as a function of electron energy in cadmium.

first ionization potential near 9 eV, and includes the lowest few doubly-excited states from 12 to 13 eV.

At energies below 1 eV, not shown in Figure 1, a single, large resonance is present in each of the elements studied here. These features are shape resonances caused by formation of $(ns^2np)\ ^2P$ states of the negative ions and have been discussed elsewhere.[3]

Although classification of the resonances seen in Figure 1 is incomplete, a few of the features are worth noting here. At the lowest optically allowed state, near 5.4 eV in Cd, a pronounced structure appears which does not have the characteristic resonance profile. We attribute this feature to a Wigner cusp occurring at the transition threshold. Similar abrupt changes in the total cross sections of each of these elements will serve as useful energy calibration points.

The excited states of Cd are grouped in Figure 1 according to principal quantum number. Close examination of the figure indicates that the profiles of the Feshbach resonances associated with each group are replicated as the principal quantum number is increased. This is easy to see by comparing the resonances between 6.5 and 7.5 eV with those between 7.7 and 8.3 eV.

Above the ionization potential, large resonances are observed in the range from 11 to 13 eV. These are attributed to Feshbach resonances associated with the virtual excitation of inner-shell 4d electrons, rather than the valence $5s^2$ electrons. In the case of mercury, these inner-shell resonances fall below the lowest ionization potential and overlap the usual valence state resonances, causing much confusion in earlier attempts to classify the negative ion states.

References

1. G. J. Schulz, Rev. Mod. Phys. 45, 378 (1973).
2. L. Sanche and G. J. Schulz, Phys. Rev. A 5, 1672 (1972).
3. P. D. Burrow, J. A. Michejda, and J. Comer, J. Phys. B: Atom. Molec. Phys. 9, 3225 (1976).

ELECTRON SCATTERING BY Li IN GLAUBER APPROXIMATION*

C. H. Chang,† F. T. Chan,†‡ and Y.-K. Kim

Differential cross sections for elastic scattering and for the excitation of the $2p^2P$, $3p^2P$, and $3s^2S$ states of Li have been calculated at 5.4, 10, 20, and 60 eV electron-impact energies in the frozen core Glauber approximation. It is found that the Glauber results are in reasonable agreement with the recent experimental measurements of Williams et al.[1] The polarization fraction of the resonance lines of Li is also calculated in the Glauber approximation. The theoretical results are in good agreement with the existing experimental data of Leep and Gallagher[2] in the incident energy range from 30 to 1000 eV.

References

1. W. Williams, S. Trajmar, and D. Bozinis, J. Phys. B 9, 1529 (1976).
2. D. Leep and A. Gallagher, Phys. Rev. A 10, 1082 (1974).

*Abstract of a paper presented at the Annual Meeting of the American Physical Society, Chicago, 7–10 February 1977.

†Department of Physics, University of Arkansas, Fayetteville, Arkansas 72701.

‡Participant, June–August 1976, Faculty Research Participation Program, Argonne Center for Educational Affairs.

ENERGY DISTRIBUTIONS OF SECONDARY ELECTRONS. III. PROJECTILE ENERGY DEPENDENCE FOR IONIZATION OF He, Ne, AND Ar BY PROTONS*

L. H. Toburen,† Steven T. Manson,‡ and Yong-Ki Kim

A theoretical analysis of secondary electron spectra, which has previously been applied to electron-impact ionization of atoms and molecules, is applied to the experimental data on ionization of He, Ne, and Ar by protons in the 0.1 to 1.5 MeV energy range. The data are also compared with ab initio Born approximation calculations. Our theoretical analysis clearly brings out expected features in the secondary-electron spectra for incident proton energies of ~1 MeV and up. Inner-shell contributions and the charge transfer to the continuum process tend to obscure the appearance of a simple asymptotic behavior at lower proton energies; for a given incident energy, the analysis is simpler for atoms and molecules with lower nuclear charge.

---

*Abstract of a paper published in Phys. Rev. A 17, 148 (1978).

†Battelle Northwest Laboratory, Richland, Washington 99352.

‡Consultant, RER Division. Permanent address: Department of Physics, Georgia State University, Atlanta, Georgia 30303.

OSCILLATOR STRENGTHS IN THE Ag-ISOELECTRONIC SEQUENCE*

K. T. Cheng† and Y.-K. Kim

Excitation energies and oscillator strengths for dipole-allowed transitions between low-lying states in the Ag-isoelectronic sequence are studied using relativistic Hartree-Fock wavefunctions.[1] It is found that from Pm^{14+} ($Z=61$) and up, the ground state is 4f rather than 5s, while the transitions 5s-5p and 4f-5g are strong throughout the sequence. The theoretical wavelengths for the Pr^{12+} ion are in excellent agreement ($\sim 1\%$ or better) with recent experimental data.[2]

References

1. J. P. Desclaux, Comput. Phys. Commun. 9, 31 (1975).
2. J. Sugar, J. Opt. Soc. Am. 67, 1518 (1977).

*Abstract of a paper presented at the 9th Annual Meeting of the Division of Electronic and Atomic Physics of the American Physical Society, Knoxville, Tennessee, 5–7 December 1977.

† Postdoctoral appointee from the University of Notre Dame.

TRANSITION PROBABILITIES FOR THE RESONANCE TRANSITIONS OF Na-LIKE IONS*

Yong-Ki Kim and Kwok-tsang Cheng†

Theoretical wavelengths and transition probabilities for the 3S-3P and 3S-4P transitions of Na-like ions are presented. The theoretical data are computed from relativistic Hartree-Fock wavefunctions. Similar data for additional transitions between low-lying states (n=3 and 4) of the Fe^{15+}, Mo^{31+}, W^{63+}, and Au^{68+} ions are also reported. Relativistic effects in the oscillator strengths for the resonance transitions are qualitatively similar to those already observed in the Li sequence. Comparison with available experimental data on wavelengths for Fe^{15+} and Mo^{31+} ions shows excellent agreement (1% or better).

*Abstract of a paper to appear in J. Opt. Soc. Am.

†Postdoctoral Appointee from the University of Notre Dame.

BORN CROSS SECTIONS FOR ION-ATOM COLLISIONS*

George H. Gillespie,† Yong-Ki Kim, and Kwok-tsang Cheng‡

Selected total cross sections are calculated in the closure-Born approximation for the ions Li^+, Cs^+, and Au^+ incident on several gas constituents. Targets included are H, H_2, He, C, N, and O. Four general types of cross section are considered depending on whether the incident ion or target atom is scattered elastically or inelastically. Expressions are given for the Born cross sections to the first two orders in an expansion in β^{-2}, where $\beta = v/c$ and v is the relative velocity. The atomic form factors and incoherent scattering functions for the ions Cs^+ and Au^+, which are required in order to evaluate the leading order cross section parameters, are calculated from the relativistic and nonrelativistic Hartree-Fock wavefunctions. Results are also given for some of the energy moments of the dipole oscillator strength distributions for Cs^+ and Au^+, as determined from the ground state wavefunctions. These parameters, together with atomic properties taken from the literature for Li^+, and the various targets considered are then used to evaluate the cross sections to the first two orders in the expansion.

---

*Abstract of a paper to appear in Phys. Rev. A.

†Physical Dynamics, Inc., P.O. Box 556, La Jolla, California 92038.

‡Postdoctoral Appointee from the University of Notre Dame.

BETHE CROSS SECTIONS FOR Na-LIKE IONS*

Yong-Ki Kim and Kwok-tsang Cheng†

Bethe cross sections for the excitation of Na-like ions to the $3^2P_{\frac{1}{2}}$, $3^2P_{\frac{3}{2}}$, $4^2P_{\frac{1}{2}}$, and $4^2P_{\frac{3}{2}}$ states from the ground state by electron impact are computed from the relativistic Hartree-Fock wavefunctions. As the nuclear charge is increased, excitation to the $^2P_{\frac{3}{2}}$ state is affected far more by relativistic effects than excitation to the $^2P_{\frac{1}{2}}$ state. The asymptotic ionization cross sections for the neutral Na atom and Fe^{15+} ion are computed from a sum rule, i.e., by subtracting the sum of the discrete excitation cross sections from the total inelastic-scattering cross section obtained from the sum rule. In the evaluation of the sum-rule cross section, a dipole oscillator-strength moment L(-1) is needed. A value of L(-1) for the Fe^{15+} ion was provided by Baer.[3] The ionization cross sections thus obtained are

$$\sigma_{ion}(Na) = \beta^2\{2.51\,[\ln(\frac{\beta^2}{1-\beta^2}) - \beta^2] + 26.3\} \times 10^{-20}\ cm^2\ , \quad (1)$$

$$\sigma_{ion}(Fe^{15+}) = \beta^{-2}\{0.209\,[\ln(\frac{\beta^2}{1-\beta^2}) - \beta^2] + 1.64\} \times 10^{-20}\ cm^2\ , \quad (2)$$

where β is the incident electron speed divided by that of light. The cross section for Na is in agreement with that calculated by McGuire,[1] but not with the epxeriment by McFarland and Kinney.[2]

References

1. E. J. McGuire, Phys. Rev. A 3, 267 (1971).
2. R. H. McFarland and J. D. Kinney, Phys. Rev. 137, A1058 (1965).
3. T. Baer, Moments of the Oscillator-Strength Distribution for the Fe^{15+} Ion, this report.

*Abstract of a paper to be published in Phys. Rev. A.

†Postdoctoral Appointee from the University of Notre Dame.

MOMENTS OF THE OSCILLATOR-STRENGTH DISTRIBUTION FOR THE Fe^{15+} ION

T. Baer*

We have used potentials calculated by a Hartree-Slater self-consistent atomic field program[1] to generate the dipole oscillator-strength distribution for Fe^{15+}. The result was then used to calculate moments of the dipole oscillator-strength distribution as in previous studies.[2]

The dipole strength distributions of the separate shells in Fe^{15+} all showed hydrogenic behavior, that is, monotonic decreasing behavior as a function of energy in the continuum region. In particular, the maximum which occurs just above threshold in the 2p-d channel in the oscillator-strength distribution in the Fe neutral has disappeared. This behavior is expected since the wavefunctions of Fe^{15+} will quickly assume hydrogenic form because of the high ionic charge.

Table 1 gives the calculations of the moments of the dipole oscillator strength. The quantities tabulated have the analytical form

$$S(\mu) = \int (E/R)^{\mu} (df/dE)\, dE ,$$

$$L(\mu) = \int (E/R)^{\mu} \ln (E/R)\, (df/dE)\, dE ,$$

where df/dE is the oscillator-strength distribution, R is the Rydberg energy, and the integral includes a sum over all allowed discrete transitions.

TABLE 1. Moments of the Dipole Oscillator Strength Distribution for Fe^{15+}

μ	-6	-5	-4	-3	-2	-1	0
$S(\mu)$	0.192(-2)	0.457(-2)	0.109(-1)	0.260(-1)	0.642(-1)	0.275	0.109(2)
$L(\mu)$	0.167(-2)	0.397(-2)	0.945(-2)	0.227(-1)	0.628(-1)	0.657	0.504(2)

The format A(B) means $A \times 10^{B}$.

* Resident Graduate Student Associate, RER Division, July–September 1977. Permanent address: Department of Physics, The University of Chicago, Chicago, Illinois 60637.

Since experimental data for Fe^{15+} are not available, we have tested the overall accuracy of this method by comparing our results with more realistic calculations. S(-1) was found to agree within 5% with a nonrelativistic Hartree-Fock calculation.[3] (The Hartree-Fock value was S(-1) = 0.282.) Both oscillator strengths and energy levels of the discrete states of the 3s valence shell also agreed with a relativistic Hartree-Fock calculation[3] to within 10%. Finally, we note that the 600 Rydberg cut-off energy, which we used in the numerical evaluation of the above integrals, gave a value of S(0) within 1% of the expected 11.0. The accuracy of the $\mu < 0$ moments should be affected less by this high energy cut-off of the integration since they depend on a negative power of the energy.

This method should prove useful in the systematic study of the ionic properties of elements in the periodic table. Some of the present results are immediately useful. Indeed, the present value of L(-1) was used by Kim and Cheng[4] in an evaluation of the total inelastic-scattering cross section for electron impact on Fe^{15+} at high energies.

References

1. F. Herman and S. Skillman, Atomic Structure Calculations, Prentice-Hall, Englewood Cliffs, N. J. (1963).
2. J. L. Dehmer, M. Inokuti, and R. P. Saxon, Phys. Rev. A 12, 102 (1975).
3. Yong-Ki Kim, private communication.
4. Y.-K. Kim and K. T. Cheng, Bethe cross sections for Na-like ions, this report.

RELATIVISTIC EFFECTS IN EXCITATION CROSS SECTIONS FOR STRIPPED IONS*

Yong-Ki Kim

Asymptotic Born cross sections for the resonance transitions of Mo and W ions (Li- and Na-like) show 20 to 50% reductions when relativistic wavefunctions are used instead of nonrelativistic ones. The smaller cross sections result both (a) from relativistic contraction of orbitals (reduced geometrical cross sections) and (b) from reduced range of momentum transfers (increase in the lower limit of the momentum transfer) when the spin-orbit splitting increases the excitation energy. The latter effect is most conspicuous in the $ns_{\frac{1}{2}} - np_{\frac{3}{2}}$ transitions. The use of appropriate relativistic data would be necessary to obtain reliable (20% or better) cross sections for discrete excitations by electron impact.

*Abstract of a paper presented at the American Physical Society Topical Conference on Atomic Processes in High-Temperature Plasmas, Knoxville, Tenn. 16–18 February 1977.

ATOMIC FORM FACTORS AND INCOHERENT SCATTERING FUNCTIONS OF Xe, Hg, AND U IONS

Kwok-tsang Cheng* and Yong-Ki Kim

Atomic form factors and incoherent-scattering functions of Xe^{n+} (n = 1-6), Hg^{n+} (n = 2,5,10,20,34,52), and U^{n+} (n = 1,6) were computed from relativistic Hartree-Fock wavefunctions. These data are needed in estimating total cross sections for inelastic scattering of the ions by background gases in storage rings proposed in various heavy-ion fusion schemes.

Introduction

Some scenarios proposed for the inertial-confinement (pellet) fusion by energetic heavy ions[1] use storage rings to accumulate the ions before the final focusing on the pellet. To determine vacuum requirements of the storage ring, it is necessary to estimate stripping cross sections of the ions by background gases in the ring. The terminal velocity of the ions is expected to be a sizable fraction of the speed of light ($v_{ion}/c \sim 2/3$), and hence we can use the Born approximation for the ion-gas collision.

A sum-rule method can be applied to the Born cross sections for the ion-atom collision[2] in much the same way as was done for electron-atom collisions.[3] The sum rule reduces final expressions for the collision cross sections to terms involving the atomic form factors F(K) and incoherent-scattering function $S_{inc}(K)$ of the ions and the target gases. The functions F(K) and $S_{inc}(K)$ are also used in calculating cross sections for x-ray and electron scattering.[4]

For application to heavy-ion fusion schemes, F(K) and $S_{inc}(K)$ for ions of various atoms and charge states are needed. A comprehensive tabulation exists in the literature for neutral atoms.[5] For ions, however, F(K) was calculated only for a limited number of ions (mostly singly charged ones for crystallographic applications), and no table of $S_{inc}(K)$ for ions is available in the literature.

*Postdoctoral Appointee from the University of Notre Dame.

Definitions

Both $F(K)$ and $S_{inc}(K)$ are functions of the momentum transfer $\vec{K}\hbar$, and are defined in terms of an atomic wavefunction Ψ as

$$F(K) = \langle \Psi \left| \sum_{j=1}^{N} \exp(i\vec{K} \cdot \vec{r}_j) \right| \Psi \rangle , \tag{1}$$

and

$$NS_{inc}(K) = \langle \Psi \left| \sum_{j,k=1}^{N} \exp[i\vec{K} \cdot (\vec{r}_j - \vec{r}_k)] \right| \Psi \rangle - |F(K)|^2 , \tag{2}$$

where N is the total number of atomic electrons and $\vec{r}_j$ is the position vector of the jth electron from the nucleus. In most applications, the target atom is in the ground state, and the ground-state wavefunction is used for Ψ. (When high precision is unnecessary, a molecule can be approximated as the collection of constituent atoms, and the corresponding cross section can be approximated as the sum of cross sections for scattering by these atoms.)

Results

In the course of computing Born cross sections for ion-atom collisions, we have calculated $F(K)$ and $S_{inc}(K)$ for a number of heavy ions from relativistic Hartree-Fock wavefunctions. We used Desclaux's computer codes[6] to produce the wavefunctions. For open-shell configurations, we used average configurations. Some of our results are being published elsewhere.[7]

As can be seen from the definitions 1 and 2, $F(K)$ and $S_{inc}(K)$ are even functions of K, i.e., functions of K^2. A convenient dimensionless variable to be used is $Q \equiv (Ka_0)^2$, where $a_0 = 0.529$ Å. We have tabulated $F(Q)$ and $S_{inc}(Q)$ of selected ions of Xe, Hg, and U in Tables 1–7. The net charges on some of the ions were chosen such that remaining electrons form closed shells.

The data for Hg ions [Hg^{2+} ($5d^{10}$); Hg^{5+} ($5d^7$); Hg^{10+} ($5d^2$); Hg^{20+} ($4f^{14}$); Hg^{34+} ($4d^{10}$); Hg^{52+} ($3d^{10}$)] are also plotted in Figures 1 and 2. By definition, $F(Q) = N$ at $Q = 0$, and $S_{inc}(Q) = 1$ at $Q \to \infty$.

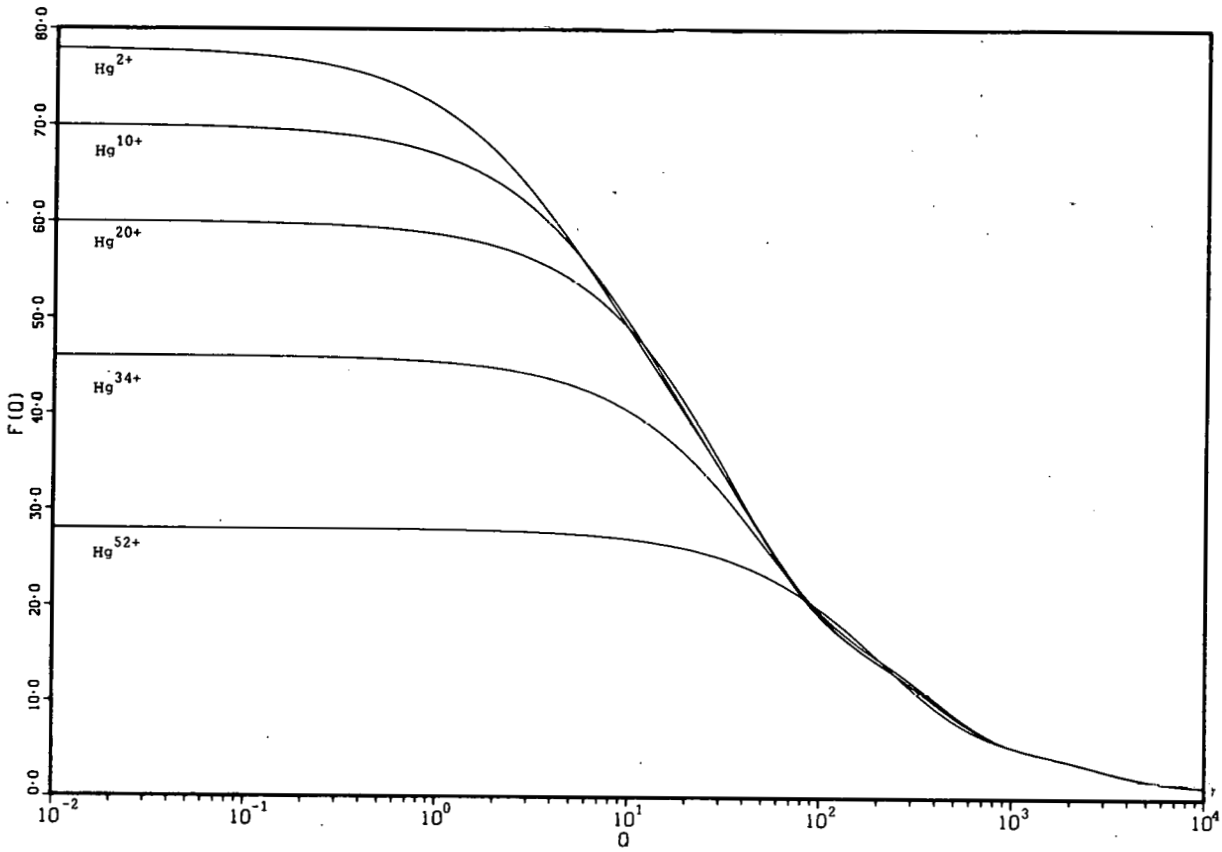

FIG. 1.--Atomic form factors of Hg ions. $Q = (Ka_0)^2$.

In Figure 1, curves for different net charges all merge to a common curve (within some tolerance) as Q increases. The values of F(K) for large K are basically determined from the charge distribution of core electrons, and the existence of the common curve is a clear indication that the core charge distribution is not affected much by the presence (or absence) of the outer electrons.

No such common trait is observed in $S_{inc}(Q)$ (Figure 2), because $S_{inc}(Q)$ is sensitive to outer charge distribution, i.e., large $\vec{r}_i - \vec{r}_j$ (see Eq. 2), for small Q, and, as noted earlier, approaching unity for large Q. In both ranges of Q, the ions have little in common.

For large values of Ka_0 (> 30) F(K) requires closely tabulated wavefunctions to avoid numerical cancellations from rapidly oscillating integrands (see Eq. 1). Some of the existing tables of F(K) for neutral atoms suffer from this defect.[5] We interpolated wavefunctions to insure four significant figures for Tables 1–7.

TABLE 1 COHERENT AND INCOHERENT ATOMIC FORM FACTORS FOR XE + & XE 2+

	XE +		XE 2+	
Q	F(Q)	SINC(Q)	F(Q)	SINC(Q)
0.0	5.300D+01	0.0	5.200D+01	0.0
0.01	5.292D+01	9.493D-02	5.193D+01	7.933D-02
0.02	5.283D+01	1.887D-01	5.186D+01	1.579D-01
0.03	5.275D+01	2.812D-01	5.179D+01	2.356D-01
0.04	5.266D+01	3.726D-01	5.172D+01	3.126D-01
0.05	5.258D+01	4.628D-01	5.164D+01	3.888D-01
0.06	5.250D+01	5.520D-01	5.157D+01	4.642D-01
0.07	5.242D+01	6.400D-01	5.151D+01	5.389D-01
0.08	5.233D+01	7.270D-01	5.144D+01	6.129D-01
0.09	5.225D+01	8.129D-01	5.137D+01	6.862D-01
0.10	5.217D+01	8.978D-01	5.130D+01	7.587D-01
0.20	5.139D+01	1.694D+00	5.063D+01	1.448D+00
0.30	5.065D+01	2.406D+00	4.999D+01	2.077D+00
0.40	4.995D+01	3.049D+00	4.938D+01	2.654D+00
0.50	4.929D+01	3.633D+00	4.880D+01	3.186D+00
0.60	4.866D+01	4.169D+00	4.824D+01	3.680D+00
0.70	4.806D+01	4.662D+00	4.770D+01	4.140D+00
0.80	4.749D+01	5.121D+00	4.719D+01	4.570D+00
0.90	4.695D+01	5.550D+00	4.669D+01	4.974D+00
1.00	4.643D+01	5.952D+00	4.622D+01	5.354D+00
2.00	4.231D+01	9.062D+00	4.234D+01	8.307D+00
3.00	3.944D+01	1.124D+01	3.952D+01	1.037D+01
4.00	3.727D+01	1.288D+01	3.735D+01	1.195D+01
5.00	3.552D+01	1.419D+01	3.558D+01	1.322D+01
6.00	3.405D+01	1.526D+01	3.408D+01	1.428D+01
7.00	3.277D+01	1.619D+01	3.279D+01	1.520D+01
8.00	3.163D+01	1.701D+01	3.164D+01	1.602D+01
9.00	3.060D+01	1.775D+01	3.060D+01	1.676D+01
10.00	2.967D+01	1.843D+01	2.966D+01	1.744D+01
20.00	2.344D+01	2.350D+01	2.343D+01	2.251D+01
30.00	2.019D+01	2.694D+01	2.018D+01	2.594D+01
40.00	1.822D+01	2.944D+01	1.822D+01	2.844D+01
50.00	1.685D+01	3.131D+01	1.685D+01	3.031D+01
60.00	1.575D+01	3.275D+01	1.575D+01	3.175D+01
70.00	1.481D+01	3.391D+01	1.481D+01	3.291D+01
80.00	1.396D+01	3.487D+01	1.396D+01	3.387D+01
90.00	1.318D+01	3.570D+01	1.318D+01	3.470D+01

TABLE 1 CONTINUED

	XE +		XE 2+	
Q	F(Q)	SINC(Q)	F(Q)	SINC(Q)
100.00	1.246D+01	3.642D+01	1.246D+01	3.542D+01
200.00	7.831D+00	4.101D+01	7.831D+00	4.001D+01
300.00	6.021D+00	4.348D+01	6.022D+00	4.248D+01
400.00	5.218D+00	4.509D+01	5.218D+00	4.409D+01
500.00	4.732D+00	4.623D+01	4.732D+00	4.523D+01
600.00	4.352D+00	4.710D+01	4.351D+00	4.610D+01
700.00	4.015D+00	4.779D+01	4.015D+00	4.679D+01
800.00	3.708D+00	4.834D+01	3.707D+00	4.734D+01
900.00	3.427D+00	4.879D+01	3.427D+00	4.779D+01
1000.00	3.174D+00	4.916D+01	3.173D+00	4.816D+01
2000.00	1.774D+00	5.095D+01	1.774D+00	4.995D+01
3000.00	1.339D+00	5.157D+01	1.339D+00	5.057D+01
4000.00	1.154D+00	5.192D+01	1.154D+00	5.092D+01
5000.00	1.040D+00	5.215D+01	1.040D+00	5.115D+01
6000.00	9.518D-01	5.232D+01	9.518D-01	5.132D+01
7000.00	8.762D-01	5.245D+01	8.762D-01	5.145D+01
8000.00	8.091D-01	5.255D+01	8.092D-01	5.155D+01
9000.00	7.489D-01	5.263D+01	7.490D-01	5.163D+01
10000.00	6.947D-01	5.269D+01	6.948D-01	5.169D+01

TABLE 2 COHERENT AND INCOHERENT ATOMIC FORM FACTORS FOR XE 3+ & XE 4+

	XE 3+		XE 4+	
Q	F(Q)	SINC(Q)	F(Q)	SINC(Q)
0.0	5.100D+01	0.0	5.000D+01	0.0
0.01	5.094D+01	6.722D-02	4.995D+01	5.739D-02
0.02	5.088D+01	1.339D-01	4.990D+01	1.144D-01
0.03	5.082D+01	2.000D-01	4.985D+01	1.711D-01
0.04	5.076D+01	2.656D-01	4.980D+01	2.274D-01
0.05	5.070D+01	3.307D-01	4.975D+01	2.833D-01
0.06	5.064D+01	3.953D-01	4.969D+01	3.389D-01
0.07	5.058D+01	4.594D-01	4.964D+01	3.941D-01
0.08	5.052D+01	5.229D-01	4.959D+01	4.490D-01
0.09	5.046D+01	5.860D-01	4.954D+01	5.035D-01
0.10	5.040D+01	6.485D-01	4.949D+01	5.577D-01
0.20	4.983D+01	1.248D+00	4.901D+01	1.081D+00
0.30	4.928D+01	1.805D+00	4.853D+01	1.574D+00
0.40	4.875D+01	2.323D+00	4.807D+01	2.038D+00
0.50	4.824D+01	2.806D+00	4.763D+01	2.475D+00
0.60	4.774D+01	3.259D+00	4.719D+01	2.889D+00
0.70	4.727D+01	3.684D+00	4.677D+01	3.280D+00
0.80	4.681D+01	4.084D+00	4.637D+01	3.651D+00
0.90	4.636D+01	4.463D+00	4.597D+01	4.003D+00
1.00	4.593D+01	4.821D+00	4.559D+01	4.338D+00
2.00	4.232D+01	7.614D+00	4.226D+01	6.974D+00
3.00	3.959D+01	9.562D+00	3.964D+01	8.807D+00
4.00	3.743D+01	1.106D+01	3.751D+01	1.022D+01
5.00	3.565D+01	1.228D+01	3.573D+01	1.138D+01
6.00	3.414D+01	1.332D+01	3.421D+01	1.239D+01
7.00	3.282D+01	1.423D+01	3.287D+01	1.328D+01
8.00	3.166D+01	1.505D+01	3.169D+01	1.408D+01
9.00	3.061D+01	1.579D+01	3.063D+01	1.482D+01
10.00	2.966D+01	1.647D+01	2.967D+01	1.550D+01
20.00	2.342D+01	2.153D+01	2.340D+01	2.055D+01
30.00	2.018D+01	2.495D+01	2.018D+01	2.396D+01
40.00	1.823D+01	2.745D+01	1.823D+01	2.645D+01
50.00	1.685D+01	2.932D+01	1.685D+01	2.832D+01
60.00	1.576D+01	3.076D+01	1.576D+01	2.976D+01
70.00	1.481D+01	3.191D+01	1.481D+01	3.092D+01
80.00	1.396D+01	3.288D+01	1.396D+01	3.188D+01
90.00	1.318D+01	3.370D+01	1.318D+01	3.270D+01

TABLE 2 CONTINUED

Q	XE 3+		XE 4+	
	F(Q)	SINC(Q)	F(Q)	SINC(Q)
100.00	1.246D+01	3.443D+01	1.246D+01	3.343D+01
200.00	7.831D+00	3.901D+01	7.830D+00	3.801D+01
300.00	6.022D+00	4.148D+01	6.022D+00	4.049D+01
400.00	5.218D+00	4.309D+01	5.218D+00	4.209D+01
500.00	4.732D+00	4.423D+01	4.732D+00	4.323D+01
600.00	4.351D+00	4.510D+01	4.350D+00	4.410D+01
700.00	4.014D+00	4.579D+01	4.013D+00	4.479D+01
800.00	3.707D+00	4.634D+01	3.706D+00	4.534D+01
900.00	3.426D+00	4.679D+01	3.426D+00	4.579D+01
1000.00	3.173D+00	4.716D+01	3.172D+00	4.616D+01
2000.00	1.774D+00	4.895D+01	1.773D+00	4.795D+01
3000.00	1.339D+00	4.957D+01	1.339D+00	4.857D+01
4000.00	1.154D+00	4.992D+01	1.154D+00	4.892D+01
5000.00	1.040D+00	5.015D+01	1.040D+00	4.915D+01
6000.00	9.519D-01	5.032D+01	9.520D-01	4.932D+01
7000.00	8.763D-01	5.045D+01	8.763D-01	4.945D+01
8000.00	8.092D-01	5.055D+01	8.093D-01	4.955D+01
9000.00	7.490D-01	5.063D+01	7.491D-01	4.963D+01
10000.00	6.948D-01	5.069D+01	6.949D-01	4.969D+01

TABLE 3 COHERENT AND INCOHERENT ATOMIC FORM FACTORS FOR XE 5+ & XE 6+

	XE 5+		XE 6+	
Q	F(Q)	SINC(Q)	F(Q)	SINC(Q)
0.0	4.900D+01	0.0	4.800D+01	0.0
0.01	4.896D+01	4.983D-02	4.796D+01	4.343D-02
0.02	4.891D+01	9.936D-02	4.793D+01	8.661D-02
0.03	4.887D+01	1.486D-01	4.789D+01	1.295D-01
0.04	4.883D+01	1.975D-01	4.786D+01	1.722D-01
0.05	4.878D+01	2.462D-01	4.782D+01	2.147D-01
0.06	4.874D+01	2.946D-01	4.778D+01	2.569D-01
0.07	4.870D+01	3.426D-01	4.775D+01	2.988D-01
0.08	4.866D+01	3.904D-01	4.771D+01	3.406D-01
0.09	4.861D+01	4.379D-01	4.768D+01	3.821D-01
0.10	4.857D+01	4.852D-01	4.764D+01	4.233D-01
0.20	4.816D+01	9.427D-01	4.729D+01	8.234D-01
0.30	4.775D+01	1.375D+00	4.694D+01	1.202D+00
0.40	4.735D+01	1.783D+00	4.661D+01	1.561D+00
0.50	4.697D+01	2.170D+00	4.627D+01	1.901D+00
0.60	4.659D+01	2.536D+00	4.595D+01	2.225D+00
0.70	4.622D+01	2.885D+00	4.563D+01	2.533D+00
0.80	4.586D+01	3.216D+00	4.532D+01	2.826D+00
0.90	4.551D+01	3.531D+00	4.501D+01	3.106D+00
1.00	4.517D+01	3.831D+00	4.471D+01	3.373D+00
2.00	4.213D+01	6.231D+00	4.196D+01	5.533D+00
3.00	3.966D+01	7.943D+00	3.964D+01	7.112D+00
4.00	3.759D+01	9.292D+00	3.764D+01	8.389D+00
5.00	3.582D+01	1.043D+01	3.591D+01	9.487D+00
6.00	3.429D+01	1.142D+01	3.438D+01	1.046D+01
7.00	3.294D+01	1.231D+01	3.302D+01	1.135D+01
8.00	3.174D+01	1.312D+01	3.181D+01	1.215D+01
9.00	3.067D+01	1.386D+01	3.072D+01	1.290D+01
10.00	2.969D+01	1.454D+01	2.973D+01	1.358D+01
20.00	2.338D+01	1.957D+01	2.335D+01	1.860D+01
30.00	2.017D+01	2.297D+01	2.015D+01	2.198D+01
40.00	1.823D+01	2.546D+01	1.822D+01	2.447D+01
50.00	1.686D+01	2.733D+01	1.686D+01	2.634D+01
60.00	1.576D+01	2.877D+01	1.577D+01	2.778D+01
70.00	1.482D+01	2.992D+01	1.482D+01	2.893D+01
80.00	1.396D+01	3.088D+01	1.397D+01	2.989D+01
90.00	1.318D+01	3.171D+01	1.318D+01	3.071D+01

TABLE 3 CONTINUED

Q	XE 5+ F(Q)	XE 5+ SINC(Q)	XE 6+ F(Q)	XE 6+ SINC(Q)
100.00	1.246D+01	3.243D+01	1.246D+01	3.144D+01
200.00	7.829D+00	3.701D+01	7.828D+00	3.602D+01
300.00	6.022D+00	3.949D+01	6.022D+00	3.849D+01
400.00	5.218D+00	4.109D+01	5.218D+00	4.009D+01
500.00	4.731D+00	4.223D+01	4.731D+00	4.124D+01
600.00	4.350D+00	4.310D+01	4.349D+00	4.210D+01
700.00	4.013D+00	4.379D+01	4.012D+00	4.279D+01
800.00	3.705D+00	4.434D+01	3.704D+00	4.334D+01
900.00	3.425D+00	4.479D+01	3.424D+00	4.379D+01
1000.00	3.171D+00	4.516D+01	3.170D+00	4.416D+01
2000.00	1.773D+00	4.695D+01	1.772D+00	4.595D+01
3000.00	1.339D+00	4.757D+01	1.339D+00	4.657D+01
4000.00	1.154D+00	4.792D+01	1.154D+00	4.692D+01
5000.00	1.040D+00	4.815D+01	1.040D+00	4.715D+01
6000.00	9.520D-01	4.832D+01	9.521D-01	4.732D+01
7000.00	8.764D-01	4.845D+01	8.765D-01	4.745D+01
8000.00	8.093D-01	4.855D+01	8.094D-01	4.755D+01
9000.00	7.491D-01	4.863D+01	7.492D-01	4.763D+01
10000.00	6.949D-01	4.869D+01	6.950D-01	4.769D+01

TABLE 4 COHERENT AND INCOHERENT ATOMIC FORM FACTORS FOR HG 2+ & HG 5+

	HG 2+		HG 5+	
Q	F(Q)	SINC(Q)	F(Q)	SINC(Q)
0.0	7.800D+01	0.0	7.500D+01	0.0
0.01	7.793D+01	7.489D-02	7.495D+01	5.006D-02
0.02	7.786D+01	1.492D-01	7.490D+01	9.989D-02
0.03	7.779D+01	2.230D-01	7.485D+01	1.495D-01
0.04	7.772D+01	2.963D-01	7.480D+01	1.989D-01
0.05	7.766D+01	3.691D-01	7.475D+01	2.480D-01
0.06	7.759D+01	4.414D-01	7.470D+01	2.970D-01
0.07	7.752D+01	5.131D-01	7.465D+01	3.457D-01
0.08	7.745D+01	5.843D-01	7.460D+01	3.942D-01
0.09	7.739D+01	6.551D-01	7.455D+01	4.425D-01
0.10	7.732D+01	7.253D-01	7.450D+01	4.906D-01
0.20	7.665D+01	1.402D+00	7.400D+01	9.598D-01
0.30	7.601D+01	2.034D+00	7.351D+01	1.409D+00
0.40	7.538D+01	2.625D+00	7.304D+01	1.840D+00
0.50	7.477D+01	3.180D+00	7.257D+01	2.253D+00
0.60	7.418D+01	3.702D+00	7.211D+01	2.649D+00
0.70	7.360D+01	4.194D+00	7.165D+01	3.030D+00
0.80	7.303D+01	4.658D+00	7.121D+01	3.397D+00
0.90	7.248D+01	5.097D+00	7.077D+01	3.750D+00
1.00	7.194D+01	5.513D+00	7.035D+01	4.090D+00
2.00	6.722D+01	8.776D+00	6.644D+01	6.938D+00
3.00	6.343D+01	1.109D+01	6.312D+01	9.104D+00
4.00	6.031D+01	1.296D+01	6.027D+01	1.088D+01
5.00	5.768D+01	1.457D+01	5.779D+01	1.240D+01
6.00	5.543D+01	1.601D+01	5.562D+01	1.376D+01
7.00	5.348D+01	1.733D+01	5.370D+01	1.500D+01
8.00	5.176D+01	1.855D+01	5.199D+01	1.615D+01
9.00	5.023D+01	1.968D+01	5.046D+01	1.721D+01
10.00	4.886D+01	2.074D+01	4.907D+01	1.821D+01
20.00	3.978D+01	2.831D+01	3.981D+01	2.547D+01
30.00	3.439D+01	3.279D+01	3.436D+01	2.986D+01
40.00	3.049D+01	3.590D+01	3.045D+01	3.294D+01
50.00	2.747D+01	3.834D+01	2.744D+01	3.536D+01
60.00	2.507D+01	4.038D+01	2.505D+01	3.739D+01
70.00	2.313D+01	4.215D+01	2.313D+01	3.915D+01
80.00	2.157D+01	4.371D+01	2.157D+01	4.071D+01
90.00	2.029D+01	4.511D+01	2.029D+01	4.212D+01

TABLE 4 CONTINUED

	HG 2+		HG 5+	
Q	F(Q)	SINC(Q)	F(Q)	SINC(Q)
100.00	1.923D+01	4.639D+01	1.924D+01	4.339D+01
200.00	1.423D+01	5.499D+01	1.423D+01	5.200D+01
300.00	1.186D+01	5.951D+01	1.186D+01	5.651D+01
400.00	1.001D+01	6.225D+01	1.001D+01	5.925D+01
500.00	8.571D+00	6.414D+01	8.569D+00	6.114D+01
600.00	7.488D+00	6.557D+01	7.486D+00	6.257D+01
700.00	6.693D+00	6.670D+01	6.692D+00	6.370D+01
800.00	6.112D+00	6.764D+01	6.111D+00	6.464D+01
900.00	5.682D+00	6.843D+01	5.682D+00	6.543D+01
1000.00	5.356D+00	6.911D+01	5.357D+00	6.611D+01
2000.00	3.840D+00	7.286D+01	3.842D+00	6.986D+01
3000.00	2.930D+00	7.446D+01	2.931D+00	7.146D+01
4000.00	2.316D+00	7.531D+01	2.317D+00	7.231D+01
5000.00	1.925D+00	7.582D+01	1.925D+00	7.282D+01
6000.00	1.673D+00	7.616D+01	1.673D+00	7.316D+01
7000.00	1.506D+00	7.640D+01	1.506D+00	7.340D+01
8000.00	1.389D+00	7.659D+01	1.389D+00	7.359D+01
9000.00	1.302D+00	7.674D+01	1.302D+00	7.374D+01
10000.00	1.235D+00	7.686D+01	1.235D+00	7.386D+01

TABLE 5 COHERENT AND INCOHERENT ATOMIC FORM FACTORS FOR HG 10+ & HG 20+

	HG 10+		HG 20+	
Q	F(Q)	SINC(Q)	F(Q)	SINC(Q)
0.0	7.000D+01	0.0	6.000D+01	0.0
0.01	6.997D+01	3.004D-02	5.999D+01	9.834D-03
0.02	6.994D+01	6.000D-02	5.997D+01	1.965D-02
0.03	6.990D+01	8.988D-02	5.996D+01	2.947D-02
0.04	6.987D+01	1.197D-01	5.995D+01	3.928D-02
0.05	6.984D+01	1.494D-01	5.993D+01	4.908D-02
0.06	6.981D+01	1.791D-01	5.992D+01	5.888D-02
0.07	6.978D+01	2.087D-01	5.991D+01	6.867D-02
0.08	6.974D+01	2.382D-01	5.990D+01	7.845D-02
0.09	6.971D+01	2.676D-01	5.988D+01	8.823D-02
0.10	6.968D+01	2.970D-01	5.987D+01	9.801D-02
0.20	6.936D+01	5.867D-01	5.974D+01	1.954D-01
0.30	6.905D+01	8.695D-01	5.961D+01	2.923D-01
0.40	6.874D+01	1.146D+00	5.948D+01	3.886D-01
0.50	6.843D+01	1.415D+00	5.935D+01	4.844D-01
0.60	6.813D+01	1.679D+00	5.922D+01	5.797D-01
0.70	6.783D+01	1.936D+00	5.910D+01	6.743D-01
0.80	6.753D+01	2.188D+00	5.897D+01	7.685D-01
0.90	6.724D+01	2.434D+00	5.884D+01	8.621D-01
1.00	6.695D+01	2.675D+00	5.871D+01	9.552D-01
2.00	6.420D+01	4.826D+00	5.747D+01	1.858D+00
3.00	6.172D+01	6.611D+00	5.627D+01	2.713D+00
4.00	5.947D+01	8.138D+00	5.511D+01	3.525D+00
5.00	5.742D+01	9.476D+00	5.399D+01	4.295D+00
6.00	5.556D+01	1.067D+01	5.290D+01	5.028D+00
7.00	5.385D+01	1.176D+01	5.186D+01	5.726D+00
8.00	5.227D+01	1.277D+01	5.084D+01	6.393D+00
9.00	5.082D+01	1.370D+01	4.986D+01	7.029D+00
10.00	4.948D+01	1.457D+01	4.891D+01	7.638D+00
20.00	4.001D+01	2.108D+01	4.090D+01	1.257D+01
30.00	3.433D+01	2.518D+01	3.503D+01	1.612D+01
40.00	3.036D+01	2.813D+01	3.065D+01	1.889D+01
50.00	2.735D+01	3.049D+01	2.734D+01	2.116D+01
60.00	2.499D+01	3.248D+01	2.480D+01	2.309D+01
70.00	2.309D+01	3.422D+01	2.283D+01	2.477D+01
80.00	2.155D+01	3.577D+01	2.128D+01	2.627D+01
90.00	2.029D+01	3.716D+01	2.004D+01	2.763D+01

TABLE 5 CONTINUED

Q	HG 10+ F(Q)	HG 10+ SINC(Q)	HG 20+ F(Q)	HG 20+ SINC(Q)
100.00	1.925D+01	3.843D+01	1.904D+01	2.886D+01
200.00	1.423D+01	4.702D+01	1.425D+01	3.717D+01
300.00	1.184D+01	5.152D+01	1.181D+01	4.159D+01
400.00	9.997D+00	5.425D+01	9.930D+00	4.431D+01
500.00	8.557D+00	5.614D+01	8.493D+00	4.620D+01
600.00	7.478D+00	5.757D+01	7.431D+00	4.763D+01
700.00	6.686D+00	5.871D+01	6.658D+00	4.877D+01
800.00	6.108D+00	5.965D+01	6.093D+00	4.970D+01
900.00	5.680D+00	6.044D+01	5.675D+00	5.049D+01
1000.00	5.356D+00	6.112D+01	5.356D+00	5.116D+01
2000.00	3.846D+00	6.487D+01	3.834D+00	5.489D+01
3000.00	2.934D+00	6.646D+01	2.919D+00	5.648D+01
4000.00	2.319D+00	6.731D+01	2.308D+00	5.732D+01
5000.00	1.926D+00	6.782D+01	1.919D+00	5.783D+01
6000.00	1.674D+00	6.816D+01	1.670D+00	5.817D+01
7000.00	1.506D+00	6.840D+01	1.504D+00	5.841D+01
8000.00	1.389D+00	6.859D+01	1.388D+00	5.859D+01
9000.00	1.302D+00	6.874D+01	1.302D+00	5.874D+01
10000.00	1.235D+00	6.886D+01	1.234D+00	5.887D+01

TABLE 6 COHERENT AND INCOHERENT ATOMIC FORM FACTORS FOR HG 34+ & HG 52+

	HG 34+		HG 52+	
Q	F(Q)	SINC(Q)	F(Q)	SINC(Q)
0.0	4.600D+01	0.0	2.800D+01	0.0
0.01	4.599D+01	5.164D-03	2.800D+01	8.763D-04
0.02	4.599D+01	1.032D-02	2.800D+01	1.743D-03
0.03	4.598D+01	1.547D-02	2.800D+01	2.610D-03
0.04	4.597D+01	2.062D-02	2.800D+01	3.477D-03
0.05	4.597D+01	2.576D-02	2.799D+01	4.344D-03
0.06	4.596D+01	3.091D-02	2.799D+01	5.210D-03
0.07	4.596D+01	3.605D-02	2.799D+01	6.077D-03
0.08	4.595D+01	4.119D-02	2.799D+01	6.944D-03
0.09	4.594D+01	4.633D-02	2.799D+01	7.810D-03
0.10	4.594D+01	5.147D-02	2.799D+01	8.677D-03
0.20	4.587D+01	1.027D-01	2.798D+01	1.734D-02
0.30	4.581D+01	1.538D-01	2.797D+01	2.599D-02
0.40	4.575D+01	2.047D-01	2.796D+01	3.465D-02
0.50	4.569D+01	2.554D-01	2.795D+01	4.329D-02
0.60	4.562D+01	3.060D-01	2.794D+01	5.193D-02
0.70	4.556D+01	3.563D-01	2.793D+01	6.056D-02
0.80	4.550D+01	4.065D-01	2.792D+01	6.919D-02
0.90	4.544D+01	4.565D-01	2.791D+01	7.782D-02
1.00	4.537D+01	5.063D-01	2.790D+01	8.643D-02
2.00	4.476D+01	9.945D-01	2.779D+01	1.723D-01
3.00	4.416D+01	1.466D+00	2.769D+01	2.576D-01
4.00	4.358D+01	1.921D+00	2.759D+01	3.424D-01
5.00	4.300D+01	2.360D+00	2.749D+01	4.267D-01
6.00	4.244D+01	2.785D+00	2.739D+01	5.104D-01
7.00	4.189D+01	3.195D+00	2.728D+01	5.936D-01
8.00	4.136D+01	3.593D+00	2.718D+01	6.762D-01
9.00	4.083D+01	3.977D+00	2.708D+01	7.584D-01
10.00	4.032D+01	4.350D+00	2.699D+01	8.400D-01
20.00	3.574D+01	7.523D+00	2.602D+01	1.629D+00
30.00	3.204D+01	9.964D+00	2.510D+01	2.370D+00
40.00	2.904D+01	1.193D+01	2.423D+01	3.068D+00
50.00	2.660D+01	1.359D+01	2.339D+01	3.726D+00
60.00	2.460D+01	1.502D+01	2.260D+01	4.347D+00
70.00	2.295D+01	1.629D+01	2.184D+01	4.933D+00
80.00	2.159D+01	1.743D+01	2.112D+01	5.488D+00
90.00	2.045D+01	1.846D+01	2.044D+01	6.013D+00

TABLE 6 CONTINUED

	HG 34+		HG 52+	
Q	F(Q)	SINC(Q)	F(Q)	SINC(Q)
100.00	1.950D+01	1.940D+01	1.978D+01	6.511D+00
200.00	1.462D+01	2.571D+01	1.469D+01	1.035D+01
300.00	1.217D+01	2.904D+01	1.147D+01	1.285D+01
400.00	1.026D+01	3.117D+01	9.399D+00	1.464D+01
500.00	8.748D+00	3.273D+01	8.031D+00	1.599D+01
600.00	7.609D+00	3.396D+01	7.105D+00	1.707D+01
700.00	6.768D+00	3.496D+01	6.459D+00	1.795D+01
800.00	6.153D+00	3.581D+01	5.991D+00	1.870D+01
900.00	5.699D+00	3.653D+01	5.639D+00	1.934D+01
1000.00	5.357D+00	3.716D+01	5.361D+00	1.990D+01
2000.00	3.828D+00	4.081D+01	3.814D+00	2.317D+01
3000.00	2.928D+00	4.243D+01	2.871D+00	2.463D+01
4000.00	2.317D+00	4.329D+01	2.269D+00	2.542D+01
5000.00	1.926D+00	4.381D+01	1.893D+00	2.589D+01
6000.00	1.674D+00	4.415D+01	1.654D+00	2.621D+01
7000.00	1.506D+00	4.440D+01	1.494D+00	2.644D+01
8000.00	1.389D+00	4.459D+01	1.381D+00	2.662D+01
9000.00	1.303D+00	4.474D+01	1.298D+00	2.676D+01
10000.00	1.235D+00	4.486D+01	1.232D+00	2.688D+01

TABLE 7 COHERENT AND INCOHERENT ATOMIC FORM FACTORS FOR U + & U 6+

	U +		U 6+	
Q	F(Q)	SINC(Q)	F(Q)	SINC(Q)
0.0	9.100D+01	0.0	8.600D+01	0.0
0.01	9.086D+01	1.947D-01	8.593D+01	6.570D-02
0.02	9.071D+01	3.834D-01	8.587D+01	1.310D-01
0.03	9.057D+01	5.664D-01	8.580D+01	1.960D-01
0.04	9.044D+01	7.440D-01	8.573D+01	2.605D-01
0.05	9.030D+01	9.163D-01	8.566D+01	3.247D-01
0.06	9.016D+01	1.084D+00	8.560D+01	3.885D-01
0.07	9.003D+01	1.246D+00	8.553D+01	4.519D-01
0.08	8.990D+01	1.404D+00	8.547D+01	5.150D-01
0.09	8.977D+01	1.558D+00	8.540D+01	5.777D-01
0.10	8.964D+01	1.707D+00	8.533D+01	6.400D-01
0.20	8.841D+01	3.010D+00	8.468D+01	1.244D+00
0.30	8.730D+01	4.051D+00	8.405D+01	1.816D+00
0.40	8.629D+01	4.919D+00	8.343D+01	2.357D+00
0.50	8.535D+01	5.669D+00	8.283D+01	2.872D+00
0.60	8.448D+01	6.335D+00	8.224D+01	3.361D+00
0.70	8.367D+01	6.938D+00	8.166D+01	3.828D+00
0.80	8.291D+01	7.493D+00	8.110D+01	4.274D+00
0.90	8.219D+01	8.008D+00	8.056D+01	4.701D+00
1.00	8.150D+01	8.491D+00	8.002D+01	5.110D+00
2.00	7.600D+01	1.220D+01	7.529D+01	8.485D+00
3.00	7.190D+01	1.484D+01	7.148D+01	1.105D+01
4.00	6.862D+01	1.700D+01	6.834D+01	1.315D+01
5.00	6.589D+01	1.884D+01	6.571D+01	1.493D+01
6.00	6.357D+01	2.042D+01	6.345D+01	1.646D+01
7.00	6.156D+01	2.181D+01	6.149D+01	1.780D+01
8.00	5.979D+01	2.304D+01	5.976D+01	1.897D+01
9.00	5.820D+01	2.415D+01	5.821D+01	2.003D+01
10.00	5.677D+01	2.516D+01	5.681D+01	2.098D+01
20.00	4.694D+01	3.259D+01	4.709D+01	2.799D+01
30.00	4.102D+01	3.760D+01	4.109D+01	3.286D+01
40.00	3.688D+01	4.137D+01	3.687D+01	3.654D+01
50.00	3.374D+01	4.432D+01	3.369D+01	3.942D+01
60.00	3.121D+01	4.668D+01	3.114D+01	4.174D+01
70.00	2.909D+01	4.861D+01	2.903D+01	4.364D+01
80.00	2.727D+01	5.024D+01	2.722D+01	4.526D+01
90.00	2.568D+01	5.165D+01	2.565D+01	4.666D+01

TABLE 7 CONTINUED

Q	U +		U 6+	
	F(Q)	SINC(Q)	F(Q)	SINC(Q)
100.00	2.429D+01	5.292D+01	2.427D+01	4.792D+01
200.00	1.662D+01	6.160D+01	1.663D+01	5.661D+01
300.00	1.386D+01	6.694D+01	1.386D+01	6.195D+01
400.00	1.226D+01	7.053D+01	1.227D+01	6.554D+01
500.00	1.098D+01	7.304D+01	1.099D+01	6.805D+01
600.00	9.855D+00	7.488D+01	9.866D+00	6.989D+01
700.00	8.887D+00	7.631D+01	8.896D+00	7.132D+01
800.00	8.069D+00	7.747D+01	8.077D+00	7.247D+01
900.00	7.394D+00	7.843D+01	7.401D+00	7.343D+01
1000.00	6.844D+00	7.926D+01	6.849D+00	7.426D+01
2000.00	4.623D+00	8.390D+01	4.623D+00	7.890D+01
3000.00	3.820D+00	8.596D+01	3.820D+00	8.095D+01
4000.00	3.191D+00	8.712D+01	3.192D+00	8.212D+01
5000.00	2.699D+00	8.787D+01	2.700D+00	8.286D+01
6000.00	2.330D+00	8.837D+01	2.331D+00	8.337D+01
7000.00	2.058D+00	8.873D+01	2.059D+00	8.373D+01
8000.00	1.858D+00	8.900D+01	1.859D+00	8.400D+01
9000.00	1.709D+00	8.920D+01	1.709D+00	8.420D+01
10000.00	1.593D+00	8.937D+01	1.594D+00	8.437D+01

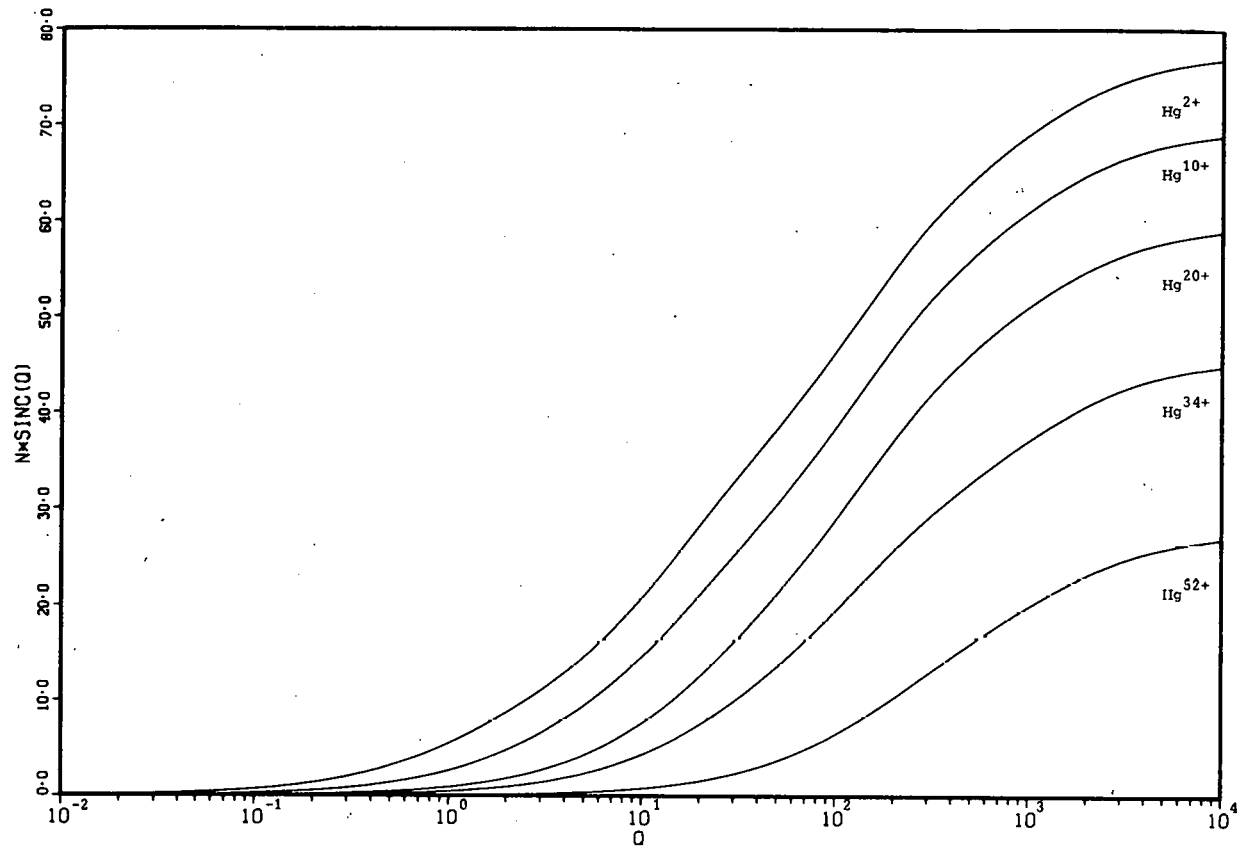

FIG. 2.--Incoherent scattering functions of Hg ions. $Q = (Ka_0)^2$, N = number of bound electrons.

For small Q, F(Q) and $S_{inc}(Q)$ can be expanded in powers of Q. The coefficients are expressed in terms of various powers of r of the atomic electrons. Table 8 lists the power series expansion coefficients for small Q:

$$F(Q) = N + \sum_{i=1}^{3} A_i Q^i \tag{3}$$

$$S_{inc}(Q) = \sum_{i=1}^{3} B_i Q^i . \tag{4}$$

Table 8. Power Series Expansion Coefficients for F(Q) and $S_{inc}(Q)$ (See Eqs. 3 and 4)

Ions	N	F(Q) A_1	A_2	A_3	$S_{inc}(Q)$ B_1	B_2	B_3
Xe^{+}	53	-8.516	2.498	-0.6864	9.554	-6.145	4.022
Xe^{2+}	52	-7.186	1.728	-0.3869	7.974	-4.068	2.124
Xe^{3+}	51	-6.080	1.209	-0.2260	6.749	-2.752	1.126
Xe^{4+}	50	-5.133	0.8346	-0.1304	5.757	-1.859	0.5539
Xe^{5+}	49	-4.333	0.5684	-0.07347	4.998	-1.503	0.4131
Xe^{6+}	48	-3.625	0.3649	-0.03648	4.356	-1.257	0.3332
Hg^{2+}	78	-6.919	0.9871	-0.1422	7.515	-2.705	0.9011
Hg^{5+}	75	-5.094	0.4778	-0.04124	5.017	-1.137	0.2491
Hg^{10+}	70	-3.221	0.1764	-0.008519	3.007	-0.3753	0.04735
Hg^{20+}	60	-1.308	0.02256	-3.055×10^{-4}	0.9828	-0.02839	8.214×10^{-4}
Hg^{34+}	46	-0.6325	0.006933	-5.374×10^{-5}	0.5156	-0.009462	1.599×10^{-4}
Hg^{52+}	28	-0.1040	2.593×10^{-4}	-4.680×10^{-7}	0.08670	-2.779×10^{-4}	7.703×10^{-7}
U^{+}	91	-14.43	8.516	-5.942	19.78	-31.42	48.86
U^{6+}	86	- 6.752	0.8609	-0.09582	6.590	- 1.961	0.6039

References

1. Proceedings of the Workshop on Heavy-Ion Fusion, Brookhaven National Laboratory, 17–21 October 1977, Brookhaven National Laboratory Report, BNL 50769, p. 43.
2. G. H. Gillespie, Phys. Rev. A 15, 563 (1977).
3. M. Inokuti, Y.-K. Kim, and R. L. Platzman, Phys. Rev. 164, 55 (1967).
4. Y.-K. Kim and M. Inokuti, Phys. Rev. 165, 39 (1968).
5. J. H. Hubbell, W. J. Veigele, E. A. Briggs, R. T. Brown, D. T. Cromer, and R. J. Howerton, J. Phys. Chem. Ref. Data 4, 471 (1975).
6. J. P. Desclaux, Comp. Phys. Commun. 9, 31 (1975).
7. G. H. Gillespie, Y.-K. Kim, and K. T. Cheng, Phys. Rev. A 17, 1284 (1978). also Born cross sections for ion-atom collisions, this report.

RELATIVISTIC FORMULAS FOR MULTIPOLE-TRANSITION PROBABILITIES

K. T. Cheng*

Electromagnetic multipole transitions are discussed in the framework of quantum electrodynamics. Gauge invariance of the transition is discussed, with emphasis on its relation to the nonrelativistic length and velocity form calculations. Relativistic forms of the multipole transition matrix elements are reduced to radial integrals convenient for computation.

We shall consider radiative transitions of an atom or ion from state $|a\rangle$ to $|b\rangle$ by emission of a photon γ from the point of view of the S-matrix theory. Conventions and notations used here are standard (see Appendix I for details).

S-Matrix of Radiative Transitions

In quantum electrodynamics the interaction between the electromagnetic field and the electron-positron field is described by a Hamiltonian density of the form

$$H_{int} = -\frac{1}{c} j_\mu A_\mu \ , \tag{1}$$

where j_μ is the Dirac current density operator

$$j_\mu = i e c \bar{\psi} \gamma_\mu \psi \ , \tag{2}$$

and A_μ is the electromagnetic 4-potential given in Appendix II.

In our present case, the initial state of the whole system is described by $|a\rangle \otimes |0\rangle$, where $|0\rangle$ is the vacuum state of the photon field, and the final state is $|b\rangle \otimes |\gamma \vec{k} \hat{\epsilon}\rangle$. The S-matrix element of transition then becomes

$$S_{a\to b} = -\frac{i}{\hbar} \langle b, \gamma | H_{int} | a \rangle$$

*Postdoctoral Appointee from the University of Notre Dame.

$$= \frac{i}{\hbar c}\int \langle b|j_\mu|a\rangle \langle \gamma|A_\mu|0\rangle d^4x$$

$$= -\frac{e}{\hbar}\sqrt{\frac{2\pi\hbar c^2}{\omega V}}\int \bar{\psi}_b \gamma_\mu \epsilon_\mu e^{-ik_\nu x_\nu} \psi_a d^4x \ , \qquad (3)$$

Here the unperturbed electron states ψ are given by

$$\psi(x) = u(\vec{x})\, e^{-iEt/\hbar} \ , \qquad (4)$$

where $u(\vec{x})$ satisfies the single-particle Dirac equation in an external potential U

$$(c\vec{\alpha}\cdot\vec{p} + \beta mc^2 + U)\, u(\vec{x}) = E\, u(\vec{x}) \ . \qquad (5)$$

As a result, we can factor out the temporal part of $S_{a\to b}$ and Eq. 3 becomes

$$S_{a\to b} = -\frac{e}{\hbar}\sqrt{\frac{2\pi\hbar c^2}{\omega V}}\int u_b^+ \gamma_4\gamma_\mu\epsilon_\mu e^{-i\vec{k}\cdot\vec{x}} u_a d^3x$$

$$\times \int e^{-i(\omega_{ab}-\omega)t} dt \ , \qquad (6)$$

where $\omega_{ab} = (E_a - E_b)/\hbar$, and V is a volume element. Define transition matrix $U_{a\to b}$ as

$$U_{a\to b} = -\sqrt{\frac{2\pi e^2 c^2}{\hbar\omega V}}\int u_b^+ (\vec{A}^*\cdot\vec{\alpha} - \phi^*)\, u_a d^3x \ , \qquad (7)$$

where $\vec{A} = \hat{\epsilon}\, e^{i\vec{k}\cdot\vec{x}}$ and $\phi = \epsilon_0 e^{i\vec{k}\cdot\vec{x}}$ being the vector and scalar potentials, respectively. We then have

$$S_{a\to b} = -2\pi i\, \delta(\omega_{ab}-\omega)\, U_{a\to b} \ . \qquad (8)$$

The probability of transition from $|a\rangle$ to $|b\rangle$ by emission of a photon with wave vector lying between $\vec{k}$ and $\vec{k}+d\vec{k}$ is given by

$$dW_{\vec{k}} = |S_{a\to b}|^2 \times \text{density of photon states}$$

$$= 2\pi\delta(\omega_{ab}-\omega)\,|U_{a\to b}|^2\, \frac{Vk^2 dk d\Omega_{\vec{k}}}{(2\pi)^3} \ , \qquad (9)$$

where we have made the standard replacement: $[2\pi\delta(x)]^2 \to 2\pi\delta(x)$. By virtue

of the relation $|\vec{k}| = \omega/c$ (Appendix II), the probability of transition per unit solid angle is

$$\frac{dW_{\vec{k}}}{d\Omega_{\vec{k}}} = 2\pi |U_{a\to b}|^2 \frac{V\omega_{ab}^2}{(2\pi c)^3} \quad . \tag{10}$$

For simplicity, we write ω for ω_{ab}, and define a dimensionless T matrix as

$$T_{a\to b} = \int u_b^+ (\vec{A}^* \cdot \vec{\alpha} - \phi^*) u_a d^3x \; . \tag{11}$$

Equation 10 then becomes

$$\frac{dW_{\vec{k}}}{d\Omega_{\vec{k}}} = \frac{\alpha\omega}{2\pi} |T_{a\to b}|^2 \quad , \tag{12}$$

where $\alpha = e^2/\hbar c$ is the fine structure constant.

Multipole Expansion of the Electromagnetic Field

The vector and scalar potentials $\vec{A}$ and ϕ can be expanded into multipoles (eigenstates of J^2) in terms of vector spherical harmonics $\vec{Y}^{(\lambda)}_{JM}$ described in Appendix III. Details of this expansion can be found, for example, in Ref. 1. Here we simply state the results

$$\vec{A}(\vec{x}) = \hat{\epsilon}\, e^{i\vec{k}\cdot\vec{x}} = \sum_{JM\lambda} c^{(\lambda)}_{JM}(\hat{k})\, \vec{a}^{(\lambda)}_{JM}(\vec{x}), \qquad \lambda = 0, \pm 1$$

$$\phi(\vec{x}) = \epsilon_0 e^{i\vec{k}\cdot\vec{x}} = i\sum_{JM} c^{(-1)}_{JM}(\hat{k})\, \phi_{JM}(\vec{x}) \; . \tag{13}$$

Here, $c^{(\lambda)}_{JM}$ are the expansion coefficients

$$c^{(\lambda)}_{JM} = 4\pi i^{J-|\lambda|} \vec{Y}^{(\lambda)+}_{JM}(\hat{k}) \cdot \hat{\epsilon} \quad . \tag{14}$$

The scalar multipole fields ϕ_{JM} are given by

$$\phi_{JM} = j_J\left(\frac{\omega r}{c}\right) Y_{JM}(\hat{r}) \; , \tag{15}$$

where j_J is the spherical Bessel function of order J, and Y_{JM} is the spherical harmonic. The three multipole vectors $\vec{a}^{(\lambda)}_{JM}$ correspond to electric, magnetic, and longitudinal types for $\lambda = +1, 0, -1$, respectively. They are, like ϕ_{JM}, spherical tensors of rank J and are given by

$$\text{electric:} \qquad \vec{a}^{(1)}_{JM} = A_J\left(\frac{\omega r}{c}\right)\vec{Y}^{(1)}_{JM}(\hat{r}) + B_J\left(\frac{\omega r}{c}\right)\vec{Y}^{(-1)}_{JM}(\hat{r}) ,$$

$$\text{magnetic:} \qquad \vec{a}^{(0)}_{JM} = j_J\left(\frac{\omega r}{c}\right)\vec{Y}^{(0)}_{JM}(\hat{r}) ,$$

$$\text{longitudinal:} \qquad \vec{a}^{(-1)}_{JM} = B_J\left(\frac{\omega r}{c}\right)\vec{Y}^{(1)}_{JM}(\hat{r}) + C_J\left(\frac{\omega r}{c}\right)\vec{Y}^{(-1)}_{JM}(\hat{r}) , \tag{16}$$

where

$$A_J(x) = j_{J-1}(x) - \frac{J}{x} j_J(x) ,$$

$$B_J(x) = \sqrt{J(J+1)}\, j_J(x)/x ,$$

$$C_J(x) = j_{J-1}(x) - \frac{J+1}{x} j_J(x) . \tag{17}$$

Define multipole transition operators $A^{(\lambda)}_{JM}$ as

$$A^{(\lambda)}_{JM} = \vec{\alpha}\cdot\vec{a}^{(\lambda)}_{JM} , \qquad \lambda = 0, 1$$

$$A^{(-1)}_{JM} = \vec{\alpha}\cdot\vec{a}^{(-1)}_{JM} - i\phi_{JM} . \tag{18}$$

We can then rewrite the T matrix as

$$T_{a\to b} = \sum_{JM\lambda} c^{(\lambda)*}_{JM} M^{(\lambda)}_{JM}(a,b) , \tag{19}$$

where the multipole transition matrix element $M^{(\lambda)}_{JM}$ is

$$M^{(\lambda)}_{JM}(a,b) = \int u^{+}_{b} A^{(\lambda)*}_{JM} u_a \, d^3x . \tag{20}$$

As a result, the total transition probability becomes

$$W_{a\to b} = \frac{\alpha\omega}{2\pi} \sum_{\substack{JM\lambda \\ J'M'\lambda'}} \left[\int d\Omega_{\vec{k}}\, c_{JM}^{(\lambda)*} c_{J'M'}^{(\lambda')}\right] M_{J'M'}^{(\lambda')} M_{JM}^{(\lambda)*} . \tag{21}$$

By summing over the photon polarization $\hat{\epsilon}$ and making use of the orthonormality condition of the vector spherical harmonics (Appendix III) we can show that

$$\int d\Omega_{\vec{k}}\, c_{JM}^{(\lambda)*}\, c_{J'M'}^{(\lambda')} = 16\pi^2 \delta_{JJ'} \delta_{MM'} \delta_{\lambda\lambda'} . \tag{22}$$

Thus, the total transition probability becomes

$$W_{a\to b} = 8\pi\alpha\omega \sum_{JM\lambda} \left| M_{JM}^{(\lambda)}(a,b) \right|^2 . \tag{23}$$

Gauge Invariance of the Transition Matrix

By virtue of gauge invariance of the electromagnetic field, it can be shown that for an electron moving in a local potential,

$$M_{JM}^{(-1)}(a,b) = \langle b \left| \vec{a}_{JM}^{(-1)*} \cdot \vec{\alpha} + i\phi_{JM}^{*} \right| a \rangle \equiv 0 . \tag{24}$$

The proof of this relation can be found in Refs. 1 and 2, and will not be repeated here. Physically this means that there is no contribution from the scalar and longitudinal photons, in accordance with the transverse nature of the electromagnetic field. As a result, we can always make a gauge transformation of the type

$$A_{JM}^{(\lambda)} \to A_{JM}^{(\lambda)} + GA_{JM}^{(-1)} , \tag{25}$$

where G is some constant, without affecting $M_{JM}^{(\lambda)}$ and hence the transition rate. Because of the parity selection rule, however, magnetic multipole transitions are never affected, as $A_{JM}^{(0)}$ and $A_{JM}^{(-1)}$ have different parities (see Appendix III, or for more details, Ref. 1). Electric multipole transition operators $A_{JM}^{(1)}$, on the other hand, will be arbitrary up to a gauge transformation. Among infinitely many gauges suggested in Eq. 25, two are of particular interest:

Coulomb Gauge: $G = 0$

This is also known as the transverse gauge. The multipole transition operator A^{v}_{JM} in this gauge is simply equal to $A^{(1)}_{JM}$. As pointed out in Ref. 2, electric dipole (E1) transitions calculated in this gauge lead to the velocity-form results in the nonrelativistic limit. For convenience, we shall refer to this gauge also as the velocity gauge in the following.

Length Gauge: $G = -\sqrt{(J+1)/J}$

This is equivalent to replacing $A^{(1)}_{JM}$ by

$$A^{\ell}_{JM} = \vec{\alpha} \cdot \vec{a}_{JM} + i b_{JM} , \tag{26}$$

where

$$\vec{a}_{JM} = -j_{j+1}\left(\frac{\omega r}{c}\right) \left[\vec{Y}^{(1)}_{JM}(\hat{r}) - \sqrt{\frac{J+1}{J}}\, \vec{Y}^{(-1)}_{JM}(\hat{r}) \right] ,$$

$$b_{JM} = \sqrt{\frac{J+1}{J}}\; j_J\left(\frac{\omega r}{c}\right) Y_{JM}(\hat{r}) . \tag{27}$$

Nonrelativistically, this leads to the length form calculations for E1 transitions, as can be seen in Appendix V.

Reduction to Radial Integrals

The unperturbed electron wavefunctions $u(\vec{x})$ can be written in terms of 4-component spinors as

$$u_{n\kappa m}(\vec{x}) = \frac{1}{r} \begin{pmatrix} P_{n\kappa}(r)\, \Omega_{\kappa m}(\hat{r}) \\ i\, Q_{n\kappa}(r)\, \Omega_{-\kappa m}(\hat{r}) \end{pmatrix} . \tag{28}$$

Here, n, κ, and m are the principal, angular and magnetic quantum numbers, respectively, P and Q are the large and small components, and Ω's are the spherical spinors

$$\Omega_{\kappa m}(\hat{r}) = \sum_{\mu} C(\ell\, \tfrac{1}{2}\, j;\, m-\mu\mu m)\, Y_{\ell\, m-\mu}\, \chi_{\mu} , \tag{29}$$

with Clebsch-Gordan coefficients $C(\ell\, \frac{1}{2}\, j;\, m-\mu\mu m)$, and Pauli spinors

$$\chi_{\frac{1}{2}} = \begin{pmatrix} 1 \\ 0 \end{pmatrix}, \quad \chi_{-\frac{1}{2}} = \begin{pmatrix} 0 \\ 1 \end{pmatrix} . \tag{30}$$

The total transition rate W is obtained by summing over the final state magnetic quantum numbers m_b, and averaging over the initial state's m_a

$$W_{a\to b} = 8\pi\alpha\omega \frac{1}{2j_a+1} \sum_{m_a m_b} \sum_{JM\lambda} |M^{(\lambda)}_{JM}(a,b)|^2 . \tag{31}$$

To complete the discussion, we reduce the multipole transition matrix elements $M^{(\lambda)}_{JM}$ to a sum of radial integrals.

Magnetic Multipole Transitions

$$M^{m}_{JM}(a,b) = \langle b|A^{(0)*}_{JM}|a\rangle = \int u^{+}_{b} \vec{a}^{(0)*}_{JM} \cdot \vec{\alpha} u_a d^3x$$

$$= \int dr d\Omega \left(P_b \Omega^{+}_{\kappa_b m_b}, -i Q_b \Omega^{+}_{-\kappa_b m_b}\right) j_J\left(\frac{\omega r}{c}\right) \vec{Y}^{(0)+}_{JM}$$

$$\times \begin{pmatrix} 0 & \vec{\sigma} \\ \vec{\sigma} & 0 \end{pmatrix} \begin{pmatrix} P_a \Omega_{\kappa_a m_a} \\ i Q_a \Omega_{-\kappa_a m_a} \end{pmatrix}$$

$$= i \int dr j_J\left(\frac{\omega r}{c}\right) (P_a Q_b + Q_a P_b) \int d\Omega \Omega^{+}_{-\kappa_a m_a} \vec{\sigma} \cdot \vec{Y}^{(0)}_{JM} \Omega_{\kappa_b m_b} .$$

According to angular recoupling formulas given in Appendix IV, we have

$$M^{m}_{JM}(a,b) = \frac{i}{\sqrt{J(J+1)}} I_{-\kappa_a m_a \kappa_b m_b JM} R^{m}_{J}(a,b) , \tag{32}$$

where the angular recoupling function $I_{-\kappa_a m_a \kappa_b m_b JM}$ is defined in Appendix IV, and the magnetic type radial integral is given by

$$R^{m}_{J}(a,b) = (k_b + k_a) \int j_J\left(\frac{\omega r}{c}\right) (P_a Q_b + P_b \omega_a) dr . \tag{33}$$

Electric Multipole Transitions

Velocity Gauge

$$M^{v}_{JM}(a,b) = \langle b|A^{v*}_{JM}|a\rangle = \int u^{+}_{b} \vec{a}^{(1)*}_{JM} \cdot \vec{\alpha} u_a d^3x .$$

Again, using formulas in Appendix IV, we have

$$M^{v}_{JM}(a,b) = \frac{i}{\sqrt{J(J+1)}} \; I_{\kappa_a m_a \kappa_b m_b JM} R^{v}_{J}(a,b) \,, \tag{34}$$

where

$$R^{v}_{J}(a,b) = \int dr \left\{ P_a Q_b \left[(J+1)(\Delta\kappa + J) \frac{c}{\omega r} j_J \left(\frac{\omega r}{c}\right) - \Delta\kappa \, j_{J+1}\left(\frac{\omega r}{c}\right) \right] \right.$$

$$\left. + P_b Q_a \left[(J+1)(\Delta\kappa - J) \frac{c}{\omega r} j_J \left(\frac{\omega r}{c}\right) - \Delta\kappa \, j_{J+1}\left(\frac{\omega r}{c}\right) \right] \right\} \,, \tag{35}$$

with $\Delta\kappa = \kappa_b - \kappa_a$.

Length Gauge

$$M^{\ell}_{JM}(a,b) = \langle b | A^{\ell}_{JM} | a \rangle$$

$$= \int u^{+}_{b} \left(\vec{a}^{*}_{JM} \cdot \vec{\alpha} - i b^{*}_{JM} \right) u_a \, d^3$$

$$= \frac{-i}{\sqrt{J(J+1)}} \; I_{\kappa_a m_a \kappa_b m_b JM} R^{\ell}_{J}(a,b) \,, \tag{36}$$

where

$$R^{\ell}_{J}(a,b) = \int dr \left\{ (J+1) j_J \left(\frac{\omega r}{c}\right) (P_a P_b + Q_a Q_b) \right.$$

$$\left. + j_{J+1}\left(\frac{\omega r}{c}\right) \left[(\Delta\kappa - (J+1)) P_a Q_b + (\Delta\kappa + (J+1)) P_b Q_a \right] \right\} \,. \tag{37}$$

Conclusion

From Eqs. 32, 34, and 36, we can see that the multipole transition matrix elements can be written as

$$M_{JM}(a,b) = \frac{\pm i}{\sqrt{J(J+1)}} \; I_{\pm \kappa_a m_a \kappa_b m_b JM} R_J(a,b) \,. \tag{38}$$

Since

$$\sum_{m_a m_b M} I^2_{\pm \kappa_a m_a \kappa_b m_b JM} = \frac{1}{4\pi}(2J+1)(2j_a+1)(2j_b+1)\Lambda_{\pm \kappa_a J \kappa_b}, \tag{39}$$

where

$$\Lambda_{\kappa J \kappa'} = \frac{C^2(jJj';\tfrac{1}{2}0\tfrac{1}{2})}{2j'+1}\Pi_{\ell J \ell'}, \tag{40}$$

and $\Pi_{\ell J \ell'}$ is the parity selection function defined in Appendix IV, the total transition rate, from Eq. 31, then becomes

$$W_{a\to b} = 2\alpha\omega(2j_b+1)\sum_{J,\lambda}\frac{2J+1}{J(J+1)}\Lambda_{\pm \kappa_a J \kappa_b}[R^{(\lambda)}_J(a,b)]^2. \tag{41}$$

In the above equation, + and - signs correspond to electric and magnetic multipole transitions, respectively, and $R^{(\lambda)}_J$ are given by corresponding radial integrals defined in Eqs. 33, 35, and 37. While there are sums over J and λ in Eq. 41, the above expression usually reduces to one or a few terms by virtue of angular and parity selection rules in the function $\Lambda_{\kappa J \kappa'}$.

We note in closing that although this discussion is confined to one-electron systems only, generalization to many electron cases and multiconfiguration calculations are straightforward if we make the independent particle approximation in which $u(\vec{x})$ is replaced by one or a weighed sum of Slater determinants. In these cases, Eq. 31 for total transition rates still holds, and the angular recoupling formula (reduction to radial integrals) between pairs of single-particle orbitals, i.e., Eqs. 32, 34, and 36, will not be altered.

References

1. A. I. Akhiezer and V. B. Berestetskii, Quantum Electrodynamics Interscience, New York (1965).
2. I. P. Grant, J. Phys. B 7, 1458 (1974).

APPENDIX I. Notations and Conventions

Greek subscripts refer to 4-vectors and repeated indices imply summation. Some of the 4-vectors used in this article are

$x_\mu = (\vec{x}, ict)$	position vector
$A_\mu = (\vec{A}, i\phi)$	electromagnetic potential
$k_\mu = (\vec{k}, i\omega/c)$	photon wave vector
$\epsilon_\mu = (\hat{\epsilon}, i\epsilon_0)$	photon polarization vector
$\gamma_\mu = (\vec{\gamma}, \gamma_4)$ $\alpha_\mu = i\gamma_4\gamma_\mu = (\vec{\alpha}, i)$	Dirac matrices

The Dirac matrices are defined in the usual way, in particular

$$\vec{\alpha} = \begin{pmatrix} 0 & \vec{\sigma} \\ \vec{\sigma} & 0 \end{pmatrix} , \qquad \beta = \gamma_4 = \begin{pmatrix} 1 & 0 \\ 0 & -1 \end{pmatrix} ,$$

and the adjoint Dirac field operator $\bar{\psi}$ is defined as

$$\bar{\psi} = \psi^+ \beta .$$

APPENDIX II. Free-Photon Field

The electromagnetic potential A_μ satisfies Maxwell's equation

$$\nabla^2 A_\mu - \frac{1}{c^2} \frac{\partial^2 A_\mu}{\partial t^2} = 0 , \tag{A 2.1}$$

and the subsidiary condition (also known as the Lorentz condition)

$$\vec{\nabla} \cdot \vec{A} + \frac{1}{c} \frac{\partial \phi}{\partial t} = 0 . \tag{A 2.2}$$

Let a_γ^+ (a_γ) be the creation (annihilation) operator of a photon γ, quantization of the free photon field over a volume V leads to (see Ref. 1)

$$A_\mu = \sum_{k,\epsilon} \sqrt{\frac{2\pi\hbar c^2}{\omega V}} \, \epsilon_\mu [a^+_{k,\epsilon} e^{-ik \cdot x} + c.c.] . \tag{A 2.3}$$

From Maxwell's equation we have

$$|\vec{k}| = \frac{\omega}{c} \quad . \tag{A 2.4}$$

Another important relation comes from the subsidiary condition

$$\epsilon_0 = \hat{k} \cdot \hat{\epsilon} \quad . \tag{A 2.5}$$

APPENDIX III. Vector Spherical Harmonics

Vector spherical harmonics are eigenfunctions of J^2. They couple the angular momentum L and the photon spin S = 1 to a total angular momentum J as

$$\vec{Y}_{JLM}(\hat{n}) = \sum_{\mu} C(L1J; M-\mu\mu\ M) Y_{LM-\mu}(\hat{n}) \vec{\xi}_{\mu} \quad , \tag{A 3.1}$$

where $\vec{\xi}_{\mu}$ is the photon spinor

$$\vec{\xi}_0 = \begin{pmatrix} 0 \\ 0 \\ 1 \end{pmatrix} \quad , \quad \vec{\xi}_{\pm 1} = \mp \frac{1}{\sqrt{2}} \begin{pmatrix} 1 \\ \pm i \\ 0 \end{pmatrix} \quad . \tag{A 3.2}$$

Vector spherical harmonics satisfy the orthonormality condition

$$\int \vec{Y}^{+}_{JLM} \cdot \vec{Y}_{J'L'M'} \, d\Omega = \delta_{JJ'} \delta_{LL'} \delta_{MM'} \quad . \tag{A 3.3}$$

From $\vec{Y}_{JLM}$ we can construct three new vector spherical harmonics $\vec{Y}^{(\lambda)}_{JM}$ $\lambda = 0, \pm 1$, as

$$\vec{Y}^{(1)}_{JM} = \sqrt{\frac{J+1}{2J+1}} \ \vec{Y}_{JJ-1\,M} + \sqrt{\frac{J}{2J+1}} \ \vec{Y}_{JJ+1\,M} \quad ,$$

$$\vec{Y}^{(0)}_{JM} = \vec{Y}_{JJM} \quad ,$$

$$\vec{Y}^{(-1)}_{JM} = \sqrt{\frac{J}{2J+1}} \ \vec{Y}_{JJ-1\,M} - \sqrt{\frac{J+1}{2J+1}} \ \vec{Y}_{JJ+1\,M} \quad . \tag{A 3.4}$$

In particular, the first two $\vec{Y}^{(\lambda)}_{JM}$ are transverse, i.e., $\hat{n} \cdot \vec{Y}^{(\lambda)}_{JM}(\hat{n}) = 0$ for $\lambda = 0, 1$, while the last one is longitudinal: $\hat{n} \times \vec{Y}^{(-1)}_{JM}(\hat{n}) = 0$. Furthermore,

$\vec{Y}^{(\lambda)}_{JM}$ have definite parities $(-1)^{J-|\lambda|}$, and they satisfy the orthonormality conditions

$$\int \vec{Y}^{(\lambda)+}_{JM} \cdot \vec{Y}^{(\lambda')}_{J'M'} \, d\Omega = \delta_{JJ'}\delta_{MM'}\delta_{\lambda\lambda'} \, . \tag{A 3.5}$$

APPENDIX IV. Some Useful Formulas

Some of the angular recoupling formulas used in the text are given below:

$$\int \Omega^{+}_{\kappa m} Y_{JM} \Omega_{\kappa' m'} d\Omega = I_{\kappa m \kappa' m' JM} \, , \tag{A 4.1}$$

$$\int \Omega^{+}_{-\kappa m} \vec{\sigma} \cdot \vec{Y}^{(1)}_{JM} \Omega_{\kappa' m'} \, d\Omega = \frac{\kappa' - \kappa}{\sqrt{J(J+1)}} I_{\kappa m \kappa' m' JM} \, , \tag{A 4.2}$$

$$\int \Omega^{+}_{-\kappa m} \vec{\sigma} \cdot \vec{Y}^{(0)}_{JM} \Omega_{\kappa' m'} \, d\Omega = \frac{\kappa' + \kappa}{\sqrt{J(J+1)}} I_{-\kappa m \kappa' m' JM} \, , \tag{A 4.3}$$

$$\int \Omega^{+}_{-\kappa m} \vec{\sigma} \cdot \vec{Y}^{(-1)}_{JM} \Omega_{\kappa' m'} d\Omega = -I_{\kappa m \kappa' m' JM} \, , \tag{A 4.4}$$

where

$$I_{\kappa m \kappa' m' JM} = I_{-\kappa m -\kappa' m' JM}$$

$$= (-1)^{j' + J - j} \sqrt{\frac{(2j'+1)(2J+1)}{4\pi(2j+1)}} \, C(j' J j; \tfrac{1}{2}\, 0\, \tfrac{1}{2})$$

$$\times C(j' J j; m' M m) \, \Pi_{\ell J \ell'} \, , \tag{A 4.5}$$

and $\Pi_{\ell J \ell'}$ is the parity selection function

$$\Pi_{\ell J \ell'} = \begin{cases} 1 & \text{if } \ell + J + \ell' \text{ is even} \\ 0 & \text{otherwise} \end{cases} \, . \tag{A 4.6}$$

APPENDIX V. Relations Between Transition Rate, Absorption Oscillator Strength, and Line Strength

In transition probability calculations, it is often convenient to deal with the line strength

$$S_{ab} = \frac{6\pi\alpha\hbar c^3}{\omega^2} \sum_{m_a m_b} \sum_{JM\lambda} |M^{(\lambda)}_{JM}(a,b)|^2 \qquad \text{(A 5.1)}$$

which is symmetric with respect to the initial and final states. Transition rate $W_{a\to b}$ and absorption line strength $f_{b\to a}$ can then be expressed in terms of S_{ab} as

$$W_{a\to b} = \frac{4\omega^3}{3\hbar c^3} \frac{S_{ab}}{2j_a+1} \quad , \qquad \text{(A 5.2)}$$

$$f_{b\to a} = \frac{2m\omega}{3\hbar e^2} \frac{S_{ab}}{2j_b+1} \quad . \qquad \text{(A 5.3)}$$

For the E1 transition, S_{ab} in the length gauge can be written, from Eq. 41, as

$$S_{ab} = \left(\frac{3ec}{2\omega}\right)^2 (2j_a+1)(2j_b+1)\Lambda_{\kappa_a 1 \kappa_b} [R^{\ell}_{J=1}(a,b)]^2 \quad . \qquad \text{(A 5.4)}$$

In the nonrelativistic limit, $\frac{\omega}{c} \to 0$, and by retaining the leading $\frac{\omega r}{c}$ terms in the expansions of the spherical Bessel functions, we have

$$R^{\ell}_{J=1}(a,b) \to \frac{2\omega}{3c} \int (P_a P_b + Q_a Q_b)\, r dr \quad . \qquad \text{(A 5.5)}$$

As a result

$$S_{ab} \to (2j_a+1)(2j_b+1)\Lambda_{\kappa_a 1 \kappa_b} \langle b|er|a\rangle^2$$

$$= \sum_{m_a m_b} |\langle b|e\vec{r}|a\rangle|^2 \quad . \qquad \text{(A 5.6)}$$

This is just the relativistic analog of the length-form line strength for E1 transitions in nonrelativistic calculations.

THIS PAGE

WAS INTENTIONALLY

LEFT BLANK

furthermore, we use these integration formulas for the calculation of the potentials as well as the wavefunctions.

The use of higher order integration formulas poses a special problem. Namely, if these formulas are used in the most straightforward and obvious manner where one always calculates the next point in a numerically tabulated function, they are inherently unstable. As a matter of fact, even the Numerov formula is already unstable for the calculation of the potentials; this is, of course, the reason that the alternative, two-step process is used in currently available programs.

However, if we use the Numerov formula, or any of its higher order generalizations, in conjunction with a Gaussian pivoting scheme, these inherent instabilities can easily be surmounted. Using a particular integration formula results in a system of difference equations replacing the differential equations. This system of difference equations is then first transformed by a suitably chosen Gaussian pivoting scheme before the solution is attempted; and the latter then becomes a stable process.

In actual practice, the calculation of the Hartree-Fock potentials by this method has, at this point, been fully tested. With about 100 integration points, the potentials arising from 1s, 2s, and 2p orbitals have been calculated with the three-, five-, and seven-point formulas, yielding an accuracy of 10^{-7}, 10^{-10}, and 10^{-12}, respectively.

A second major improvement is achieved by treating the Hartree-Fock equations as a homogeneous linear system of equations, rather than treating the integration of each wavefunction as a separate problem. From this vantage point, the nature of the solution in the boundary regions $r \to 0$ and $r \to \infty$ becomes much more transparent. In the process, the concept of a Wronskian for a single second-order differential equation is generalized to a Wronskian matrix for a system of such equations; and the latter, in turn, leads to the definition of cannonical solution sets, for which the Wronskian matrix assumes a particularly simple form. It is gratifying that in the boundary regions $r \to 0$ and $r \to \infty$ the most natural solution sets are canonical sets.

As already intimated, in the boundary regions the solutions can be obtained in analytical form. For $r \to 0$, the solutions permit series expansions, and for $r \to \infty$, they permit asymptotic expansions. In a computer program now being developed, the expansion lengths can be chosen by the user as run-time parameters. Of course, the actual points at which origin and tail expansions take over, and match points for orbital energy adjustments, as well as all relevant tolerances and maximum counts for iterative processes, are also run-time parameters under control of the user.

A computer program implementing the analysis as outlined above is in an advanced state of preparation. The calculation of the Hartree-Fock potentials, as well as the determination of the origin and tail expansions of the wavefunctions, has at this time been checked out and thoroughly tested. A complete operating program should be available some time in the fall of 1978.

INNER-SHELL PROPERTIES OF ATOMIC IONS*

S. T. Manson,† J. L. Dehmer, and M. Inokuti

Various properties of atomic ions have been studied extensively using Hartree-Slater wavefunctions. Among the quantities calculated are dipole matrix elements and oscillator strengths, and $\langle r^{\nu} \rangle$ for $-3 \leq \nu \leq 2$; these basic quantities are related to a number of measurable properties, such as polarizability, magnetic susceptibility, and spin-orbit coupling. An outstanding feature of the results is that all of the above quantities for inner shells are virtually unaffected by removal of outer shell electrons. The implications for ion-atom collision experiments are discussed and the systematics of the variation of these quantities over Z and N are presented.

*Abstract of a contributed paper presented at the IXth Annual Meeting of the Division of Electron and Atomic Physics, American Physical Society, 5–7 December 1977, Knoxville, Tennessee.

†Consultant, RER Division. Permanent address: Department of Physics, Georgia State University, Atlanta, Georgia 30303.

ENERGY DEPENDENCE OF ATOMIC QUANTUM DEFECTS THROUGHOUT THE DISCRETE SPECTRUM

C. Greene* and J. L. Dehmer

Recent efforts to map out the behavior of the atomic quantum defect function as a smooth function of energy throughout the discrete part of the spectrum are summarized.

Introduction

Efforts to reduce and unify the data provided by atomic spectroscopists have inspired the development, in the course of twenty years, of the quantum-defect method (QDM).[1,2] The QDM serves to classify atomic properties in terms of a minimal set of parameters whose energy dependence tends to be weak. The simplest application of the QDM is to the single-channel problem, in which the outer atomic electron possesses a Rydberg series of energy levels converging to a single ionization threshold, I_0. For this problem the minimal set of parameters consists of the ionization threshold value I_0 and a quantum defect μ_ℓ for each partial wave. Previous studies[2-4] have made extensive use of the near energy independence of each μ_ℓ, regarding it as a constant or as a linear function of the electronic energy ϵ. While this approximation is good near the ionization threshold, drastic departures arise as ϵ decreases beyond the lower limit of a Rydberg series, where $\mu_\ell(\epsilon)$ assumes a sawtooth energy dependence. In this report we attempt to identify characteristic classes of behavior of the quantum defect function $\mu_\ell(\epsilon)$, illustrating our qualitative expectations with quantitative examples.

Summary of the QDM

The primary assumption of the QDM is that the outer atomic electron moves in an average radial potential field V(r), which behaves asymptotically

* Department of Physics, The University of Chicago; Guest Graduate Student Appointee, ANL Center for Educational Affairs. Work supported in part by U.S. Department of Energy, Division of Basic Energy Sciences, Contract No. COO-1674-139.

as an attractive Coulomb potential $V_0(r) = -1/r$. In atomic units the radial Schrodinger equation for this electron is

$$P''(r) - \left[\frac{\ell(\ell+1)}{r^2} + 2V(r) - 2\epsilon\right] P(r) = 0 \ , \tag{1}$$

where primes denote differentiation with respect to r. A pair of reference or comparison functions* (f,g) can be defined as regular and irregular solutions to Eq. 1, with V(r) replaced by the Coulomb potential $V_0(r)$. Provided that $V(r) = V_0(r)$ for r larger than some finite radius r_0, the wavefunction P(r) in the outer region can be written as

$$P(r) = \alpha[f(r)\cos\pi\mu - g(r)\sin\pi\mu] \ , \qquad r \geq r_0 \tag{2}$$

where α and μ are constants. In order for the electron to be bound, its wavefunction must tend to zero at large r. Defining the effective quantum number ν by $\epsilon = -\frac{1}{2}\nu^{-2}$, the asymptotic expansions of the Coulomb functions below threshold are:

$$f(r) = u(r)\sin\pi\nu - v(r)\cos\pi\nu \tag{3}$$

$$g(r) = -u(r)\cos\pi\nu - v(r)\sin\pi\nu \ , \tag{4}$$

where

$$u \xrightarrow[r>>\nu]{} \text{const} \times (2r/\nu)^{-\nu} e^{r/\nu} \tag{5}$$

$$v \xrightarrow[r>>\nu]{} \text{const} \times (2r/\nu)^{\nu} e^{-r/\nu} \ . \tag{6}$$

Upon substituting these expressions into Eq. 2 and requiring the coefficient of u to vanish, we find that for bound states $\sin\pi(\nu+\mu) = 0$, or $\nu+\mu = n$, an integer (it turns out that $n - \ell - 1$ is the number of radial nodes of P(r), as for the one-electron atoms). This bound-state condition, which was first derived by Seaton in 1958,[1] allows us to discuss quantum defects and phase shift synonymously. Its usefulness in classifying spectra stems primarily from the near constancy of μ within a Rydberg series. In the remainder of this

---

*The functions (f,g) of this report are defined by the German-type comparison functions of Ref. 5.

report we look more closely at the quantum-defect energy dependence, particularly focusing on non-Rydberg spectral ranges where μ varies sharply with ϵ.

Radial Phase Functions

The language of the phase-amplitude method (PAM) is especially suited to the ensuing discussion. The PAM treats μ and α as r-dependent functions inside the core, $r \geq r_0$, so that the validity of Eq. 2 extends to all r. Here we are particularly interested in $\mu(r)$, which satisfies[5-7] the nonlinear first-order equation

$$\pi\mu(r) = \frac{2}{W(f,g)} \int_0^r dr' \, [V_0(r') - V(r')] \, [f(r') \cos \pi\mu(r') - g(r') \sin \pi\mu(r')]^2 , \tag{7}$$

where $W(f,g) \equiv fg' - f'g$ is the position-independent Wronskian of the comparison functions. In Eq. 7 note that if the potential difference $U(r) \equiv V_0(r) - V(r)$ is of constant sign, as for the Hartree-Slater potential used in the calculations below, then $\mu(r)$ is a monotonic function. Also, points of inflection of $\mu(r)$ correspond to nodes of $P(r)$, a fact which is critically important in the analysis below. While Eq. 7 for μ depends on the three functions f,g, and U, an alternative expression in terms of f,g, and P is especially convenient for describing the energy dependence of $\mu(r)$. The functional form, which is an immediate consequence of the "constraint" equation[7] used in deriving Eq. 7, is simply

$$\tan \pi\mu = W(f,P)/W(g,P) \, . \tag{8}$$

This expression for $\mu(r)$ is equivalent to the solution of Eq. 7 if we adopt the modulus-determining provisos that $\mu(r)$ be continuous and that $\mu(0) = 0$. Equation 8 is useful because the three functions f,g, and P have well-understood energy variations and because the functional form is simple. The computations of μ discussed below were performed by integrating Eq. 1 using the Numerov method; $\mu(r)$ was then found directly from Eq. 8. This procedure bypassed complications involved in the direct solution of Eq. 7, which arise at radii where μ increases rapidly by very nearly unity over a small range in r. This step-like behavior of $\mu(r)$ is examined in detail below.

Since we are considering the quantum defect as a difference between the phase of P(r) and the reference function phase, it is convenient to introduce one more definition, that of the phase of any radial function P(r) as

$$\cot \phi_P(r) = P'(r)/P(r) \ . \tag{9}$$

(Note that, according to this definition, ϕ_P is a multiple of π at each node and an odd multiple of $\pi/2$ at each antinode.) In terms of such phase functions, Eq. 8 can be rewritten as

$$\tan \pi\mu = \frac{\cot \phi_P - \cot \phi_f}{\cot \phi_P - \cot \phi_g} \cdot \frac{f}{g} \ . \tag{10}$$

For purposes of qualitative discussion, this can be approximated by

$$\pi\mu \sim \phi_P - \phi_f \ , \tag{11}$$

provided that f and g oscillate roughly 90° out of phase. [Equation 11 is exact if f and g satisfy $f=g'$, $f'=-g$.] Thus our picture of $\pi\mu$ as a phase difference is reinforced. It is useful to explore further the behavior of the radial phase functions ϕ, as they will play a central role in our analysis of the quantum defect function $\mu(\epsilon,r)$. The overall energy dependence of these phases is well understood. For example, it is well known that the position of any node monotonically decreases as the energy ϵ increases.[8] In fact, we can be still more explicit about the phase function energy dependence. Combining Eq. 9 with Eq. 1 yields

$$\frac{d\phi_P}{dr} = \cos^2 \phi_P + 2T(r) \sin^2 \phi_P \ , \tag{12}$$

where $T(r) = \epsilon - \ell(\ell+1)/2r^2 - V(r)$ is the local kinetic energy.

Equation 12 permits a clarification of the phase function behavior. Three aspects are most relevant to our purpose. First, we address the dependence of $\phi_P(r)$ on T(r). This encompasses variations of ϕ_P as a function of ϵ, of ℓ, and of V. Given two alternative expressions for T(r) such that $T_1(r) \geq T_2(r)$ for all r, the resulting phases are ordered as well, meaning $\phi_1(r) \geq \phi_2(r)$ for all r [provided, of course, that $\phi_1(0) = \phi_2(0)$]. The monotonic

decrease of node positions as a function of ϵ (but at fixed ℓ and V) is a specific example of this phase ordering principle. Similarly the phase decreases as ℓ increases and, conversely, it increases when the potential V is made everywhere more attractive. Second, we note that the phase function $\phi_P(r)$ increases in a step-wise fashion in regions of large kinetic energy T(r). In such regions the phase increases relatively slowly at the nodes of P, where $d\phi_P/dr = 1$, but quite rapidly at the antinodes, where $d\phi_P/dr = 2T(r)$. This behavior gives rise to rapid small-r jumps in $\mu(r)$. Finally, we examine the behavior of $\phi_P(r)$ in regions of space where T(r) goes through zero and approaches a negative value at large r. This corresponds to the present problem involving electronic energies below threshold, with $\epsilon = -\frac{1}{2}\nu^{-2}$. Inspection of Eqs. 2–6 shows that at energies where the electron is not bound, the phase ϕ_P approaches the Coulomb phase ϕ_u at larger r (actually they only approach one another modulo π). That is,

$$\phi_P \xrightarrow[r>>\nu]{} m\pi + \cot^{-1}\left(\frac{1}{\nu}\right) , \qquad \text{for } \nu \neq \nu_m , \tag{13}$$

where the inverse cotangent is chosen to lie between 0 and π. In Eq. 13 m is the number of radial nodes. At the bound energies ($\epsilon_m = -\frac{1}{2}\nu_m^{-2}$), though, ϕ_P approaches ϕ_v, implying

$$\phi_P \xrightarrow[r>>\nu]{} m\pi - \cot^{-1}\left(\frac{1}{\nu}\right) , \qquad \text{for } \nu = \nu_m . \tag{14}$$

Each of these three features is present in the s-wave phase functions of atomic potassium. Figure 1 shows ϕ_P as a function of r at four sample energies in the immediate neighborhood of an eigenvalue of Eq. 1. First we see the ordering of the phase as a function of energy. At any given radius ϕ_P decreases as ν decreases. Second, the step-like increase of ν_P at small r is evident in the jump centered at $r \sim 0.05$ a.u.; this corresponds to an antinode in the radial wavefunction P. The second step, located at $r \sim 0.32$ a.u., is significantly less sharp since T(r) in Eq. 12 is considerably smaller. Finally, the phase behaves asymptotically as expected, approaching $2\pi + \cot^{-1}(1/\nu)$ at energies just above the eigenvalue, while approaching $\pi + \cot^{-1}(1/\nu)$ at energies slightly below the eigenvalue. At the eigenvalue itself

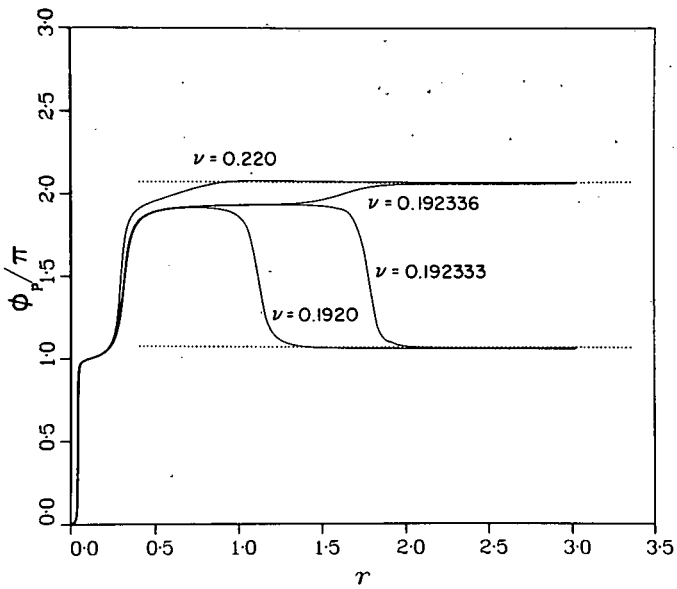

FIG. 1.--Radial phase functions $\phi_P(r)$ calculated for s-wave atomic potassium at four values of the effective quantum number ν. The dashed lines represent $\phi_P = 2\pi + \cot^{-1}(1/0.22)$ and $\pi + \cot^{-1}(1/0.22)$. Note the dramatic changes in ϕ_P as ν sweeps out a tiny range centered on an eigenvalue of Eq. 1.

($\nu_m \sim 0.192335$), ϕ_P will tend toward the line $2\pi - \cot^{-1}(1/\nu)$, as was anticipated above. A remarkable feature in Figure 1 is that a very small change in ν produces such an abrupt change in the large-r behavior of ϕ_P, causing a dramatic variation in the quantum defect μ in this energy range also, as we discuss below.

Variations of μ with Radius

The features of phase function behavior noted above facilitate a detailed examination of $\mu(\epsilon)$ for discrete atomic spectra. We begin by examining the radial variations of the quantum defect. Figure 2 shows μ as a function of r at two fixed energies ($\epsilon = 0$, -10 a.u.), calculated for s waves of atomic potassium with the Hartree-Slater model potential. For now, consider the zero-energy (dashed) curve of Figure 2. The rapid jump of the quantum defect at $r \sim 0.05$ a.u. is quite similar to the small r jump of the phase function $\phi_P(r)$ in Figure 1. To understand this recall our picture of the quantum defect as a phase difference (Eq. 11). The phase of the comparison function $\phi_f(r)$ is determined in Eq. 12, with T(r) replaced by a Coulombic $T_0(r)$. At small r the atomic kinetic energy is much greater than the unit charge Coulomb kinetic energy. Accordingly, $\phi_P(r)$ increases much more rapidly than $\phi_f(r)$, and the gross behavior of $\pi\mu$ follows that of ϕ_P very closely. On the other hand, as r increases through the rest of the atom, T(r) and $T_0(r)$ come closer in magnitude,

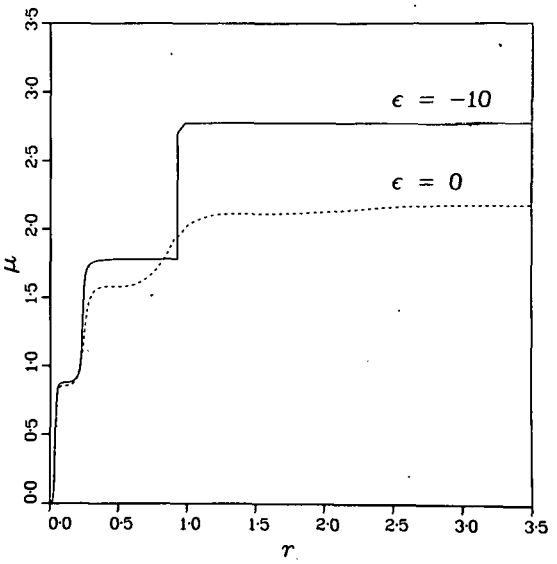

FIG. 2.--Radial dependence of the s-wave quantum defect function of potassium; $\mu(r)$ was calculated at two energies (0 and -10 a.u.) using the Hartree-Slater model potential.

so that ϕ_p and ϕ_f increase at a more nearly comparable rate. As a result, the steps in $\mu(r)$ become less abrupt and smaller at successively larger radii, until at $r \sim 2.3$ a.u. the antinode of P produces an increase in μ of only about 0.1. The $\epsilon = 0$ curve for $\mu(r)$ typifies the Rydberg spectral range which extends from $\epsilon = 0$ to roughly $\epsilon = -0.15$ a.u. for the alkali metals.

The upper solid curve of Figure 2 represents $\mu(r)$ calculated at $\epsilon = -10$ a.u., an energy far below the Rydberg range. Still, the small-r behavior of μ is affected very little by the considerable energy change. This is not surprising, since at $r \sim 0.05$ a.u. a change in ϵ of 10 a.u. is small relative to the value of T(r), which is roughly 400 a.u. at that distance. The outer jump in the $\epsilon = -10$ a.u. curve (near $r \sim 0.8$ a.u.) contrasts strongly with the slower and smaller step which occurs in the $\epsilon = 0$ quantum-defect curve at the same radius. At first sight this is surprising. Both ϕ_p and ϕ_f at this energy increase more slowly with r than at $\epsilon = 0$ because of the phase-ordering principle discussed after Eq. 12. So, the extreme sharpness of this outer step in $\mu(r)$ is only possible when the approximation inherent in Eq. 11 breaks down completely. Then we must return to the exact Eq. 10 to acquire a full understanding of these unusually rapid steps.

Variations of μ with Energy

Since the structure of $\mu(r)$ can vary strongly from one spectral range to the next, it is appropriate to examine the energy dependence of μ explicitly. Figure 3 shows μ (at a fixed radius $r=r_0$) as a function of the effective quantum number ν for four neutral atoms ranging from $Z=11$ to $Z=19$. These s-wave quantum defects were calculated over a broad spectrum, ranging from -136 keV at the left portion of Figure 3 to -0.136 eV at the right edge. The potassium quantum defect, shown as the solid, uppermost curve, is the quantity of primary interest. The three curves representing the quantum defects of other atoms should be ignored for now; they will be discussed briefly later. One feature of Figure 3 should be kept in mind. That is, although a continuous curve is drawn for the energy dependence of μ, the only physically observable bound states of a given atom occur at intersections of the μ curves with the dashed lines $\mu+\nu=n$. It is helpful, however, to suspend application of the large r boundary condition, as we have done here, and to calculate μ continuously below threshold; this conveys a clearer picture than would a small number of separated points, i.e., at the discrete eigenvalues. In addition, the energy normalization of P depends on the derivative $\partial\mu/\partial\epsilon$, which is more difficult to estimate if the quantum defect is calculated only at the bound states.

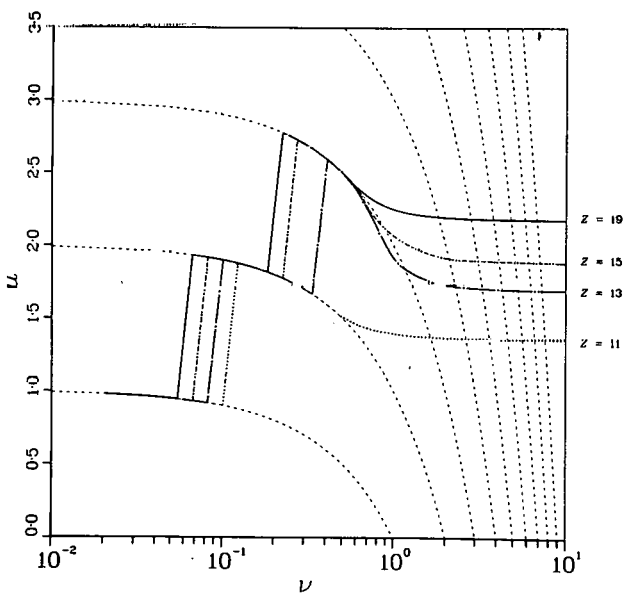

FIG. 3.--The s-wave quantum defect at $r=r_0$ as a function of the effective quantum number for sodium (....), aluminum (-.-.), phosphorus (--..--) and potassium (—). The grid of dashed lines represents $\mu+\nu=$integer, which would appear as straight lines if the ν axis was linear instead of logarithmic. The quantum defect for each atom is level at the right of the figure, and as ν decreases, each converges to one of the lines $\nu+\mu=n$. Each quantum defect experiences one or two rapid jumps of -1 as ν decreases until $\nu\sim0.055$, below which the four curves have collapsed into one.

It is instructive to trace out the potassium quantum defect and to identify the main features of interest. A distinct class of behavior dominates the right-hand portion of Figure 3, from $\nu \sim 2$ to $\nu = 10$, where μ deviates very little from its threshold value $\mu(\epsilon = 0) = 2.177$. We denote this near energy independence of μ near threshold as the Rydberg class of behavior. A rather different class persists throughout the left-hand section of this plot, say from $\nu = 0.01$ to $\nu \sim 0.6$. In this region of large negative energies μ stays very rigidly on top of the dashed family of lines representing $\nu + \mu = integer$. This is typical of the low-ν class of behavior. Nonetheless, two obvious and dramatic exceptions to this behavior appear in Figure 3 as rapid unit changes of μ occurring near $\nu = 0.19$ and $\nu = 0.055$. We will see below that these changes result from the striking energy dependence of $\phi_P(r)$ observed in Figure 1 at energies in the immediate neighborhood of an eigenvalue of Eq. 1. Finally, there is a transition region between the two classes of behavior, which extends from roughly $\nu \sim 0.6$ to $\nu \sim 2$ for the potassium quantum defect function.

These two dominant classes of quantum defect behavior warrant separate analyses. Initially we discuss the more familiar Rydberg class; for most atoms μ is nearly independent of ϵ at all discrete levels above the ground state. This energy independence arises for two main reasons. First the phases ϕ_P and ϕ_f are individually insensitive to changes in ϵ (less than ~ 0.15 a.u.) for $r \lesssim 1$, where T(r) and the Coulombic $T_0(r)$ are both much greater than $|\epsilon|$. Second, in the outer portion of the core ($r \gtrsim 1$), where the kinetic energies and ϵ are more comparable, T(r) merges closer to $T_0(r)$ and the energy dependence of ϕ_P and ϕ_f partially cancel in Eq. 11. A similar partial cancellation in the radial derivative of the quantum defect was noted earlier, and is responsible for the near constancy of μ throughout $r \gtrsim 1$ in the $\epsilon = 0$ curve of Figure 2.

Next we turn to the low-ν class of behavior of $\mu(\epsilon, r)$. At small r, where $r_0/\nu >> 1$, the Coulomb comparison functions (f,g) begin to assume their asymptotic forms within the atom. This is the important difference between the two classes. Then the alternative Coulomb solutions (u,v) defined in

Eq. 3 and Eq. 4 are more appropriate for discussion, and Eq. 8 becomes

$$\tan \pi(\nu+\mu) = \frac{W(v,P)}{W(u,P)} = \frac{\cot\phi_P - \cot\phi_v}{\cot\phi_P - \cot\phi_u} \cdot \frac{v}{u} \quad . \tag{15}$$

For large r/ν, as is the case here, (u,v) are exponentially rising and falling functions and this ratio of Wronskians is of the order $e^{-2r/\nu}$ except where $\cot\phi_P \approx \cot\phi_u$. This behavior explains the tendency of each curve of Figure 3 to remain rigidly on top of the dashed lines $\nu+\mu=n$ at low-ν. Note that it is not surprising for $\nu=1$ to mark the onset of low-ν behavior; for $\ell=0$ that is the energy at which the last Coulomb node moves to infinity and below which (f,g) begin their asymptotic growth within the core (i.e., for $r < r_0$). Then $\nu+\mu \sim n$, to within an exponentially small number. This concept breaks down, however, when $P'/P = u'/u$ (recall that $u'/u \sim 1/\nu$ for $r/\nu \gg 1$). If this critical value of $\cot\phi_P \sim 1/\nu$ is attained with increasing r, then $\tan\pi(\nu+\mu)$ changes from nearly 0 to ∞ and back to nearly 0 over an incredibly small distance. This is, in fact, the cause of the rapid outer radial step in the $\epsilon = -10$ quantum-defect curve of Figure 2.

It is highly instructive to compare $\mu(r)$ with $\phi_P(r)$ at this energy. The potassium phase function ϕ_P at $\epsilon = -10$ a.u. is represented by the uppermost ($\nu = 0.22$) curve of Figure 1. As noted above, the first step in $\mu(r)$ follows the first step in $\phi_P(r)$ quite closely. The second steps of μ and of ϕ_P are also qualitatively similar. But the last step in $\mu(r)$ does not correspond to any step-like feature in $\phi_P(r)$. In fact, that rapid last jump in μ is caused entirely by the seemingly innocuous crossing of $\phi_P(r)$ with the horizontal line $2\pi + \cot^{-1}(1/0.22)$ at $r=0.8$, which zeroes the denominator of Eq. 15.

By looking at the other phase functions in Figure 1, it is possible to understand what happens to μ as the energy is lowered from just above the eigenvalue at $\nu_m = 0.192335$ to just below it. As ν is lowered from 0.22, the last node (the point where $\phi_P(r) = 2\pi$) moves monotonically outward. Similarly the radius at which μ undergoes a rapid outer unit step [where $\phi_P(r)$ crosses the line $2\pi + \cot^{-1}(1/\nu)$] also moves steadily outward. If ν is decreased further, a critical value ν_{cr} will be reached, at which this crossing of $\cot\phi_P$

and $\cot\phi_u$ occurs precisely at the distance r_0 where the atomic potential becomes Coulombic (the position r_0 is defined quite exactly in the Hartree-Slater approximation). At $\nu = \nu_{cr}$ it is clear that $\cot\phi_P$ and $\cot\phi_u$ must also coincide at larger r, since the Wronskian W(u,P) must be constant for $r \geq r_0$. For $\nu < \nu_{cr}$ this rapid outer step in $\mu(r)$ will be absent, since ϕ_P never reaches the line $2\pi + \cot^{-1}(1/\nu)$, though it does still approach it asymptotically from below. It is at $\nu = \nu_{cr}$ that the jump in μ as a function of ν occurs (for the potassium curve in Figure 3, $\nu_{cr} \sim 0.192335$). A further decrease in ν eventually causes the outer radial node of P to move to infinity when the actual eigenvalue $\nu = \nu_2$ is reached. Here and at successively smaller ν the quantum defect remains fixed to the curve $\nu + \mu = 2$, until near $\nu_1 = 0.055$ a similar scenario is enacted. Numerically the two values ν_{cr} and ν_2 are so close as to be indistinguishable (at least to within six significant digits), a consequence of the lightning speed of outer node progression at energies near eigenvalues of the differential equation, Eq. 1. Below the first eigenvalue at $\nu_1 \sim 0.055$ the radial wavefunction P(r) has no nodes, its phase $\phi_P(r)$ has no more rapid changes with energy, and μ remains fixed to the line $\nu + \mu = 1$ as $\epsilon \to -\infty$.

Summary

We have investigated the structure of the single-channel s-wave quantum defect μ as a smooth function of the energy ϵ of the outer electron. Below the ionization threshold there are two notable classes of behavior of $\mu(\epsilon, r)$. Within the Rydberg class μ is nearly independent of energy; also, μ increases with r slowly and smoothly in the outer portion of the ionic core. This may be contrasted with the low-ν class of behavior, which is characterized by μ remaining fixed rigidly to values $\mu = n - \nu$, where n is an integer. The rapid variation of the phase ϕ_P of the electronic wavefunction as the energy decreases through a discrete level induces a rapid unit drop of μ. The radial structure of the quantum defect is also quite different in the low-ν class, which is manifested by rapid unit steps in μ as a function of r in the outer portion of the ionic core. These two distinct classes of behavior are separated by a transition region around $\nu \sim 1$ in which μ is more difficult to discuss qualitatively, but which occurs always at $\nu \sim 1$.

The numerical work discussed above consisted of detailing these features of the quantum defect behavior for a single atom and partial wave (potassium, s-wave). The tools of analysis apply readily, however, to a discussion of different atoms and higher partial waves. An indication of the Z-dependence of $\mu(\epsilon)$ is embodied in the quantum defect curves plotted in Figure 3 for four atoms ranging from potassium to sodium, although some of the details may depend strongly on the model chosen for V(r). Clearly, as Z decreases from 19 to 11 the potential seen by the outer electron decreases in strength, and an overall decrease in μ with decreasing Z is expected. The specifics of this decrease in μ remain to be explained, particularly in the transition region between the Rydberg and low-ν classes of behavior, but they should be accessible within the framework discussed in this report. An investigation of this topic and a similar analysis for higher partial waves will be published at a later date.

Acknowledgements

We acknowledge a number of stimulating discussions with U. Fano and M. Kohmoto. We also thank M. Inokuti for reading the manuscript critically and offering a number of useful suggestions.

References

1. M. J. Seaton, Mon. Not. R. Astron. Soc. 118, 504 (1958); Proc. Phys. Soc. London 88, 801 (1966).
2. U. Fano, Phys. Rev. A 2, 353 (1970).
3. K. T. Lu, Phys. Rev. A 4, 579 (1971).
4. C. M. Lee and K. T. Lu, Phys. Rev. A 8, 1241 (1973).
5. J. L. Dehmer and U. Fano, Phys. Rev. A 7, 4 (1970).
6. U. Fano, C. E. Theodosiou, and J. L. Dehmer, Rev. Mod. Phys. 48, 59 (1976).
7. F. Calogero, Variable Phase Approach to Potential Scattering, Academic Press, New York (1967).
8. R. Courant and D. Hilbert, Methods of Mathematical Physics, Interscience Publishers, New York, Vol. I, p. 454 (1953).

OSCILLATOR-STRENGTH MOMENTS, STOPPING POWERS, AND TOTAL INELASTIC-SCATTERING CROSS SECTIONS OF FAST CHARGED PARTICLES FOR ALL NEUTRAL ATOMS THROUGH STRONTIUM*

Mitio Inokuti, T. Baer,† J. L. Dehmer, and J. D. Hanson‡

Systematics of the atomic properties named in the title and of other related quantities (e.g., mean excitation energies for straggling) have been comprehensively studied. Our calculations are based on a single-electron approximation using the Hartree-Slater central-field potential—a model that represents a reasonable compromise between two goals, i.e., a sensible description of the major features of atomic dynamics and an economical computational scheme indispensable for an exhaustive survey of many atoms. Our results not only quantify the general trends of the atomic properties expected from the periodic table, but also provide a useful guide to experiment (on atoms for which no other data are available), to theory (for which we suggest several aims of more advanced analysis), and to applications including radiological physics and charged-particle microscopy.

*Summary of a paper under preparation for publication.

†Resident Graduate Student Associate, RER Division, June–September 1977. Permanent address: Department of Physics, The University of Chicago, Chicago, Illinois 60637

‡Appointee, Undergraduate Research Participation Program, Argonne Center for Educational Affairs, Fall 1974. Present address: Department of Physics, Cornell University, Ithaca, New York 14853.

INEQUALITIES THAT BOUND MEAN EXCITATION ENERGIES WITH RESPECT TO THE OSCILLATOR-STRENGTH DISTRIBUTION

Mitio Inokuti

The logarithmic mean excitation energies, which determine the total inelastic-scattering cross section, the stopping power, the straggling for fast charged particles, and other atomic or molecular properties, are bound from above and below by moments of the oscillator-strength distribution.

Consider the moment

$$S(\mu) = \int (df/dE)\, E^{\mu} dE \qquad (1)$$

and the quantity

$$L(\mu) = \int (df/dE)\, E^{\mu} \ln E \, dE \ , \qquad (2)$$

where df/dE is the oscillator-strength distribution as a function of the excitation energy E measured from the ground state of any atom or molecule. The integrals include contributions of sums over discrete spectra. The mean excitation energies $I(\mu)$ of various orders μ, defined by

$$\ln I(\mu) = L(\mu)/S(\mu) \ , \qquad (3)$$

are crucial to many properties of the atom or molecule.[1-4] For example, $I(-1)$ appears in the expression for the total inelastic-scattering cross section,[5] $I(0)$ in the famous Bethe formula for the stopping power,[2] $I(1)$ in the Fano[2] formula for straggling, and $I(2)$ in the expression for the Lamb shift of energy levels.[1]

Precise calculation of $L(\mu)$, in general, requires the complete knowledge of df/dE over the entire spectrum. By contrast, $S(\mu)$ values for $\mu = 2, 1, 0, -1, -2, -4, -6, \ldots$ are either calculable as certain ground-state expectation values by virtue of sum rules,[1-4] or derivable from experiment. Therefore, it is useful to explore means of mathematically relating $L(\mu)$ with $S(\mu)$ and thereby estimating $L(\mu)$ without the knowledge of full df/dE. As an example of approaches in this direction, one may fit the $S(\mu)$ data as a function of

continuous variable μ either graphically or analytically and obtain $L(\mu) = dS(\mu)/d\mu$ as the slope of the $S(\mu)$ vs. μ curve.[6-9] A second approach is to use the moment theory.[10] It is the purpose of this note to point out a set of simple and general inequalities useful for studying $L(\mu)$.

It is possible to show that

$$\ln [S(\mu)/S(\mu-1)] \leq L(\mu)/S(\mu) \leq \ln [S(\mu+1)/S(\mu)] \tag{4}$$

for any $\mu < 1.5$ (i.e., under the condition that all the quantities in the inequalities are well defined), so long as df/dE is non-negative for any $E > 0$. The equality results only if df/dE degenerates into a single-line spectrum of the form $\delta(E - E_0)$, E_0 being a constant.

The inequalities (4) can be proved by use of Jensen's theorem concerning convex functions.[11]

Table 1 demonstrates the inequalities for $\mu = -1$ and $\mu = 0$ by use of data on H, He, and Ne.[5,12,13] It is seen that $I(0)$, and especially $I(-1)$, are bound rather tightly by the inequalities. Further, the tightness of the bounds for other rare gases is readily found by inspection of Table II of Ref. 3. The inequalities often permit a quick estimate of the mean excitation energies, especially for light atoms and molecules.

Table 1. Test of the inequalities for H, He, and Ne atoms. All the values of $S(\mu)$ and $L(\mu)$ used here are defined by Eqs. 1 and 2 with excitation energies E measured in units of the Rydberg energy (13.606 eV). Entries for each column increase steadily as one goes from top to bottom, according to the inequalities.

Terms in the inequalities	Atoms		
	H	He	Ne
$\ln [S(-1)/S(-2)]$	-0.1178	0.777	1.04
$L(-1)/S(-1)$	-0.07325	0.848	1.25
$\ln [S(0)/S(-1)]$	0	0.978	1.67
$L(0)/S(0)$	0.09698	1.13	2.31
$\ln [S(1)/S(0)]$	0.2877	1.407	3.46

References

1. H. A. Bethe and E. Salpeter, Quantum Mechanics of One- and Two-Electron Atoms (Springer-Verlag, Berlin and Academic Press, New York, 1957).
2. U. Fano, Ann. Rev. Nucl. Sci. 13, 1 (1963).
3. U. Fano and J. W. Cooper, Rev. Mod. Phys. 40, 441 (1968).
4. M. Inokuti, Rev. Mod. Phys. 43, 297 (1971).
5. M. Inokuti, Y.-K. Kim, and R. L. Platzman, Phys. Rev. 164, 55 (1967).
6. C. L. Pekeris, Phys. Rev. 115, 1216 (1959).
7. A. Dalgarno, Proc. Phys. Soc., London 76, 422 (1960).
8. R. J. Bell and A. Dalgarno, Proc. Phys. Soc., London 86, 375 (1965).
9. R. J. Bell and A. Dalgarno, Proc. Phys. Soc., London 88, 55 (1966).
10. P. W. Langhoff and A. C. Yates, J. Phys. B 5, 1071 (1972).
11. G. H. Hardy, J. E. Littlewood, and G. Polya, Inequalities, 2nd Ed., Cambridge University Press, London, p. 150 (1952).
12. M. Inokuti, Argonne National Laboratory Radiological Physics Division Summary Report, July 1962–June 1963, ANL-6769, p. 7.
13. R. P. Saxon, Phys. Rev. A 8, 839 (1973).

ADDENDA: INELASTIC COLLISIONS OF FAST CHARGED PARTICLES WITH ATOMS AND MOLECULES—THE BETHE THEORY REVISITED [Rev. Mod. Phys. 43, 297 (1971)]*

Mitio Inokuti, Yukikazu Itikawa,† and James E. Turner‡

Since the appearance of the title paper, a number of new developments have occurred which need to be included in that body of material. We present additional remarks and clarifications which supplement and update numerous aspects of the Bethe theory discussed in the earlier paper. We also bring the bibliography up to date. Plasma stopping power, the z^3 effect, and stopping power for particles at extreme relativistic energies are among the new topics included. We also make several comments on Fano's earlier review article.[1]

Reference

1. U. Fano, Ann. Rev. Nucl. Sci. 13, 1 (1965).

---

*Abstract of an article published in Rev. Mod. Phys. 50, 23 (1978).

†Visiting Scientist, 1971–1972. Permanent address: Institute of Space and Aeronautical Science, University of Tokyo, Meguro-ku, Tokyo 153, Japan.

‡Oak Ridge National Laboratory, Oak Ridge, Tennessee 37830

INTEGRALS OF THE SQUARED FORM FACTOR OVER THE MOMENTUM TRANSFER*

Michio Matsuzawa,† Seiji Mitsuoka,‡ and Mitio Inokuti

Consider the integrals of the form factor $F_{nm}(K)$ over the momentum transfer $\hbar K$, i.e.,

$$H_{nm}(\mu, \epsilon) = a_0^{\mu+1} \int_{\epsilon}^{\infty} K^{\mu} |F_{nm}(K)|^2 \, dK \,, \tag{1}$$

where

$$F_{nm}(K) = \int e^{i\vec{K}\cdot\vec{r}} \rho_{nm}(\vec{r}) \, d\vec{r} \,, \tag{2}$$

a_0 is the Bohr radius, ϵ is a small positive parameter, μ is an integer, and $\rho_{nm}(\vec{r})$ is the transition density of the atom (or molecule). The cases with $\mu \geqq 0$, where one can put $\epsilon = 0$, have been treated by various authors. (For example, see Ref. 1.) Here we discuss the integrals for $\mu \geqq 0$, such as $\mu = -3$, which is closely related to the Bethe asymptotic cross section. We assume that the atoms (or molecules) are either spherical or randomly oriented. Under this assumption we can write expression 1 with $\mu = -2\nu - 1$ by changing the order of integrations. The result is

$$H_{nm}(-2\nu-1, \epsilon) = \sum_{i=0}^{\nu-1} (-1)^i \langle (R/a_0)^{2i} \rangle_{nm} / \{ 2(\nu - i)(2i+1)! (\epsilon a_0)^{2\nu-2i} \}$$

$$+ \{ (-1)^{\nu}/(2\nu+1)! \} [\{ \psi(2\nu+2) - \ln(\epsilon a_0) \} \langle (R/a_0)^{2\nu} \rangle_{nm}$$

$$- \langle (R/a_0)^{2\nu} \ln(R/a_0) \rangle_{nm}] + O(\epsilon^2 a_0^2) \,, \tag{3}$$

---

*Abstract of a paper presented at the Xth Int. Conf. on the Physics of Electronic and Atomic Collisions, Paris, July 1977. A full account of the work is being prepared for publication.

† Department of Engineering Physics, The University of Electro-Communications, Chofu-shi, Tokyo, Japan. Visiting Scientist at ANL, 1972–1974.

‡Nippon Electric Co., Ltd., Minato-ku, Tokyo, Japan.

where $\langle A \rangle_{nm} = \int d\vec{r} \int d\vec{r'}\, \rho_{nm}^{*}(\vec{r'})\, A(\vec{r},\vec{r'})$, $\vec{R} = \vec{r} - \vec{r'}$ and $\psi(x)$ is the diagamma function. For $\mu = -2\nu$, similar procedures show that $H_{nm}(-2\nu, \epsilon)$ can be expressed in terms of $\langle (R/a_0)^{2i} \rangle_{nm} (i = 0, \ldots \nu - 1)$ and $\langle (R/a_0)^{2\nu - 1} \rangle_{nm}$. In Table 1 we summarize our results. The integral for $\mu = 0$ is proportional to the exchange integral, as discussed by Lassettre and Dillon.[1] The integral for $\mu = -3$ is the most interesting because total scattering cross sections can be written in terms of it. In general, one can identify each integral as a simple atomic (or molecular) property.

Table 1. Operators Characterizing Integrals $H_{nm}(\mu, \epsilon)$

μ	Operator	Remarks
0	$(\pi/2)(R/a_0)^{-1}$	Exchange integral
-1	$-\ln(R/a_0)$	Polarization (of lights emitted after collision), average deflection (of a charged-particle beam)
-2	$(\pi/4)(R/a_0)$	
-3	$(1/6)(R/a_0)^2 \ln(R/a_0)$	Total cross section, average deflection
-4	$(\pi/48)(R/a_0)^3$	
-5	$(1/120)(R/a_0)^4 \ln(R/a_0)$	Polarization, average deflection

A previous report[2] applied the integral for $\mu = -3$ to the total cross section for elastic scattering of fast charged particles. Similarly, the total cross section $\sigma_{nm}(v)$ for inelastic scattering can be written in terms of $H_{nm}(-3, K_{min})$, i.e.,

$$\sigma_{nm}(v) = 8\pi a_0^{\,2} (e^2/\hbar v)^2 \left[\{ -\ln(K_{min} a_0) + \psi(4) \} M_{nm}^{\,2} \right.$$

$$\left. + (1/6) \langle (R/a_0)^2 \ln(R/a_0) \rangle_{nm} + O(K_{min}^{\,2} a_0^{\,2}) \right] , \qquad (4)$$

where $\hbar K_{min}$ is the minimum momentum transfer, and v is the velocity of the incident particle, and $M_{nm}^{\,2}$ is the squared dipole matrix element measured in

atomic units. Here we have used the relation $\langle (R/a_0)^2 \rangle_{nm} = 6\, M_{nm}^2$.

Equation 4 expresses the cross sections in terms of the transition density directly, and thus bypasses the form factor. This may be advantageous in some numerical computations because some theories can produce the transition density (as opposed to wavefunctions) of atoms and molecules. (For example, see Ref. 3.)

For the hydrogen atom we have

$$(1/6)\langle (R/a_0)^2 \ln(R/a_0) \rangle = \begin{cases} -(2^{14}/3^{10})\,[-2\ln(3/2) + 2\psi(4) + \psi(6) + \gamma]\,, & \text{for 1s}\rightarrow\text{2p excitation} \\ 2^{12}/(5\times 3^{10}) & \text{for 1s}\rightarrow\text{2s excitation}\,, \end{cases}$$

in agreement with the standard calculation, making use of the form factors. Using Hartree-Fock wavefunctions,[4] we have computed integrals for the elastic scattering of the first row atoms in the periodic table and some excitation cross sections for helium.

References

1. E. N. Lassettre and M. A. Dillon, J. Chem. Phys. 59, 4778 (1973).
2. M. Matsuzawa and M. Inokuti, Electron and Photon Interactions with Atoms, H. Kleinpoppen and M.R.C. McDowell, Eds., Plenum Press, New York p. 595 (1976).
3. C. W. McCurdy and V. McKoy, J. Chem. Phys. 61, 2820 (1974).
4. E. Clementi, IBM J. Res. Div. Suppl. 9, 2 (1965).

INTERPRETATION OF AVOIDED-CROSSING PATTERNS OF THE MAXIMUM-AMPLITUDE TRAJECTORY FOR LOW-ENERGY Li^+-He SCATTERING*

Smio Tani† and Mitio Inokuti

The low-energy phase shifts in the Li^+-He scattering are investigated in detail, using the Sutherland potential model to simplify the numerical work. Comprehensive data on phase shifts are analyzed in terms of the resultant maximum-amplitude trajectory (MAT) (introduced in Ref. 1). Two factors control the behavior of MAT at low energies: The first is the resonance-tunneling through the centrifugal barrier, and the second is the applicability of the JWKB approximation in a wide domain of linear and angular momenta. The second factor is a consequence of the fact that the attractive potential between a Li^+ ion and a He atom is very strong. In the MAT diagram, the avoided-crossing patterns mark those areas in which an interplay between the two factors, as well as significant features in the differential cross section, occurs. Because the attractive potential is very strong and the reduced mass is large, many partial waves contribute significantly, even at low energies, and this makes a quantum-mechanical effect less noticeable. An avoided-crossing pattern marks the position at which a clear manifestation of quantum-mechanical effect occurs.

Introduction

The existence of seven bound states (vibrational levels of the bound molecule) with zero angular momentum in the Li^+-He system clearly indicates the strong attraction between Li^+ and He. In fact, if the angular momentum ℓ is equal to or less than 16, there is at least one bound state. When the phase shift is examined for a fixed linear momentum k as a function of ℓ, it is seen to be large in the domain of large ℓ, even when k is small. If the phase shift is examined for a fixed ℓ as a function of k, it is found to be large even when k is fairly large, if ℓ remains less than, say, 30. We have studied the low-energy ion-atom scattering in the Li^+-He system and have found that there are two controlling factors which crucially affect the behavior of the system.

*Paper presented at the Xth Int. Conf. on the Physics of Electronic and Atomic Collisions, Paris, July 1977.

†Consultant RER Division. Present address: Physics Department, Marquette University, Milwaukee, Wisconsin 53233.

The first factor is a resonance-tunneling through the centrifugal barrier that can occur if neither k nor ℓ is large. The attractive part of the Li^+-He interaction potential is not of long range, and consequently the centrifugal potential dominates at large distances, making the effective potential, i.e., the sum of the interaction and centrifugal potentials, repulsive. At intermediate distances, the attractive potential dominates, and consequently, there is a peak of the effective potential. Let us consider the phase shift δ as a function of linear and angular momenta, k and ℓ,

$$\delta = \delta(k, \ell) \ . \tag{1}$$

If the wavefunction outside the potential barrier resonantes with that inside, δ varies abruptly by an amount approximately equal to π in a small interval. For a fixed ℓ, δ rises rapidly with increasing k; for a fixed k, δ falls rapidly with increasing ℓ.

The second controlling factor is the applicability of the JWKB approximation, which is valid except in the vicinity of a classical turning point. Generally speaking, the JWKB approximation is applicable if the attractive potential is strong and the local de Broglie wavelength is short (see p. 2266 of Ref. 5). Ford and Wheeler[6,7] pointed out that the abrupt change of the phase shift resulting from a resonance-tunneling through the centrifugal barrier might not seriously hurt the over-all applicability of the JWKB approximation. This expectation is particularly true if a resonance is sharp so that the phase shift deviates from a smooth function of k and ℓ in only a small interval. The scattering amplitude is a weighted sum of the partial-wave amplitudes,

$$A(k, \ell) = \sin \delta(k, \ell) \exp [i \, \delta(k, \ell)] \ , \tag{2}$$

and remains unchanged if δ is changed by an integer multiple of π. When the discontinuity in δ is nearly equal to π, this noticeable deviation from smooth behavior may be reduced without changing the amplitude (Eq. 2) by lowering the higher branch precisely by π. Thus, if the quantum phase shift, after this smoothing procedure, agrees fairly well with the smooth JWKB phase shift, then the Ford-Wheeler argument is valid. The results reported by Krishna and

Tani[8] include an example of this situation.

The fact that a sum over many partial waves is required to determine the scattering amplitude in ion-atom scattering, even when energy E is very low, marks a characteristic difference from the general situation in electron-atom or nuclear scattering at low energies. In the latter case only a limited number of partial waves is important. Generally speaking, some typically quantum-mechanical effect should be found if we search for one near zero energy in any system. In the Li^+-He system there are many partial waves that contribute significantly, even at low energies, and although resonance-tunneling is, itself, a typically quantum-mechanical effect, it may not greatly affect the cross sections. Here we are searching for some characteristic quantum event in low-energy ion-atom scattering, which will affect the cross sections.

The Potential Model

Our earlier work[1] showed that the over-all characteristics of a given system may be shown graphically by tracing on the (k, ℓ) plane the loci of points at which

$$\delta(k, \ell) = [n \mp (\tfrac{1}{2})]\pi \tag{3}$$

for an integer n. When a curve on the (k, ℓ) plane represents the effect of an attractive (repulsive) potential, the integer n is positive (negative). When n is positive (negative), the minus (plus) sign must be used on the right side of Eq. 3. For the reasons discussed in detail in Ref. 1, such a curve on the (k, ℓ) plane is called the maximum-amplitude trajectory (MAT).

In Figure 4 of Ref. 1, the MAT's were determined for the Sutherland potential, i.e.,

$$V_S(\rho) = \begin{cases} \infty, & \rho \leq 1 , \\ -\zeta^2 \rho^{-4}, & \rho > 1 , \end{cases} \tag{4}$$

where $\rho = r/a$ measures the distance r between a Li^+ ion and a He atom in units of $a = 2.97$ a.u., which is the sum of the Li^+ and He hard-core radii.

The parameter ζ in Eq. 4 is equal to 27.0 a.u. The shape of the Sutherland potential is somewhat unnatural when compared to results of quantum-chemical calculations:[4] the Sutherland potential has a narrow sharp spike right outside the hard core which tends to exaggerate the attractive part of the potential. However, as discussed in Ref. 5, the errors incurred by using this potential may remain within an over-all limit of 10%. Since the numerical work is simpler for this potential, an extensive survey of the phase shift has been carried out.

In order to find if there is any significant difference between the behavior of a set of MAT curves based on the Sutherland potential and one based on a more realistic potential, we also examined the Lennard-Jones (8,4) potential, i.e.,

$$V_{LJ}(\rho) = \zeta^2 \rho^{-4} [(\xi/\rho)^4 - 1] , \qquad (5)$$

where $\xi = 1.036$; this value of ξ is determined so that the scattering length (at $k = \ell = 0$) assumes a value that corresponds precisely with the midpoint between the seventh and eighth zero-energy resonances. The MAT's obtained by using the Lennard-Jones potential are shown in Figure 1. When Figure 1 is compared with Figure 4 of Ref. 1, we find little difference among the main MAT features obtained by using the two potentials. If

$$\ell < 37.68 , \qquad (6)$$

there is a peak of the effective potential outside the hard core. Otherwise, the effective potential decreases monotonically outside the hard core without producing any peak.

The Vertical Cliff in the Constant-k Profile

The phase shifts have been surveyed in the domain defined by $0 \leq k \leq 15$ and $0 \leq \ell \leq 40$. A curve that shows $\delta(k,\ell)$ as a function of ℓ for a fixed value of k will be called the constant-k profile hereafter. Figure 2 is based on the sixteen constant-k profiles for k from 0 to 15 with an interval of $\Delta k = 1$.

Levinson's theorem states that the zero linear momentum phase shift $\delta(0,\ell)$ is equal to π times the number N_b of the bound states with the same

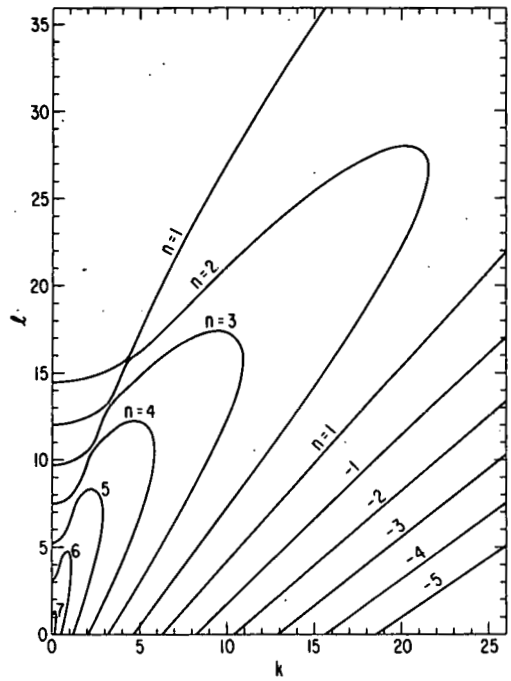

FIG. 1.--The MAT's determined from the Lennard-Jones potential defined by Eq. 5.

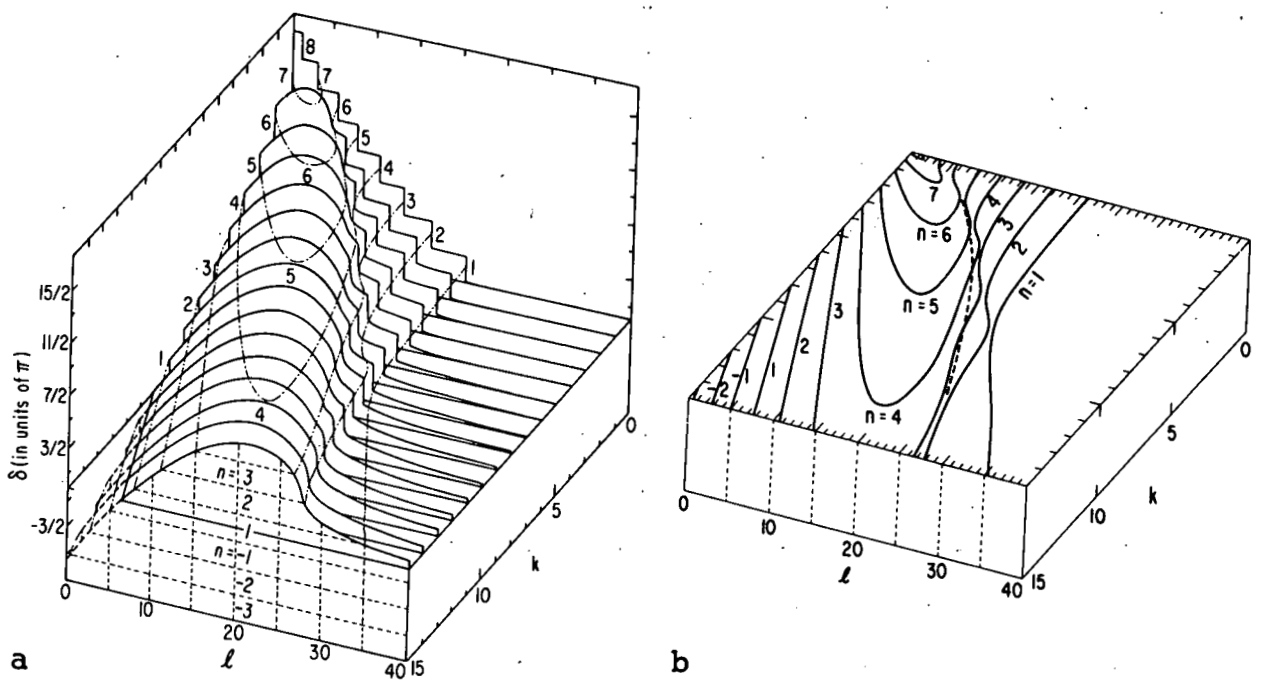

FIG. 2.--a) Three-dimensional graph of phase shifts obtained from the Sutherland potential (Eq. 4). b) The MAT's for the Sutherland potential shown using the (k, ℓ) coordinates on the base plane, $\delta = 0$, Figure 2a; redrawn from the data presented in Figure 4 of Ref. 1.

angular momentum quantum number ℓ, i.e.,

$$\delta(0,\ell) = \pi N_b(\ell) \ . \tag{7}$$

Since N_b in Eq. 7 is an integer, the constant-k profile at k = 0 is a step function of ℓ. A sharp rectangular edge marks the value of ℓ for which a zero-energy bound state exists. The radial quantum number n (n = 1, 2..., 8) is larger than the number of nodes of the bound-state wavefunction by one.

As k increases, the sharp rectangular edges are rounded. Unless they are completely rounded, one observes a "vertical cliff" in a constant-k profile. Such a vertical cliff appears along a smooth curve on the (k,ℓ) plane. This smooth curve originates from a bound-state trajectory obtained when E is negative; for $E < 0$, a Regge trajectory may be determined on a plane using $|E|^{\frac{1}{2}}$ for the abscissa and ℓ for the ordinate. When this trajectory is extended to positive E, we obtain the above-mentioned curve along which a vertical cliff moves; hence, a vertical cliff marks the value of ℓ at which a MAT is located. The rounding process starts to develop for large n with small values of k; e.g., at k = 2 the vertical cliff for n = 6 is completely rounded and has disappeared. However, for smaller values of n the vertical cliff remains unrounded, even when k is larger; e.g., at k = 7 the vertical cliff for n = 1 appears in a very clear-cut form. These general trends agree with the results obtained by Catlow et al.[2]

It is important to note that the ℓ-coordinate of a vertical cliff moves relatively little as k varies; i.e., the trajectory on the (k,ℓ) plane along which a vertical cliff moves has a small slope relative to the k axis. As to the behavior of the wavefunction when E is positive, we can point out that the rapid change of phase shift δ indicated by a vertical cliff is caused by a resonance-tunneling through the centrifugal barrier. Accordingly, the part of the MAT accompanied by a vertical cliff in the constant-k profile will be called the resonance-tunneling-effect representative. The slope of the resonance-tunneling-effect representative is small relative to the k axis.

The JWKB Approximation of Phase Shifts

Krishna and Tani[8] examined two constant-k profiles at k = 8 and k = 9 and compared the quantal and the JWKB phase shifts. As shown in Figure 2 of Ref. 8, orbiting occurs when k = 9 and $\ell = 21.55$. The height of the peak produced by the sum of the interaction and centrifugal potentials becomes equal to the value of energy E = 81.0. When the value of ℓ is in the domain

$$21.55 < \ell < 27.96 , \tag{8}$$

the wavefunction oscillates in two separate domains. Because condition 6 is satisfied everywhere in domain 8, there is a peak of the effective potential outside the hard core. There are three classical turning points: The wavefunction oscillates outside the outermost turning point, as well as in the domain bounded by the other two turning points.

When ℓ is equal to or larger than 27.96, the centrifugal potential becomes so large that the inner region in which the wavefunction oscillates disappears. In this domain the quantal phase shift and the JWKB phase shift agree very well with each other. If ℓ is less than 21.55, the energy E = 81.0 is higher than the curve of effective potential everywhere outside the hard core; hence, the wavefunction oscillates everywhere outside the hard core, and the classical turning point is located at the outer surface of the hard core, $\rho = 1$.

A vertical cliff appears at $\ell = 23.5$ in the constant-k profile for k = 9. As remarked in the preceding section, this is due to the resonance-tunneling through the potential barrier, and it occurs in domain 8 as it should. By using the data presented in Figure 2 of Ref. 8, we can show that the quantal phase shift may be smoothed by applying the procedure sketched in the introduction. The branch of the original quantal phase shift in the domain $\ell < 23.5$ will be lowered by precisely π to obtain a much smoother function of ℓ. The smoothed quantal phase shift thus obtained agrees with the corresponding JWKB phase shift in domain 8 within an error limit of 15° or so. Even though a resonance-tunneling through the centrifugal barrier is quantum-mechanical by itself, the amplitude calculation based on the JWKB (semicalssical) phase

shift may still be considered a useful approximation, a situation which is a consequence of having a strongly attractive potential, as Ford and Wheeler expected.[6] (Compare Fig. 3 of Ref. 6 with Fig. 2 of Ref. 8.)

The quantal phase shift for $k=9$ becomes equal to $\pi/2$ at $\ell=25.4$, and one MAT must be located here. Its radial quantal number n must be equal to unity according to Eq. 3. As shown by the constant-k profiles between $k=9$ and $k=15$ in Figure 2, the $n=1$ MAT in the k domain $k \geq 9$ is lying on a smooth curve on the (k,ℓ) plane. As shown in Figure 2 of Ref. 8, the JWKB phase shift for $k=9$ takes the value $\pi/2$ at ℓ slightly below 25.4. The constant-k profiles in Figure 2 show that the part of the $n=1$ MAT in the k domain $9 \leq k \leq 15$ is found in an area in which the quantal phase shift is smoothly changing as a function of ℓ for a fixed k and completely free of a vertical cliff. Because this part of the MAT is accompanied by the events in its close vicinity so that the JWKB phase shift becomes equal to $\pi/2$, we call it the semiclassical-effect representative. Note that the semiclassical-effect representative has a much larger slope than the resonance-tunnelling-effect representative does.

The Avoided-Crossing Pattern of the MAT

The avoided-crossing pattern with its center located at $k=7.9$ and $\ell=23$ is a typical example, and similar explanations apply to any other avoided-crossing pattern of the MAT.

In Figure 2 it is observed that the $n=1$ MAT, which is accompanied by a vertical cliff, and hence is the resonance-tunneling-effect representative, follows a smooth curve in the k domain $0 \leq k \leq 7$. When this smooth curve on the (k,ℓ) plane is extended beyond $k=7$, we find a gap that occupies the k domain $7 < k < 9$. After the gap, however, one sees again a similar smooth curve in the k domain $9 \leq k \leq 12$. This second segment of what is apparently the same curve is followed by the $n=2$ MAT, and is the resonance-tunneling-effect representative accompanied by a vertical cliff. The curve discussed here has a fairly small slope relative to the k axis.

The $n=1$ MAT in Figure 2 is the k domain $9 \leq k \leq 15$ is free from a vertical cliff and is the semiclassical-effect representative. When we extend the smooth curve on the (k,ℓ) plane, followed by this portion of the $n=1$ MAT, to smaller values of k, we find a gap around $k=8$. However, the same smooth curve is recovered in the k domain $6 \leq k \leq 7$ and followed by the $n=2$ MAT, which is also free of a vertical cliff and the semiclassical-effect representative. The slope of this curve is remarkably large, relative to the k axis. At the center of the gap region we find the center of the avoided-crossing pattern.

The avoided-crossing pattern is produced by the interplay of the $n=1$ and $n=2$ MAT's. Below the avoided-crossing center, i.e., $k<7.9$ and $\ell<23.0$, the $n=1$ MAT has larger values of the ℓ-coordinate than the $n=2$ MAT. Since the $n=1$ MAT is the resonance-tunneling-effect representative and its slope relative to the k axis is small, and since the $n=2$ MAT is the semiclassical-effect representative and its slope is large, the $n=2$ MAT approaches the $n=1$ MAT from below, tending to become confluent at the avoided-crossing center. Above the avoided-crossing center, i.e., $k>7.9$ and $\ell>23.0$, the $n=1$ MAT gains its slope by becoming the semiclassical-effect representative, while the $n=2$ MAT loses its slope by becoming the resonance-tunneling-effect representative.

Once we understand the basic mechanism by which an avoided-crossing is caused among the MAT's in the case of the Sutherland potential, we may turn to the more realistic Lennard-Jones (8,4) potential and understand how the avoided-crossing patterns of the MAT's in Figure 1 are produced. The close vicinity of an avoided-crossing pattern is influenced by two factors: (i) the JWKB phase shift is close to one of the values specified by Eq. 3, and (ii) a resonance-tunneling is bound to occur.

Krishna and Tani[8] examined the constant-k profile for the Sutherland potential at $k=8$, which is close to the k-coordinate of the avoided-crossing center at $k=7.9$ and $\ell=23.0$. As the data presented in Figure 1 of Ref. 8 show, the Ford-Wheeler argument fails in such an ℓ-domain, although it may be justified if k is changed to $k=9$. Thus, a deviation from the semiclassical theory occurs more extensively near an avoided-crossing pattern of MAT's.

Concluding Remarks

An avoided-crossing pattern of MAT's is produced by an interplay of two factors. The first factor is that up to a certain value of k near $k=0$ a resonance-tunneling through the centrifugal barrier occurs. It is tied to the respective zero-energy bound states at $k=0$; and the values of k and ℓ at which it occurs are closely related to the corresponding Regge trajectory that may be determined when E is negative. The second factor is that, owing to the large strength of the attractive potential, the JWKB approximation is valid in a wide domain of the (k,ℓ) plane.

A large deviation from the JWKB approximation may occur in the close neighborhood of an avoided-crossing pattern. Let us briefly mention our study of the scattering cross sections without touching on its details. The neighborhood of a particular energy that coincides with the center of one particular avoided-crossing pattern produced by the Sutherland potential has been scanned, and the features of the cross sections have been examined. The feature that appears in the total cross section is relatively insignificant. A resonance-like rapid change occurs in a particular partial wave as k sweeps past the value at the avoided-crossing center. However, because there are many other partial waves involved, there is a large background amplitude produced by other partial waves; consequently, the feature in the total cross section produced by a particular partial wave becomes a relatively small portion of an otherwise smooth function of E. On the other hand, in the differential cross section for backward scattering, the background becomes small because of the substantial cancellation of contributions from both even and odd ℓ's. Thus, there is a remarkable feature in the differential cross section. In these respects, an avoided-crossing pattern of the MAT's marks the position at which a remarkable quantum-mechanical effect may be expected in low-energy ion-atom scattering.

Acknowledgement

The authors express their gratitude to Y. M. Jan for the assistance rendered in preparing Figure 2.

References

1. Smio Tani and Mitio Inokuti J. Chem. Phys. 61, 4422 (1974).
2. G. W. Catlow, M. R. C. McDowell, J. J. Kaufman, L. M. Sachs and E. S. Chang, J. Phys. B3, 833 (1970).
3. W. F. Morrison, G. R. Akridge, H. W. Ellis R. Y. Pai, E. W. McDaniel, L. A. Viehland and E. A. Mason, J. Chem. Phys. 63, 2238 (1975).
4. I. R. Gatland, W. F. Morrison, H. W. Ellis, M. G. Thackson, W. E. McDaniel, M. H. Alexander, L. A. Viehland and E. A. Mason, J. Chem. Phys. 66, 5121 (1977).
5. S. Tani and M. Inokuti, J. Chem. Phys. 54, 2265 (1971).
6. K. W. Ford and J. A. Wheeler, Ann. Phys. (N.Y.) 7, 259, 287 (1959).
7. R. B. Bernstein, Adv. Chem. Phys. 10, 75 (1966).
8. V. S. Krishna and S. Tani, Argonne National Laboratory Radiological and Environmental Research Division Annual Report, July 1973–June 1974, ANL-75-3, Part I, p. 124.

REMARKS ON THE FUTURE OF ATOMIC-COLLISION THEORY*

Mitio Inokuti

Important problems in inelastic collisions of electrons with atoms, ions, and molecules, as well as in related topics, are pointed out. Possible lines of approach are suggested.

Quantum-Defect Theory and Its Future

In a Rydberg state of an atom or molecule, there is one electron moving in a large orbit around an ion core A^+ that consists of nuclei and tightly bound electrons. That single electron spends most of the time far outside the core. The energy level E_n measured from the ground state of the whole system A may be written as $E_n = I - R/(n^*)^2$, where I is the ionization energy, R = 13.6 eV is the Rydberg unit of energy, and n^* is called the effective quantum number. If A^+ is a point charge (i.e., if A is a hydrogenic atom), n^* is the principal quantum number n itself. If A^+ is a closed shell (such as in Na^+), then one sets $n^* = n - \mu$ and calls μ the quantum defect. The quantity μ depends on the orbital quantum number and is an index of the difference between the field of A^+ and that of a point charge. So long as $I - E_n \ll I$, μ is insensitive to E_n. If A^+ has an internal structure, there are many ionization energies I_α ($\alpha = 1, 2, 3 \ldots$), each corresponding to a different quantum state of A^+. In Ar^+, for example, there are two I_α's corresponding to $J = \frac{1}{2}$ and $J = \frac{3}{2}$, even within the lowest-energy configuration $3s^2 3p^5\ ^1P$. If A^+ is a molecular ion, there are numerous I_α's specified by rotational and vibrational quantum numbers; then one writes $E_n = I_\alpha - R/(n - \mu_\alpha)^2$ and obtains a set of μ_α, each corresponding to different I_α. The totality of μ_α may be considered as describing the interactions of an electron with the ion core A^+.

The quantum defect also concerns the continuum states of the system $e - A^+$, i.e., the collision of an electron with A^+. The phase shift at zero collision energy is given as $\pi\mu + \eta$, where μ is the quantum defect at $E_n \to I$

*A summary of seminars given on various occasions. Similar material was published in Butsuri (Bull. Phys. Soc. Japan) 32, 273 (1977) in Japanese.

and η is the analytically known phase shift for a pure Coulomb field.

A comprehensive treatment of the quantum defect and of related collision quantities is known as the quantum-defect theory (QDT), developed by Seaton, Fano, Lu, and others (see, for example, Ref. 1). Recent years have seen remarkable progress in the QDT applications to atomic and molecular spectra, especially in the multichannel case, in which A^+ has an internal structure.

There are now at least two principal directions to which QDT must be extended. First, one should develop treatments of Rydberg states under the influence of external agents such as, for instance, an electric or magnetic field. Another, more complicated, example is the interaction of a Rydberg state with another atom or molecule. This problem was first treated by Fermi[2] in the interpretation of pressure shifts of spectral lines due to Rydberg states, and has recently been extensively studied by many workers in both theory and experiment. A more advanced problem along these lines concerns the so-called excess electrons in nonmetallic solids or liquids—a matter of intense interest in radiation chemistry and other contexts. Examples are electrons in liquid hydrocarbons and polarons in solids. The state of an excess electron may be viewed as an extremely perturbed Rydberg state. An analysis of this problem from the QDT standpoint may be highly profitable. In this respect, it is heuristic to recall that the QDT had a successful application to the band theory of crystals.[3]

Second, one should address the problem of two (or more) Rydberg electrons. It is true that photoabsorption by A seldom results in two excited or ionized electrons, but e-A collisions at sufficiently high energies frequently lead to ionization, i.e., a final state consisting of A^+ and two electrons with modest kinetic energies. Even when the outcome is not that drastic, one often sees an electronic excitation, i.e., a final state A^*+e. In this instance, the scattered electron and the excited electron must have experienced a period of time in which they shared comparable energies within the field of A^+. (This period is unusually long when a resonance is involved.) Such an intermediate state of the inelastic collision may be viewed as a two-electron Rydberg state.

Consequently, it is important to develop a treatment of the motion of two electrons in a Coulomb-like field of A^+, in order to establish a comprehensive theory of inelastic collisions. (An exception occurs when the incident electron is far more energetic than the atomic electrons; then, one may use the familiar Born approximation or distorted-wave approximations.)

Unfortunately, the two-electron problem remains poorly understood. Some of the elements of long-range correlations of an eventual theory have been established by the Wannier work[4] and its pursuant developments,[5-7] including corroborating experiments.[8,9] But there must be other crucial points to be uncovered in the future. Fano and I[10,11] have recently stressed the importance of this general problem and have indeed discussed in some detail what one might attempt to achieve its solution.

One method of approach is to use the hyperspherical coordinates. One combines the usual Cartesian coordinates $\vec{r}_1$ and $\vec{r}_2$ of the two electrons to form a set of new variables: $R=(r_1^2+r_2^2)^{\frac{1}{2}}$, $\alpha = \tan^{-1}(r_2/r_1)$ and $\theta_{12}=\cos^{-1}[(\vec{r}_1 \cdot \vec{r}_2)/r_1 r_2]$, and three other angles specifying the orientation of the whole system. The Schrödinger equation for the two electrons, expressed in these ordinates, is approximately separable into R on one hand and α and θ_{12} on the other. The dependence on R describes the size of the entire system. The range of R obviously extends from zero to infinity, and therefore, the R-part of the Schrödinger equation leads to an eigenvalue spectrum <u>containing continuum</u>, as well as discrete states. In contrast, the α- and θ_{12}-parts of the equation describe correlation of the two electrons and lead to <u>discrete spectra only</u>, because both α and θ are <u>angular variables</u> whose interval is necessarily finite.

According to Fano[12] and others, it is possible to treat the R-motion almost adiabatically, i.e., in almost the same way nuclear coordinates are treated in the Born-Oppenheimer theory of molecular structure and in the standard theory of interatomic collisions at low energies. It is fascinating to see here a formal similarity in theory between two entirely different classes of phenomena, i.e., electron-atom collisions and interatomic collisions.

R-Matrix Theory

If one pursues the idea of the QDT further, one arrives at the R-matrix theory in a broad sense.[11] In the QDT, one distinguishes the two situations, i.e., one in which an electron is far away from the ion core and the other in which the electron is moving within A^+. Only in the former situation is the close-coupling treatment suitable. In the latter situation, it is appropriate to treat the electron on a par with (valence) core electrons because all of these electrons have comparable energies and move in the same spatial extent. The R-matrix theory provides a framework by which one connects the treatment of the two situations. This idea was first advocated by Wigner and others in nuclear-reaction theory, but its application to atomic physics started only recently.[13,14] Full implementation of the R-matrix theory in atomic and molecular collisions presents many challenging problems to be attacked in the future.

Scattering by Nonspherical Potential Fields

Despite its wide range of possible applications (including all chemical reactions, for example), the theory in this area has hardly been explored, even in its very basics. For instance, standard textbooks tell much about general properties of the S-matrix, the behavior of the phase shift at low energies (as treated by the effective-range theory), Levinson's theorem (concerning the relation between the zero-energy phase shift and the number of bound states), and dispersion relations, but most of the discussion concerns spherical potentials exclusively. Indeed, a generalized version of Levinson's theorem for nonspherical potentials has been formulated only very recently by Newton.[15]

To recognize the difficulty of the problem with a nonspherical potential (which does not allow a separation of variables), one needs to recall the following point. In a three-body problem (of spinless particles), which remains a challenge in either classical or quantum mechanics, among the nine variables there are three variables describing the center-of-mass motion, and three variables describing the rotation of the system as a whole. The three remaining variables describe the internal motion. In the space of these three variables,

one has, in general, a nonspherical inseparable potential. Thus, the essence of the three-body problem is equivalent to that of a three-dimensional nonspherical-potential problem. In other words, the nonspherical-potential problem is a kind of many-body problem.

From this basic point of view, any serious approach to nonspherical-potential problems is to be encouraged. An application of the multiple-scattering method to electronic continua of molecules by Dill and Dehmer[16] is noteworthy because of its adaptability to any geometry.

An overview of electron-atom inelastic collisions

It is instructive to consider the applicability of various theories in different circumstances. Obviously, one of the decisive variables distinguishing different circumstances is the electron incident energy $(\hbar k)^2/2m$, where k is the wave number. The next variable is the incident orbital angular momentum $\ell\hbar$. If $\ell \gg 1$, the electron wave will glance at the atom at large distances. (In the classical picture, the impact parameter b is related to ℓ by $\ell = kb$).

Let us then consider a classification of collisions in terms of k and ℓ. (For further analysis, one needs classification in terms of the final-state orbital angular momentum, too. But we shall omit this in the present discussion.) For the construction of a Cartesian plane, we label the horizontal axis with $(ka_0)^2$, where $a_0 = 0.529 \times 10^{-18}$ cm is the Bohr radius. The variable $(ka_0)^2$ is the incident kinetic energy measured in Rydberg units. We label the vertical axis with $\ell(\ell+1)$, which is an index of the strength of the centrifugal potential $\ell(\ell=1)(a_0/r)^2R$, r being the electron radial position. Each point on the Cartesian plane represents a specific collision situation for which certain kinds of treatment are suitable. Thus we can make a map showing the suitability of various treatments.

Figure 1 is an example of the map, tentatively drawn for discrete-level excitations of helium: $e + He \rightarrow e + He^*$ for definiteness. Each domain is given a nickname that sounds like a country name and reminds one of a kind of treatment. I have consulted various theoretical and experimental data in drawing the boundaries, but the precise position of the boundaries is uncertain and

is subject to debates as in international politics; the map will certainly have to be improved in the future.

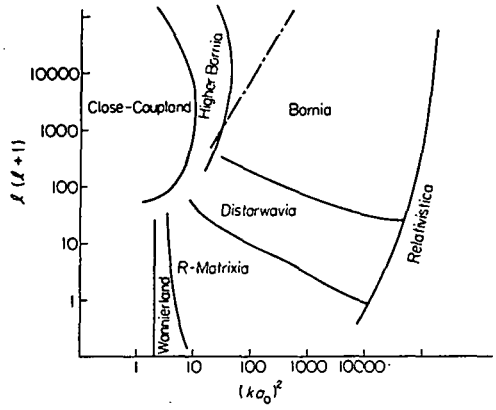

FIG. 1.--Map showing the suitability of different treatments of the process $e + He \rightarrow e + He^*$. The horizontal axis represents $(ka_0)^2$, and the vertical axis $\ell(\ell+1)$, both on logarithmic scales.

In Relativistica, there are strong relativistic and radiative effects. Bornia is the domain of the first Born approximation, limited by low values of both k and ℓ. Going to lower k values, one reaches Higher Bornia, the domain of the higher-order Born approximations, which seems to be rather narrow. Going to lower ℓ values from Bornia, one enters Distorwavia, i.e., the region of distorted-wave approximations, including eikonal and related approximations. For sufficiently high ℓ and lower k, as indicated as Closecoupland, the close-coupling method is suitable. For low k and ℓ, elements of the R-matrix theory are necessary, and this is shown as R-Matrixia. At incident energies close to inelastic thresholds, the long-range correlations between the scattered electron and the excited atomic electron are important, and call for a more advanced treatment than we possess at present. After the pioneer of the analysis of the long-range Coulomb correlations, we call the pertinent domain Wannierland. Finally, the region above the dashed curve to the left of Bornia makes small contributions to the total cross section, as can be understood from general kinematic considerations.

It is clear that the drawing of similar maps for different collisions (including atom-atom collisions and nucleon-nucleus collisions, for example)

will be useful. One merit of such a map-drawing is that it obliges us to consider all possible collision circumstances together and to relate different treatments to one another. The idea of the mapping was conceived at a Workshop on Momentum Wavefunction Determinations, Bloomington, Indiana, 1976.[17] I thank the organizers for that opportunity and Dr. E. F. Redish for stimulating discussions.

References

1. U. Fano, J. Opt. Soc. Am. 65, 979 (1975).
2. E. Fermi, Nuovo Cimento 11, 157 (1934) (Engl. transl. NTC-TRANS-II-580).
3. F. S. Hamm, Solid State Physics, Vol. 1, F. Seitz and D. Turnbull, Eds., Academic Press, New York, p. 127 (1955).
4. G. H. Wannier, Phys. Rev. 90, 817 (1953).
5. R. Peterkop, J. Phys. B 4, 513 (1971).
6. R. K. Peterkop, Theory of Ionization of Atoms by Electron Impact, translation edited by D. G. Hummer from a draft translation by E. Aronson, Colorado Associated University Press, Boulder (1977).
7. A.R.P. Rau, Phys. Rev. A 4, 207 (1971).
8. S. Cvejanovic and F. H. Read, J. Phys. B 7, 1841 (1974).
9. D. Spence, Phys. Rev. A 11, 1539 (1975).
10. U. Fano and M. Inokuti, Radiological and Environmental Research Division Annual Report, July 1975–June 1976, ANL-76-88, Part I, p. 146.
11. M. Inokuti, Photoionization and Other Probes of Many-Electron Interactions, F. Wuilleumier, Ed., Plenum Press, New York, p. 165 (1976).
12. U. Fano, Phys. Today 29(9), 32 (1976).
13. P. G. Burke and W. D. Robb, Advances in Atomic and Molecular Physics, Vol. 11, D. R. Bates and B. Bederson, Eds., Academic Press, New York, p. 143 (1975).
14. C. M. Lee, Phys. Rev. A 10, 584 (1974).
15. R. G. Newton, J. Math. Phys. 13, 1348 (1977).
16. D. Dill and J. L. Dehmer, J. Chem. Phys. 61, 692 (1974).
17. Momentum Wave Functions—1976, D. W. Devins, Ed., AIP Conference Proceedings No. 36, American Institute of Physics, New York (1977).

DEGRADATION OF SUBEXCITATION ELECTRONS IN MOLECULAR HYDROGEN

D. A. Douthat*

The yields of vibrational and rotational excitations and negative ions in molecular hydrogen are computed in a CSDA from the subexcitation spectrum and cross sections in the subexcitation range based on data from swarm and beam experiments.

A previous report[1] dealt with the degradation of keV electrons in H_2 over the energy region in which electronic energy losses predominate. The calculation has been extended to include further degradation of electrons through the energy region below E_0, the lowest electronic excitation energy. Energy is lost in this region in elastic collisions, as well as in rotational, vibrational, and simultaneous vibrational-rotational excitations. Although the scattering data to analyze the degradation below E_0 are incomplete, a set of data based on the Gerjuoy-Stein scaling of the available experimental results permits construction of a complete set of inelastic cross sections.

The Subexcitation Spectrum

If electronic excitation and ionization are the only energy-loss modes, the initial energy distribution of subexcitation electrons[2] is given by[3,4]

$$N(T) = \sum_n y(T+E_n)\,k(T+E_m,E_n) + \int_I^{\lambda} y(T+E)\,k(T+E,E)\,dE + \int_{2T+1}^{T_0} y(T')\,k(T',T+I)\,dT' + S(T); \qquad T < E_0 . \tag{1}$$

This is the usual Spencer-Fano equation in which $y(T)$ is the degradation spectrum, $k(T,E)\,dE$ the probability per unit path length that an electron of energy T loses energy E, and $S(T)$ is the source strength. When moderation by other energy-loss modes (vibration, rotation, elastic) is considered, the

*Kennedy-King College, Chicago, Illinois 60621. Consultant, RER Division.

spectrum for $T < E_0$ is given in a continuous slowing-down approximation (CSDA) by

$$y(T_0, T) = \int_T^{E_0} N(T')dT'/s(T) , \qquad (2)$$

where $s(T)$ is the stopping power. Since the energy losses for $T < E_0$ are small, the CSDA is expected to be accurate in this region.

Given the spectrum $y(T)$, the absolute yield $N_s(T_0)$ of primary excitations of state s following the complete degradation of an electron of initial energy T_0 and of all ejected electrons is given by[5]

$$N_s(T_0) = N \int_{E_s}^{T_0} y(T_0, T)Q_s(T)dT . \qquad (3)$$

The cross section for excitation of the state is $Q_s(T)$, and E_s is the threshold energy.

Vibrational, Rotational, and Elastic Energy Losses

The stopping cross sections for these modes are displayed in Figure 1. For elastic collisions, the stopping cross section $\frac{1}{N}\left(-\frac{dT}{dx}\right)$, where N is the molecular number density, is given by

$$Q^{stop}_{elastic}(T) = (2m/M)TQ_D(T) ,$$

where $Q_D(T)$ is the diffusion cross section. The values of Crompton et al.[6] for $Q_D(T)$ were used for $T \leq 2$ eV, and the data of Englehardt and Phelps[7] were used for $T > 2$ eV.

At 23°C, only the $v = 0$ vibrational level is significantly populated. The experimental data of Linder and Schmidt[8] were used for the vibrational cross section and for the simultaneous vibration-rotation excitation ($v = 0 \rightarrow 1$; $j = 1 \rightarrow 3$).

The population of rotational states is given by

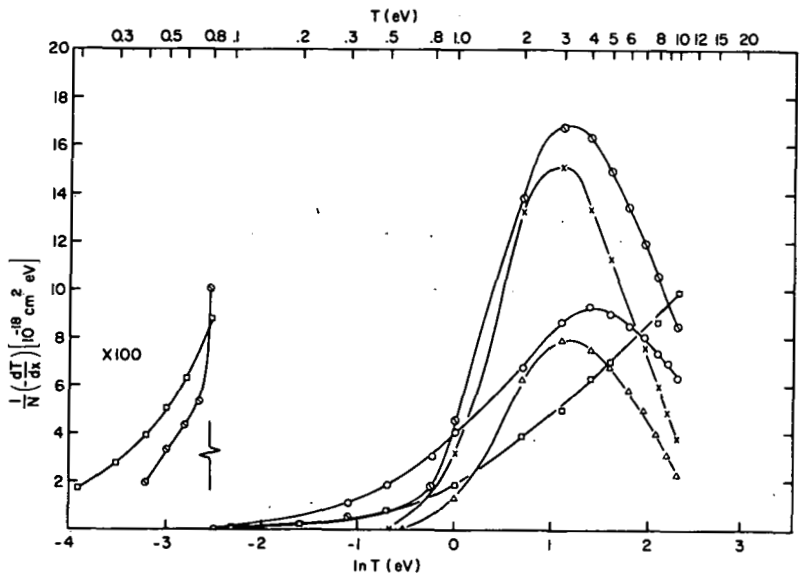

FIG. 1.--Stopping cross sections for rotational, vibrational, and elastic energy losses, and the total at 23°C for H_2. □, 2× elastic; O, $j=1\rightarrow3$; x, $v=0\rightarrow1$; Δ, $v=0\rightarrow1$; $j=1\rightarrow3$; ϕ, $\frac{1}{2}$ total at 23°C.

$$n(j) \propto (2I_t+1)(2j+1)\exp\left[\frac{-Bj(i+1)}{kT_g}\right] .$$

where T_g is the temperature and $B=7.54$ meV. The symbol I_t stands for the total spin of nuclei, i.e., the two protons in H_2; one sets $I_t=0$ for even j, and $I_t=1$ for odd j. At 23°C, the population by percent of the $j=0$ through $j=4$ states is 13.4, 66.7, 11.4, 8.1, and <0.33. For the $j=0\rightarrow2$ transition, the electron-impact data of Crompton, Gibson, and McIntosh[6] were used from threshold (0.0439 eV) to 0.50 eV. The data of Linder and Schmidt[8] for the $j=1\rightarrow3$ excitation were selected for the energy range 0.3 to 10 eV. Following Linder and Schmidt, the Gerjuoy-Stein[9,10] scaling relation was used to provide a complete set of rotational and simultaneous vibrational-rotational excitation cross sections from threshold to 10 eV for the initial states $j=0$ through 4. This procedure works well in tests using both theoretical and experimental data.

H^- Production

The dissociative electron attachment cross section for the formation of H^- from H_2 was measured by Schulz,[11] Schulz and Asundi,[12] and by Rapp, Sharp, and Briglia.[13] Since the process is only competitive below E_0, the data of Schulz and Asundi are sufficient for this calculation, although the cross

section for this 3.75 eV peak is normalized to their larger result for the 14 eV peak.

Results

Table 1 gives the G values for production of vibrational, rotational, and simultaneous vibrational-rotational excitation following complete absorption of a 10 keV electron as computed from Eqs. 2 and 3. The G value is defined by

$$G(T_0) = \frac{N_s(T_0)}{(T_0/100)} \quad .$$

The primary yield of H^- is 3.6×10^{-3}, which gives a value of 8.2×10^4 for the ratio of the primary or initial yield of positive ions to that of H^-. The amount of energy dissipated in elastic collisions is 123 eV, which follows from conservation of energy,[5] knowledge of the mean subexcitation electron energy (3.46 eV), and the mean energy per ion pair (34.0 eV).

Table 1. Vibrational and Rotational Yields $T_0 = 10$ keV at 23°C

Transition	E_s, eV	N_s	$E_s N_s$, eV	$G = N_s \times 100/T_0$
$v = 0 \rightarrow 1$	0.516	720	372	7.2
$\Delta V = 0$; $j = 0 \rightarrow 2$	0.0439	1250	55	12.5
$1 \rightarrow 3$	0.0727	3530	257	35.3
$2 \rightarrow 4$	0.1008	470	47	4.7
$3 \rightarrow 5$	0.1280	320	41	3.2
$4 \rightarrow 6$	0.1539	12	19	0.1
$v = 0 \rightarrow 1$; $j = 0 \rightarrow 2$	0.557	38	21	0.38
$1 \rightarrow 3$	0.589	112	66	1.12
$2 \rightarrow 4$	0.609	17	10	0.17
$3 \rightarrow 5$	0.633	11	7	0.11
$4 \rightarrow 6$	0.654	0.4	0.3	0.004

Acknowledgements

I have benefitted from discussions with Dr. Mitio Inokuti and correspondence with Prof. K. Takayanagi. I wish also to thank the Centre for Interdisciplinary Studies in Chemical Physics at the University of Western Ontario, where this calculation began, for their hospitality and provision of a Visiting Fellowship.

References

1. D. A. Douthat, Radiological and Environmental Research Division Annual Report, July 1975–June 1976, ANL-76-88, Part I, p. 170.
2. R. L. Platzman, Radiat. Res. 2, 1–7 (1955).
3. L. V. Spencer and U. Fano, Phys. Rev. 93, 1172–1181 (1954).
4. D. A. Douthat, Radiat. Res. 61, 1–20 (1975).
5. R. L. Platzman, Int. J. Appl. Radiat. Isot. 10, 116–127 (1961).
6. R. W. Crompton, D. K. Gibson, and A. I. McIntosh, Aust. J. Phys. 22, 715–731 (1969).
7. A. G. Englehardt and A. V. Phelps, Phys. Rev. 131, 2115–2128 (1963).
8. F. Linder and H. Schmidt, Z. Naturforsch. 26a, 1603–1617 (1971).
9. E. Gerjuoy and S. Stein, Phys. Rev. 97, 1671–1679 (1955).
10. E. Gerjuoy and S. Stein, Phys. Rev. 98, 1848–1851 (1955).
11. G. J. Schulz, Phys. Rev. 113, 816–819 (1959).
12. G. J. Schulz and R. K. Asundi, Phys. Rev. 158, 25–29 (1967).
13. D. Rapp, T. E. Sharp, and D. D. Briglia, Phys. Rev. Lett. 14, 533–535 (1965).

ELECTRON TERMINAL TIMES IN HELIUM AND HYDROGEN

D. A. Douthat*

The times required for moderation in gaseous helium and hydrogen of keV electrons to terminal energies in the range 0.1 to 1 eV are computed using the subexcitation electron energy distributions and data for the stopping cross sections in the subexcitation region. These computed terminal times are compared with results extracted from the experimental rate constant data of Warman and Sauer.

The process of electron moderation in irradiated systems is of interest for several reasons. These include establishment of the duration of the physical stage during which the kinetic energy of the incident particles and that of ejected electrons is degraded. The energy degradation occurs mainly through inelastic collisions with molecules with the concomitant production of ions and excited electronic states in atomic media, as well as excited internal states (vibration, rotation) in molecular media. Platzman[1,2] defined the temporal stages of an irradiated system and observed[3] that while moderation of electrons with kinetic energy T in excess of the threshold for electronic excitation E_0 occurs very rapidly, moderation of electrons with $T < E_0$ occurs much more slowly. Eventually, of course, the remaining free electrons are thermalized and their final energy distribution will be Maxwellian. Following the establishment of thermal equilibrium, the system enters the chemical stage.

Warman and Sauer[4,5] recently investigated electron moderation by observing the electron concentration in a microwave cavity following irradiation of a gas containing a small amount of CCl_4 with a pulse of 600 keV x rays. (A full description is contained in Ref. 5.)

Of special interest to us is the fact that Warman and Sauer were able to exact electron thermalization times by analyzing the rate constant data for electron attachment to CCl_4. In the course of theoretical studies of electron degradation in gases, we have computed the energy spectrum of free electrons

*Consultant, RER Division. Permanent address: Kennedy-King College, Chicago, Illinois.

in irradiated helium[6] and hydrogen.[7] These energy distributions, together with the known momentum transfer cross section and, for molecules, the cross sections for vibrational and rotational excitation, permit a direct calculation of mean electron terminal times. In this report we sketch the calculation and compare our results with those of Warman and Sauer.

Since the moderation of a primary electron from the initial energy of about 600 keV to E_0 proceeds rapidly and since most of the secondary electrons are ejected with low kinetic energies, we can focus our attention on the moderation in the region $T < E_0$, i.e., in the subexcitation region. In atomic gases, further energy losses occur through elastic collisions, while vibrational and rotational excitation also contribute energy losses in molecular media. The average rate of energy loss in excitation from the initial state j is given by[8]

$$\langle \frac{dE}{dt} \rangle_j = n v q_m(E) \left[\lambda \frac{mv^2}{2} - \frac{3kT_g}{2} \left(\frac{4}{3} + \frac{1}{3} \frac{d \ln q_m(E)}{d \ln v}\right)\right] , \qquad (1)$$

where

$$\lambda = \frac{2m}{M} + \frac{1}{E q_m(E)} \sum_k (E_k - E_j) Q_{jk}(E) .$$

The temperature of the gas is T_g, m is the electron mass, M is the molecular mass, N is the molecular number density, v is the speed, $q_m(E)$ is the momentum transfer cross section, and $Q_{jk}(E)$ is the cross section for excitation to state k. Summing $\langle -dE/dt \rangle_j \alpha_j(T_g)$ over j, where $\alpha_j(T_g)$ is the relative population of state j at temperature T_g, gives the total rate of energy loss $\langle -dE/dt \rangle$.

Hence, the mean time required for moderation of an electron from an initial energy T_0 to a terminal energy T is given in the continuous slowing-down approximation by

$$t(T) = \int_T^{T_0} dE \langle \frac{dE}{dt} \rangle^{-1} . \qquad (2)$$

Braglia, de'Munari, and Mambriani[9] calculated values of t(T) for low energy electrons in rare gases. These results, however, are not directly applicable

to irradiated gases since electrons are produced in the subexcitation range with a characteristic subexcitation energy distribution. This distribution, N(T)dT, was first studied by Platzman,[3] who defined it and obtained a semiempirical curve for helium. In work on helium,[6,10] and hydrogen,[7] we obtained numerical solutions of the Spencer-Fano equation for the electron-energy distribution. We found that Platzman's result for the helium spectrum is accurate to within about 10% in the subexcitation range and that the shape of the subexcitation spectrum is insensitive to the source electron energy.

We assume that the prevailing energy distribution immediately following irradiation in the Warman-Sauer experiment is the (non-Maxwellian) distribution where

$$\bar{t}(E_f) = \int_{E_f}^{E_0} p(T)\, t(T)\, dT \qquad (3)$$

and

$$p(T) = N(T) / \int_{E_f}^{E_0} N(E)\, dE \ .$$

The analysis of Warman and Sauer assumed the energy distribution in the microwave experiment to be the same as that in equilibrium swarm studies and an effective initial electron energy of about 1 eV. (Computed subexcitation spectra[3,11,6] lead to a mean subexcitation energy of about 7 eV for helium and about 3.5 eV for molecular hydrogen.[7])

Computed values of $\bar{t}(E_f)$ for the terminal energy range 0.1 to 1 eV are shown in Table 1, together with values of $\bar{t}(E_f)$ given by extension of the Warman-Sauer analysis of their rate constant data to this energy range. Since the Warman-Sauer data analysis emphasized the determination of the time required for moderation to a final energy $E_f = 1.1 \times \frac{3}{2}kT$ (the "thermalization time"), it is not surprising that the difference between theory and experiment becomes less satisfactory with increasing terminal energy. Extraction of terminal times from the more recent experiments of Warman and de Haas[12] might provide a more reliable comparison around 1 eV, but this analysis has

not yet been performed.

The values of $q_m(T)$ chosen for helium are those of Crompton, Elford, and Robertson[13] as recommended by Itikawa,[14] and are accurate to ± 2% over most of the range. The values of $q_m(T)$ above 6 eV are those recommended by Braglia et al.,[15] reduced by a constant factor to produce a smooth junction at 6 eV. Assembly of the cross sections for H_2 has been discussed in the preceding article in this report. Details of the calculations for He and H_2 will be reported in a future publication.

Acknowledgements

I wish to thank Dr. Mitio Inokuti for introducing me to this problem, for helpful discussions, and for showing me unpublished related work by himself, R. L. Platzman, and K. Takayanagi. I have also benefitted from correspondence with Dr. Y. Itikawa, Prof. A. Gilardini, and Dr. J. M. Warman.

This calculation was begun at the University of Western Ontario. The hospitality of the Centre for Interdisciplinary Studies in Chemical Physics and their provision of a Visiting Fellowship from September 1976 to August 1977 are gratefully acknowledged.

Table 1. Average Unit-Pressure Terminal Times $P\bar{t}_f$ (s · torr) in Helium and Molecular Hydrogen. (23°C)

	Helium		Hydrogen	
E_f(eV)	Eq. 3	Experiment (Ref. 5)	Eq. 3	Experiment (Ref. 5)
0.1	19×10^{-6}	12×10^{-6}	7.7×10^{-7}	6.9×10^{-7}
0.2	11	7.7	4.0	4.5
0.4	6.6	4.1	1.8	2.4
0.6	4.9	2.2	1.3	1.8
0.8	3.9	0.8	0.57	0.48
1.0	3.3	—	0.36	—

References

1. R. L. Platzman, Radiation Biology and Medicine, Ed., W. D. Claus, Addison-Wesley Press, Reading, Mass., p. 15 (1958).
2. R. L. Platzman, Radiation Research, Ed., G. Silini, North-Holland Publ. Co., Amsterdam, p. 20 (1967).
3. R. L. Platzman Radiat. Res. 2, 1 (1955).
4. J. M. Warman and M. C. Sauer, Jr., J. Chem. Phys. 52, 6428 (1970).
5. J. M. Warman and M. C. Sauer, Jr., J. Chem. Phys. 62, 1971 (1975).
6. D. A. Douthat, Radiat. Res. 61, 1 (1975).
7. D. A. Douthat, Degradation of Subexcitation Electrons in Molecular Hydrogen, this report.
8. A. Gilardini, Low Energy Electron Collisions in Gases, John Wiley and Sons, p. 33 (1972).
9. G. L. Braglia, G. M. de'Munari, and G. Mambriana, Il Nuovo Cimento, XLI, 288 (1968).
10. D. A. Douthat, Radiat. Res. 64, 141 (1975).
11. G. D. Alkhasov, Zh. Tekh. Fiz. 41, 2513 (1971) [English translation Soviet Phys. Tech. Phys. 16, 1995 (1972)].
12. J. M. Warman and M. P. de Haas, J. Chem. Phys. 63, 2094 (1975).
13. R. W. Crompton, M. T. Elford, and A. G. Robertson, Aust. J. Phys. 23, 667 (1970).
14. Y. Itikawa, Atomic Data and Nuclear Data Tables 14, 1 (1974).
15. G. L. Braglia, G. M. de'Munari, and G. Mambriani, Elastic Cross Sections of Low Energy Electrons in Rare Gases, RT, FI965)60, Comitato Nazionale Energia Nucleare, Rome (1965).

GAUSSIAN RANGES AND ENERGY STRAGGLING IN GASES*

Daryl A. Douthat† and William J. Meath‡

Energy and range fluctuations are obtained for Gaussian (long path length) distributions in several gases for incident protons and alpha particles over a substantial range of energy loss and incident energy. The calculations are based on Fano's equation for the mean square energy loss per unit path length and utilize accurate straggling and stopping-power parameters principally determined by Zeiss, Meath, MacDonald, and Dawson from dipole oscillator-strength distributions. The results are compared with experimental data on energy straggling of 2 to 4 MeV alpha particles in helium, and further experiments are suggested.

Introduction

Studies of the penetration of heavy charged particles[1-6] in matter have dealt chiefly with mean values of the range and energy loss. Recently the statistical fluctuations in range and energy loss have become subjects of considerable interest.[7-10] These fluctuations possess intrinsic as well as practical importance in several research areas, including charged-particle microscopy,[11] particle identification and energy measurement,[12] and in ion backscattering analysis of materials.[13] Despite considerable effort, discrepancies among several experiments remain,[7] and the ranges of validity of the several high energy theories are not yet completely determined. Experiments using metal foils as absorbers[14] are plagued with the difficulty of producing uniform foils since observed straggling can arise in part from the effects of foil nonuniformity.[1] On the other hand, experiments with foil absorbers can be restricted to the case in which the accumulated energy loss

*Part of this work was performed at the University of Western Ontario, London, Ontario.

†Consultant, RER Division; present address: Kennedy-King College, Chicago, Illinois 60621

‡Dept. of Chemistry and The Centre for Interdisciplinary Studies in Chemical Physics, University of Western Ontario, London, Ontario, Canada.

is a sufficiently small fraction of the incident energy so that the stopping power varies negligibly over the path length and comparison with theory is somewhat simpler.

Experiments on straggling in gases circumvent the problem of nonuniformity[14] but are often performed for very thin absorbers where the straggling is not Gaussian and the theory is more complex. We have calculated straggling widths for range and energy in ten gases for mean energy loss large enough so that the straggling distribution is Gaussian. There exists for this case a well-defined, although largely untested, theory due to Fano.[1] Implementation of the theory requires values of the stopping power parameter I_0 and the straggling parameters I_1 and S(1). These parameters are reliably obtained from the dipole oscillator strength distribution (DOSD) of the medium. Since the absorbers are "thick," i.e., the mean energy loss constitutes an appreciable fraction of the incident energy, integration over the path length is necessary. While this integration cannot be performed analytically, it is a straightforward numerical task. In view of the simplicity of implementing straggling theory for this thick-absorber case, we recommend that the high-energy theories be tested by further experiments with thick gaseous absorbers. Once the range of validity is firmly established for gases, high-energy straggling theory for foils can also be tested.

Theory

Heavy charged particles traversing matter lose energy primarily through electronic excitations and ionizations of the target medium. The cross sections for occurrence of the individual events depend on the charge and speed of the projectile. At sufficiently high energies, $\gtrsim$ 100 keV for protons, charge exchange can be neglected,[5] and the theory then simplifies considerably. Under the conditions of high incident energy and small total energy loss, the mean square energy fluctuation was given by Bohr[6]

$$\langle E^2 \rangle - \langle E \rangle^2 = \langle \Delta E^2 \rangle = 4\pi z^2 Z e^4 N \Delta R \quad , \qquad (1)$$

where z is the charge of the projectile, Z that of the target atoms, N the target

number density, and ΔR the target thickness. This theory is based on four conditions: (1) projectile speeds much greater than orbital electron speeds for the target species, (2) total mean energy loss much less than the initial projectile energy, (3) random distribution of target atoms, (4) ΔR large enough that the straggling distribution is nearly Gaussian. If the mean energy loss is large enough that the stopping power cannot be considered constant, then integration over the total path length must be performed. Bohr's formulation for the case in which integration over the path length traversed is required gives[6]

$$\langle \Delta E^2 \rangle = N \int_0^S \Sigma_n E_n^{\ 2} \sigma_n \, ds = \int_{\langle E \rangle}^{E_0} \frac{N_n \Sigma_n E_n^{\ 2} \sigma_n}{(-dE/ds)} \, dE \ , \qquad (2)$$

where E_n is the excitation energy of state n with cross section $\sigma_n(E)$, and N is the number density. We use the notation of Fano and follow closely his compact review[1] of heavy-particle straggling. Bohr provided a criterion for the occurrence of Gaussian straggling, namely, that the maximum energy loss, Q_{max}, of the heavy particle in a single collision be much smaller than the accumulated mean energy loss $\langle \Delta E \rangle$, i.e.,

$$\Delta E >> Q_{max} \cong 4 \frac{m}{M} E_0 \ ,$$

where m is the electron mass, M the heavy particle mass, and E_0 the incident heavy-particle energy. When this condition is satisfied, the energy distribution is given by

$$f(E, \langle E \rangle) = (2\pi \langle \Delta E^2 \rangle)^{\frac{1}{2}} \exp \left[- \frac{(E - \langle E \rangle)^2}{2 \langle \Delta E^2 \rangle} \right] \ , \qquad (3)$$

where the path length s and the mean energy are related in the continuous slowing-down approximation by

$$s = \int_{\langle E \rangle}^{E_0} \frac{dE}{(-dE/ds)} \ . \qquad (4)$$

The quantity (-dE/ds) is the stopping power given in the Bethe approximation by

$$\left(-\frac{dE}{ds}\right) = \frac{4\pi z^2 e^4}{mv^2} NZ \left[\ln\left(\frac{2mv^2}{I_0}\right) - \ln(1-\beta^2) - \beta^2\right], \qquad (5)$$

when shell corrections and the density effect are neglected. The path length distribution is given by

$$f(s, \langle s\rangle) = (2\pi\langle \Delta s^2\rangle)^{\frac{1}{2}} \exp\left[-\frac{(s-\langle s\rangle)^2}{2\langle \Delta s^2\rangle}\right] . \qquad (6)$$

where

$$\langle \Delta s^2\rangle = \int_{\langle E\rangle}^{E_0} \frac{N\Sigma_n {}^2\sigma_n}{(-dE/ds)3}\, dE . \qquad (7)$$

The central quantity in these relations is the mean square energy loss per unit path length, which is given by Fano as

$$N\Sigma_n E_n {}^2\sigma_n(E) = 4\pi z^2 e^4 NZ \left\{\frac{1-\beta^2/2}{1-\beta^2} + \frac{S(1)}{mv^2} \ln\frac{2mv^2}{I_1}\right\}. \qquad (8)$$

Livingston and Bethe[5] in an earlier semiempirical theory wrote Eq. 8 in terms of ionization potentials and effective nuclear charges for the various electronic shells. This can now be improved upon since the quantities I_0, S_0, I_1, and S(1) represent moments of the dipole oscillator strength distribution and sufficient information exists from a variety of experiments to establish the DOSD and its moments accurately for several gases. While the establishment of the DOSD and its moments for a given species still requires a substantial effort, computation of $\langle \Delta E^2\rangle$ and $\langle \Delta s^2\rangle$ requires little effort. It is thus a simple matter, given the parameters for the stopping power and straggling, to evaluate $\langle \Delta E^2\rangle$ and $\langle \Delta s^2\rangle$. Comparison with experiments using thick gas targets becomes a straightforward matter.

Results

We have computed $\langle \Delta s^2\rangle$ and $\langle \Delta E^2\rangle$ for the gases He, Ne, Ar, H_2, N_2, O_2, NH_3, H_2O, NO, and N_2O. The data of Saxon[15] are used for Ne,

those of Miller[16] for He, of Eggarter[17] for Ar, and those of Zeiss, Meath, MacDonald, and Dawson[2] for the other gases. Extensive tabulations of the results are planned for publication. Apparently, comparison with experiment is now possible only for the case of helium. In general, experimental straggling data are discordant[7] and often done over an energy range in which existing high-energy theories are not expected to be reliable. Table 1 displays the full-width-half-maximum for energy straggling of alpha particles in helium over the incident energy range 1.624 to 3.493 MeV. While the present results are 15 to 30% larger than those from the Bohr theory, the experimental results of Ramirez et al.,[3] which are stated as being accurate within ±5%, are still a factor of two larger. Ramirez et al. attributed the discrepancies between earlier theoretical results and their data to charge exchange. This is puzzling since the incident energy range is high enough so that charge exchange should be a small effect. It would be useful to extend the experiments for the heavier noble gases to higher incident energies in order to resolve these discrepancies. Inspection of the second term in braces of Eq. 8 shows that $2mv^2/I_1 > 1$ is a necessary condition.

Table 1. Energy Straggling of Alpha Particles in Helium

Initial energy, MeV	Final energy, MeV	FWHM, MeV Bohr	Fano	Exp. (Ref. 3)
1.624	1.324	0.0150	0.0194	0.0416
1.853	1.603	0.0145	0.0183	0.0446
2.098	1.850	0.0151	0.0188	0.0397
2.328	2.101	0.0150	0.0185	0.0417
2.578	2.376	0.0147	0.0179	0.0370
2.814	2.615	0.0151	0.0182	0.0407
3.042	2.869	0.0145	0.0174	0.0374
3.270	3.076	0.0158	0.0187	0.0370
3.493	3.321	0.0153	0.0180	0.0362

Acknowledgements

One of us (D.A.D.) would like to express gratitude to the members of the Centre for Interdisciplinary Studies in Chemical Physics at the University of Western Ontario for their hospitality and provision of a Visiting Fellowship. We also thank Dr. Mitio Inokuti for helpful discussions of straggling parameters.

References

1. U. Fano, Ann. Rev. Nucl. Sci. 13, 1 (1963).
2. G. D. Zeiss, William J. Meath, J. C. F. MacDonald, and D. J. Dawson, Radiat. Res. 70, 284 (1977).
3. J. J. Ramirez, R. M. Prior, J. B. Swint, A. R. Quinton, and R. A. Blue, Phys. Rev. 179, 310 (1969).
4. H. A. Bethe and J. Ashkin, Experimental Nuclear Physics, E. Segre, Ed., Wiley, New York, pp. 165–357 (1953).
5. M. S. Livingston and H. A. Bethe, Rev. Mod. Phys. 9, 245 (1937).
6. N. Bohr, Kgl. Danske Vidensk. Selsk. Mat.-Fys. Medd. 18, 8 (1948).
7. C. J. Scofield, N. E. B. Cowern, J. M. Freeman, and K. Parthasaradhi, Phys. Rev. A 15, 2221 (1977).
8. W. K. Chu, Phys. Rev. A 13, 2057 (1976).
9. W. K. Chu and D. Powers, Phys. Rev. 187, 478 (1969).
10. W. K. Chu and D. Powers, Phys. Rev. B 4, 10 (1971).
11. R. Levi-Setti, Scanning Electron Microscopy/1974 (Part I), Proc. 7th Ann. SEM Symp., ITT Res. Inst., pp. 125–134 (1974).
12. P. V. Ramona Murthy and G. D. Demeester, Nucl. Instrum. Methods 56, 93 (1967).
13. W. K. Chu, J. W. Mayer, M-A. Nicolet, T. M. Buck, G. Ansel, and F. Eisen, Thin Solid Films 17, 1 (1973).
14. D. L. Mason, R. M. Prior, and A. R. Quinton, Nucl. Instrum. Methods 45, 41 (1966).
15. R. P. Saxon, Phys. Rev. A 8, 839 (1973).
16. W. F. Miller, Ph.D. Thesis, Purdue University (1956).
17. E. Eggarter, J. Chem. Phys. 62, 833 (1975).

REVIEW OF CURRENT KNOWLEDGE OF IONIZATION YIELDS, STOPPING POWER, AND RELATED QUANTITIES OF RADIOLOGICAL PHYSICS

Mitio Inokuti

Work since 1973 for the International Commission on Radiation Units and Measurements toward publication of two committee reports is outlined. A manuscript for a report on ionization yields has recently been completed. Work on stopping powers and related quantities is in an initial stage.

In the beginning of 1973, the International Commission on Radiation Units and Measurements (ICRU) created a Committee on W — Average Energy Required to Produce an Ion Pair. A. Allisy (Bureau International des Poids et Mesures) was named the ICRU Sponsor, and H. Bichsel (U. of Washington) the Chairman. W. Boring (U. of Virginia), A. E. S. Green (U. of Florida), W. Gross (Columbia U., deceased in 1975), G. S. Hurst (Oak Ridge National Laboratory), M. Inokuti (Argonne National Laboratory), and D. W. Peirson (Atomic Energy Research Establishment, Harwell) were named members.

The Committee met several times (including a meeting on 14–17 October 1976 at Argonne), reviewed all the experimental and theoretical material in the literature, and produced, in early 1977, a manuscript with 162 typewritten pages of text and a bibliography. The text contains chapters on experimental methods, theory, gas mixtures, W values for gases, and ionization in solids and liquids. Experimental data for gases are thoroughly discussed, and some W values are recommended for use in dosimetry. I took up the task of writing a major part of the chapter on theory and participated in the editorial adjustment of the whole text. In August 1977, the ICRU approved, in principle, the manuscript for publication after minor revisions.

In the beginning of 1976, the ICRU called for the formation of another Committee, i.e., Committee on Stopping Powers, and designated M. J. Berger (National Bureau of Standards) as Chairman, and M. Inokuti (Argonne National Laboratory) as Vice-Chairman. H. H. Andersen (U. of Aarhus), H. Bichsel (U. of Washington), J. A. Dennis (National Radiological Protection Board, Harwell), D. Powers (Baylor U.), and J. E. Turner (Oak Ridge National

Laboratory) were appointed members.

The Committee has developed plans for a report which will include data tabulation as well as chapters on theory, experiment, the dependence of stopping power on physical aggregation and chemical combination effects, and relations of stopping power to more detailed treatment of charged-particle transport in matter. Restricted stopping power, various ranges, straggling, and degradation spectra are among related quantities to be treated. The discussion will deal with diverse charged particles, e.g., electrons, muons, pions, protons, deuterons, alpha particles, and heavy ions. Target materials to be considered include familiar gases such as air, nitrogen, argon, methane, and carbon dioxide, liquids such as water, and solids such as soft tissues, bones, plastics, inorganic scintillator crystals, and selected metals.

PROGRESS AND PROSPECTS IN PHYSICS AS A PART OF RADIATION RESEARCH*

Mitio Inokuti

It is instructive to classify radiation-physics problems into two classes. Class I problems concern the fate of the incident radiation in its penetration through matter. These problems are, in principle, easy to study, both experimentally and theoretically. To obtain the stopping power of a material for a particle, for instance, one merely measures the kinetic energy of the particle twice, i.e., before its entering a film of the material and after its emerging from it. The famous Bethe stopping-power theory uses a theorem that says that a certain average of the energy transfer from the particle to the material is independent of the electronic structure and thus bypasses detailed knowledge of individual energy-transfer processes. Indeed, much had been accomplished in the treatment of Class I problems twenty-five years ago, when the Radiation Research Society was formed.

Problems of Class II concern the fate of matter that has received energy from radiations. All questions about radiation effects belong to this class. Here one must study the state of matter in as much detail as required for the purpose. This study is much harder and also richer than in Class I problems. The creation of the Radiation Research Society marks the shift of attention from Class I problems to Class II problems.

Major events, including discoveries and important meetings, are shown in Figure 1. In the center there is a time scale. To its left, major meetings are named. To its right, major scientific achievements are indicated.

Full discussion of the chronology would explain the significance of these achievements, all initially in physics, and point out their impact on radiation research in general. The topics of discussion are diverse, and in the present summary only the following list of the topics may be included.

---

*Summary of an invited speech presented at the Symposium on Historical Views and Perspectives in Radiation Research, 25th Annual Meeting of the Radiation Research Society, San Juan, Puerto Rico, 8–12 May 1977. Publication of a full text of the speech is now being planned.

1. PENETRATION AND DIFFUSION OF RADIATIONS IN MATTER
    a. General Problems (Transport Theory and Monte-Carlo Simulations)
    b. Special Phenomena (Channeling and Blocking; Passage of Molecular Species Through Matter)
    c. Electron Degradation Spectra
2. PLATZMAN'S ANALYSIS OF THE PRIMARY ACTIVATION
3. MOLECULAR PHYSICS AS A SOURCE OF DATA
    a. Vacuum Ultraviolet Spectroscopy
    b. Photoelectron Spectroscopy
    c. Electron Collision Studies
    d. Secondary-Electron Spectra
    e. Mass Spectrometry
    f. Close Collisions between Atomic Particles, or Intershell Penetration Phenomena
    g. Collective Excitation
    h. Radiationless Transitions and Other Decays of Excited Molecules
4. EXPERIMENTS ON THE KINETICS IN GASES UNDER IRRADIATION
    a. The Jesse Effect
    b. Hurst's Analysis of Energy Pathways
    c. Laser Detection of Excited Species
5. SPATIAL DISTRIBUTION OF THE ENERGY DELIVERY
    a. The Origin of Interest
    b. Microdosimetry; Stochastic Aspects of the Energy Delivery to Small Volumes
    c. Track-Structute Analysis
6. NEW INSTRUMENTATION
    a. Pulse Radiolysis; Initial Work by Boag and Hart; Stroboscopic Method of Hunt
    b. ESR and NMR
    c. Various Uses of Lasers
7. NEW RADIATION SOURCES
    a. Electron Synchrotrons and Storage Rings, Useful for Molecular Spectroscopy and Structure Determination
    b. Field Emission and Microscopy by Charged Particles
    c. Fast Neutrons
    d. Heavy Ions
    e. Negative Pions
8. EXTENDED GOALS
    a. Atmospheric Chemistry. Behavior of U, Pu, and Th Atoms and of Non-Nuclear Pollutants
    b. Design of New Lasers (Especially for Ultraviolet to X-ray Ranges)
    c. Properties of MHD Plasmas
    d. Contributions to Fusion Research

History attests to the important role of physics as a component of radiation research. This role is twofold. First, work in physics has greatly enriched radiation research by providing new instrumentation, in a broad sense. Here, the instrumentation includes new radiation sources, such as electron synchrotrons or storage rings for generation of far ultraviolet and soft x-ray photons, and heavy-ion accelerators. Another kind of instrumentation includes various devices for measuring radiation fields, and, more importantly, radiation effects. This class may be exemplified by ESR, now used extensively and routinely for the detection of free radicals, pulse-radiolysis absorption spectroscopy, photoelectron spectroscopy, scanning-electron microscopy, tunable-laser spectroscopy, and resonance-ionization spectroscopy. Second, and perhaps more important, are the contributions of physics to the elucidation of elementary processes in the early stages of radiation action on matter. Many crucial concepts were generated in this area and have contributed greatly to the basic understanding of radiation-induced phenomena. Examples in this category are plentiful; we now recognize the importance of such concepts as collective excitation, the subexcitation electrons, the super-excited states of molecules, and the degradation (or slowing down) spectra of particles under irradiation.

The role of physics will continue to grow in these two areas. It will also be extended to respond to needs of work in new areas closely related to the traditional radiation research but which are becoming more and more important because of the acute necessity of developing diverse energy technologies. Physics will contribute greatly to the study of atmospheric pollutants (both radioactive and nonradioactive), the development of new lasers to work at shorter and shorter wavelengths, the fusion-energy technology (both in assisting its development and in assessing its environmental and health impact), and the technology of efficient and safe coal burning (including magneto-hydrodynamic-power generation), to name a few such areas.

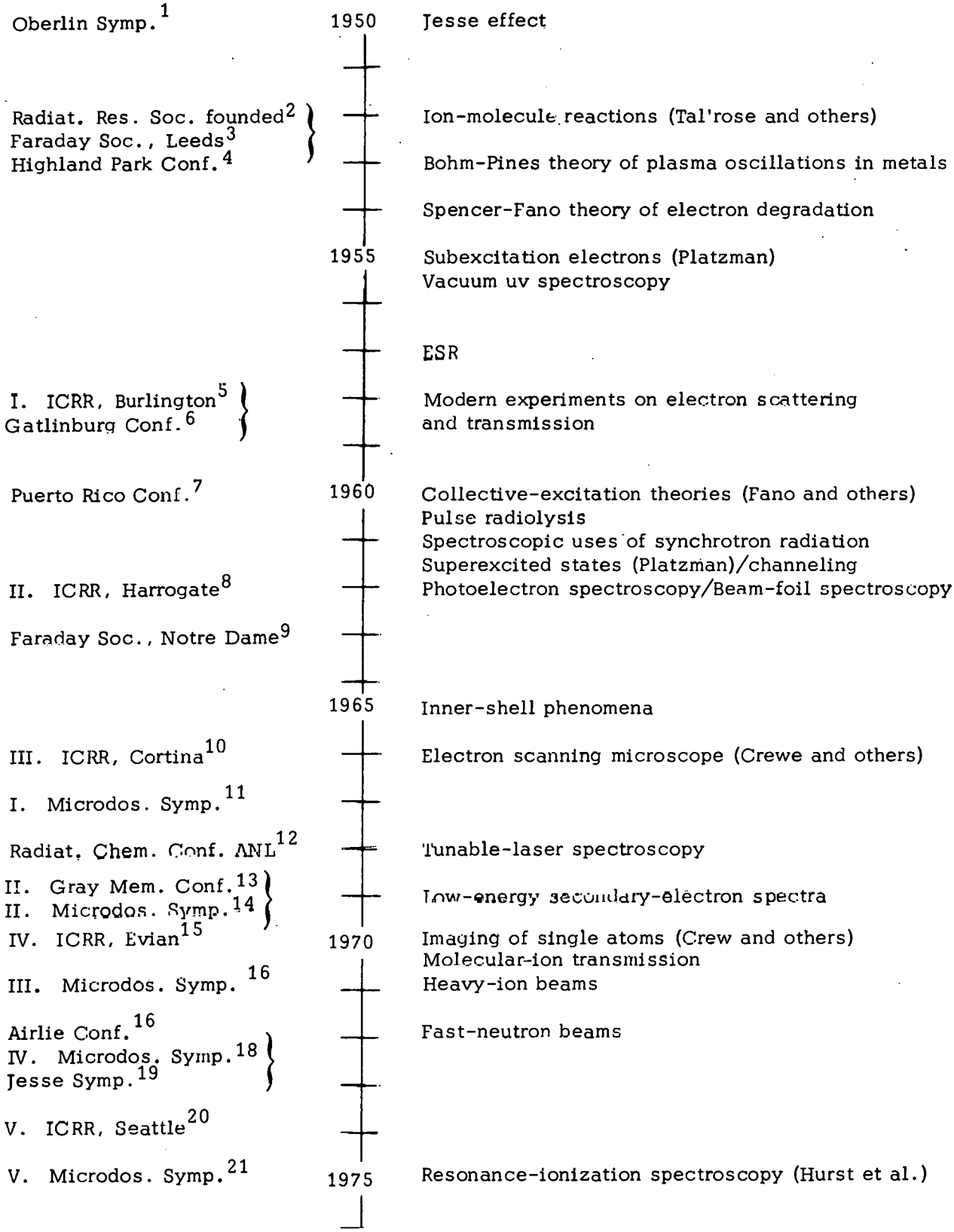

FIG. 1.--Chronology of Major Events of Interest to Radiation Physics.

References

1. Symposium on Radiobiology. The Basic Aspects of Radiation Effects on Living Systems, Oberlin College, June 14–18, 1950, J. J. Nickson, Ed., John Wiley and Sons, Inc., New York (1952).
2. For the history of the Radiation Research Society, see H. M. Patt, A. M. Brues, A. P. Casarett, A. Hollaender, J. L. Magee, O. F. Nygaard, and H. O. Wyckoff, Radiat. Res. 70, 3 (1977).
3. A General Discussion on Radiation Chemistry, Leeds, England, April 8–10, 1952. Disc. Faraday Soc. No. 12 (1952).
4. Physical and Chemical Aspects of Basic Mechnaisms in Radiobiology, Proc. Informal Conference held at Highland Park, Illinois, May 7–9, 1953, J. L. Magee, M. D. Kamen, and R. L. Platzman, Eds., National Academy of Sciences, National Research Council, Publication 305, Washington, D.C. (1953).
5. Proc. of the International Congress of Radiation Research, Burlington, Vermont, August 11–15, 1958, D. E Smith, Ed., Radiat. Res. Suppl. 1, 1 (1959).
6. Penetration of Charged Particles in Matter, Proc. Informal Conference, Gatlinburg, Tennessee, September 15–18, 1958, E. A. Uehling, Ed., National Academy of Sciences, National Research Council, Publication 753, Washington, D.C. (1960).
7. Comparative Effects of Radiation, Report of a Conference held in San Juan, Puerto Rico, February 15–19, 1960, M. Burton, J. S. Kirby-Smith, and J. L. Magee, Eds., John Wiley and Sons, Inc., New York (1960).
8. Radiation Effects in Physics, Chemistry, and Biology, Proc. Second Int. Cong. of Radiation Research, Harrogate, England, August 5–11, 1962, M. Ebert and A. Howard, Eds., North-Holland Publ. Co., Amsterdam (1963).
9. A General Discussion on Fundamental Processes in Radiation Chemistry, Notre Dame, Indiana, September 2–4, 1963, Disc. Faraday Soc. No. 36 (1963).
10. Radiation Research 1966, Proc. Third Int. Cong. of Radiation Research, Cortina d'Ampezzo, Italy, June 26–July 2, 1966, G. Silini, Ed., North-Holland Publ. Co., Amsterdam (1967).
11. Proceedings of the Symposium on Microdosimetry, Ispra, Italy, November 13–15, 1967, H. G. Ebert, Ed., EUR 3747 d-e-f, The European Communities, Brussels (1968).
12. Radiation Chemistry, An International Conference Sponsored by Argonne National Laboratory, August 12–15, 1968, Advan. Chem. Ser. 81, American Chemical Society, Washington, D.C. (1968).
13. Charged Particle Tracks in Solids and Liquids, Proc. Second L. H. Gray Memorial Conf., Cambridge, England, April 1969, G. E. Adams, D. K. Bewley, and J. W. Boag, Eds., The Institute of Physics and The Physical Society, London (1970).
14. Proceedings of the Second Symposium on Microdosimetry, Stresa, Italy, October 20–24, 1969, H. G. Ebert, Ed., EUR 4452 d-e-f, Commission of the European Communities, Brussels (1970)

15. Advances in Radiation Research, Proc. Fourth Int. Cong. of Radiation Research, Evian, France, June 28–July 4, 1970 (three volumes on Biology and Medicine and two volumes on Physics and Chemistry), J. F. Duplan and A. Chapiro, Eds., Gordon and Breach Science Publ., New York (1973).
16. Proceedings of the Third Symposium on Microdosimetry, Stresa, Italy, October 18–22, 1971, H. G. Ebert, Ed., ERU 4810 d-e-f, Commission of the European Communities, Lumexbourg (1972).
17. Physical Mechanisms in Radiation Biology, Proc. Conf. held at Airlie, Virginia, October 11–14, 1972, R. D. Cooper and R. W. Wood, Eds., CONF-721001 (Technical Information Center, Office of Information Services, U.S. Atomic Energy Commission, Oak Ridge, Tennessee, 1974).
18. Proceedings of the Fourth Symposium on Microdosimetry, Verbania Pallanza, Italy, September 1973, J. Booz, H. G. Ebert, R. Eickel, and a Walker, Eds., EUR 5122 d-e-f, The Commission of the European Communities, Luxembourg (1974).
19. Symposium on the Jesse Effect and Related Phenomena, Gatlinburg, Tennessee, November 9–11, 1973. Radiat. Res. 59, 337 (1974).
20. Radiation Research, Biomedical, Chemical, and Physical Perspectives, Proc. Fifth Int. Cong. of Radiation Research, Seattle, Washington, July 14–20, 1974, O. F. Nygaard, H. I. Adler, and W. K. Sinclair, Eds., Academic Press, Inc., New York (1975).
21. Proceedings of the Fifth Symposium on Microdosimetry, Verbania Pallanza, Italy, September 22–26, 1975, J. Booz, H. G. Ebert, and B. G. R. Smith, Eds., EUR 5452 d.e.f, The Commission of the European Communities, Luxembourg, 1976.

PUBLICATIONS BY THE STAFF OF THE FUNDAMENTAL MOLECULAR PHYSICS AND CHEMISTRY SECTION FOR THE PERIOD OCTOBER 1976–SEPTEMBER 1977.

MAJOR PAPERS

J. L. Dehmer and Dan Dill, Angular distributions of Xe 5s→εp photoelectrons: Direct evidence for anisotropic final-state interaction, Phys. Rev. Lett. 37(16), 1049–1052 (1976).

J. L. Dehmer and Dan Dill, Molecular effects on inner-shell photoabsorption: K-shell spectrum of N_2, J. Chem. Phys. 65(12), 5327–5334 (1976).

J. L. Dehmer and P. M. Dehmer, Photoelectron angular distribution and branching ratios for atomic oxygen at 304 Å, J. Chem. Phys. 67(4), 1782–1783 (1977).

P. M. Dehmer and W. A. Chupka, On the mechanism for vibrational autoionization in H_2, J. Chem. Phys. 66(5), 1972–1981 (1977).

P. M. Dehmer, W. L. Luken, and W. A. Chupka, Competition between autoionization and radiative emission in the decay of excited states of the oxygen atom, J. Chem. Phys. 67(1), 195–203 (1977).

P. M. Dehmer and J. L. Dehmer, Photoelectron spectrum of the Xe_2 van der Waals molecule, J. Chem. Phys. 67(4), 1774–1775 (1977).

Dan Dill, Jon Siegel, and J. L. Dehmer, Spectral variation of fixed-molecule photoelectron angular distributions, J. Chem. Phys. 65(8), 3158–3160 (1976).

Mitio Inokuti, The future of atomic collision theories, Butsuri [Bull. Phys. Soc. Japan] 32, 273–276 (1977) (in Japanese).

Michio Matsuzawa, Kazem Omidvar, and Mitio Inokuti, Minima in generalized oscillator strengths for initially excited hydrogen-like atoms, J. Phys. B: At. Mol. Phys. 9(13), 2173–2179 (1976).

D. Spence, Prediction of low energy molecular Rydberg states from Feshbach resonance spectra, J. Chem. Phys. 66(2), 669–674 (1977).

D. Spence, New aid to classification of Feshbach resonances. Application to Ne, Kr, Ar, and Xe, Phys. Rev. A 15(3), 883–886 (1977).

Kenneth B. Wiberg, Kevin S. Peters, G. Barney Ellison, and Joseph L. Dehmer, Rydberg states of butadiene, J. Chem. Phys. 66(3), 2224–2226 (1977).

C. E. Young, R. B. Cohen, P. M. Dehmer, L. G. Pobo, and S. Wexler, Survey of chemi-ionization reactions in accelerated atom-O_2 crossed-molecular beams, J. Chem. Phys. 65(7), 2562–2567 (1976).

CONFERENCE PAPERS AND ABSTRACTS

29th Annual Gaseous Electronics Conference, Cleveland, Ohio, 19–22 October 1976 (General Electric Lighting Institute, Nela Park, Cleveland, Ohio, 1976).

D. Spence, New applications of Schulz's trapped electron method, Abstract L5.

D. Spence, Feshbach resonances in CH_2X(X=Cl, Br, I). Classification of resonances and prediction of Rydberg states, Abstract NA7.

VIIIth Annual Meeting of the Division of Electron and Atomic Physics, Lincoln, Nebraska, 6–8 December 1976, published in Bull. Am. Phys. Soc. 21, (November 1976).

J. L. Dehmer, Photoion angular distribution from dissociative photoionization of H_2, p. 1254.

J. L. Dehmer and P. M. Dehmer, Wavelength dependence of the photoelectron angular distributions for atomic oxygen, p. 1263.

P. M. Dehmer and W. A. Chupka, Mechanism of vibrational autoionization in H_2, p. 1262.

P. M. Dehmer and W. A. Chupka, Photoionization of N_2, p. 1262.

R. H. Huebner, R. J. Celotta, and S. R. Mielczarek, Electron energy-loss analysis of carbon tetrafluoride and carbon tetrachloride, p. 1257.

Jon Siegel, Dan Dill, and J. L. Dehmer, Halogen K-shell photoionization: Calculated HX and X_2 photoelectron cross sections, random- and fixed-molecule angular distributions, p. 1263.

D. Spence, Clarification of Feshbach resonances in Ne, Ar, Kr, and Xe, p. 1252.

L. H. Toburen, S. T. Manson, and Y.-K. Kim, Secondary electron distributions from proton impact ionization of noble gas atoms, p. 1258.

ERDA Summer Study of Heavy Ions for Inertial Fusion, Claremont Hotel, Oakland/Berkeley, California 19–30 July 1976, R. O. Bangerter W.B. Hermannsfeldt, D. L. Judd and L. Smith, Eds., Report No. LBL-5543 (December 1976).

Yong-Ki Kim, Atomic and molecular physics, p. 11.

Yong-Ki Kim, Estimate of the cross section for the charge transfer between ions, p. 58.

1977 Annual Meeting of the American Physical Society, Chicago, Illinois 7–10 February 1977, published in Bull. Am. Phys. Soc. 22(1) (January 1977).

D. Spence, Feshbach resonances in CH_3X(X=cl, Br, I). Classification of resonances and prediction of Rydberg states, p. 89.

R. H. Huebner and M. E. O'Connor, Apparent oscillator strengths for water vapor, p. 89.

C. H. Chang, F. T. Chan, and Y.-K. Kim, Electron scattering by Li in Glauber approximation, p. 89.

American Physical Society Topical Conference on Atomic Processes in High Temperature Plasmas, Knoxville, Tenn., 16–18 February 1977. Program and Abstracts, published as an unnumbered Oak Ridge National Laboratory Report.

Y.-K. Kim, Relativistic effects in excitation cross sections for stripped ions.

Xth International Conference on the Physics of Electronic and Atomic Collisions, Paris, 21–27 July 1977, Commissariat a l'Energie Atomique.

Mitio Inokuti, Total cross sections for collisions between atomic particles at high relative speeds, p. 280.

Michio Matsuzawa, Seiji Mitsuoka, and Mitio Inokuti, Integrals of the squared form factors over the momentum transfer, p. 446.

Smio Tani and Mitio Inokuti, Interpretation of avoided-crossing patterns of the maximum-amplitude-trajectory for low-energy Li^+-He scattering, p. 734.

S. T. Manson, L. H. Toburen, and Y.-K. Kim, Energy distribution of secondary electrons ejected from krypton by proton impact ionization, p. 988.

Dan Dill and J. L. Dehmer, Electron-molecule scattering and molecular photoionization cross sections by multiple-scattering methods, p. 1182.

J. C. Person, R. H. Huebner, R. J. Celotta, and S. R. Mielczarek, The oscillator-strength distribution of water. A comparison of new photoabsorption and electron energy-loss measurements, p. 1214.

Vth International Conference on Vacuum Ultraviolet Radiation Physics, Montpellier, France, 5–9 September 1977, M. C. Castex, M. Pouey, and N. Pouey, Eds., VUV5, CNRS, Meudon, France.

J. L. Dehmer, Angular distributions of photoelectrons and non-thermal photoions from atoms and molecules, p. 85.

James C. Person and Paul P. Nicole, Absorption cross sections at high energies. Neopentane from 10 to 21 and ethane from 22 to 54 eV, p. 111.

Distribution of ANL-77-65 Part I

Internal:

R. G. Sachs
M. V. Nevitt
R. V. Laney
S. A. Miller
W. K. Sinclair
R. H. Huebner
R. J. Royston
D. C. Price
P. R. Fields
P. M. Failla
P. F. Gustafson
S. Wexler
S. Gordon
J. Berkowitz
T. Gilbert
M. C. Sauer
T. Dunning
K-T. Lu
G. T. Garvey
F. Clark
J. Dehmer
P. M. Dehmer
M. A. Dillon
P. Frenzen
P. Groer
Y.-K. Kim
P. Nicole
R. C. Person
R. E. Rowland
F. E. Throw
R. Schlenker
D. Spence
A. F. Stehney
O. J. Steingraber
C. Yack
Y. Band
G. Berry
J. Eland
M. Peshkin
RER Division (100)
A. B. Krisciunas (15)
E. N. Pettitt
M. Fieldhouse
ANL Contract File
ANL Libraries (5)
TIS Files (4)

External:

DOE-TIC, for distribution per UC-48 (201)
Manager, Chicago Operations Office
Chief, Chicago Patent Group
President, Argonne Universities Association
Radiological and Environmental Research Division Review Committee:
F. I. Badgley, U. Washington
W. J. Bair, Pacific Northwest Labs.
R. S. Caldecott, U. Minnesota
A. W. Castleman, Jr., U. Colorado
H. L. Friedell, Case Western Reserve U. Hospitals
E. D. Goldberg, Scripps Inst. Oceanography
D. Kleppner, Massachusetts Inst. Technology
G. H. Lauff, Michigan State U.
W. H. Smith, Yale U.
AUA Biology Representatives:
S. Abrahamson, U. Wisconsin, Madison
W. C. Ashby, Southern Illinois U., Carbondale
W. Chavin, Wayne State U.
J. Courtright, Marquette U.
W. F. Danforth, Illinois Inst. Technology
H. S. Ducoff, U. Illinois, Urbana
A. Eisenstark, U. Missouri, Columbia
D. Feir, St. Louis U.
D. L. Hartl, Purdue U.
B. H. Judd, U. Texas at Austin
A. L. Koch, Indiana U.
J. C. Loper, U. Cincinnati
W. R. Martin, U. Chicago
H. J. McDonald, Loyola U. Medical Center
R. P. McIntosh, U. Notre Dame
W. C. Myser, Ohio State U.

R. R. Novales, Northwestern U.
J. W. Osborne, U. Iowa
R. J. Perkins, U. Kansas
R. J. Robel, Kansas State U.
R. C. Rustad, Case Western Reserve U.
S. Silver, Washington U.
E. A. Stull, U. Arizona
A. S. Sussman, U. Michigan
P. W. Todd, Pennsylvania State U.
M. J. Ulmer, Iowa State U.
I. Ungar, Ohio U.
J. J. Wolken, Mellon Institute
L. Wolterink, Michigan State U.
O. W. Adams, Div. Basic Energy Sciences, USDOE
W. J. Argersinger, Jr., U. Kansas
Arkansas, U. of, Library for Medical Sciences, Little Rock
P. Ausloos, National Bureau of Standards
J. A. Auxier, Oak Ridge National Lab.
N. F. Barr, Div. Technology Overview, USDOE
E. C. Beaty, JILA, U. Colorado
B. Bederson, New York U.
M. Berger, National Bureau of Standards
C. C. Bhalla, Kansas State U.
H. Bichsel, U. Washington
R. D. Birkhoff, Oak Ridge National Lab.
W. H. Blahd, Veterans Administration Ctr., Los Angeles
R. P. Blaunstein, Div. Technology Overview, USDOE
M. J. W. Boness, Avco Everett Research Corp., Everett, Mass.
R. A. Bonham, Indiana U.
J. W. Boring, U. Virginia
W. Brandt, New York U.
A. B. Brill, Vanderbilt U.
B. H. Bruckner, National Ctr. for Radiological Health, USHEW, Rockville, MD
S. R. Bull, U. Missouri
R. A. Burnstein, Illinois Inst. Technology
W. W. Burr, Jr., Div. Biomedical and Environmental Research, USDOE
P. D. Burrow, U. Nebraska
L. K. Bustad, Washington State U.
T. A. Carlson, Oak Ridge National Lab.
R. S. Caswell, National Bureau of Standards
R. J. Celotta, National Bureau of Standards
C. Y. Chen, U. California, San Diego
J. E. Christian, Purdue U.
L. G. Christophorou, Oak Ridge National Lab.
W. A. Chupka, Yale U.
R. G. Cochran, Texas A&M U.
S. H. Cohn, Brookhaven National Lab.
Colorado, U. of, Joint Inst. for Laboratory Astrophysics (JILA)
R. N. Compton, Oak Ridge National Lab.
F. J. Congel, Macalester College
J. W. Cooper, National Bureau of Standards
M. Cooper, Div. Physical Research, USDOE
Cornell University, Library, Geneva, N.Y.
J. A. Cummings, Wisconsin State U.

A. Dalgarno, Harvard College Observatory and Smithsonian Astrophysical Observ.
D. Dill, Boston U.
M. P. Durso, Health and Safety Lab., USDOE, New York
D. L. Ederer, National Bureau of Standards
C. E. Edmund, Milwaukee, Wis.
R. D. Evans, Scottsdale, Arizona
U. Fano, U. Chicago
M. R. Flannery, Georgia Inst. Technology
W. R. Garrett, Oak Ridge National Lab.
R. Geballe, U. Washington
S. Geltman, U. Colorado
W. A. Glass, Battelle Northwest Lab.
M. Goldman, U. California, Davis
E. S. Green, U. Florida
T. A. Green, Sandia Labs.
R. Grunewald, U. Wisconsin, Milwaukee
A. J. Haverfield, Battelle Northwest Lab.
G. R. Holeman, Yale U.
Houston, U. of, Libraries
F. P. Hudson, Div. Biomedical and Environmental Research, USDOE
G. S. Hurst, Oak Ridge National Lab.
Illinois, U. of, Library, Chicago
K. H. Johnson, Massachusetts Inst. Technology
W. V. Kessler, Purdue U.
E. W. Klappenbach, USEPA, Chicago
M. O. Krause, Oak Ridge National Lab.
A. Kupperman, California Inst. Technology
C. E. Kuyatt, National Bureau of Standards
P. Lambropoulos, U. Southern California
E. N. Lassettre, Carnegie-Mellon U.
S. H. Levine, Pennsylvania State U.
W. C. Lineberger, U. Colorado
S. Lipsky, U. Minnesota
L. Lohr, Jr., U. Michigan
C. D. Lorents, Stanford Research Inst.
H. Maccabee, Lawrence Berkeley Lab.
J. H. Macek, U. Nebraska
R. P. Madden, National Bureau of Standards
J. L. Magee, U. Notre Dame
C. J. Maletskos, Gloucester, Mass.
S. T. Manson, Georgia State U.
E. A. Martell, NCAR, Boulder
Mayo Clinic Library, Rochester
S. P. McGlynn, Louisiana State U.
D. H. McKelvie, U. Arizona
V. McKoy, California Inst. Technology
J. E. McLaughlin, Health and Safety Lab., USDOE, New York
R. Meer, Massachusetts General Hospital
G. G. Meisels, U. Nebraska
J. Mentall, NASA Goddard Space Flight Center
Michigan Technological U. Library, Houghton
D. W. Moeller, Kresge Center for Environmental Health, Boston
R. D. Moseley, Jr., U. New Mexico Medical School
G. Murphy, Iowa State U.

W. G. Myers, Ohio State U. Hospital
D. P. Naismith, U. North Dakota
W. R. Ney, National Council on Radiation Protection and Measurements, Bethesda
G. Nichols, Jr., Boston, Mass.
M. J. Ohanian, U. Florida
A. L. Orvis, Mayo Clinic
J. Ovadia, Michael Reese Hospital, Chicago
J. Pan, Purdue U., Calumet Campus
A. V. Phelps, U. Colorado
M. L. Pool, Western Illinois U.
M. Pope, New York U.
C. Powell, National Bureau of Standards
A. R. P. Rau, Louisiana State U.
W. P. Reinhardt, U. Colorado
J. S. Robertson, Mayo Clinic
W. C. Roesch, Battelle Northwest Lab.
H. H. Rossi, Columbia U.
M. E. Rudd, U. Nebraska
J. H. Rust, U. Chicago
E. L. Saenger, Cincinnati General Hosp.
E. Salmon, McLean, Va.
J. A. R. Samson, U. Nebraska
R. P. Saxon, Stanford Research Inst.
R. H. Schuler, U. Notre Dame
Searle Diagnostics Inc., Des Plaines, Ill.
D. A. Shirley, U. California, Berkeley
T. W. Shyn, U. Michigan
J. B. Smathers, Texas A&M U.
F. T. Smith, Stanford Research Inst.
L. V. Spencer, National Bureau of Standards
A. F. Starace, U. Nebraska
P. M. Stone, Div. Magnetic Fusion Energy, USDOE
S. Tani, Marquette U.
H. S. Taylor, U. Southern California
L. S. Taylor, National Bureau of Standards
P. E. Thiess, Catholic U. of America
J. Thomas, Ebasco Services, Inc., New York
J. K. Thomas, U. Notre Dame
C. A. Tobias, Donner Lab., U. California, Berkeley
L. H. Toburen, Battelle Northwest Lab.
S. Trajmer, Jet Propulsion Lab.
M. Truppa, Waldie & Briggs, Chicago
A. C. Upton, SUNY at Stony Brook
D. Varney, Eastern Kentucky U.
D. A. Vroom, Gulf Energy & Environmental Systems, San Diego
R. H. Williams, U. Michigan
W. E. Wilson, Battelle Northwest Lab.
W. F. Witzig, Pennsylvania State U.
R. W. Wood, Div. Biomedical and Environmental Research, USDOE
K. F. Wylie, U. Mississippi
R. N. Zare, Stanford U.
Biblioteca sede Central, Buenos Aires, Argentina
Comision Nacional de Energia Atomica, Library, Buenos Aires, Argentina
Cancer Institute Library, Melbourne, Australia

R. A. Dudley, IAEA, Vienna, Austria
J. M. Debois, St. Norbertus Hospital, Duffel, Belgium
A. Heyndrickx, U. Ghent, Belgium
N. Brearley, U. British Columbia, Vancouver, Canada
C. E. Brion, U. British Columbia, Vancouver, Canada
Canadian Forces Base, Halifax, Canada
J. D. Carette, Universite Laval, Quebec, Canada
G. Cowper, Atomic Energy of Canada Ltd., Chalk River
Defence Scientific Information Service, Ottawa, Canada
J. W. McGowan, U. Western Ontario, London, Canada
Radiation Protection Bu., Health and Welfare Canada, Ottawa
A. G. Szabo, National Research Council of Canada, Ottawa
Toronto, U. of, Library, Canada
C. Willis, National Research Council of Canada, Ottawa
C. H. Cheng, Tsing Hua U., China
V. Cermak, Czechoslovak Academy of Sciences, Prague
Czechoslovak Atomic Energy Commission
M. Faber, Finsen Inst. Copenhagen, Denmark
P. Sigmund, U. Odense, Denmark
J. W. Boag, Sutton, Surrey, England
J. S. Briggs, U. K. AERE, Harwell, England
P. R. J. Burch, U. Leeds, England
K. Codling, U. Reading, England
K. T. Dolder, The University, Newcastle-upon-Tyne, England
J. A. Edgington, Queen Mary College, London, England
J. F. Fowler, Mt. Vernon Hospital, Northwood, England
S. J. Harris, U. Surrey, Guildford, England
C. R. Hill, Inst. of Cancer Research, Belmont, England
W. V. Mayneord, Tadworth, Surrey, England
M. R. C. McDowell, Royal Holoway College, Surrey, England
MRC Radiobiology Unit, Librarian, Harwell, England
National Radiological Protection Board, Library, Harwell, England
D. H. Peirson, U. K. AERE, Harwell, England
E. E. Pochin, National Radiological Protection Board, Harwell, England
F. H. Read, U. Manchester, England
M. J. Seaton, U. College London, England
A. J. Swallow, Christie Hospital & Holt Radium Inst., Manchester, England
J. B. West, Daresbury Lab., Daresbury, England
R. Åberg, Helsinki U. of Technology, Otaniemi, Finland
Institute of Radiation Protection, Library, Helsinki, Finland
J-P. Briand, Lab. de Physique Atomique et Nucleaire, Paris, France
J. Coursaget, CEA, Saclay, France
J.-P. Desclaux, CEN/G DRF-CPN, Grenoble, France
J. Durup, U. de Paris-Sud, Orsay, France
P. M. Guyon, U. Paris, Orsay, France
M. Tronc, Lab. de Collisions Electroniques, Orsay, France
R. Voltz, Centre de Recherches Nucleaires, Strasbourg-Cronenbourg, France
F. Wuilleumier, U. Paris, Orsay, France
R. J. Buenker, U. Bonn, Germany
G. Drexler, Institut für Strahlenschutz, Munich
H. Ehrhardt, Trier-Kaiserslautern U., Germany
J. Geiger, Trier-Kaiserslautern U., Germany
Gesellschaft für Strahlenforschung m.b.H., Frankfurt, Germany
R. Haensel, U. Kiel, Germany

H. Hotop, U. Kiel, Germany
A. Kaul, Klinikum Steglitz der F.U. Berlin, Germany
W. Mehlhorn, U. Freiburg, Germany
H. Muth, U. Saarlandes, Homburg, Germany
A. Niehaus, U. Freiburg, Germany
E. Oberhausen, U. Saarlandes, Homburg, Germany
H. G. Paretzke, Institut für Strahlenschutz, Munich, Germany
S. D. Peyerimhoff, U. Bonn, Germany
B. Sonntag, Deutsches Elektronen Synchrotron, Hamburg, Germany
K. J. Vogt, Kernforschungsanlage, Julich, Germany
R. K. Hukkoo, Bhabha Atomic Research Centre, Bombay, India
I. B. Berlman, Hebrew U., Jerusalem, Israel
Y. Feige, Israel AEC, Yavne, Israel
A. Benco, CCR EURATOM, Ispra, Italy
E. Casnati, CNEN, Rome, Italy
A. Cigna, CNEN, Rome, Italy
G. F. Clemente, CNEN, Rome, Italy
F. A. Gianturco, U. degli Studi, Bari, Italy
O. Rimondi, Istituto di Fisica, Bologna, Italy
Y. Hatano, Tokyo Inst. Tech., Tokyo, Japan
T. Higashimura, Kyoto U., Japan
H. Inokuchi, Inst. for Molecular Science, Okazaki, Japan
Y. Itikawa, U. Tokyo, Japan
S. Kaneko, U. Tokyo, Japan
M. Matsuzawa, U. of Electro-Communications, Tokyo, Japan
N. Oda, Tokyo Inst. of Technology, Tokyo, Japan
T. Sasaki, U. Tokyo, Japan
H. Suzuki, Sophia U., Tokyo, Japan
T. Takahashi, Inst. of Physical and Chemical Res., Saitama-ken, Japan
K. Takayanagi, U. Tokyo, Japan
K. Tanaka, Inst. for Molecular Science, Okazaki, Japan
T. Watanabe, U. Tokyo, Japan
Sang-Soo Lee, The Korea Advanced Inst. of Science, Seoul, Korea
Korean Atomic Energy Research Inst., Seoul, Korea
H. H. Brongersma, Philips Research Laboratories, Eindhoven, The Netherlands
F. J. de Heer, FOM Inst. for Atomic and Molecular Physics, Amsterdam, The Netherlands
J. Kistemaker, FOM Inst. for Atomic and Molecular Physics, Amsterdam, The Netherlands
M. van der Wiel, FOM Inst. for Atomic and Molecular Physics, Amsterdam, The Netherlands
P. G. Burke, The Queen's University of Belfast, Northern Ireland
M. U. Shaikh, Pakistan Atomic Energy Commission, Rawalpindi, Pakistan
R. D. Cherry, U. Cape Town, South Africa
K. Liden, Radiation Phys. Dept., Lasarettet, Lund, Sweden
National Institute of Radiation Protection, Stockholm, Sweden
G. Wedin, Inst. of Theoretical Physics, Göteborg, Sweden
A. Donath, Service Cantonal de controle des irradiations, Geneva, Switzerland
A. Gunther, CERN, Geneva, Switzerland
H. Willax, Schweizerisches Inst. fur Nuklearforschung, Zurich, Switzerland
E. Komarov, Central Res. Inst. of Roentgenology and Radiology, Leningrad, U.S.S.R.
V. Tal'roze, Academy of Sciences of the USSR, Moscow, U.S.S.R.
D. Srdoc, Rudjer Boskovic Inst., Zagreb, Yugoslavia

☆ U.S. GOVERNMENT PRINTING OFFICE: 1977 750-133/40